Tailoring nanomaterials for energy applications



Santamon Luanwuthi

Wolfson College, University of Oxford

A thesis submitted for the degree of

Doctor of Philosophy

Trinity 2019

Declaration

This thesis is submitted for the degree of Doctor of Philosophy in Materials at the University of Oxford. I confirm that this thesis is my own work and I have been indicated the data which has been obtained from others. No part or information of this thesis has been submitted or accepted for a degree in elsewhere.

Preface

Oral presentations

05/2017 **(Invited) Free-Standing Si-functionalised MWCNT Anodes for Lithium-Ion Batteries**, S Luanwuthi, A Naylor, M Roberts, V Babenko, P Bruce and N Grobert, United Kingdom-South Africa Workshop: Low-dimensional Nanomaterials, Cape town, South Africa

02/2017 **Free-standing Si-functionalised MWCNT anode for lithium-ion batteries**, S Luanwuthi, V Babenko, A Naylor, M Roberts, J Hong, P Bruce, N Grobert Oxford Department 2nd DPhil presentation 2017, Oxford, UK

Poster presentations

03/2018 **Free-Standing Binder-Free Multi-wall Carbon Nanotube/Silicon Anodes for Lithium-Ion Batteries,** S Luanwuthi, V Babenko, A Naylor, M Roberts, J Hong, J Kasemchainan, P Bruce, N Grobert, 233rd ECS Meeting, Seattle, USA

04/2018 **Free-Standing Si-CNT-SiC-C Hybrid Electrodes for Anodes in Lithium-Ion Batteries**, S Luanwuthi, V Babenko, A Naylor, M Roberts, J Hong, P Bruce, and N Grobert**,** Advanced Battery Power 2018, Munster, Germany

02/2018 **Free-standing Si-CNT-SiC-C Hybrid Electrodes for Anodes in Lithium-ion Batteries**, S Luanwuthi, V Babenko, A Naylor, M Roberts, J Hong, P Bruce, N Grobert , Oxford Department 3rd DPhil Poster Session, Oxford, UK

Publications

2020 **Flexible multi walled carbon nanotube papers for anodes in lithium-ion batteries**, S Luanwuthi, V Babenko, A Naylor, M Roberts, P G Bruce and N Grobert, *Chemical Communications*, In preparation

2020 **Free-standing Si-functionalised carbon nanotube anodes for lithium-ion batteries**, S Luanwuthi, V Babenko, A Naylor, M Roberts, J Hong, J Kasemchainan, LY Jin, N Young, P Holdway, PG Bruce, and N Grobert, *Energy storage materials*, In prepration

2017 **Vertically aligned silicon carbide nanowires as visible-light-driven photocatalysts**, J Hong, SS Meysami, V Babenko, C Huang, S Luanwuthi, J Acapulco, P Holdway, PS Grant, and N Grobert, *Applied Catalysis B*: *Environmental* **218**, 267-276 (2017)

Acknowledgement

This thesis is submitted for the degree of Doctor of Philosophy in Materials Science at the University of Oxford. I confirm that this thesis is my own work and I have indicated the data which has been obtained from others. No part or information of this thesis has been submitted or accepted for a degree elsewhere.

This thesis would not finish without the grateful contribution of many great people. The thankful acknowledgement is written to everyone who helped and supported me throughout my DPhil study. Firstly, I would like to thank my supervisor, Professor Nicole Grobert. She always shared valuable knowledge and suggestions to me. Specifically, she made me become a curious person that always asks myself 'Why I am doing this?' or 'How it is different from what others have done?' Moreover, she supported my ideas and gave me useful feedback on my research. She encouraged me to talk and to ask for help with friends in the Nanomaterials by Design group and people from other research groups. She also gave me opportunities to work with a company and a small business which helped me to learn how to present the scientific work to different levels of expertise audiences. During the three-year study, I have gained much confidence, and I am very thankful to her. I am very thankful to Professor Peter G Bruce, my supervisor, for allowing me to work in his world-class battery laboratory and with talented people in Bruce's group. He further supported me with facilities, materials, and funding that are very helpful to my research.

I owe special thanks to Dr. Viltaliy Babenko for his generosity. I would not pass the difficulties of my DPhil study without his help and assistance. He guided my research direction with worthwhile suggestions and assisted me in solving experimental problems. Although he moved to work at the University of Cambridge, he still gave very appreciated feedback while being there and was dedicated to correcting my research and my written papers. I also would like to thank you Dr. Matthew Robert

and Dr. Andrew Naylor for their contribution to my work in particular to both battery knowledge and electrochemical parts. I am obliged for their devotion to revise and edit my work. Moreover, I would like to specially thank you Dr. Barbara Maciejewska for her help to review and correct my thesis structure. I am also deeply grateful for the support I have received from her.

I am indebted for Dr. Jitti Kasemchainan for advising me in terms of the battery work. Although he was not directly responsible for supervising me, he always offered me with his help generously. I would like to give thanks to Dr. Paul Adam, Ruth Jones, Daniel Woodward, Dillon McGurty, Eoin O'Sullivan, John Ballentine and Anuchaya Montakantiwong for reviewing and amending my written work. I also would like to acknowledge Koen Evers for making the sample holder for the chemical vapour deposition experiment and Dr. Seyyed Shayan Meysami for training me on AACVD method. I am thankful to Zhenjie Mi, a summer student from Shanghai Jiao Tong University in China, for her help in the part of the freestanding silicon-carbon nanotube paperwork. I would like to thank Zsofia Lazar for her cooperation with the paperwork and group issues. I would like to thank you colleagues in Nanomaterials by Design group as well as Bruce's group for the enjoyable working environment.

I also would like to thank you David Cockayne Centre for Electron Microscopy and Oxford Materials Characterisation Services for the excellent scientific facilities. I am very thankful to Dr. Neil Young and Jennifer Holter, for training me on the electron microscope, and Dr. Phil Holdway, Dr. Colin Johnston, Dr. Liyu Jin, Greg Cook and Graham Wyatt for providing technical support. I would like to thank the Royal Thai Government Scholarship for sponsoring my DPhil study. I am also very thankful to Assistant Professor Montree Sawangphurk, who inspired me to study for a DPhil at the University of Oxford and to become a diligent and passionate Thai researcher.

This DPhil study would not fulfil with joy and happiness without Thai friends and international friends who study and work in Oxford. I owe thanks to Pattarachai Srimuk, Pawin

Iamprasertkun and Pichamon Sirisinudomkit for very useful advice and especially the beautiful moment and travel journeys we have spent together during the time of my study.

Finally, I am deeply grateful for my family and friends who always listen to me and support me in every way. This DPhil study would not have been accomplished without the dedication of my father, mother, grandmother and grandfather.

Abstract

Silicon-based materials present high theoretical capacities (4200 mAh/g), making them among the most promising materials for Li-ion battery anodes. However, the major problem with them is massive volume change (~ 300%) that occurs during cycling, resulting in pulverisation and significant capacity drop of these anode materials. Besides, the use of additives and metallic current collectors to make the anodes reduces the overall battery energy density as these components could not contribute any capacities to the battery. In this work, free-standing silicon-coated multi-wall carbon nanotube (MWCNT) anodes were developed without any polymeric binders and carbonaceous additives being added. These materials were achieved through exploiting atmospheric pressure chemical vapour deposition as well as advanced nanomaterials fabrication and processing methods. Electrodes were prepared utilising MWCNT papers (so-called buckypapers) as robust, electrically conductive flexible (22.2 S/cm) and free-standing scaffolds since the capacity of these buckypapers is too low to use as a new active material for the battery (0.3 mAh/cm^2 in the 300th cycle). Hence, these buckypapers were functionalised with silicon nanoparticles attached through a strong silicon carbide interface and coated with a protective amorphous carbon layer. The SiC interface was partially developed between Si NPs and MWCNTs as excessive SiC could reduce electrochemical capability on the material due to its low electroactivity. The coin cell battery test demonstrated a high areal capacity of up to 2.01 mAh/cm^2. These free-standing Si-CNT-SiC-C materials showed good rate capability and stability performance (0.55 mAh/cm^2 after 300 cycles with coulombic efficiency of 99.7%). As a result, the material interface design, which is the key of this work, enhances the connection of Si NPs to the MWCNT walls and addresses the issue of Si detachment. A post-mortem result also revealed the structural stabilisation of the electrode after the repeated cycling test. In addition, the pouch-cell battery was fabricated to confirm the use of this free-standing Si-CNT-SiC-C electrode without the influence of the battery component. This new anode architecture performs better than the buckypaper, thereby increasing the areal capacity by 83.3%, allowing better functionality for this material to be implemented in a full-cell battery system.

Contents

Declaration i

Preface ii

Acknowledgement iii

Abstract vi

Contents vii

List of tables xi

List of figures xii

List of Abbreviations xx

List of Symbols xxii

Chapter 1 1

Literature review 1

1.1) The basic concepts of Li-ion batteries 1

1.1.1) A lithium-ion battery as an alternative energy storage device to lead-acid, nickel-metal hydride, and nickel-cadmium batteries 1

1.1.2) Lithium-ion battery electrochemistry 3

1.1.3) Thermodynamics and kinetics related to LIBs 5

1.1.4) Theoretical cell energy and capacity calculations 7

1.1.5) The shapes of voltage profiles and their relation to phase diagrams 8

1.1.6) Main challenges of LIB development 10

1.2) Recent developments in Li-ion battery research 11

1.2.1) Alternative anode electrodes in Li-ion batteries 12

1.2.2) MWCNTs as an anode material 13

1.2.3) Silicon as an anode material 14

1.2.4) Methods for improving the performance of Si anodes 16

1.2.5) Silicon-MWCNT composites as anode materials 17

1.2.6) Silicon-amorphous carbon composites as anode materials 20

1.2.7) The development of electrode architectures 21

1.2.8) The effect of the coin-cell battery components to the battery performance 23

1.2.9) Areal capacity of the Si electrode challenge 24

1.3) Conclusions and challenges to overcome 25
1.4) References 26
Chapter 2 31
Lithiation and Volume Expansion of Silicon Anodes in Li-ion batteries 31
2.1) Crystalline silicon 32
2.1.1) Li-Si alloy in crystalline Si 32
2.1.2) Volume change and fracture induction in crystalline Si 35
2.1.3) Size-dependent fracture of crystalline Si 39
2.2) Amorphous silicon 43
2.2.1) Li-Si alloy in amorphous Si 43
2.2.2) Volume change and fracture induction in amorphous Si 45
2.2.3) Size-dependent fracture of amorphous Si 47
2.3) Conclusions 48
2.4) References 50
Chapter 3 52
Experimental methodologies 52
3.1) Synthesis methodologies 52
3.1.1) Principles of a chemical vapour deposition method 53
3.1.2) Aerosol assisted chemical vapour deposition (AACVD) 55
3.1.3) Atmospheric-pressure CVD with a gas mixture system for Si deposition 58
3.2) Characterisation techniques 61
3.2.1) Scanning electron microscopy (SEM) 62
3.2.2) Transmission electron microscopy (TEM) 63
3.2.3) Energy-dispersive X-Ray Spectroscopy (EDX/EDS) 66
3.2.4) Scanning transmission electron microscopy (STEM) 67
3.2.5) X-ray photoelectron spectroscopy (XPS) 69
3.2.6) X-ray Diffraction (XRD) 71
3.2.7) Raman spectroscopy 73
3.2.8) Thermogravimetric analysis (TGA) 74
3.2.9) Four-point-probe resistivity measurement 75
3.2.10) Galvanostatic cycling 77
3.3) Material synthesis and fabrication of electrodes in this work 79
3.3.1) Synthesis of MWCNTs 79

3.3.2) Fabrication of buckypapers 80
3.3.3) Fabrication of pure MWCNT electrodes 80
3.3.4) Synthesis of Si-CNT materials 81
3.3.5) Preparation of the Si-CNT-SiC-C nanocomposites 81
3.3.6) Fabrication of pure Si electrodes 82
3.4) Cell assembly and battery testing in this work 83
3.4.1) Fabrication of coin cell and pouch cell batteries 83
3.4.2) Battery performance testing 84
3.5) Preparation the electrode for post-cycling analysis in this work 84
3.6) Conclusions 84
3.7) References 85
Chapter 4 88
Free-standing Si-CNT anode for Li-ion batteries 88
4.1) Introduction 88
4.2) Experimental 91
4.3) Characterisation 91
4.4) Results and discussions 92
4.4.1) Morphological, structural and chemical characterisation of the MWCNTs 92
4.4.2) Morphological, structural and chemical characterisation of the buckypapers 94
4.4.3) Cell fabrication and electrochemical tests of the buckypaper electrodes 97
4.4.4) The battery design and the effect of the cell component study 99
4.4.5) Post-cycling analysis of the BP electrode 100
4.4.6) Morphological, structural, and chemical characterisation of free-standing Si-CNT electrodes 101
4.4.7) Cell fabrication and electrochemical tests of the free-standing Si-CNT electrodes 105
4.4.8) Post-cycling analysis of the free-standing Si-CNT electrode 108
4.5) Conclusions 110
4.6) References 111
4.7) Supporting information 115
Chapter 5 124
Si-CNT-SiC-C hybrid materials for anodes in Li-ion batteries 124
5.1) Introduction 125
5.2) Experimental 128

5.3) Characterisation 128
5.4) Results and discussions 129
5.4.1) Morphological, structural, and chemical characterisation of the Si-CNT-C (CH_4) material, Case I 130
5.4.2) Cell fabrication and electrochemical tests of the Si-CNT-C (CH_4) electrode, Case I 132
5.4.3) Morphological, structural, and chemical characterisation of the Si-CNT-C (C_2H_2) material, Case II 134
5.4.4) Cell fabrication and electrochemical tests of the Si-CNT-C (C_2H_2) electrode, Case II 136
5.4.5) Morphological, structural, and chemical characterisation of the Si-CNT-SiC-C material 139
5.4.6) Cell fabrication and electrochemical tests of the Si-CNT-SiC-C electrode 145
5.4.7) The battery performance of the Si-CNT-SiC-C pouch cell 149
5.4.8) Post-cycling analysis of the Si-CNT-SiC-C electrode 150
5.5) Conclusions 154
5.6) References 155
5.7) Supporting information 158
Chapter 6 168
Summary and future work 168
6.1) Summary of the research 168
6.2) Future work 172
6.3) References 176

List of tables

Table 1.1. The properties of currently used batteries, showing that LIBs have in most cases superior properties over other rechargeable batteries. 3
Table 1.2. Theoretical capacity, density, volume change, and voltage of anode materials [41]. 12
Table 1.3. Electrochemical performance of MWCNT anodes for Li-ion batteries. 14
Table 1.4. Problems and suggested solutions for Si-based anodes [74]. 17
Table 1.5. Electrochemical performance of silicon-carbon nanotube composite anodes for Li-ion batteries. 19
Table 3.1. Common silicon CVD processes classifying by pressure and temperature [10]. 59
Table 4.1. The electrical conductivity of the materials confirming outstanding electrical conductivity of BPs compared to other materials. 96
Table 4.2. The electrical conductivity of BP 45 and Si-CNT material revealing good conductivity of the free-standing Si-CNT materials compared to conventional Si electrodes. 104
Table 5.1. The conductivity of the as-prepared materials showing the good conductivity of the free-standing Si-CNT-SiC-C materials compared to other materials. 145
Table 5.2. The battery performance of all as-prepared electrodes showing the best battery performance of the Si-CNT-SiC-C electrode compared to other electrodes in this work. 154

List of figures

Figure 1.1. Comparison of different commercial batteries; a Li-ion battery has higher specific energy and specific power than other batteries [2]. 3
Figure 1.2. A diagram of the lithium-ion battery mechanism showing the movement of Li ions during charging and discharging. 4
Figure 1.3. A) Actual discharge curves (1 and 2) showing different characteristics from an ideal discharge curve [19], and B) the common discharge curve exhibiting various types of polarisation [8]. 7
Figure 1.4. Schemetric dischage curves of the electrode; A) the potential varies with the state of charge for the case where F is not zero, B) the potential is independent of the electrode composition as the value of F is zero and C) the series of multiphase reactions in which F is zero result in a set of constant voltage plateaus [1]. 9
Figure 1.5. A) A schematic graph presenting the change of the potential with the composition relating to B) the binary phase diagram at T_1 which shows the formation of an intermediate phase β and its solubility in phases α and γ [1]. 10
Figure 1.6. A schemic of SEI formation on silicon surface; the volume change of silicon causes thick SEI layers forming continueosly to cover its surface during cycling [5]. 16
Figure 1.7. SEM and TEM images of a,b) pristine vertically aligned CNTs, c-d) silicon coated vertically aligned CNTs, e,f) carbon and silicon coated vertically aligned CNTs showing their structural change after coating with Si and C, and g) a graphic image showing the final material structure [7]. 18
Figure 1.8. a-b) Structural diagrams of the silicon-carbon permanganate material; the inner void space allowed the volume expansion of Si NPs [3]. 21
Figure 1.9. A) An illustrative of the silicon-coated CNT fabric battery, B-E) images of pristine CNT and silicon coated CNT fabrics showing their flexibility, F) cycling stability, G) stress and strain testing, and H) specific strength of the as-fabricated electrode (redrawn from [4]) confirming its performance and mechanical property. 23
Figure 1.10. A) The cyclic voltammograms of 304 stainless steel, and B) XPS spectra of Fe2p and C2p after polarization at 0 V vs Li/Li^+ showing the formation of iron oxide and chromium oxide on the stainless steel during the cycling test [6]. 24
Figure 2.1. A) Phase boundary configurations during the lithiation of crystalline Si at different orientations; Si-Si bonds between (111) planes are shown as red lines. The Si-Si bond position strongly affects the thickness of the phase boundary. The Si (110) shows the thickest phase boundary because Li atoms require longer time to accumulate into the tetrahedral sites between (111) planes. The atom colours represent the charge state, *i.e.*, green indicates neutral atoms, blue indicates Si atoms, and red indicates Li atoms. The figure reproduced from Kim *et al.* 2014 [7]. B) The two-phase boundaries are formed at (100), (110) and (111) Si orientations. Red and yellow balls denote the Li and Si atoms, respectively. The valley-like structure is found at the (110) Si surface which leads to the enhancement of the Li concentration and then the high rate of the Li-Si reaction at the phase boundary. The figure adapted from Jung *et al.* 2012 [11]. 33

Figure 2.2. The two phase lithiation of crystalline Si and amorphous Si; A) the concentration of Li (green) is high at the facet of c-Si (red) and B) these Li atoms weaken Si bonds leading to the dissolution of Si atoms from the c-Si [8], C) similar to c-Si, the Li concentration is high near the interface leading to D) the easy dissolution of Si atoms from the a-Si into Li_xSi alloy[5]. 34
Figure 2.3. STEM images and SAED patterns showing the congruent phase transition from a-Li_xSi to c-$Li_{15}Si_4$ when x reaches a critical value of 3.75; (a) STEM image of a-Li_xSi nanowire, (b) atomic configuration of a-Li_xSi. (c) Electron diffraction pattern of a-Li_xSi, (d) STEM image showing the polycrystalline c-Li15Si4, (e) atomic configuration of c-$Li_{15}Si_4$, and (f) electron diffraction pattern of c-$Li_{15}Si_4$ [29]. 35

Figure 2.4. The structural change of A) crystalline Si and B) amorphous Si at different lithiation stages (t =0-15.0 ps); Si and Li atoms present as spheres in cyan and purple colour, respectively [2]. 36

Figure 2.5. The graph showing the change of volume (normalized with respect to the volume of c-Si) and density of Li_ySi alloys as a function of the Li content; the volume of the material increases linearly with the content of Li, while the density shows the opposite trend [4]. 36
Figure 2.6. The anisotropic change of crystalline silicon nanopillars with three different orientations during lithiation; silicon expanded preferably along the <110> orientation [1]. 37
Figure 2.7. Simulations of lithiation and stress induction in Si NPs. The dot-dash line represents the location of the interface. A) Radial distribution of hoop stress $\sigma_{\theta\theta}$ and von Mises stress σ_{Mises} confirms that the hoop stress is compressive at the interface and plastic yielding (σ_{Mises} = the yield stress of 1.5 GPa) is arisen in the surface layer. The inset sphere shows the Li concentration (blue and red indicate a low and high concentration of Li respectively) and the particle size before lithiation is presented as the dashed line. B) At the following lithiation, the hoop tension conversely takes place in the outer layer; as the tensile hoop stress in the surface is larger than that in the centre, it facilitates fracture from the surface [6]. C) Hoop stress contours of the cross-sections of crystalline <100>, <110>, <111> and amorphous silicon nanotubes; the tensile hoop stress concentration occurs at the surface between <110> directions in crystalline Si due to the preferential lithiation along this direction, while the homogeneous hoop stress takes place in amorphous silicon resulting in the isotropic expansion [3]. 39
Figure 2.8. The stress distribution in Si wires with the radii of A) R_0 and B) $R_{0/2}$; the size of the stress release area strongly depends on the cross-sectional radii of the material. C) The plots showing the J-integral (the strain energy release rate) near the fracture as a function of the fraction of lithiation; the J-integral strongly depends on the size of the material. Green and red circles represent the J-integral of the crack in A and B wires. σ_Y and a_0 is surface energy and the crack length in the material [6]. 41
Figure 2.9. SEM images showing the size-dependent fracture of Si nanopillar with different orientations, <100>, <110>, and <111>; red arrows indicate the initiated crack areas and all scale bars are 500 nm. The graphs present the effect of the size on the fracture ratio for Si with three orientations; the fracture ratio is described as dividing the number of fractured nanopillars by the total number of samples. The <110> exhibits the larger critical size (*ca.* 360-390 nm) for the fracture formation than others [9]. 43

Figure 2.10. A two-phase lithiation mechanism in A) a crystalline Si and B) an amorphous Si; a phase boundary between Si and Li_xSi can be observed in both the crystalline and amorphous Si, but it clearly distinguishes as a sharp interface in the crystalline material [5]. 44
Figure 2.11. Schematics showing that A) single-phase lithiation in amorphous Si leads to compressive hoop stress near the surface and tensile hoop stress inside the particle, B) single-phase delithiaiton in lithiated amorphous Si which was not crystallised into the $Li_{15}Si_4$ results in the tensile hoop stress near the surface and compressive hoop stress inside the particles and C) two-phase lithiation of amorphous Si which has a sharp interface separating two phases with different Li concentrations causes compressive hoop stress in the Si core and tensile hoop stress at the lithiated Si area (shade of grey colour represents the concentration of Li) [10]. 46
Figure 2.12. SEM images of amorphous Si nanotubes before and after lithiation; the isotropic expansion occurred both inside and outside the amorphous Si NTs [3]. 47
Figure 3.1. A schematic diagram showing mechanistic steps of the CVD process for coating a thin film on a substrate; the process includes 1) gases conveyed into a furnace, 2) intermediate reactant formed, 3) the reactant diffused through the boundary layer to a heated substrate, 4) gas adsorbed on the surface of the substrate, 5) reactions occurred at the substrate surface, 6) by-product gases desorbed from the substrate surface, and 7) exhausted from the furnace [4]. 54
Figure 3.2. A) A sonication mechanism and a cavitation formation within the liquid [2], and B) aerosol initially forming on the surface of a precursor in the aerosol generator. 56
Figure 3.3. The growth mechanism of MWCNTs - A) a tip-growth model, where MWCNTs emerge out from the bottom of the metal catalyst, pushing the catalyst particles off the substrate and B) a base-growth model, where MWCNTs start to grow from the top of the catalyst [6]. The type of growth mechanism depends on the interaction between the catalyst and the substrate. 57
Figure 3.4. APCVD setup showing the molcules of SiH_4 in the pure gas and mixture gas system; the SiH_4 molecules are surrounded by Ar molecules in the mixture gas system resulting in a reduced number of SiH_4 molecules presence in this system. 59
Figure 3.5. A schematic mechanism of Si film deposition on the substrate using SiH_4 as a precursor; the overall reaction of SiH_4 pyrolysis is exhibited. 61
Figure 3.6. The interaction between incident electrons and samples (left); when an electron beam hits on a sample surface, the interaction between electrons and the surface generate SE, BSE and X-ray radiation [8] and a schematic of scanning electron microscopy (right) [3]. 62
Figure 3.7. SEM images of Si-CNT materials at low and high magnifications. Si (higher atomic number) scatters more electrons than the lighter carbon, thus revealing brighter in the SEM image.63
Figure 3.8. A) Diagrams for imaging (left) and diffraction (right) in a transmission electron microscopy [3], B) TEM image of MWCNTs showing a contrast between iron catalysts and MWCNTs, and C) SAED of the Si-CNT-SiC-C material indicating the presence of SiC in the material. 65
Figure 3.9. A) A schematic of an atom where X-ray is emitted; the inner electron is firstly rejected from the atom due to the electron bombardment and the hole is filled by the outer electron. The change of the state of the electron releases X-rays which can be detected by a detector, B-E) EDX

maps showing Si coating on the BP and EDX spectrum confirming the component of the Si-CNT material. 67
Figure 3.10. STEM scan coil installed in A) TEM [7] and B) STEM detectors placed in a sample chamber of SEM [9], and C) STEM image of Si-CNT-C material and EDX elemental mapping of silicon and carbon showing their uniform distribution of Si NPs on the MWCNT. 69
Figure 3.11. A) A diagram of a photoemission process; photoelectrons escape from the specimen surface due to the irradiation of X-ray beam, B) XPS survey spectrum, and C) high-resolution Si2p spectrum of Si-CNT-C (CH_4) material confirming unexpected SiC formation after coating amorphous carbon on the material. 71
Figure 3.12. A) A scheme of X-rays reflection based on Bragg's Law; X-ray beams are scattered from different lattice planes which are divided by the interplanar distance (d) and B) XRD patterns of Si-CNT based material, Si peak can be observed only in the material which consisted of crystalline Si.72
Figure 3.13. A) Raman spectrum of MWCNT 45 showing the characteristic D and G peaks of carbon material and B) the carbon atom movement in the D and G vibration modes [5]. 74
Figure 3.14. TGA curve of MWCNT 45; the average oxidation temperature of the material was 588 °C and the MWCNT content was 96.6 wt.% 75
Figure 3.15. A schematic of the four-point probe measurement; the probes are set colinearly at equal spacing X, while the voltage and the current are measured separately. 77
Figure 3.16. A) A galvanostatic cycling technique showing a constant current applied to the tested cell (excitation) and the potential determined as a function of time (response) [1], B) the current-time and charge-discharge graphs of BP 45 tested at C/5 rate; its capacity could be determined by calculating the area of the current-time graph, while plateaus in the discharge curve indicated the SEI formation (0.8 V) and Li insertion into the carbon (0.25 V). 79
Figure 3.17. A schematic diagram showing the experiment set up of the used AACVD apparatus for MWCNT synthesis. 80
Figure 3.18. A schematic revealing the APCVD method for Si deposition on a BP by using a gas mixture set-up. 81
Figure 3.19. Photographs showing A) a conventional Si electrode made by uniformly casting B) Si mixture paste on C) a copper foil current collector. 83
Figure 3.20. A scheme exhibiting the coin cell battery (left) and pouch cell battery (right) configurations. 84
Figure 4.1. A) A schematic diagram showing the configuration of the buckypaper [1], B) SEM images of the buckypaper showing bundles of entangled carbon nanotubes [3], C) a photograph of buckypaper electrode showing its smooth surface, and D-E) photographs of a buckypaper showing its bendability; it can be bended and rolled [6]. 90
Figure 4.2. SEM images and length histogram of A) MWCNT 15, B) MWCNT 30, C) MWCNT 45, D) MWCNT 60 confirming a tendency to produce longer MWCNTs with longer synthesis time, E) thermal gravimetric graphs of the MWCNTs showing the decomposition of the MWCNTs after 590 °C under air atmosphere, and F) Raman spectra of the MWCNTs revealing the characteristic peaks (D and G bands) of the carbon material in the samples. 93

Figure 4.3. A) SEM image and inset photograph showing a flat surface and a free-standing feature of BP 45, and B) SEM image at high magnification revealing the smooth surface of BP 45 with small pores of the entangled MWCNTs. 94
Figure 4.4. Photographs of A) C-BP and B) BP 45 showing the flexibility of both types of BPs; the C-BP could be bent to 180 degree while the BP 45 could be bend to 160 degrees. 97
Figure 4.5. A) The charge-discharge graph of the BP revealing the areal capacity of 0.3 mAh/cm^2 after 300 cycles at C/5 rate, B) the voltage profiles of the BP showing high irreversible capacity of the electrode in the 1^{st} cycle, C) the dQ/dV charts showing the Li-ion storage mechanism of the BP electrode, and D) the rate capability plot of the BP electrode showing the good battery performance of the BP electrode at different C-rate testing. 99
Figure 4.6. The battery performance of the BPs electrode in the coin cell and pouch cell battery configurations confirming that the capacity is mostly attributed from the BP electrode instead of the cell components. 100
Figure 4.7. SEM images of the BP A) before and B) after battery testing showing its surface without structural change. 101
Figure 4.8. A) A schematic and B) TEM image of the Si-CNT material structure showing silicon nanoparticles coated on the surface of the carbon nanotubes, and C) TEM image and fast Fourier transformation of the selected image area revealing the diffuse rings of amorphous Si. 102
Figure 4.9. A) XRD patterns of Si-CNT and reference materials; an absence of Si peaks confirms an amorphous Si structure in the Si-CNT material. 103
Figure 4.10. A) XPS survey spectrum, and high-resolution spectra of the Si-CNT material corresponding to B) Si2p and C) O1s confirming the Si structure in the Si-CNT material. 104
Figure 4.11. A) The charge-discharge graph of Si-CNT electrode showing the areal capacity of 0.09 mAh/cm^2 after 300 cycles at C/5 rate, B) the voltage profiles of the Si-CNT electrode confirmed the two-phase lithiation of crystalline Si, C) the differential areal capacity plot of the Si-CNT electrode presenting the Li-ion storage mechanism of the electrode, D) the rate capability graph of the Si-CNT electrode revealing poor battery performance of the Si-CNT electrode at faster-charging rates. 106
Figure 4.12. Post-cycling SEM images of the Si-CNT electrode at A) low and B) high magnification showing cracking observed on the Si-CNT electrode surface after battery testing. 108
Figure 4.13. Post-cycling TEM images of the Si-CNT electrode at A) low and B) high magnification; a significant change of the Si structure can be observed after cycling. 109
Figure 4.14. A) The areal capacity of Si-CNT, BP 45 and pure Si electrodes tested at C/10 rate confirming the higher areal capacity of Si-CNT electrode compared to others and B) a bar chart showing the areal capacity of all materials at 1^{st} cycle and 20^{th} cycle; the areal capacity of Si-CNT electrode was the highest indicating that this electrode is promising to study further for improving the stability of the electrode. 110
Figure 5.1. A-B) TEM images of the Si/MWCNT after annealing at 1000 ^oC and 1300 ^oC showing the silicon carbide formation on the surface of MWCNTs, and C) the battery performance of the annealing Si/MWCNT electrodes showing the stability improvement after annealing the material at high temperature (1000 ^oC) to form silicon carbide interface [1]. 126

Figure 5.2. Schematic diagrams showing the amorphous carbon coating process in which two carbon sources were used (Case I: methane gas and Case II: acetylene gas); traces of SiC were found in the material after coating in Case I due to the high temperature (900 °C) used in the experiment. 129
Figure 5.3. A) A schematic of the desired structure of Si-CNT-C after coating amorphous carbon and B) TEM image of Si-CNT-C (CH_4) material (Case I) showing thick amorphous carbon (8-10 nm) coated on the material surface, and C) TEM image and fast Fourier transformation of the selected image area showing the spot pattern of crystalline Si. 130
Figure 5.4. XRD patterns of Si-CNT-C (CH_4) material (Case I); a small SiC peak can be seen confirming SiC in the Si-CNT-C (CH_4) material. 131
Figure 5.5. A) XPS survey spectrum and high-resolution spectra of Si-CNT-C (CH_4) material (Case I) corresponding to B) Si2p and C) O1s presenting unpredicted SiC formation after coating amorphous carbon by using methane as a carbon source at 900 °C. 132
Figure 5.6. The charge-discharge graph of the Si-CNT-C (CH_4) electrode showing the areal capacity of 0.37 mAh/cm^2 after 300 cycles at C/5 rate. 133
Figure 5.7. A) The voltage profiles of Si-CNT-C (CH_4) revealing the lithiation of crystalline Si due to a presence of the plateau at 0.15 V in the 1st cycle, and B) the differential areal capacity plot presenting the Li ion storage mechanism of the Si-CNT-C (CH_4) electrode. 134
Figure 5.8. A) A schematic of the desired structure of Si-CNT-C and B-C) TEM images presenting the thin amorphous carbon (3-8 nm) coated on the Si-CNT-C (C_2H_2) material (Case II); C) fast Fourier transformation of the selected image area also present the ring pattern of polycrystalline Si. 135
Figure 5.9. XRD patterns of Si-CNT-C (C_2H_2) material (Case II) confirming that SiC did not form in the material after amorphous coating. 135
Figure 5.10. A) XPS survey spectrum and high-resolution spectra of Si-CNT-C (C_2H_2) material (Case II) corresponding to B) Si2p and C) O1s; no silicon carbide formation occurred after coating amorphous carbon using acetylene gas. 136
Figure 5.11. The charge-discharge graph of the Si-CNT-C (C_2H_2) electrode (Case II) showing the areal capacity of 0.17 mAh/cm^2 after 300 cycles at C/5 rate. 137
Figure 5.12. A) The voltage profiles of Si-CNT-C (C_2H_2) revealing a plateau at 0.14 V in the 1st cycle which confirms the lithiation of crystalline Si in the two-phase region, and B) the differential areal capacity plot revealing the lithiation/delithiation process of the Si-CNT-C (C_2H_2) electrode. 137
Figure 5.13. The battery performance of Si-CNT-C (CH_4) (Case I) and Si-CNT-C (C_2H_2) (Case II) confirming the superior stability of the Si-CNT-C (CH_4) (Case I) due to a presence of SiC in the material. 138
Figure 5.14. Schematic and TEM images of Si-CNT-SiC-C materials showing the SiC formation in the material at the different annealing temperature conditions A) 990 °C, B) 1000 °C, C) 1100 °C and D) 1200 °C; the SiC initially formed when the temperature reaching 1000 °C and the Si NP immersed inside MWCNTs to completely form SiC at 1100-1200 °C. 140

Figure 5.15. HRTEM images of Si-CNT-SiC-C materials annealed at A-B) 990 °C and C-D) 1000 °C ; the observed lattice spacing confirms the silicon carbide formation after increasing the annealing temperature to 1000 °C. 141
Figure 5.16. HRTEM images of Si-CNT-SiC-C materials annealed at A-B) 1100 °C and C-D) 1200 °C; the Si was almost completely converted to SiC after 1100 °C, SiC also changed to a layered structure after increasing the temperature to 1200 °C. 142
Figure 5.17. XRD patterns of Si-CNT-SiC-C materials showing the change of the Si structure at different annealing temperature conditions; SiC was partly formed at 1000 °C as Si peak can be still detected in this material condition but Si completely converted to SiC at 1100 °C. 143
Figure 5.18. A) SEM image showing the selected area of the material for studying the electron diffraction, B) electron diffraction pattern from the area revealing the diffraction pattern of SiC, C) SEM image showing selected particle for electron diffraction, and D) NBDP from the area confirming the silicon carbide interface of the Si-CNT-SiC-C material (1000 °C annealing temperature condition). 144
Figure 5.19. The charge-discharge graph of the Si-CNT-SiC-C (1000 °C) electrode showing the areal capacity of 0.55 mAh/cm^2 after 300 cycles at C/5 rate. 147
Figure 5.20. A) The voltage profiles of the Si-CNT-SiC-C (1000 °C) electrode showing a plateau at 0.15 V in the first cycle which attributes to the two-phase lithiation of crystalline Si in the material, and B) the differential areal capacity plot of the Si-CNT-SiC-C electrode showing Li ion storage mechanism of the electrode. 148
Figure 5.21. A) The areal capacity graph of BP 45 and Si-CNT-SiC-C electrodes tested at C/10 showing that the capacity of Si-CNT-SiC-C electrode (0.95 mAh/cm^2) is double to that of the pure BP electrode (0.46 mAh/cm^2) after 100 cycles, B) the rate capability graph of these electrodes showing superior battery performance of Si-CNT-SiC-C than the buckypaper at the fast C-rates, and C) the areal capacity plot of buckypaper and Si-CNT-SiC-C coin cells and pouch cells carried out at 1 mA showing the influence of the coin-cell components on the battery performance of the free-standing electrodes. 149
Figure 5.22. A-D) Cross-sectional SEM images of the Si-CNT-SiC-C electrode at low and high magnification before and after 300 cycles showing the increase in the electrode thickness from 200 microns to 310 microns after battery testing; voids in the BP also became smaller after cycling which is due to the SEI formation inside the pores. 151
Figure 5.23. A-D) SEM images at a low and high magnification of Si-CNT-SiC-C surface before and after the 300-cycling test showing the thick SEI layer formation on the surface of the electrode after cycling; cracking cannot be observed on the electrode surface after 300th cycle of the battery testing. 152
Figure 5.24. A) The areal capacity of all Si-CNT based electrodes tested at C/5 showing the best stability of the Si-CNT-SiC-C electrode when compared with the materials prepared in this work, and B) the bar chart showing the areal capacity of all materials at 1st cycle and 300th cycle; the areal capacity difference between 1st and 300th of Si-CNT-SiC-C electrode is the lowest indicating the best capacity retention after 300 cycles than other electrodes. 153

Figure 6.1. The summary of this work; five different types of the free-standing electrodes were prepared. The BP made from in-house MWCNTs showed better battery performance than that of the BP made from the commercial Nanocycl MWCNTs. The Si-CNT-SiC-C electrode showed the best capacity retention after 300 cycles (0.55 mAh/cm^2) compared with other electrodes. Its capacity was improved by 83.3% compared with the pure MWCNT paper (BP 45) electrode and the structure of the electrode was maintained after the battery testing. 169

Figure 6.2. The flow chart presenting the summary of the future work; it includes material modifications, cell component adjustment, and additional characterisations of the Si-CNT-SiC-C electrode. The approaches and expected outcomes are shown in blue and orange boxes, respectively. 172

Figure 6.3. The areal capacity of the Si-CNT-SiC-C electrodes made with and without additives (FEC and VC); there is a huge capacity drop in few cycles even though the stability of the electrode was enhanced when additives were added in the electrolyte. 174

Figure 6.4. A) A configuration of the battery cell in a TEM holder; Si and Li metal are mounted on the Pt electrode and the silicon nitride is used to seal the electrolyte [1]. B) A holder for the in situ TEM study; the battery tester (a potentiostat) is connected to the battery cell via wires in the holder shaft [2]. 175

List of Abbreviations

AACVD	Aerosol-Assisted Chemical Vapour Deposition
APCVD	Atmospheric-Pressure Chemical Vapour Deposition
a-Si	Amorphous silicon
BSE	Backscattering electrons
BP 15	Buckypaper made from 15-minute carbon nanotubes
BP 30	Buckypaper made from 30-minute carbon nanotubes
BP 45	Buckypaper made from 45-minute carbon nanotubes
BP 60	Buckypaper made from 60-minute carbon nanotubes
CMC	Sodium carboxymethyl cellulose
CNTs	Carbon nanotubes
CNT 15	15-minute carbon nanotubes
CNT 30	30-minute carbon nanotubes
CNT 45	45-minute carbon nanotubes
CNT 60	15-minute carbon nanotubes
c-Si	Crystalline silicon
CVD	Chemical Vapour Deposition
DMC	Dimethyl carbonate
EC	Ethyl carbonate
EDX	Energy Dispersive X-Ray spectroscopy
FEC	Fluoroethylene carbonate
FWHM	Full width at half maximum
HRTEM	High-resolution transmission electron microscopy
LIBs	Lithium-ion batteries
LP30	1 M $LiPF_6$ in 1:1 EC/DMC
LPCVD	Low-pressure chemical vapour deposition
MWCNT	Multi-wall carbon nanotube
NBDP	Nano-beam diffraction pattern

NiMH	Nickel-metal hydride
NiCd	Nickel-cadmium
NP	Nanoparticle
PECVD	Plasma-enhanced chemical vapour deposition
PHOTOCVD	Photochemical chemical vapour deposition
Raman	Raman spectroscopy
SAED	Selected area electron diffraction
SE	Secondary electrons
SEI	Solid electrolyte interphase
SEM	Scanning electron microscopy
SS304	Stainless Steel - Grade 304
SWCNT	Single-wall carbon nanotube
TEM	Transmission electron microscopy
TGA	Thermogravimetric analyser
VACNTs	Vertically aligned carbon nanotubes
VLS	Vapour-solid-liquid
XRD	X-ray powder diffraction
XPS	X-ray photoelectron spectroscopy
UHVCVD	Ultrahigh-vacuum chemical vapour deposition

List of Symbols

C-rate	Charge and discharge rate
C/10	Ten-hour discharge
C/5	Five-hour discharge
C/2	Two-hour discharge
C	One-hour discharge, the number of components
d	The interplanar distance
E	Cell voltage
E_{OCV}	Cell voltage at open circuit
E_T	The terminal cell voltage
E_B	Binding energy of the electron attracted to nucleus
E_k	Kinetic energy of the photoelectron
F	Faraday's constant, the number of degrees of freedom
ΔG	Change in the free energy of the reaction
ΔH	Enthalpy or energy produced by the reaction
ΔS	Entropy
We	Electrical work
P	The number of phases existing in the material system
Q	Electrical charge capacity
V	Voltage
η	Polarisation
*	Reactive surface site
2θ	Detector angle
θ	Angles of the incident X-rays on the crystal
dQ/dV	Differential capacity vs voltage
sccm	Standard cubic centimeters per minute
R	Resistance

I_D/I_G	Ratio of the D and G band intensities in carbon materials from Raman spectrum
ϕ	Work function of the spectrometer
λ	Wavelengths
ϱ	Surface resistivity
I	Current

Chapter 1

Literature review

In this chapter, the electrochemistry of Li-ion batteries (LIBs) and related parameters which are used to describe the important electrochemical properties LIBs will be studied. As the electrochemical reaction in LIBs relates to a redox reaction, the thermodynamic and kinetic fundamentals of such reactions will be reviewed. The calculation of the theoretical energy and capacity of LIBs will also be shown in this chapter. Moreover, the voltage profile characteristics of the battery will be analysed based on the Gibbs phase rule in order to understand the reaction that takes place inside the electrochemical cell. Finally, a literature review will be conducted on anode materials including Si, MWCNTs and Si-carbon based composites. The review will provide insight into the achievements and challenges of anode material development. The evolution of electrode design without binders and current collectors will additionally be reviewed as this kind of electrode has the potential to be used in new technologies such as smartphones and wearable electronic devices. Finally, the effect of the cell components and the misleading report of the battery performance in previous works will be discussed to improve the quality of future work.

1.1) The basic concepts of Li-ion batteries

1.1.1) A lithium-ion battery as an alternative energy storage device to lead-acid, nickel-metal hydride, and nickel-cadmium batteries

Energy storage systems have received significant attention by researchers, consumers, and policymakers due to the continuous increase of energy use in households and industries. Rechargeable

Li-ion batteries are one type of energy storage devices that have been of interest due to their rechargeability and high energy storage capability [8].

To select the 'right' battery for a specific application, it is necessary to assess relevant parameters such as energy and power. In particular, the specific energy or gravimetric energy density (Wh/kg) is the amount of energy that the battery can store per unit weight, while the specific power or gravimetric power density (W/kg) is the ability to deliver current loads per unit weight. Energy and power per unit volume are defined as energy density or volumetric energy density (Wh/L) and power density or volumetric power density (W/L) respectively. These two parameters are important to develop our current battery technology, as improving the specific energy (or energy density) results in a longer battery runtime, and increasing the specific power (or power density) can yield batteries for high current requirements [1, 2].

The Ragone chart (Figure 1.1) presents the relationship between specific energy and specific power for different battery systems. In comparison with other battery technologies such as lead-acid, nickel-metal hydride (NiMH), and nickel-cadmium (NiCd) batteries, the conventional LIBs exhibit many advantages including higher specific energy and specific power, higher volumetric energy density, longer cycle life and higher coulombic efficiency (Figure 1.1 and Table 1.1). Because of their superior properties, LIBs are widely applied in numerous portable devices: mobile phones, laptops *etc.* However, current development of the next-generation applications including electric vehicles and grid energy storage requires high energy and power density LIBs in order to store more energy and deliver it quicker [9, 10]. The battery cycle life needs to be enhanced so as to increase the lifetime of the battery. Therefore, several challenges such as energy and power density improvement, and cycle life prolongation need to be addressed in order to increase the practicality of LIBs in these applications [9-11].

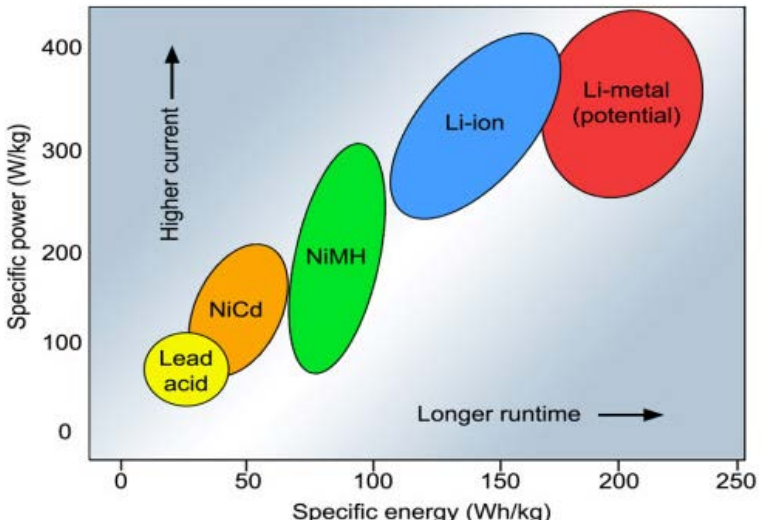


Figure 1.1. Comparison of different commercial batteries; a Li-ion battery has higher specific energy and specific power than other batteries [2].

Table 1.1. The properties of currently used batteries, showing that LIBs have in most cases superior properties over other rechargeable batteries.

Specifications	Lead acid	NiCd	NiMH	LIB
Specific energy (Wh/kg)	30-50 [2]	45-80 [2]	60-120 [2]	150-250 [2]
Specific power (W/kg)	250 [12]	200 [13]	170-1000 [13]	250-800 [12]
Energy density (Wh/L)	80-90 [12]	50-75 [14]	170-420 [14]	62-705 [12, 15]
Cycle life	200-300 [2]	1000 [2]	300-500 [2]	500-1000 [2]
Coulombic efficiency	90% [2]	70-90% [2]		99% [2]

1.1.2) Lithium-ion battery electrochemistry

In order to develop LIBs, the basic electrochemistry of the battery including the reaction mechanism needs to be studied. In general, a LIB has two main elements: a negative electrode (anode) and a positive electrode (cathode). The electrodes are separated by a separator which allows Li ions to pass through; at the same time it prevents an electrical short circuit that would arise in the case of direct contact of these electrodes. In addition, a non-aqueous electrolyte containing a Li salt is used as a medium through which the electroactive Li ions transport while the electrons traverse an external circuit with a release of energy. A graphic diagram of the intercalation-deintercalation mechanism of a LIB is demonstrated in Figure 1.2.

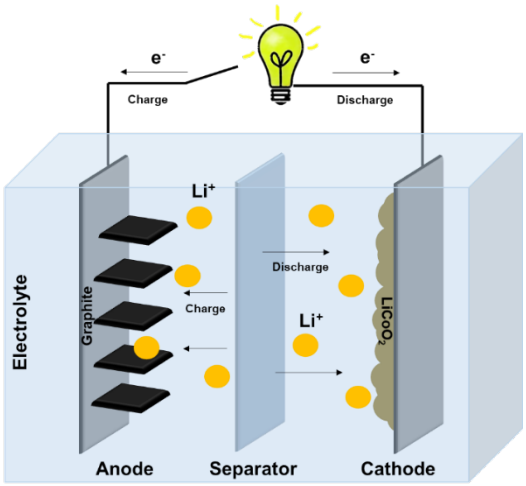


Figure 1.2. A diagram of the lithium-ion battery mechanism showing the movement of Li ions during charging and discharging.

The first commercialised LIB manufactured by Sony Corporation in June 1991 had a negative graphite anode and a positive lithium cobalt oxide ($LiCoO_2$) cathode. This Li-ion cell had a potential of over 3.6 V [16]. During charging, Li ions are deintercalated from the layers of $LiCoO_2$, which is an intercalation host, and pass through the separator via electrolyte to be intercalated between the graphene layers of the graphite anode while electrons travel through the external circuit. The reverse process occurs during the battery is discharged. This reversible reaction is the key factor for the longevity of the batteries. The respective intercalation-deintercalation of the LIB occurring at each electrode is given by the following equations.

$$\text{Cathode: } LiCoO_2 \leftrightarrow Li_{0.5}CoO_2 + 0.5Li^+ + 0.5e^- \quad (1.1)$$

$$\text{Anode: } 6C + Li^+ + e^- \leftrightarrow LiC_6 \quad (1.2)$$

The overall chemical reaction of the battery cell is presented as follows.

$$6C + 2LiCoO_2 \leftrightarrow LiC_6 + 2Li_{0.5}CoO_2 \qquad E_{cell}=3.6\ V \quad (1.3)$$

The first reaction is the oxidation of $LiCoO_2$ or delithiation. In order to maintain the structural stability and high reversibility of the reaction, half of the total amount of Li inside the $LiCoO_2$ structure is typically involved in the electrochemical reaction. The empirical formula of the material after

deintercalation is $Li_{0.5}CoO_2$ (Equation 1.1). The intercalation of Li ions in a graphite electrode is shown in Equation 1.2, where LiC_6 is the reaction product. At the beginning of the charging process, the first reaction of a graphite electrode in any polar aprotic lithium salt electrolyte consumes charge and reduces the solution species. This phenomenon causes the formation of a solid electrolyte interphase (SEI) layer, which is a barrier to prevent any further irreversible processes. Generally, each LIB contains an excess cathode material to provide extra Li ions and charge to form the SEI films on graphite [17]. Additives such as vinyl ethylene carbonate and maleimide are also added into the electrolyte in order to form a stable SEI layer resulting in the improvement of the battery performance [18].

1.1.3) Thermodynamics and kinetics related to LIBs

It is commonly known that LIBs involve the conversion of chemical energy into electrical energy or *vice versa* via a redox reaction. The energy storage principles of LIBs are based on thermodynamics and kinetics. Therefore, it is important to study the thermodynamics and kinetics of the electrochemical reaction in order to understand how the battery works theoretically and practically. The thermodynamic equation for a reversible reaction is expressed as

$$\Delta G = \Delta H - T\Delta S \tag{1.4}$$

$$\Delta G = We \tag{1.5}$$

where ΔG is the Gibbs free energy or the energy available from a reaction to do work, ΔH is enthalpy or energy produced by the reaction, ΔS is the entropy, T is temperature and We is electrical work. In terms of the electrochemical reaction, however, the total amount of energy to perform electrical work relates to the cell potential and the total number of electrons transferred during the electrochemical reaction. Therefore, the relationship between the change in free energy and the cell potential is expressed as follows [19].

$$\Delta G = -nF\Delta E \tag{1.6}$$

Where n is a number of moles of electrons involved in the reaction, F is the Faraday's constant (96485 C mol^{-1}), ΔE is the cell voltage at any state with respect to the E^o (a cell potential under standard state conditions: 1 atm, 25°C and 1 M of solutes). Note that the change in the free energy is defined as a negative number because the work is done by the system. Therefore, the above thermodynamic equation is applied to explain the equilibrium (open circuit or no current conditions) voltage in the battery cell. The open-circuit voltage for any electrochemical reaction is also unrelated to types of species in electrolytes and reactions at the electrode/electrolyte interface [1].

However, the actual voltage when discharging a battery is lower than the equilibrium voltage due to kinetic limitations of the reactions. Since the thermodynamics defines the involved reactions and the total energy released only at equilibrium, the kinetics of the electrochemical reaction is necessary to be examined [8, 19]. In an ideal discharge curve as shown in Figure 1.3A, the discharge voltage of the battery is constant at the theoretical voltage and then drops to zero when the capacity reaches the maximum value. In contrast, under the actual condition as presented in curve 1-2 (Figure 1.3A), the voltage starts lower than the theoretical value. The voltage difference known as polarisation or overvoltage (η) is described as follows [1, 8].

$$\eta = E_{OCV} - E_T \tag{1.7}$$

where E_{OCV} is the cell voltage at open circuit, and E_T is the terminal cell voltage. The initial voltage drop is caused by internal resistance, which is known as IR drop or ohmic polarisation. The IR drop is attributed to the resistance of electrolyte, electrodes, current collectors as well as the electrical contact between electrode components, *e.g.* active materials, carbonaceous electronic conductor, and current collectors. The voltage slowly drops during the polarisation since the cell resistance is higher due to an increase of activation and concentration polarisation in both electrodes (Figure 1.3B). The activation polarisation is ascribed to electrochemical reactions occurring at electrode interfaces, while the concentration polarisation is attributed to mass transfer limitation and the concentration

differences between the reactants and products at the electrode surface. Hence, the specific energy delivered from the battery should be lower than the theoretical specific energy because the battery in practice is not discharged to zero volt and the average discharge voltage is less than the theoretical value due to the polarisation [8, 19].

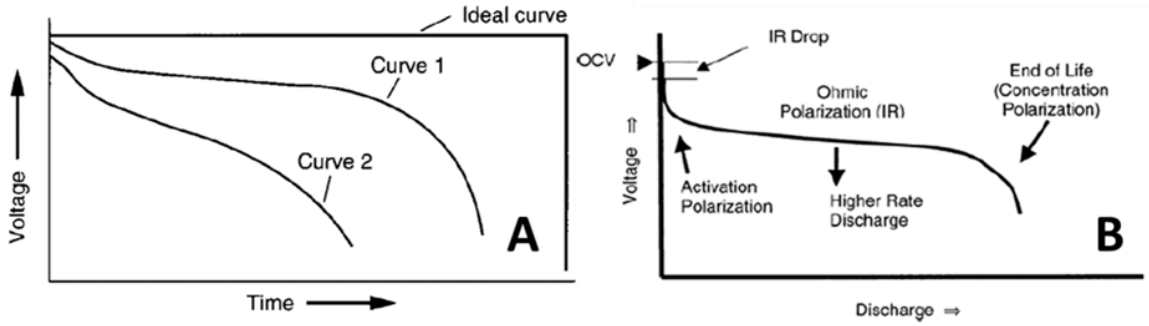


Figure 1.3. A) Actual discharge curves (1 and 2) showing different characteristics from an ideal discharge curve [19], and B) the common discharge curve exhibiting various types of polarisation [8].

1.1.4) Theoretical cell energy and capacity calculations

Based on the change of free energy during the chemical reaction, the maximum theoretical gravimetric energy of the LIB (Wh/kg) can be calculated, as shown below,

$$The\ theroretical\ gravimetric\ energy = \frac{\Delta G}{Reactant\ weight} = \frac{nFE}{Reactant\ weight} = \frac{Q}{Reactant\ weight}E \quad (1.8)$$

where Q is electrical charge capacity. According to Equation 1.3, the theoretical gravimetric energy of the battery is 360 Wh/kg (based on 267.8 g/mol of the reactant weight and 3.6 V of the cell voltage of the battery). Also, the theoretical volumetric energy (Wh/L) can be determined by dividing the change in the free energy with the volume of the battery instead of the weight.

The theoretical capacity of the battery is the total quantity of the electrical charge provided by the electrochemical reactions which is usually expressed in Coulombs (C) or Ampere-hour (Ah). According to Faraday's law, one gram equivalent of any material will transfer 96485 C or 26.8 Ah where one gram equivalent is the molecular weight of the material divided by a number of the mole electron delivered in the reaction [19]. Therefore, the theoretical specific capacity can be calculated

from the weight of the active material and a number of electrons involved in the reaction. For instance, graphite has the theoretical specific capacity of 372 mAh/g based on one-mole electron transferred in the chemical reaction shown in Equation 1.2 [1].

1.1.5) The shapes of voltage profiles and their relation to phase diagrams

In order to understand the behaviour of battery cells, the voltage profile characteristics need to be examined. As shown in Figure 1.3, the voltage profile of an electrode is dependent on the state of charge of the battery. Generally, the discharge curves are found in three shapes: flat, sloped and slanted. To interpret these curves, it is necessary to study the Gibbs phase rule which is expressed as

$$F = C - P + 2 \tag{1.9}$$

where C is the number of components, P is the number of phases existing in the material system, and F is the number of degrees of freedom which defines the number of thermodynamic parameters that must be identified to state the system [1]. It is noted that the reaction of Li with a metal or a compound in LIBs is categorised into two groups and three different types; group A: 1) a solid-solution reaction, *e.g.*, the intercalation of Li between graphite layers and 2) an addition reaction, *e.g.*, the insertion reaction of Li with crystalline Si, Sn, Al and Sb materials, and group B: 3) a displacement reaction, *e.g.*, the reaction of Li with SnO, Sn_2Fe and Cu_2O alloy compounds.

While considering the solid-solution reaction in group A, no structure and phase change can happen in the material when Li inserts into the structure. Since only one phase is present in the binary system (C=2 and P=1) and the temperature and pressure are constant, the degrees of freedom in the system are equal to one. Hence, the electrode potential of the reaction is not fixed but varies with the concentration of Li and the voltage profile shows a sloped shape (Figure 1.4A). By contrast, when considering the addition reaction in group A, the generated lithiated compound is different from the parent material which indicates that a phase change was involved (P=2). Thus, the degrees of freedom in the system are equal to zero when the temperature and pressure is constant. This means that the

electrical potential does not vary with the electrode composition. The voltage profile presents a constant plateau indicating that the potential is independent of the state of charge (Figure 1.4B). In case of the replacement reaction in group B, Li reacts with the component Y of the alloy compound XY_z and the X is displaced from the parent phase. Therefore, the potential of the reaction for the ternary system is independent of the Li concentration according to the Gibbs phase rule. That is, a plateau is clearly shown on the voltage profile. Furthermore, the discharge curve shape in the battery is attributed to the variation of the electrode potentials happening in the overall reaction. When the electrode consists of several materials and more than one reaction takes place in sequence in the system, a set of the multi-phase reactions occurs. Therefore, if the number of degrees of freedom is zero, the discharge curve of the battery presents a series of constant voltage plateaus (Figure 1.4C) [1, 20].

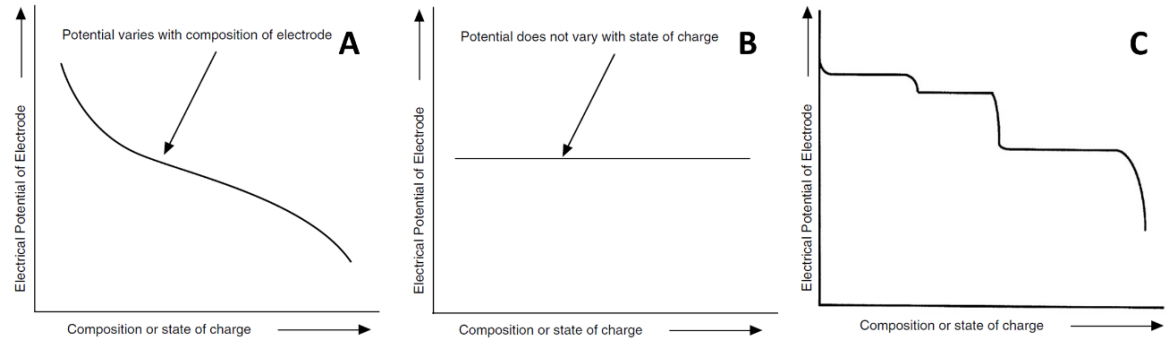


Figure 1.4. Schemetric dischage curves of the electrode; A) the potential varies with the state of charge for the case where F is not zero, B) the potential is independent of the electrode composition as the value of F is zero and C) the series of multiphase reactions in which F is zero result in a set of constant voltage plateaus [1].

Additionally, it is easy to predict the change of the electrode potential towards composition in the material when considering the phase diagram of the binary system at a fixed temperature. For instance, Figure 1.5A shows the variation of the electrical potential at temperature T_1 corresponding to the binary phase diagram in Figure 1.5B. According to the schematic potential graph (Figure 1.5A), the potential initially depends on the composition after B atoms enter into pure A and the solid solution phase α forms. After the solubility of α reaches a limit (composition A), the phase β starts

growing indicating the two-phase reaction, and a constant voltage plateau is then observed. At the composition B, all the phase α is consumed and only phase β exists. Thus, the electrical potential varies with the composition again. When reaching the solubility limit of phase β at composition C, the two-phase reaction begins to occur showing a composition-independent potential curve. Finally, the potential becomes composition-dependent when reaching composition D [1].

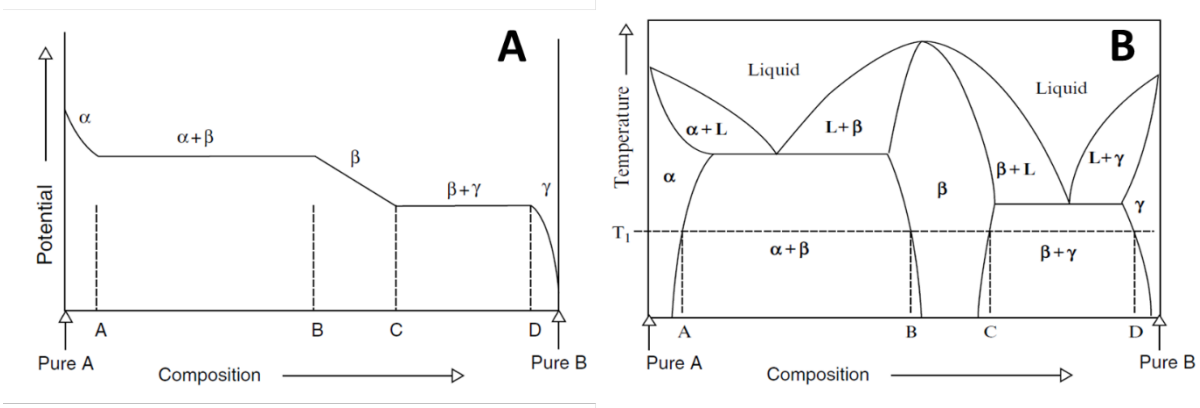


Figure 1.5. A) A schematic graph presenting the change of the potential with the composition relating to B) the binary phase diagram at T_1 which shows the formation of an intermediate phase β and its solubility in phases α and γ [1].

1.1.6) Main challenges of LIB development

Ongoing developments of flexible electronic devices, smartphones and tablets in conjunction with consumer demand and environmental challenges require thinner and lighter batteries with increased energy and power density and prolonged cycle life. Therefore, these challenges must be addressed through the modification of the material chemistry [21]. In particular, the current LIB based on intercalation chemistry in graphite and lithium cobalt oxide electrodes is not sufficient as it still has low energy and power density and moderate voltage (3.6 V). Also, new high energy density materials such as Si or Li metal lack in terms of long cycle life and high safety features which make them difficult to practically employ within batteries. Hence, further LIB research directly focuses on finding novel anode and cathode materials which have higher performance in terms of energy density, power density, lifetime, cost and safety and can replace current battery components [22]. A review of the recent LIB research will provide insight on the challenges and gaps that still needs to be addressed.

1.2) Recent developments in Li-ion battery research

There are attempts to find new inexpensive, safe, high energy density anode materials to satisfy the requirements for future applications. Numerous researches have been studied in alloys, such as Si [17, 23-25] and carbon materials [26-28] to replace current graphite anodes. Si has been of great interest due to its high theoretical capacity (4200 mAh/g) [25]. However, Si materials show poor battery performance with rapid capacity decrease when tested as an anode material in LIBs [10, 29]. Therefore, state-of-art Si-based materials have been investigated by many researchers to tackle the poor stability of Si anodes, such as silicon-carbon [30-32] and Si-MWCNT [33-35] composites. Although these carbon materials exhibit low specific capacity when testing them as an anode, it is worthwhile to use them as additive materials in Si anodes due to their high electronic conductivity and good mechanical properties [28, 36]. These novel Si-C composite materials could improve the stability and battery capability of Si anodes but the practical capacity of these electrodes is much lower than the theoretical capacity which makes them unsuitable for use as commercial anodes [33-35]. In addition, a new kind of electrode architecture which is free-standing and flexible has been developed to be applied in modern electronic devices which require bendable and light LIBs [4, 37]. Nevertheless, the production of free-standing electrodes is expensive and complicated, which poses problems for up-scaled production. Finding an alternative method to make free-standing electrodes is needed in order to use this type of electrode design into the current LIBs. In this section, the issues and challenges of Si anode material development and the configuration of the electrode are discussed.

Moreover, there are problems leading to wrong interpretations of the battery performance including the cell component effect and low mass loading of the active electrode material. These problems will be studied in this section in order to improve the standard of future work. First, the cell components in LIBs are made from stainless steel which could affect the performance of the battery. The stainless steel contains iron and chromium and these two elements are able to react with

electrolyte to form oxides. These oxides contribute additional capacity to the battery [38]. Thus, it is necessary to account for the effect of this cell component when interpreting the battery performance of the Si electrodes. Additionally, most of the previous studies showed a high specific capacity when using low mass loading (less than 0.3 mg/cm^2), which could introduce a large error in the useable capacity for the full-cell battery system [39]. When fabricating electrodes into a full-cell battery, the areal capacity of anode material is considered instead, and it is required to match with the areal capacity of cathode materials [40]. That is, the areal capacity of Si materials needs to be reported and set to match with the traditional $LiCoO_2$ cathode to achieve the targeted performance for commercial LIBs.

1.2.1) Alternative anode electrodes in Li-ion batteries

Table 1.2 gives an overview of the properties of common anode materials. Since the current commercial graphite anode has a theoretical specific capacity of only 372 mAh/g, other types of carbon materials such as MWCNTs have been investigated to improve the capacity of LIBs. There have also been many efforts to find alternative anode materials such as alloy materials which can store a higher amount of Li [29, 41]. The theoretical capacity of alloy materials is tenfold higher than that of carbon. For instance, Si has theoretical capacity of *ca.* 4200 mAh/g. In addition, electrodes made of alloy materials have a moderate operation potential of *ca.* 0.3-0.4 V vs Li/Li$^+$ which could prevent Li dendrite formation [41].

Table 1.2. Theoretical capacity, density, volume change, and voltage of anode materials [41].

Materials	Li	C	Si	Sn	Sb	Al	Mg	Bi
Density (g/cm^3)	0.53	2.25	2.33	7.29	6.7	2.7	1.3	9.78
Lithiated phase	Li	LiC_6	$Li_{4.4}Si$	$Li_{4.4}Sn$	Li_3Sb	LiAl	Li_3Mg	Li_3Bi
Theoretical specific capacity (mAh/g)	**3862**	**372**	**4200**	**994**	**660**	**993**	**3350**	**385**
Theoretical charge density (mAh/cm^3)	2047	837	9786	7246	4422	2681	4355	3765
Volume change (%)	100	12	320	260	200	96	100	215
Potential (V vs Li/Li$^+$)	0	0.05	0.4	0.6	0.9	0.3	0.1	0.8

1.2.2) MWCNTs as an anode material

One-dimensional carbonaceous materials such as carbon nanotubes (CNTs) have been studied to be applied as an anode material because of their remarkable mechanical, electrical and electrochemical properties [42]. CNTs in particular have a good mechanical property (Young's modulus of 950 GPa) [43], high electrical conductivity (10^6 S/cm) and thermal conductivity (6000 W/mK) [44]. They can be classified as single-wall carbon nanotubes (SWCNTs) and multi-wall carbon nanotubes (MWCNTs), comprising a single-rolled graphene sheet and multiple-rolled graphene sheets, respectively [45]. Compared with SWCNTs, MWCNTs show many advantages, including low catalytic residues, facile synthesis and affordability [4, 37]. The electrical and thermal conductivities of MWCNTs are *ca.* 10^3-10^5 S/cm and 2000 W/mK respectively [44].

Therefore, MWCNTs have been widely applied as an anode material in LIBs as in addition to their high conductivity values. They exhibit a reversible capacity of around 100-600 mAh/g depending on preparation methods [28]. Many studies were conducted to investigate the Li-ion storage mechanisms in CNT electrodes [42, 46-50]. In these studies, it was found that Li ions can be inserted into the centre of a six-carbon ring on the side of the nanotube wall [51] and can also be intercalated in the interstitial sites of MWCNT bundles [46]. The reversible capacity of the MWCNT electrode results from the adsorption of Li-ion on the nanotube surface since the Li ion is localised at the surface due to end-closed MWCNTs [47]. However, the Li ions can diffuse into the internal nanotubes via the open ends as well as defects on the sidewall [49, 50], and then they can be intercalated in spaces between MWCNT layers [42]. Table 1.3 shows a summary of the specific capacity values of different types of MWCNT anodes found in literature.

Table 1.3. Electrochemical performance of MWCNT anodes for Li-ion batteries.

Anode	Specific capacity (mAh/g)	Life cycles	Reference
Purified MWCNTs	351	-	[52]
Etched MWCNTs	681	-	[52]
MWCNTs	250	-	[27]
MWCNTs	273	5	[36]
Pyrolytic MWCNTs	400	20	[53]
MWCNTs	260	-	[54]

Theoretical calculations of previous studies indicated that the Li storage inside the CNTs is proportional to the diameter of the nanotubes [48, 49]. These theoretical studies were confirmed experimentally by Zhang *et al.* (2012). Their larger MWCNTs (40-60 nm in diameter) showed a better battery performance (187.4 mAh/g after the 50^{th} cycle) because large MWCNTs provide channels for Li ion and electrolyte molecule diffusion [55]. The electrochemical properties of short and long MWCNTs as anode materials were also investigated by Yang *et al.* (2008) [26]. The short MWCNTs revealed a reversible capacity of 260 mAh/g, which is about twice that of the long MWCNTs. Electrodes made with short MWCNTs had lower charge transfer resistance and superior kinetic properties during charging and discharging compared to electrodes made with long MWCNTs. However, the high irreversible capacity and low capacity retention of MWCNT electrodes limit the application of pure MWCNTs as an anode material in LIBs. This is because the reaction of Li ions with high surface area of MWCNTs is irreversible [35, 37]. Therefore, the composite of MWCNTs and alloy anode materials has been investigated instead in order to improve the electrical conductivity and the battery performance of the electrode.

1.2.3) Silicon as an anode material

As discussed earlier, Si has been considered as an anode material because of its significantly high theoretical specific capacity (4200 mAh/g), abundance and cost-effectiveness. One Si atom can alloy with 4.4 atoms of Li [56-58]. Nevertheless, at room temperature, Si can store 3.75 atoms of Li and the gravimetric capacity of Si anode is 3579 mAh/g [23, 59, 60].

In order to develop the Si material, it is essential to understand the reaction mechanism that happens in the material during the battery cycling. According to previous studies, crystalline Si is electrochemically lithiated at room temperature via a two-phase mechanism where lithiated amorphous Li_xSi is formed and separated from the unlithiated crystalline Si by a sharp boundary (Equation 1.10) [10, 61, 62].

$$Si\ (crystalline) + xLi^+ + xe^- \rightarrow Li_xSi\ (amorphous) + (3.75\text{-}x)Li^+ + (3.75\text{-}x)e^- \quad (1.10)$$

$$\rightarrow Li_{15}Si_4\ (crystalline) \quad (1.11)$$

When the electrode potential decreases to 50 mV (vs Li/Li^+), the lithiated amorphous Li_xSi phase is crystallised into the $Li_{15}Si_4$ phase which is the most highly lithiated Si phase at the room temperature (Equation 1.11). At the first delithiation, there is another two-phase region, of which the product is amorphous Si as expressed as follows.

$$Li_{15}Si_4\ (crystalline) \rightarrow Si\ (amorphous) + yLi + ye^- + Li_{15}Si_4\ (residual) \quad (1.12)$$

Some amount of residual $Li_{15}Si_4$ appears after the first lithium de-insertion. The theoretical specific capacity of this phase is about 3500 mAh/g, in agreement with the practical capacity of Si anodes at room temperature. However, the two-phase region changes to the single-phase region after the Li ions react with amorphous Si during the second cycle [59, 63].

In addition, a significant variation of the Li concentration during cycling induces inhomogeneous volume changes and fracture in the Si material [62]. The huge volume change of Si anode leads to unstable SEI layer formation. The SEI layer acts as a passivating film preventing further electrolyte decomposition because it behaves as a selectively permeable sieve. This allows only Li ions to pass through to the electrodes, while preventing any other active electrolyte components to pass through [64-67]. The issue of unstable SEI layer formation causes high irreversible capacity, poor capacity retention and failure of the battery [68-70]. As shown in Figure 1.6, the SEI layer is initially formed during a lithiated state of Si particles. During the delithiation, the physical contact between Si

particle is worsened and the interphase layer is broken apart. In subsequent cycles, new SEI layers continue to form on the fresh uncovered Si surface. Thus, the total SEI layer becomes thicker in every cycle. This causes degradation of the Si anode because the SEI layer is electronically insulating and not electrochemically active. Besides, a thicker SEI layer increases the path length of Li diffusion [5, 61]. Hence, the lithiation of Si with volume expansion remains a major challenge to overcome before the implementation within a commercial LIB can be possible.

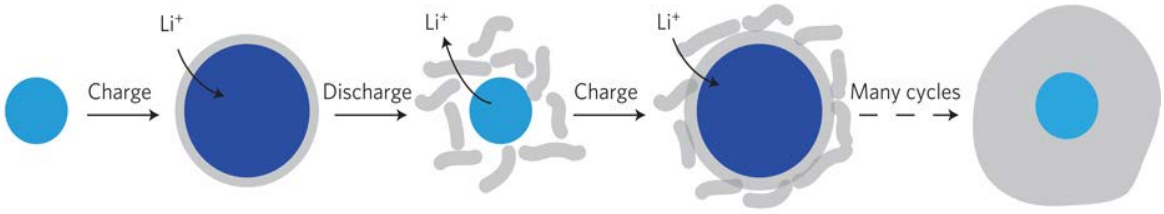


Figure 1.6. A schemic of SEI formation on silicon surface; the volume change of silicon causes thick SEI layers forming continueosly to cover its surface during cycling [5].

1.2.4) Methods for improving the performance of Si anodes

The problems of the Si anode and suggested solutions are summarised in Table 1.4. In order to minimise the first cycle irreversible capacity and the capacity fading of a Si anode, various approaches such as Si nanostructures [25], operating voltage control [71], binder and electrolyte alterations [72], and Si composites [73] have been developed.

In this work, silicon-carbon composite materials, including Si-MWCNTs and Si-amorphous carbon composites, will be mainly reviewed because they show a high potential to achieve the targeted battery performance. The main objective of mixing Si with other materials is to use a matrix to accommodate the tremendous volume changes of the Si material. Also, the host matrix behaves like a spacer to stop the agglomeration of the active materials, to allow rapid electron and Li ion transfer, and to maintain the stability of the anode [41, 90].

Table 1.4. Problems and suggested solutions for Si-based anodes [74].

Problems	Solutions
Volume Expansion	Control capacity Material structure design Electrode structure design Battery structure design
Cracking and agglomeration	Small particle size Isolated particles Surface coating
SEI	Low surface area Surface coating SEI additives Optimise binder
Volumetric capacity	Dense particle Low surface area SEI additives
Mechanical property	Tuning composition Shape control Structure control
Cost issue for scaling up	Precursor optimisation Technique optimisation

1.2.5) Silicon-MWCNT composites as anode materials

In this work, MWCNTs were used as an additive material for enhancing the electrochemical performance of Si materials due to their better mechanical strength and excellent electron and Li-ion transport. The MWCNTs function as a mechanical support to mitigate strain from the huge volume expansion of Si during the lithiation; that is, strain energy is absorbed by the ductile MWCNTs thus helping to conserve the Si structure [75, 76]. In addition, the tortuosity of MWCNTs allows them to act as a network to maintain the contact of active materials despite Si pulverisation [34]. The Si-MWCNT electrode showed a high reversible capacity of 3000 mAh/g [77]. A connection between Si and MWCNTs helped enhance the mechanical stability and electrochemical performance of the electrode. The study also indicated that Si and MWCNTs were anchored by an amorphous carbon interlayer. This amorphous interface layer was believed to form during Si deposition, where silane gas (SiH_4) was adsorbed on the MWCNT surface before its decomposition [77]. Moreover, Evanoff *et al.* (2012) carried out a study of MWCNTs coated with Si and amorphous carbon, as seen in Figure 1.7. They suggested that this architecture offered unique benefits including a vertically aligned MWCNT

structure, uniformly coated Si, and non-existence of binders which leads to the enhancement of electrode stability and performance [7]. Their results demonstrated that the MWCNT electrode provided channels for ion transport and Si expansion, as well as improved thermal and electrical conductivity of Si materials. The CNTs/Si coated with amorphous carbon also had high stability and long cycle life. They showed that the as-prepared material had a specific capacity of 3000 mAh/g with a 250 cycle retention [7]. Similar Si-MWCNT composites as anodes have been investigated by other studies as presented in Table 1.5.

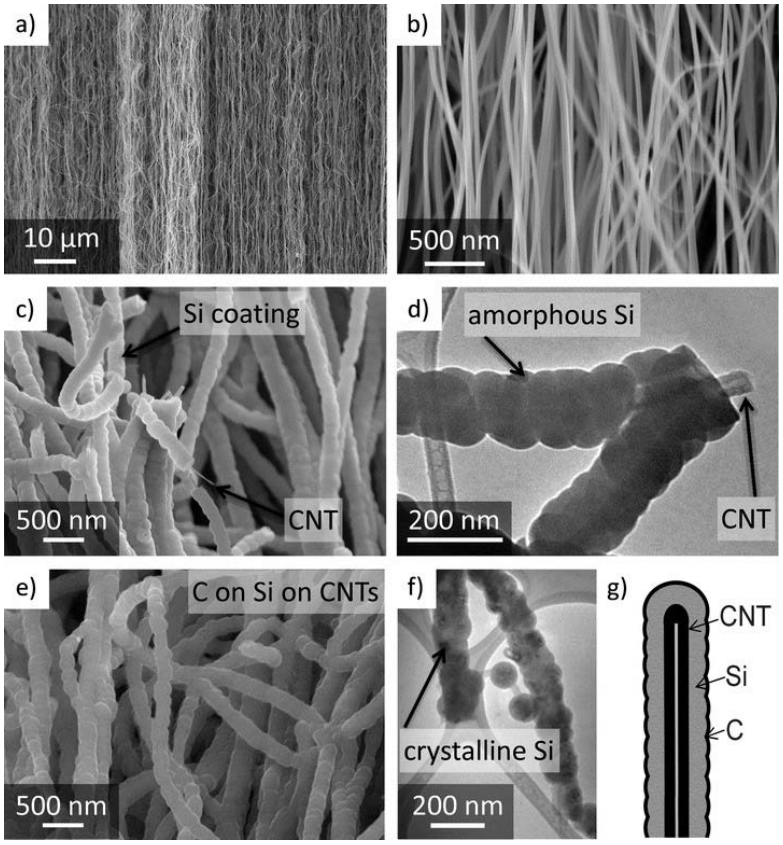


Figure 1.7. SEM and TEM images of a,b) pristine vertically aligned CNTs, c-d) silicon coated vertically aligned CNTs, e,f) carbon and silicon coated vertically aligned CNTs showing their structural change after coating with Si and C, and g) a graphic image showing the final material structure [7].

Table 1.5. Electrochemical performance of silicon-carbon nanotube composite anodes for Li-ion batteries.

Anode	Specific capacity (mAh/g)	Specific capacity after cycling (mAh/g)	Cycle	Reference
VACNTs/Si NP arrays	3000	800	100	[77]
Si/CNT/C nanofiber	1410	837	30	[78]
MWCNT-embedded Si NP film	3000	1510	100	[76]
VACNT-Si-C	3300	2000	250	[7]
CNT wrapped Si particles	2079	1031	500	[79]
MWCNT/Si composite	1770	1327	50	[35]
Cage-like CNTs/Si composite	1120	940	20	[33]
SiNP-CNT-core/carbon-shell nanofibers	1764	1000	100	[80]
Silicon decorated cone-shape CNTs clusters	1954	1260	230	[81]
SiNP-Filled CNTs	1671	1475	20	[82]
CNT-Si core-shell nanowire	2768	2500	100	[83]
Si-MWCNT Bucky paper composite	3500	620	100	[84]
Si-MWCNT nanocomposite	1447	-	-	[85]
VACNT/Si	2552	1000	100	[34]

Table 1.5 shows that it is challenging to improve the capacity retention of the Si-based electrodes since these electrodes showed a significant decrease in capacity during cycling and the electrode capacity was still far behind the theoretical capacity of Si (3579 mAh/g). As in these studies Si was indirectly anchored on MWCNTs using amorphous carbon, the Si was able to disconnect from MWCNTs resulting in poor electrode stability. Moreover, the battery performance testing in many of the previous studies was performed for 100 cycles or less which is insufficient to make any rigid conclusions on the stability of the electrode. Therefore, novel structures of Si-MWCNT materials which provide better Si anchoring need to be developed to enhance the battery performance and stability of the electrode, and these need to be tested for a sufficient amount of cycles to make solid conclusions on the usability of such structures.

1.2.6) Silicon-amorphous carbon composites as anode materials

An amorphous carbon coating has been applied to Si electrodes to improve battery stability by controlling the repeated SEI layer formation on the electrode. It was found that the Si electrode with amorphous coating showed smooth surfaces with few pores after cycling whereas some cracks and a porous structure were observed in nanostructures of pure Si electrodes [86, 87]. Ng *et al.* (2016) reported a spherical carbon-coated Si electrode which showed a first discharge capacity of 2600 mAh/g and charge capacity of 1857 mAh/g [88]. They suggested that the carbon coating promoted electrical contact and conductivity was the reason for improving the electrode performance [89]. Recently, Cui *et al.* (2014) designed spherical Si permanganate microbeads which each Si NP individually covered by carbon with well-ordered void spaces between Si and carbon (Figure 1.8). Such a design had many advantages: the nano-size of particles and the inner void space allowed the volume expansion of Si; all Si NPs were electrochemically active due to the carbon coating; the carbon, which totally covered the particle, could limit the formation of SEI to the external surface and maintain the interior void space for Si swelling. This material design showed a reversible capacity of 2350 mAh/g and excellent cycling stability (97% of cycling stability after 1000 cycles), which indicated stable and spatially confined SEI layers [3]. Thus, it is useful for future work to enhance the battery capability of Si-MWCNT based electrodes by coating them with amorphous carbon.

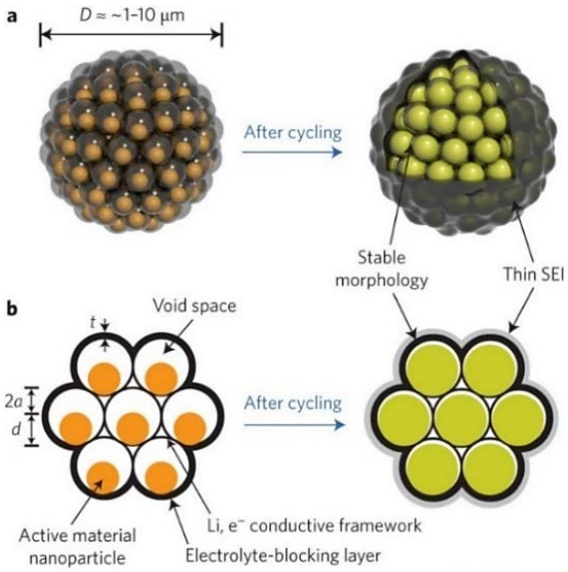


Figure 1.8. a-b) Structural diagrams of the silicon-carbon permanganate material; the inner void space allowed the volume expansion of Si NPs [3].

1.2.7) The development of electrode architectures

Traditionally, common electrodes are fabricated by casting a slurry of active materials with carbon conductive additives and polymer binders on the current collectors such as copper and aluminium foils. Although the traditional electrode design is valid to use nowadays, it still has many features that can be altered in order to enhance their performance including gravimetric energy density and stability of the battery.

The foil, considered as a deadweight, is a large component in a Li-ion cell, accounting for 10% of the total cell weight [37]. The significant weight of the current collector reduces the overall gravimetric energy density of the battery [4, 37, 90]. The metallic current collectors could also be eroded after reacting with HF from electrolyte decomposition [91]. This reaction continually leads to an increase in internal resistance and a reduction in capacity and lifetime of the electrode [92]. In addition, polymeric binders which are used to adhere these materials to current collectors decrease specific areas of the active materials, resulting in the electrochemical polarisation of the electrode, and poor lithium-ion transport [93]. Therefore, electrodes without binders and current collectors have been investigated to tackle the traditional electrode issues. Moreover, there is a need to develop thin-

and-flexible battery electrodes due to the recent technological advancement in portable electronic devices such as mobile phones, tablets, and wearable gadgets.

MWCNT papers (buckypapers, BPs) are used as a free-standing electrode to replace the metal current collector in LIBs due to good thermal, electrical and mechanical properties [4, 37, 90]. For instance, Tocoglu *et al.* (2014) produced flexible Si-MWCNT nanocomposite anodes by sputtering Si onto BPs. These electrodes exhibited good cycle stability with a specific capacity of 620 mAh/g after 100 cycles [94]. When compared with graphite on a copper current collector, the free-standing CNT-Si could significantly reduce the anode weight percentage from 20% to 2%, resulting in an increase of the gravimetric energy density [37]. The production of MWCNT nonwoven fabric coated with Si has been shown before by Evanoff *et al.* (2012). Their material displayed good electrochemical stability with a specific capacity of 494 mAh/g after 150 cycles. This type of anode also exhibited higher hardness than that of other structural materials such as copper, titanium, and even structural steels (Figure 1.9) [4]. Fu *et al.* (2013) suggested that an ideal-flexible silicon-coated-carbon nanotube anode should have the following properties: 1) no added binders, 2) no metal current collectors, 3) smooth and flexible film with low density, 4) untangled MWCNTs with adequate pores to provide a uniform coating of Si on each MWCNT, and 5) an aligned MWCNT structure for accommodating volume changes of Si during cycling. Their CNT-Si-C film showed 2270 mA/g for discharge capacity with coulombic efficiency of 79% [95]. Nevertheless, the manufacturing of the free-standing Si-based electrodes made by Fu *et al.* was expensive and required a complicated experimental procedure which makes scaling up production of these materials very difficult. Thus, it is necessary to find a new method for making the free-standing anode which is facile, cheap and scale-up-able.

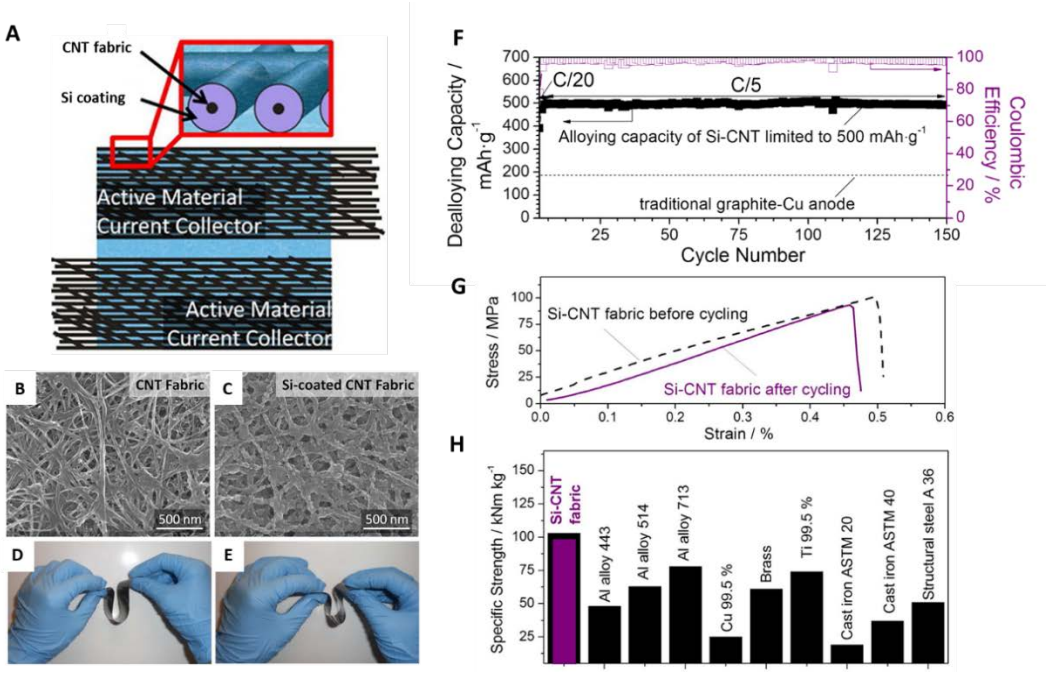


Figure 1.9. A) An illustrative of the silicon-coated CNT fabric battery, B-E) images of pristine CNT and silicon coated CNT fabrics showing their flexibility, F) cycling stability, G) stress and strain testing, and H) specific strength of the as-fabricated electrode (redrawn from [4]) confirming its performance and mechanical property.

1.2.8) The effect of the coin-cell battery components to the battery performance

The effect of the cell components has to be considered when testing the battery cells as it can influence the performance of the free-standing electrodes. Generally, a coin cell battery consists of components which are made from stainless steel (grade SS304, containing 15-20% chromium and 2-10% nickel). The stainless steel can be oxidised under air at room temperature resulting in the formation of iron oxide (both Fe_3O_4 and FeO) and chromium oxide (Cr_2O_3) [96] which is believed to contribute additional capacity to the battery. For studying the passivation reaction on the surface of this material, stainless steel (SS304) was tested in alkyl carbonate electrolyte with $LiPF_6$ salts by Myung *et al.* (2009). At a low voltage range (Figure 1.10A), anodic peaks between 1-2 V were seen which correspond to the SEI formation, the Li_2O formation and the reduction of metal oxides to metals. After etching to remove the SEI layer on the surface, the peaks related to Fe and Cr metal with small portions of metal oxides were observed (Figure 1.10B). Myung *et al.* claim in their work that no

reaction of an alloy with Li took place at near 0 V vs Li/Li^{+} [6]. However, Khateeb *et al.* (2015) reported that the electrode fabricated in the coin-cell configuration showed an extra capacity due to the presence of the Fe_3O_4 formation if the steel-made part has a chance to contact and react with an electrolyte [38]. The steel-case can be easily exposed to an electrolyte as the size of the electrode is usually less than the case [38]. Also, both iron oxide and chromium oxide were studied as anode materials in LIBs [97-99]. These oxide anodes showed a specific capacity of *ca.* 1058-750 mAh/g [98-100] and their discharge/charge voltage range was at 1-2.2 V [38, 101]. As the working voltage of these oxides was in the same range as that of Si and carbon-based electrodes (lower than 2 V), it was implied that the use of stainless steel in a coin cell inevitably contributes an additional capacity to the electrode. Therefore, it is necessary to consider this effect before interpreting the battery performance of the free-standing electrode which is fabricated in the coin-cells.

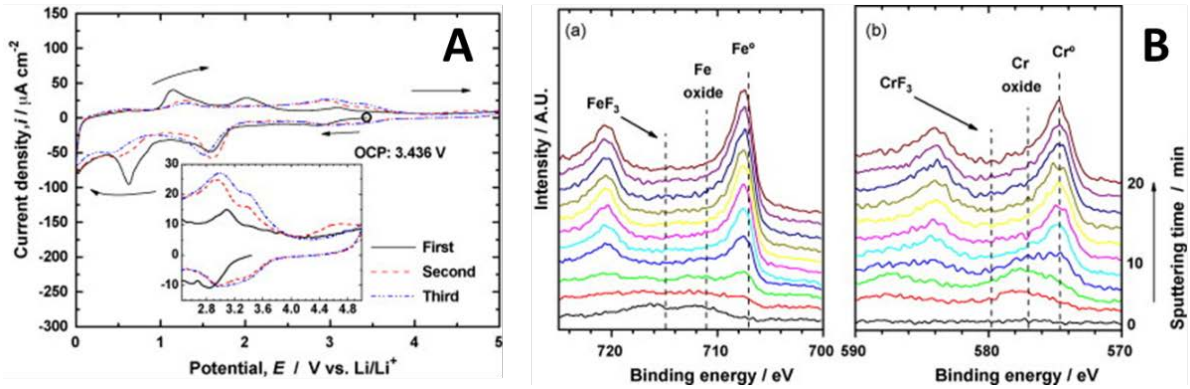


Figure 1.10. A) The cyclic voltammograms of 304 stainless steel, and B) XPS spectra of Fe2p and C2p after polarization at 0 V vs Li/Li^{+} showing the formation of iron oxide and chromium oxide on the stainless steel during the cycling test [6].

1.2.9) Areal capacity of the Si electrode challenge

In most of the reports on the performance of electrodes, only a small amount of areal mass loading (often below 0.3 mg/cm^2) is used for which the capacity is reported in mAh/g, which likely misrepresents the useable capacity for the full-cell battery system [39]. In the full-cell batteries, a major challenge is to consider anode materials that have their areal capacity matching with the areal capacity of cathode materials. Therefore, the areal capacity ratio of negative to positive electrodes (N:P) in the

full-cell batteries needs to be simultaneously set in order to achieve the targeted performance for commercial battery materials. According to previous works, the N:P ratio strongly affects the battery properties resulting in the enhancement of capacity retention [40, 102]. To obtain the best cycle life and performance of the batteries, this ratio should be close to 1:1. In general, the majority of cathode materials is coated on the current collectors in the loading of *ca.* 10 mg/cm^2 [103]. $LiCoO_2$, for example, has a specific capacity of *ca.* 140-150 mAh/g, thereby the relatively areal capacity of target anode materials should be *ca.* 1.4-1.5 mAh/cm^2 [104, 105]. Finally, it was reported that around 2 mAh/cm^2 of the areal capacity with respect to 1 mg/cm^2 of Si loading would be needed so as to compete with a commercial graphite electrode [106].

1.3) Conclusions and challenges to overcome

Lithium-ion batteries have been an energy storage technology which is used in several portable and electronic devices. As a result, over recent years the development of battery components to provide higher energy capacity has been explored so as to meet increasing future demands of energy storage applications. As discussed earlier, Si is one of the most promising anodes to replace traditional carbon-based materials due to its high specific capacity (3579 mAh/g at room temperature). Yet, Si could not be applied as a commercial electrode material in LIBs as the main problem is the large volume change during lithiation-delithiation processes. The volume expansion induces mechanical stress, which results in cracking of the electrode and then the failure of the battery during cycling.

So far, there have been many attempts to improve capacity retention and the coulombic efficiency of the Si electrode. Nonetheless, the approach which is chosen to be focused on in this chapter is the creation of silicon-carbon nanocomposites, including Si-MWCNTs and Si-amorphous carbon. Previous studies have shown that the stability of Si electrodes can be improved by exploiting the properties of silicon-carbon nanocomposites. MWCNTs in these studies were shown to enhance the mechanical stability and electrical conductivity of the electrode, thereby improving the battery

performance; the Si material was anchored on MWCNTs by an amorphous carbon layer. As a result, the Si has been able to detach from the MWCNTs during cycling, causing the decrease of the capacity retention. That is, most previous works reported the stability of the Si-MWCNT electrodes at 100^{th} cycle or less. Additionally, the specific capacity of the Si-MWCNT materials shown in the earlier studies was still below the theoretical capacity.

In addition, the gravimetric energy density of batteries has been significantly increased in recent years. Battery configurations using free-standing MWCNT-based electrodes instead of the common electrodes have shown to be able to improve the specific energy of the battery by removing the unwanted components in the electrode (polymeric binders and metal current collectors). Since the method for making free-standing MWCNTs in previous studies was expensive and difficult to scale up, it is important to explore alternative cost-effective and facile approaches. Finally, to be more accurate in further research, the replacement of the stainless-steel case with other lighter-and-inactive metal cases should be performed to prevent the component effect on battery performance. In addition, the battery performance of the electrode needs to be reported in terms of the gravimetric capacity and areal capacity in order to avoid the misleading results due to a small amount of active material loading.

1.4) References

1. Huggins, R., *Advanced Batteries: Materials Science Aspects*. 2008: Springer US.
2. Buchmann, I. and I. Cadex Electronics, *Batteries in a Portable World: A Handbook on Rechargeable Batteries for Non-engineers*. 4 ed. 2016: Cadex Electronics.
3. Liu, N., et al., *A pomegranate-inspired nanoscale design for large-volume-change lithium battery anodes*. Nat Nano, 2014. **9**(3): p. 187-192.
4. Evanoff, K., et al., *Ultra Strong Silicon-Coated Carbon Nanotube Nonwoven Fabric as a Multifunctional Lithium-Ion Battery Anode*. ACS Nano, 2012. **6**(11): p. 9837-9845.
5. Wu, H., et al., *Stable cycling of double-walled silicon nanotube battery anodes through solid-electrolyte interphase control*. Nat Nano, 2012. **7**(5): p. 310-315.
6. Myung, S.-T., et al., *Passivation behavior of Type 304 stainless steel in a non-aqueous alkyl carbonate solution containing LiPF6 salt*. Electrochimica Acta, 2009. **54**(24): p. 5804-5812.
7. Evanoff, K., et al., *Towards Ultrathick Battery Electrodes: Aligned Carbon Nanotube – Enabled Architecture*. Advanced Materials, 2012. **24**(4): p. 533-537.

8. Winter, M. and R.J. Brodd, *What Are Batteries, Fuel Cells, and Supercapacitors?* Chemical Reviews, 2004. **104**(10): p. 4245-4270.
9. Qi, W., et al., *Nanostructured anode materials for lithium-ion batteries: principle, recent progress and future perspectives.* Journal of Materials Chemistry A, 2017. **5**(37): p. 19521-19540.
10. Roy, P. and S.K. Srivastava, *Nanostructured anode materials for lithium ion batteries.* Journal of Materials Chemistry A, 2015. **3**(6): p. 2454-2484.
11. Owen, J.R., *Rechargeable lithium batteries.* Chemical Society Reviews, 1997. **26**(4): p. 259-267.
12. May, G.J., A. Davidson, and B. Monahov, *Lead batteries for utility energy storage: A review.* Journal of Energy Storage, 2018. **15**: p. 145-157.
13. Omar, N., et al., *Analysis of Nickel-Based Battery Technologies for Hybrid and Electric Vehicles*, in *Reference Module in Chemistry, Molecular Sciences and Chemical Engineering.* 2014, Elsevier.
14. Revankar, S.T., *Chapter Six - Chemical Energy Storage*, in *Storage and Hybridization of Nuclear Energy*, H. Bindra and S. Revankar, Editors. 2019, Academic Press. p. 177-227.
15. Ma, S., et al., *Temperature effect and thermal impact in lithium-ion batteries: A review.* Progress in Natural Science: Materials International, 2018. **28**(6): p. 653-666.
16. Tarascon, J.M. and M. Armand, *Issues and challenges facing rechargeable lithium batteries.* Nature, 2001. **414**(6861): p. 359-367.
17. Etacheri, V., et al., *Challenges in the development of advanced Li-ion batteries: a review.* Energy & Environmental Science, 2011. **4**(9): p. 3243-3262.
18. Haregewoin, A.M., A.S. Wotango, and B.-J. Hwang, *Electrolyte additives for lithium ion battery electrodes: progress and perspectives.* Energy & Environmental Science, 2016. **9**(6): p. 1955-1988.
19. Linden, D. and T.B. Reddy, *Handbook of batteries*. 2002, New York: McGraw-Hill.
20. Zhang, W.-J., *Lithium insertion/extraction mechanism in alloy anodes for lithium-ion batteries.* Journal of Power Sources, 2011. **196**(3): p. 877-885.
21. Goodenough, J.B. and K.-S. Park, *The Li-Ion Rechargeable Battery: A Perspective.* Journal of the American Chemical Society, 2013. **135**(4): p. 1167-1176.
22. Scrosati, B. and J. Garche, *Lithium batteries: Status, prospects and future.* Journal of Power Sources, 2010. **195**(9): p. 2419-2430.
23. Nitta, N. and G. Yushin, *High-Capacity Anode Materials for Lithium-Ion Batteries: Choice of Elements and Structures for Active Particles.* Particle & Particle Systems Characterization, 2014. **31**(3): p. 317-336.
24. Li, H., et al., *Nano-alloy anode for lithium ion batteries.* Solid State Ionics, 2002. **148**(3–4): p. 247-258.
25. Kasavajjula, U., C. Wang, and A.J. Appleby, *Nano- and bulk-silicon-based insertion anodes for lithium-ion secondary cells.* Journal of Power Sources, 2007. **163**(2): p. 1003-1039.
26. Yang, S., et al., *A comparative study of electrochemical properties of two kinds of carbon nanotubes as anode materials for lithium ion batteries.* Electrochimica Acta, 2008. **53**(5): p. 2238-2244.
27. Gao, B., et al., *Electrochemical intercalation of single-walled carbon nanotubes with lithium.* Chemical Physics Letters, 1999. **307**(3–4): p. 153-157.
28. Zhang, Q., et al., *Progress towards high-power Li/CFx batteries: electrode architectures using carbon nanotubes with CFx.* Physical Chemistry Chemical Physics, 2015. **17**(35): p. 22504-22518.
29. Besenhard, J.O., J. Yang, and M. Winter, *Will advanced lithium-alloy anodes have a chance in lithium-ion batteries?* Journal of Power Sources, 1997. **68**(1): p. 87-90.
30. Saint, J., et al., *Towards a Fundamental Understanding of the Improved Electrochemical Performance of Silicon–Carbon Composites.* Advanced Functional Materials, 2007. **17**(11): p. 1765-1774.
31. Dimov, N., S. Kugino, and M. Yoshio, *Carbon-coated silicon as anode material for lithium ion batteries: advantages and limitations.* Electrochimica Acta, 2003. **48**(11): p. 1579-1587.
32. Dimov, N., S. Kugino, and M. Yoshio, *Mixed silicon–graphite composites as anode material for lithium ion batteries: Influence of preparation conditions on the properties of the material.* Journal of Power Sources, 2004. **136**(1): p. 108-114.
33. Shu, J., et al., *Cage-like carbon nanotubes/Si composite as anode material for lithium ion batteries.* Electrochemistry Communications, 2006. **8**(1): p. 51-54.
34. Wang, W. and P.N. Kumta, *Nanostructured Hybrid Silicon/Carbon Nanotube Heterostructures: Reversible High-Capacity Lithium-Ion Anodes.* ACS Nano, 2010. **4**(4): p. 2233-2241.

35. Eom, J.Y., et al., *Electrochemical Insertion of Lithium into Multiwalled Carbon Nanotube/Silicon Composites Produced by Ballmilling.* Journal of The Electrochemical Society, 2006. **153**(9): p. A1678-A1684.
36. Frackowiak, E., et al., *Electrochemical storage of lithium in multiwalled carbon nanotubes.* Carbon, 1999. **37**(1): p. 61-69.
37. Cui, L.-F., et al., *Light-Weight Free-Standing Carbon Nanotube-Silicon Films for Anodes of Lithium Ion Batteries.* ACS Nano, 2010. **4**(7): p. 3671-3678.
38. Khateeb, S.A., et al., *Effects of Steel Cell Components on Overall Capacity of Pulsed Laser Deposited FeF2 Thin Film Lithium Ion Batteries.* Journal of The Electrochemical Society, 2015. **162**(8): p. A1667-A1674.
39. Gogotsi, Y. and P. Simon, *True Performance Metrics in Electrochemical Energy Storage.* Science, 2011. **334**(6058): p. 917.
40. Kim, C.-S., et al., *Effects of Capacity Ratios between Anode and Cathode on Electrochemical Properties for Lithium Polymer Batteries.* Electrochimica Acta, 2015. **155**(Supplement C): p. 431-436.
41. Zhang, W.-J., *A review of the electrochemical performance of alloy anodes for lithium-ion batteries.* Journal of Power Sources, 2011. **196**(1): p. 13-24.
42. Landi, B.J., et al., *Carbon nanotubes for lithium ion batteries.* Energy & Environmental Science, 2009. **2**(6): p. 638-654.
43. Yu, M.-F., et al., *Strength and Breaking Mechanism of Multiwalled Carbon Nanotubes Under Tensile Load.* Science, 2000. **287**(5453): p. 637.
44. Ma, P.-C., et al., *Dispersion and functionalization of carbon nanotubes for polymer-based nanocomposites: A review.* Composites Part A: Applied Science and Manufacturing, 2010. **41**(10): p. 1345-1367.
45. Prasek, J., et al., *Methods for carbon nanotubes synthesis—review.* Journal of Materials Chemistry, 2011. **21**(40): p. 15872-15884.
46. Song, B., et al., *Intercalation and diffusion of lithium ions in a carbon nanotube bundle by ab initio molecular dynamics simulations.* Energy & Environmental Science, 2011. **4**(4): p. 1379-1384.
47. Yang, Z.-h. and H.-q. Wu, *Electrochemical intercalation of lithium into raw carbon nanotubes.* Materials Chemistry and Physics, 2001. **71**(1): p. 7-11.
48. Zhao, M., et al., *Curvature-induced condensation of lithium confined inside single-walled carbon nanotubes: First-principles calculations.* Physics Letters A, 2005. **340**(5): p. 434-439.
49. Udomvech, A., T. Kerdcharoen, and T. Osotchan, *First principles study of Li and Li+ adsorbed on carbon nanotube: Variation of tubule diameter and length.* Chemical Physics Letters, 2005. **406**(1): p. 161-166.
50. Yang, Z.-h. and H.-q. Wu, *Electrochemical intercalation of lithium into carbon nanotubes.* Solid State Ionics, 2001. **143**(2): p. 173-180.
51. Khantha, M., et al., *Interaction and concerted diffusion of lithium in a (5,5) carbon nanotube.* Physical Review B, 2008. **78**(11): p. 115430.
52. Eom, J.Y., et al., *Lithium insertion into purified and etched multi-walled carbon nanotubes synthesized on supported catalysts by thermal CVD.* Carbon, 2004. **42**(12–13): p. 2589-2596.
53. Wu, G.T., et al., *Structure and Lithium Insertion Properties of Carbon Nanotubes.* Journal of The Electrochemical Society, 1999. **146**(5): p. 1696-1701.
54. Wang, Q., et al., *Anomalous Electrochemical Behavior of Multiwalled Carbon Nanotubes for Lithium Insertion/Extraction.* Journal of The Electrochemical Society, 2004. **151**(9): p. A1333-A1337.
55. Zhang, Y., et al., *The study of multi-walled carbon nanotubes with different diameter as anodes for lithium-ion batteries.* Applied Surface Science, 2012. **258**(10): p. 4729-4732.
56. Wen, C.J. and R.A. Huggins, *Chemical diffusion in intermediate phases in the lithium-silicon system.* Journal of Solid State Chemistry, 1981. **37**(3): p. 271-278.
57. Sharma, R.A. and R.N. Seefurth, *Thermodynamic Properties of the Lithium-Silicon System.* Journal of The Electrochemical Society, 1976. **123**(12): p. 1763-1768.
58. van der Marel, C., G.J.B. Vinke, and W. van der Lugt, *The phase diagram of the system lithium-silicon.* Solid State Communications, 1985. **54**(11): p. 917-919.
59. Obrovac, M.N. and L. Christensen, *Structural Changes in Silicon Anodes during Lithium Insertion/Extraction.* Electrochemical and Solid-State Letters, 2004. **7**(5): p. A93-A96.
60. Obrovac, M.N. and L.J. Krause, *Reversible Cycling of Crystalline Silicon Powder.* Journal of The Electrochemical Society, 2007. **154**(2): p. A103-A108.

61. Ma, D., Z. Cao, and A. Hu, *Si-Based Anode Materials for Li-Ion Batteries: A Mini Review.* Nano-Micro Letters, 2014. **6**(4): p. 347-358.
62. McDowell, M.T., et al., *25th Anniversary Article: Understanding the Lithiation of Silicon and Other Alloying Anodes for Lithium-Ion Batteries.* Advanced Materials, 2013. **25**(36): p. 4966-4985.
63. Hatchard, T.D. and J.R. Dahn, *In Situ XRD and Electrochemical Study of the Reaction of Lithium with Amorphous Silicon.* Journal of The Electrochemical Society, 2004. **151**(6): p. A838-A842.
64. Owejan, J.E., et al., *Solid Electrolyte Interphase in Li-Ion Batteries: Evolving Structures Measured In situ by Neutron Reflectometry.* Chemistry of Materials, 2012. **24**(11): p. 2133-2140.
65. Winter, M., P. Novák, and A. Monnier, *Graphites for Lithium-Ion Cells: The Correlation of the First-Cycle Charge Loss with the Brunauer-Emmett-Teller Surface Area.* Journal of The Electrochemical Society, 1998. **145**(2): p. 428-436.
66. Winter, M., *The Solid Electrolyte Interphase – The Most Important and the Least Understood Solid Electrolyte in Rechargeable Li Batteries*, in *Zeitschrift für Physikalische Chemie International journal of research in physical chemistry and chemical physics*. 2009. p. 1395.
67. Xu, K., *Nonaqueous Liquid Electrolytes for Lithium-Based Rechargeable Batteries.* Chemical Reviews, 2004. **104**(10): p. 4303-4418.
68. Radvanyi, E., et al., *Failure mechanisms of nano-silicon anodes upon cycling: an electrode porosity evolution model.* Physical Chemistry Chemical Physics, 2014. **16**(32): p. 17142-17153.
69. Ozanam, F. and M. Rosso, *Silicon as anode material for Li-ion batteries.* Materials Science and Engineering: B.
70. Netz, A., R.A. Huggins, and W. Weppner, *The formation and properties of amorphous silicon as negative electrode reactant in lithium systems.* Journal of Power Sources, 2003. **119–121**: p. 95-100.
71. Jung, H., et al., *Amorphous silicon anode for lithium-ion rechargeable batteries.* Journal of Power Sources, 2003. **115**(2): p. 346-351.
72. Li, J., R.B. Lewis, and J.R. Dahn, *Sodium Carboxymethyl Cellulose: A Potential Binder for Si Negative Electrodes for Li-Ion Batteries.* Electrochemical and Solid-State Letters, 2007. **10**(2): p. A17-A20.
73. Wang, C.S., et al., *Lithium Insertion in Carbon-Silicon Composite Materials Produced by Mechanical Milling.* Journal of The Electrochemical Society, 1998. **145**(8): p. 2751-2758.
74. Luo, F., et al., *Review—Nano-Silicon/Carbon Composite Anode Materials Towards Practical Application for Next Generation Li-Ion Batteries.* Journal of The Electrochemical Society, 2015. **162**(14): p. A2509-A2528.
75. Wang, W., R. Epur, and P.N. Kumta, *Vertically aligned silicon/carbon nanotube (VASCNT) arrays: Hierarchical anodes for lithium-ion battery.* Electrochemistry Communications, 2011. **13**(5): p. 429-432.
76. Park, K.-S., et al., *Self-supported multi-walled carbon nanotube-embedded silicon nanoparticle films for anodes of Li-ion batteries.* Materials Research Bulletin, 2013. **48**(4): p. 1732-1736.
77. Gohier, A., et al., *High-Rate Capability Silicon Decorated Vertically Aligned Carbon Nanotubes for Li-Ion Batteries.* Advanced Materials, 2012. **24**(19): p. 2592-2597.
78. Li, Y., et al., *Enhanced Rate Capability by Employing Carbon Nanotube-Loaded Electrospun Si/C Composite Nanofibers As Binder-Free Anodes.* Journal of The Electrochemical Society, 2013. **160**(3): p. A528-A534.
79. Zhou, J., et al., *In situ growth of carbon nanotube wrapped Si composites as anodes for high performance lithium ion batteries.* Nanoscale, 2016. **8**(9): p. 4903-4907.
80. Hieu, N.T., et al., *Electrospun nanofibers with a core-shell structure of silicon nanoparticles and carbon nanotubes in carbon for use as lithium-ion battery anodes.* Journal of Materials Chemistry A, 2014. **2**(36): p. 15094-15101.
81. Wang, W., et al., *Silicon Decorated Cone Shaped Carbon Nanotube Clusters for Lithium Ion Battery Anodes.* Small, 2014. **10**(16): p. 3389-3396.
82. Yu, W.-J., et al., *Lithiation of Silicon Nanoparticles Confined in Carbon Nanotubes.* ACS Nano, 2015. **9**(5): p. 5063-5071.
83. Fan, Y., et al., *High performance lithium ion battery anodes based on carbon nanotube–silicon core–shell nanowires with controlled morphology.* Carbon, 2013. **59**: p. 264-269.
84. U. Tocoglu, O.C., H. Akbulut, *Cyclic Performance Tests of Si/MWCNT Composite Lithium Ion Battery Anodes at Different Temperature.* Acta Physica Polonica A, 2015. **127**(4): p. 1059-1061.

85. Na, Y.-S., et al., *Electrochemical performance of Si-multiwall carbon nanotube nanocomposite anode synthesized by thermal plasma.* Thin Solid Films, 2015. **587**: p. 14-19.
86. Yen, Y.-C., et al., *Study on Solid-Electrolyte-Interphase of Si and C-Coated Si Electrodes in Lithium Cells.* Journal of The Electrochemical Society, 2009. **156**(2): p. A95-A102.
87. Liang, B., Y. Liu, and Y. Xu, *Silicon-based materials as high capacity anodes for next generation lithium ion batteries.* Journal of Power Sources, 2014. **267**: p. 469-490.
88. Ng, S.-H., et al., *Highly Reversible Lithium Storage in Spheroidal Carbon-Coated Silicon Nanocomposites as Anodes for Lithium-Ion Batteries.* Angewandte Chemie International Edition, 2006. **45**(41): p. 6896-6899.
89. Huang, R., et al., *Carbon-coated silicon nanowire array films for high-performance lithium-ion battery anodes.* Applied Physics Letters, 2009. **95**(13): p. 133119.
90. Erika, B., et al., *High-performance flexible nanoporous Si-carbon nanotube paper anodes for micro-battery applications.* Nanotechnology, 2016. **27**(24): p. 245401.
91. Myung, S.-T., Y. Hitoshi, and Y.-K. Sun, *Electrochemical behavior and passivation of current collectors in lithium-ion batteries.* Journal of Materials Chemistry, 2011. **21**(27): p. 9891-9911.
92. Whitehead, A.H. and M. Schreiber, *Current Collectors for Positive Electrodes of Lithium-Based Batteries.* Journal of The Electrochemical Society, 2005. **152**(11): p. A2105-A2113.
93. Li, X., et al., *Novel approach toward a binder-free and current collector-free anode configuration: highly flexible nanoporous carbon nanotube electrodes with strong mechanical strength harvesting improved lithium storage.* Journal of Materials Chemistry, 2012. **22**(36): p. 18847-18853.
94. Tocoglu, U., et al., *Coaxial silicon/multi-walled carbon nanotube nanocomposite anodes for long cycle life lithium-ion batteries.* Applied Surface Science, 2014. **305**: p. 402-411.
95. Fu, K., et al., *Aligned Carbon Nanotube-Silicon Sheets: A Novel Nano-architecture for Flexible Lithium Ion Battery Electrodes.* Advanced Materials, 2013. **25**(36): p. 5109-5114.
96. Langevoort, J.C., et al., *On the oxide formation on stainless steels AISI 304 and incoloy 800H investigated with XPS.* Applied Surface Science, 1987. **28**(2): p. 167-179.
97. Fu, Y., et al., *Chromium(III) oxide carbon nanocomposites lithium-ion battery anodes with enhanced energy conversion performance.* Chemical Engineering Journal, 2015. **277**: p. 186-193.
98. Muraliganth, T., A. Vadivel Murugan, and A. Manthiram, *Facile synthesis of carbon-decorated single-crystalline Fe3O4nanowires and their application as high performance anode in lithium ion batteries.* Chemical Communications, 2009(47): p. 7360-7362.
99. Poizot, P., et al., *Nano-sized transition-metal oxides as negative-electrode materials for lithium-ion batteries.* Nature, 2000. **407**: p. 496.
100. Li, H., P. Balaya, and J. Maier, *Li-Storage via Heterogeneous Reaction in Selected Binary Metal Fluorides and Oxides.* Journal of The Electrochemical Society, 2004. **151**(11): p. A1878-A1885.
101. Hu, J., H. Li, and X. Huang, *Cr2 O 3-Based Anode Materials for Li-Ion Batteries.* Electrochemical and Solid-State Letters, 2005. **8**(1): p. A66-A69.
102. Wu, H.M., et al., *Development of LiNi0.5Mn1.5O4 / Li4Ti5O12 System with Long Cycle Life.* Journal of The Electrochemical Society, 2009. **156**(12): p. A1047-A1050.
103. Singh, M., J. Kaiser, and H. Hahn, *Thick Electrodes for High Energy Lithium Ion Batteries.* Journal of The Electrochemical Society, 2015. **162**(7): p. A1196-A1201.
104. Koksbang, R., et al., *Cathode materials for lithium rocking chair batteries.* Solid State Ionics, 1996. **84**(1): p. 1-21.
105. Julien, M.C., et al., *Comparative Issues of Cathode Materials for Li-Ion Batteries.* Inorganics, 2014. **2**(1).
106. Leveau, L., et al., *Silicon nano-trees as high areal capacity anodes for lithium-ion batteries.* Journal of Power Sources, 2016. **316**: p. 1-7.

Chapter 2

Lithiation and Volume Expansion of Silicon Anodes in Li-ion batteries

---

Si anodes exhibit high irreversible capacity and poor stability as a result of their susceptibility to enormous volume changes that induce fracture in the material and continuous SEI formation. In order to tackle these problems and to develop stable Si anode materials, it is necessary to thoroughly understand the nature of their structural change and fracture evolution. Since crystalline and amorphous Si are used as active materials in battery electrodes and crystalline Si is converted to the amorphous phase in subsequent cycling, both Si structures will be studied in this work. They will be separately reviewed here in light of their dissimilar performance as battery materials, indicating differing electrode activities during cycling. [10]. In this chapter, the lithiation process of Si materials will be firstly discussed to comprehend the phase boundary formation and structural change of the material during cycling. The mechanical stress induction and fracture evolution in Si materials upon lithiation will be then investigated. Finally, the size-dependent fracture formation of Si materials will be examined to show how the particle size of Si affects strain relaxation and crack initiation in the material. In the case of the crystalline Si, the effect of crystallographic orientations to these processes will be discussed simultaneously.

2.1) Crystalline silicon

2.1.1) Li-Si alloy in crystalline Si

During the Li alloying reaction in crystalline Si, the material is lithiated via a two-phase reaction. After alloying, parts of the crystalline Si turn to form amorphous lithiated Si (Li_xSi). Thus, there are two coexisting phases (crystalline Si and lithiated Si), which can be observably divided by a sharp interface (Figure 2.1A) [7]. A high concentration of Li is typically found near the crystalline-amorphous interface. At the interface, the two-phase lithiation mechanism theoretically occurs due to the large activation energy required to break Si-Si bonds [10]. It was found that the lithiation at the interface depends on the crystallographic orientations of the crystalline Si. The phase boundary is preferably formed at the (110) orientation rather than at other orientations since Li prefers to diffuse along the <110> direction and accumulates at tetrahedral sites between (111) planes, which are the most stable location for Li insertion. When the concentration of Li increases, the Si-Si bond between the (111) planes will be broken up since Li atoms weaken the Si covalent bonds by charge transferred from Li filling up the antibonding sp^3 states of Si [4]. This results in the dissolution of Si atoms from the crystalline Si at the phase boundary, leading to the electrochemical solid-state amorphisation (Figure 2.2A-B) [8]. In addition, a valley-like structure of the (110) Si, where Si atoms are bonded in a zig-zag configuration at the surface, strongly affects the concentration of Li at the phase boundary (Figure 2.1B). This structural characteristic leads to the high Li density at the (110) phase boundary, causing an easier Si dissolution and a higher rate of Li-Si amorphisation at the phase boundary [11]. The thickness of the phase boundary in the Si materials is also influenced by the Si-Si bond locations between (111) planes (highlighted as red lines in Figure 2.1A). Regarding Si (100), these Si-Si bonds are slanting to the surface. Li atoms then need a longer time to occupy the tetrahedral sites, resulting in the formation of a thick phase boundary in the material. In contrast, the Si-Si bond is located at the

surface of Si (111), which leads to layer-layer peeling off at the planes. Thus, the phase boundary is unlikely to form in Si (111) [7].

More importantly, the amorphous Si in the electrode is formed when Li from the Li_xSi phase is delithiated. Therefore, after the first cycle, the crystalline Si is converted to an amorphous form and continues to be amorphous in the following cycles, *i.e.*, the lithiation of the Si material occurs through a single-phase reaction during further cycling [12, 13].

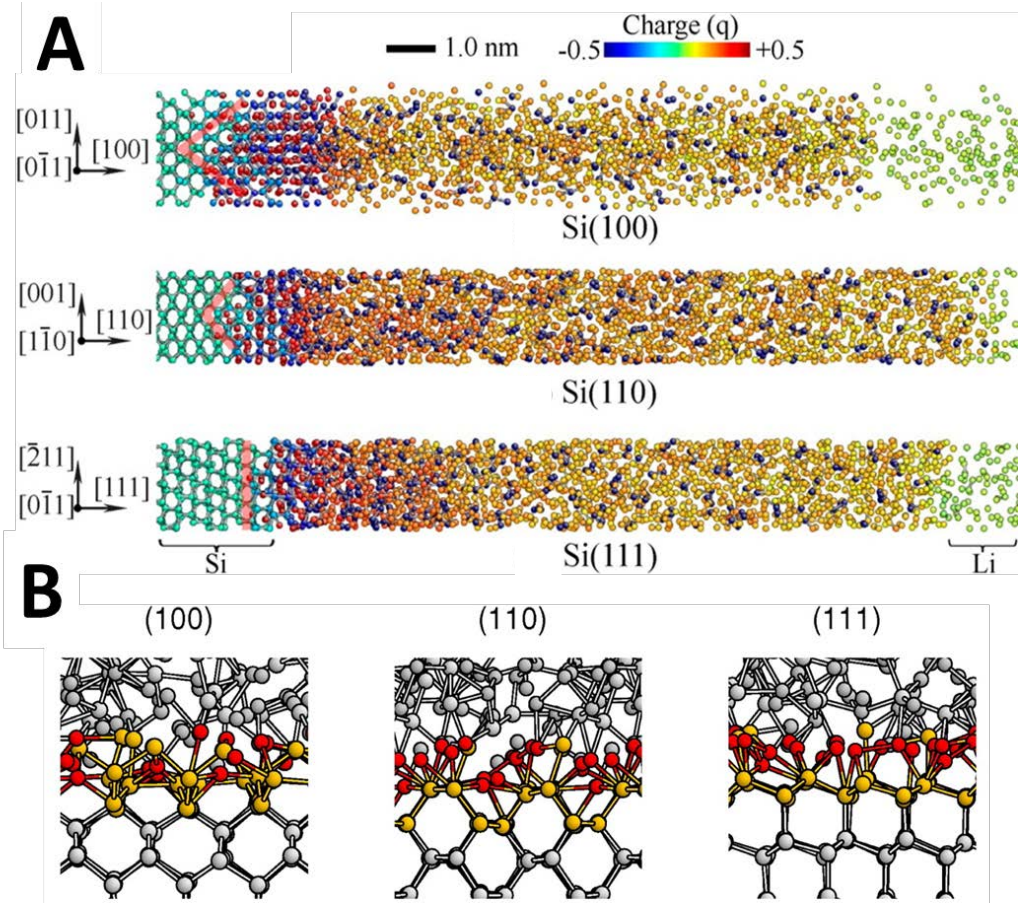


Figure 2.1. A) Phase boundary configurations during the lithiation of crystalline Si at different orientations; Si-Si bonds between (111) planes are shown as red lines. The Si-Si bond position strongly affects the thickness of the phase boundary. The Si (110) shows the thickest phase boundary because Li atoms require longer time to accumulate into the tetrahedral sites between (111) planes. The atom colours represent the charge state, *i.e.*, green indicates neutral atoms, blue indicates Si atoms, and red indicates Li atoms. The figure reproduced from Kim *et al.* 2014 [7]. B) The two-phase boundaries are formed at (100), (110) and (111) Si orientations. Red and yellow balls denote the Li and Si atoms, respectively. The valley-like structure is found at the (110) Si surface which leads to the enhancement of the Li concentration and then the high rate of the Li-Si reaction at the phase boundary. The figure adapted from Jung *et al.* 2012 [11].

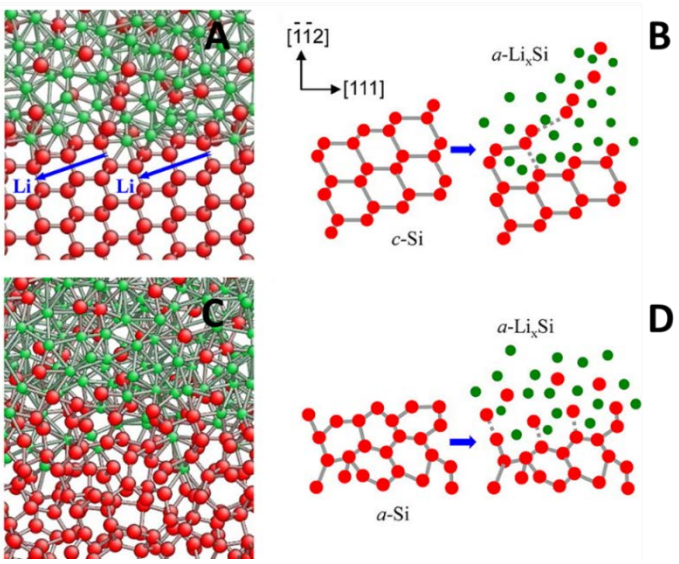


Figure 2.2. The two phase lithiation of crystalline Si and amorphous Si; A) the concentration of Li (green) is high at the facet of c-Si (red) and B) these Li atoms weaken Si bonds leading to the dissolution of Si atoms from the c-Si [8], C) similar to c-Si, the Li concentration is high near the interface leading to D) the easy dissolution of Si atoms from the a-Si into Li_xSi alloy[5].

Also, the amorphous lithiated silicon (Li_xSi) spontaneously crystallises to $Li_{15}Si_4$ (c-$Li_{15}Si_4$) when the lithiation voltage was steadily reduced until being held at 50 mV vs Li/Li^+ [30]. Another study [29] concurrently reported that the Li_xSi maintained its amorphous structure (a-$Li_{3.75}Si$) during lithiation, where x increased to 3.75 (Figure 2.3a-c). At this point, the crystallisation took place without changing the chemical composition (Figure 2.3d-f). The electrochemically driven crystallisation results from the rearrangement of the local bonding configuration. It occurs without long-range atomic diffusion which is different from a classic nucleation process [29]. When increasing Li concentration in the lithiated Si structure, the structure loses its connectivity leading to isolated Si anions. The c-$Li_{15}Si_4$ nucleates inhomogeneously from the area which highly contains isolated Si anions [31]. In addition, the local atomic distributions of a-$Li_{3.75}Si$ and c-$Li_{15}Si_4$ are similar [10]. It leads to the crystallisation of the metastable $Li_{15}Si_4$ phase because the Gibbs free energy of the crystalline lithiated Si is lower than that of the amorphous one. The resultant $Li_{15}Si_4$ is polycrystalline with a grain size of a few tens of nanometres. The c-$Li_{15}Si_4$ is also the most highly lithiated Si phase at room temperature, and its theoretical capacity is 3579 mAh/g [29].

The presence of c-$Li_{15}Si_4$, however, has a detrimental effect on battery cycling; the inhomogeneous phase transition causes high internal stress, resulting in capacity fading and the detachment of active materials from a substrate. Therefore, the capacity retention of the Si electrode could be enhanced when the cut-off voltage is set above 50 mV [32]. Furthermore, the crystallisation of a-Li_xSi was observed in both amorphous and crystalline Si; that is, this process was not depended on starting materials [29]. Still, the studies of the crystallisation of a-$Li_{3.75}Si$ into c-$Li_{15}Si_4$ are limited. Hence, more works involving simulations and characterisations are needed to further examine the local rearrangement of atomic configurations in a-$Li_{3.75}Si$ during the phase transition.

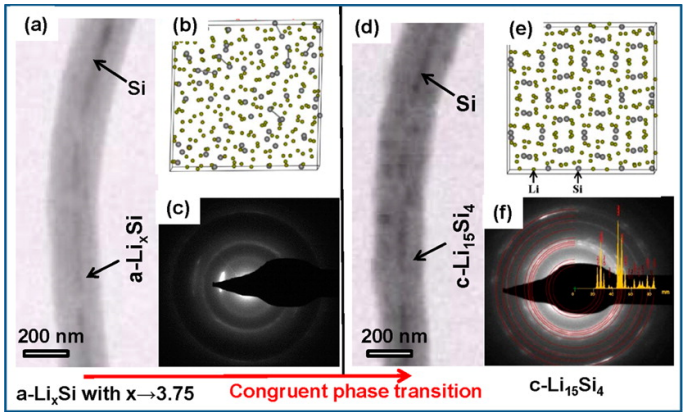


Figure 2.3. STEM images and SAED patterns showing the congruent phase transition from a-Li_xSi to c-$Li_{15}Si_4$ when x reaches a critical value of 3.75; (a) STEM image of a-Li_xSi nanowire, (b) atomic configuration in a-Li_xSi. (c) Electron diffraction pattern of a-Li_xSi, (d) STEM image of the polycrystalline c-$Li_{15}Si_4$, (e) atomic configuration of c-$Li_{15}Si_4$, and (f) electron diffraction pattern of c-$Li_{15}Si_4$ [29].

2.1.2) Volume change and fracture induction in crystalline Si

During lithiation, the Li atoms near the interface slowly move into the crystalline Si by breaking the Si bonds (Figure 2.4A). The Si then expands in order to accommodate them, resulting in the disruption of the crystalline structure [2]. It was found that the volume of the material increases linearly with the content of Li inside the Si structure. However, the density of the material decreases when Li is gradually inserted into the Si material due to the denser structure of crystalline Si compared to that of amorphous Li-Si alloy (Figure 2.5). According to the computational study by Kim *et al.*, the highly lithiated Si phase ($Li_{15}Si_4$) is predicted to have in 300% volume expansion, which is in agreement with the experimental results [4].

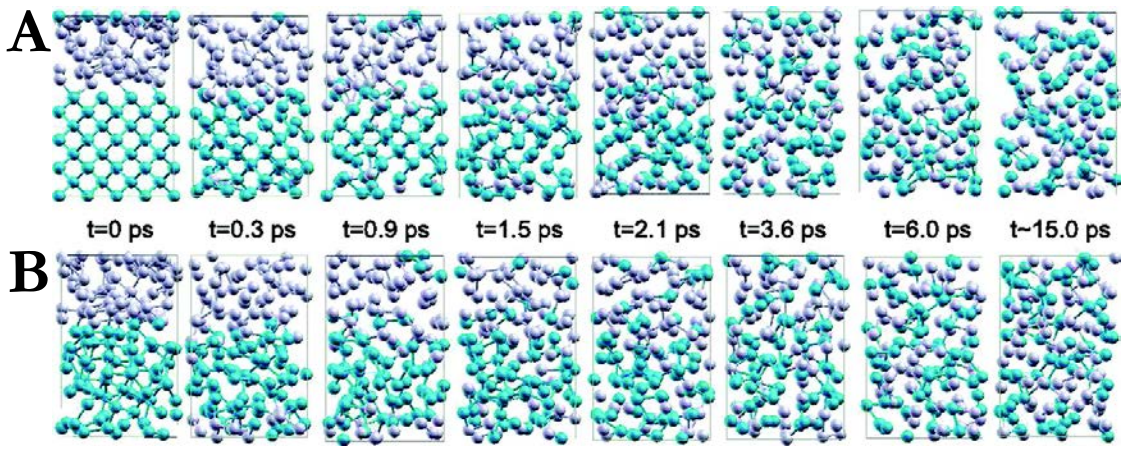


Figure 2.4. The structural change of A) crystalline Si and B) amorphous Si at different lithiation stages (t =0 - 15.0 ps); Si and Li atoms present as spheres in cyan and purple colour, respectively [2].

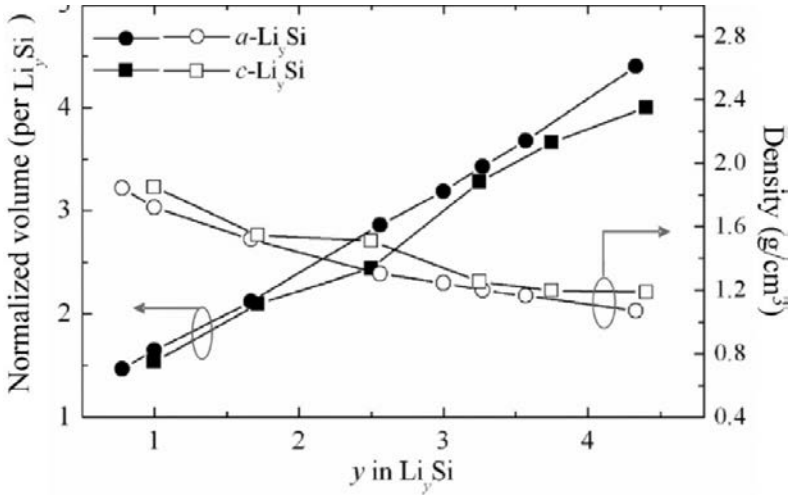


Figure 2.5. The graph showing the change of volume (normalized with respect to the volume of c-Si) and density of Li_ySi alloys as a function of the Li content; the volume of the material increases linearly with the content of Li, while the density shows the opposite trend [4].

Several studies also reported that the volume change of the crystalline Si structure during cycling is anisotropic [1, 14-16]. This anisotropic expansion is due to variations in interfacial reaction rates of crystallographic Si planes. For instance, Lee *et al.* (2011) showed anisotropic changes of Si during lithiation, where dimensional changes depended on the orientation of crystalline Si. As shown in Figure 2.6, the circular cross-sectional view of pillars with <100>, <110>, and <111> orientations was observed to change to cross, ellipse, and hexagon forms during partial lithiation, respectively. There was a significant expansion of the <100> and <110> orientation after full lithiation while the

cross-section of <111> pillars slightly changed to a hexagon. They pointed out that the Si anode expanded anisotropically especially along the <110> direction as Li atoms can break the Si crystalline lattice easily in the <110> orientation and prefer to diffuse along this orientation [1]. As aforementioned, Li atoms can penetrate and break up the Si-Si bonding between the (111) plane, the orientation of the (111) planes thereby controls the reaction rate at the interface and causes the anisotropic expansion upon the lithiation. Eventually, the anisotropic volume change phenomenon in the crystalline Si electrode leads to heterogeneous stress and fracture initiation in the Si material [8]. The nature of the stress induced and the fracture evolution in the crystalline Si material therefore needs to be examined further.

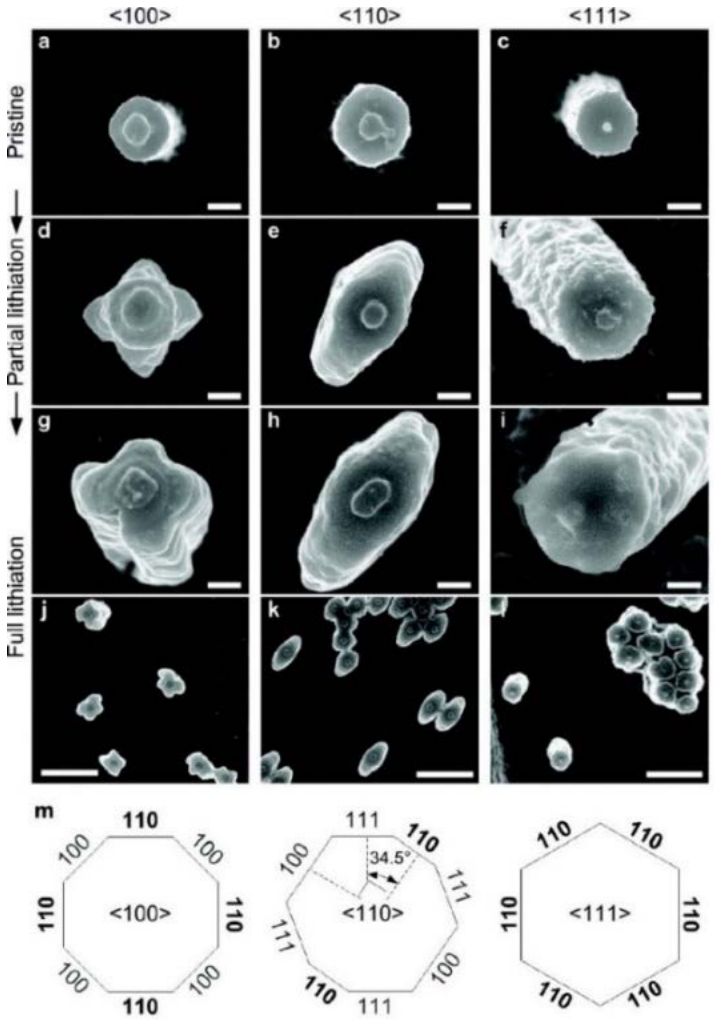


Figure 2.6. The anisotropic change of crystalline silicon nanopillars with three different orientations during lithiation; silicon expanded preferably along the <110> orientation [1].

In crystalline Si, the stress is initially induced at the region near the two-phase interface due to mismatched volume expansion of the material resulting from the different Li concentration at the interface. During the lithiation, hoop compression initially occurs at the interface because the unlithiated core acts against the induced volume expansion of the partially lithiated shell. The movement of the interfacial boundary thereby controls the stress generation in the crystalline Si. The von Mises stress then exceeds the yielding strength (1.5 GPa), causing plastic yielding of the partially lithiated Si at the interface (Figure 2.7A). When the interfacial boundary moves continuously, the pushing-out effect takes place. The radial expansion arises at the boundary, pushing out the lithiated Si nearer the surface and the initial compressive hoop stress changes into tensile hoop stress in the outer layer. The hoop compression conversely occurs inside the material (Figure 2.7B) [6, 17]. The tensile hoop stress is known to facilitate the fracture introduced at the surface, whereas the compressive stress hinders the crack induction [15]. As the lithiation continues, the unlithiated Si is depleted further. Therefore, the compressive stress region near the centre is demolished, resulting in the eventual fracture formation on the material surface [6, 15]. Furthermore, the anisotropic expansion leads to fracture initiation between crystallographic planes where preferential lithiation occurs [10]. As shown in Figure 2.7C, the preferential volume expansion along the <110> orientations then causes heightening tensile stress at the outer surfaces between these orientations, especially at the corner of the <110> orientations. The severe tensile stress eventually leads to anisotropic fractures in these areas [3].

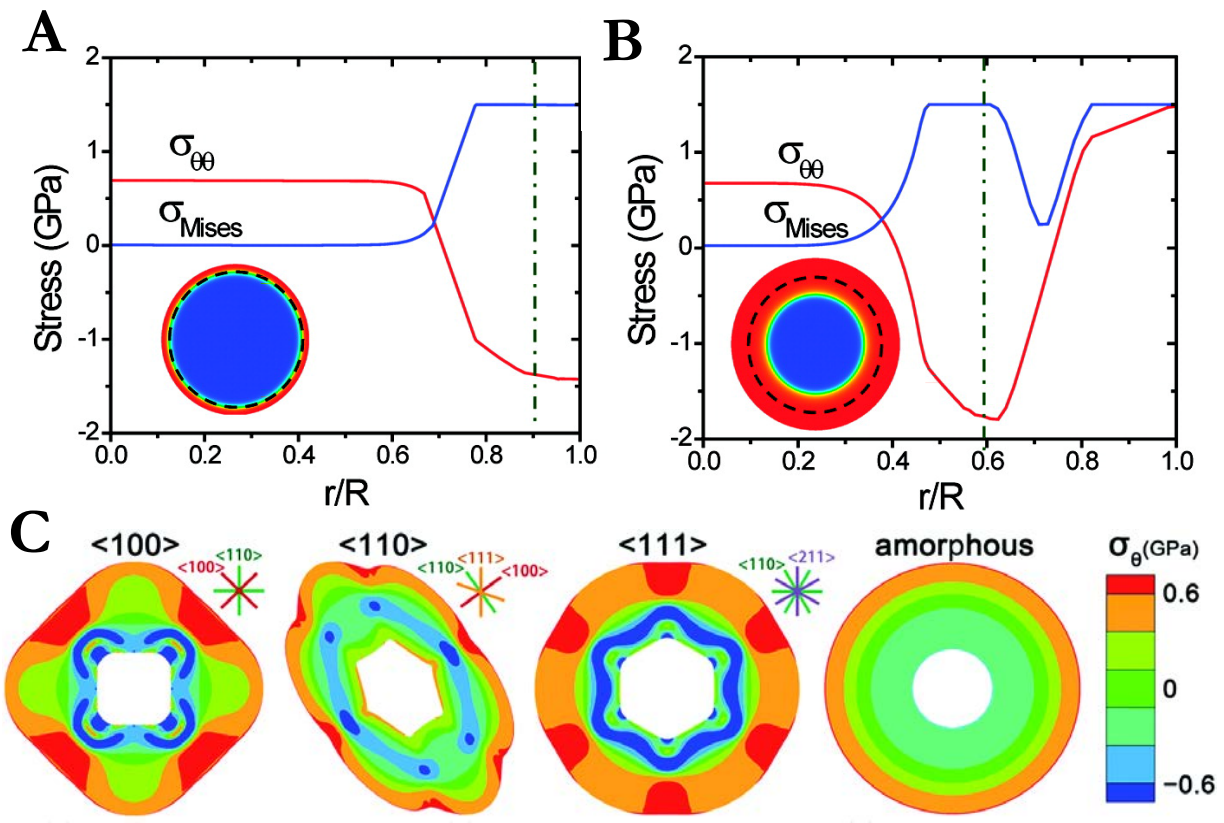


Figure 2.7. Simulations of lithiation and stress induction in Si NPs. The dot-dash line represents the location of the interface. A) Radial distribution of hoop stress $\sigma_{\theta\theta}$ and von Mises stress σ_{Mises} confirms that the hoop stress is compressive at the interface and plastic yielding (σ_{Mises} = the yield stress of 1.5 GPa) is arisen in the surface layer. The inset sphere shows the Li concentration (blue and red indicate a low and high concentration of Li respectively) and the particle size before lithiation is presented as the dashed line. B) At the following lithiation, the hoop tension conversely takes place in the outer layer; as the tensile hoop stress in the surface is larger than that in the centre, it facilitates fracture from the surface [6]. C) Hoop stress contours of the cross-sections of crystalline <100>, <110>, <111> and amorphous silicon nanotubes; the tensile hoop stress concentration occurs at the surface between <110> directions in crystalline Si due to the preferential lithiation along this direction, while the homogeneous hoop stress takes place in amorphous silicon resulting in the isotropic expansion [3].

2.1.3) Size-dependent fracture of crystalline Si

To tackle the fracture problem in crystalline Si materials, researchers have attempted to reduce the particle size of the material. It was indicated that the smaller size of crystalline Si materials tends to be less fragile than the larger ones because they facilitate fast Li diffusion and strain relaxation. [6, 18]. For example, Ryu *et al.* (2011) showed that no fracture was observed on a crystalline Si nanowire with a diameter less than 300 nm [18]. Liu *et al.* also found that crystalline Si nanoparticles (NPs) with

a diameter less than 150 nm could be lithiated without cracking, confirming that lithiation-induced fracture is size-dependent [6]. In their study, the crack was initiated when the thickness of lithiated Si was 100-200 nm. The threshold lithiated Si thickness for initial crack formation also increases with decreasing diameter of the Si particles. Additionally, the crack propagation is controlled by particle size and initial crack size [6]. In a large particle (Figure 2.8A), the induced tensile stress during the lithiation was relaxed to zero near the crack surfaces. A flaw region around the crack is caused by the release of elastic energy which is independent in particle size. Nonetheless, when the particle size is smaller (Figure 2.8B), the size of the stress-relaxation region and the elastic energy release are lower, *i.e.*, both the zero-stress and the elastic-energy-relief areas depend on the size of the particle. The J-integral or the strain energy release rate of fracture is also related to the size of the material (Figure 2.8C). Note that the crack will propagate if the strain energy release rate is larger than the surface energy. As a result, the higher J-integral in the big particle indicates a larger crack propagation driving force in the material [6]. Moreover, the difference in the critical size of Si NPs and Si NWs confirms the dissimilar behaviour of the volume expansion in the different Si morphologies. The hoop stress might be reduced when adding the dimension of length in Si NWs since they could additionally expand in the axial direction during cycling [1]. Theoretical model calculations predict that the volumetric swelling ratio of Si NPs steeply increases when their diameters increase during lithiation. This is not the case for Si NWs, which show gradual change in their volumetric swelling ratio. Consequently, Si NPs experience higher stress fractures. [19]. Thus, the critical diameter for fractures is larger in Si NWs compared to Si NPs.

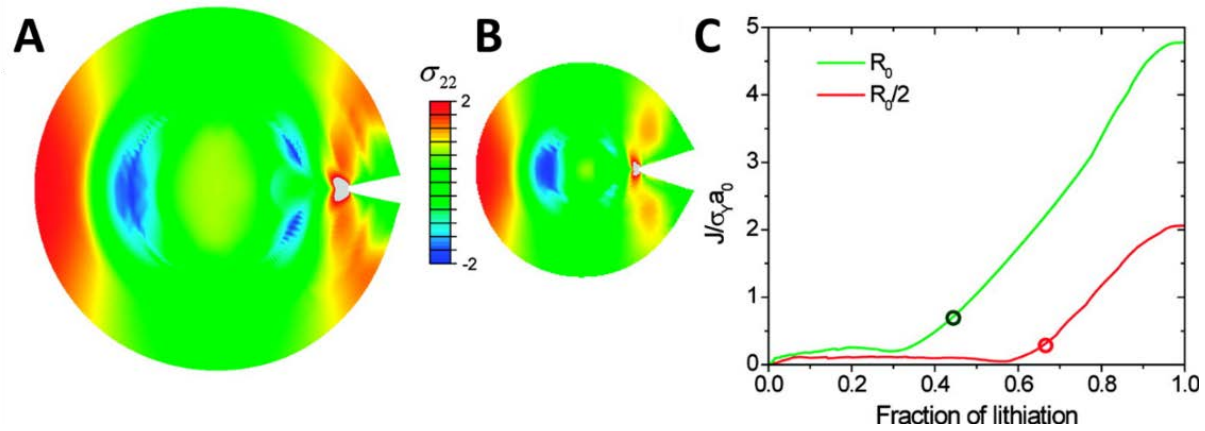


Figure 2.8. The stress distribution in Si wires with the radii of A) R_0 and B) $R_{0/2}$; the size of the stress release area strongly depends on the cross-sectional radii of the material. C) The plots showing the J-integral (the strain energy release rate) near the fracture as a function of the fraction of lithiation; the J-integral strongly depends on the size of the material. Green and red circles represent the J-integral of the crack in A and B wires. σ_γ and a_0 is surface energy and the crack length in the material [6].

The size-dependent fracture phenomenon is also related to the crystallographic orientation of the Si. The effect of size on the fracture of Si nanopillars with three different orientations, <100>, <110>, and <111> (Figure 2.9), was studied by Ryu *et al.* (2014) [9]. The <110> Si nanopillars showed a larger fracture size than Si nanopillars with other orientations. The <100> Si nanopillars exhibited a fracture ratio of 100% when the diameters of Si were 390 nm. No cracks were found after lithiation in the <100> and <110> nanopillars when their diameter was 290 nm. In contrast, the fracture initially developed in the <110> and <111> Si nanopillars when their diameter was 360 nm and 140 nm, respectively. A high fracture ratio of 88% was observed in the bigger <111> pillar with a diameter of 360 nm. [9].

In addition, the preferentially lithiated orientations of Si NPs affect the size-dependent fracture, which is similarly observed in Si nanopillars. The anisotropic volume expansion of the Si NPs results in the formation of hills along <110> and valleys in <100> and <111> directions. The hexagon-shaped Si core with (110) facets was formed, and the shape of the Si NPs then changes to be a rhombic dodecahedron after the lithiation [20]. If the size of Si NPs is larger than 150 nm, cracks

finally initiate at the surface between these facets, and fractures take place when the lithiation continues [6, 21].

It is suggested that the smaller critical fracture sizes of <100> and <111> Si (less than 360 nm in diameter of Si nanopillars) may be attributed to a high number of areas that the fracture formation could occur in Si at these orientations. As discussed earlier, anisotropic fractures take place at the area between (110) planes due to the preferential volume expansion occurring along <110> direction. Thus, as shown in Figure 2.7C fractures in the <100> Si pillar preferentially formed at four (100) surfaces (angles of 45, 135, 225, and 315°) which are 45° from the (110) planes. In the <110> nanopillar, two fracture sites were found at 145 and 325° which correlate with (100) planes situated at 90° from the (110) plane. However, the <111> nanopillar showed the six fracture sites at angles of 30, 90, 150, 210, 270 and 330° representing (112) planes which are placed between the (110) planes. Therefore, the <110> Si nanopillar presented a larger critical fracture size than Si with other orientations because they have only two small regions that fracture could initiate. Also, at areas where a high concentration of the stress building up is relatively small in the <110> Si (red areas in Figure 2.7C), the driving force for the fracture formation is lower, thus causing the larger critical size in Si at this orientation.

To conclude, the critical size of the fractures is varied in crystallographic Si orientations. It depends on the fracture localisation and the concentration of induced stress for fractures due to the anisotropic volume expansion of Si. The diameter of crystalline Si NPs in this work was limited to less than 150 nm to avoid fracture formation during cycling. Hence, the preferentially lithiated orientations of Si only influence on the final structure of the material after battery testing.

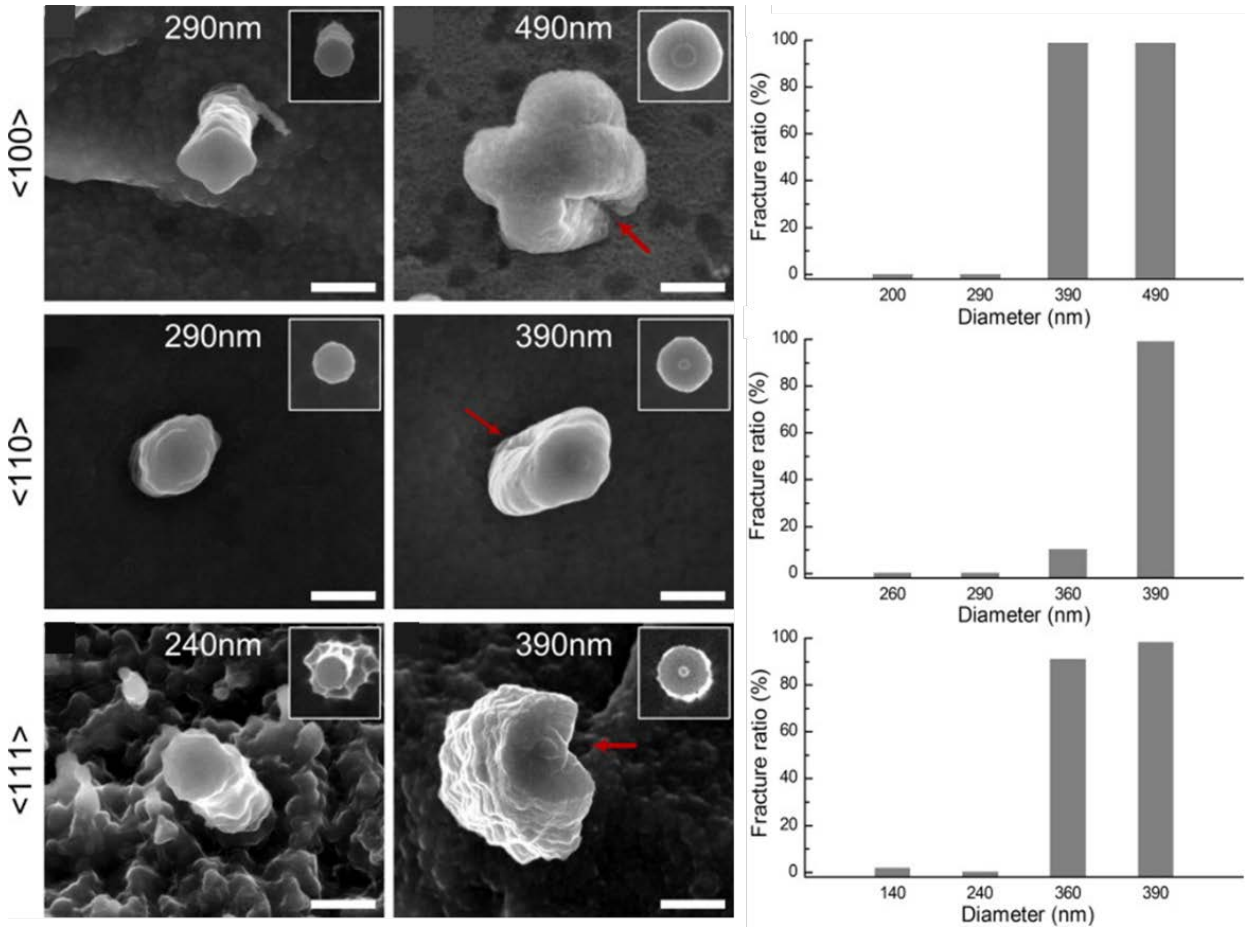


Figure 2.9. SEM images showing the size-dependent fracture of Si nanopillar with different orientations, <100>, <110>, and <111>; red arrows indicate the initiated crack areas and all scale bars are 500 nm. The graphs present the effect of the size on the fracture ratio for Si with three orientations; the fracture ratio is described as dividing the number of fractured nanopillars by the total number of samples. The <110> exhibits the larger critical size (*ca.* 360-390 nm) for the fracture formation than others [9].

2.2) Amorphous silicon

2.2.1) Li-Si alloy in amorphous Si

According to previous studies [22-25], the lithiation of the amorphous Si occurs at a higher potential (~220 mV) than that of the crystalline Si (~120 mV) and the sloping voltage profile observed for amorphous Si is different from the stepped voltage profile of crystalline Si. These results indicated that the lithiation of the amorphous Si is dissimilar to that of the crystalline Si. The sloping voltage profile also demonstrates that the lithiation of amorphous Si is a single-phase reaction which depends

on the diffusion rate of Li [26]. Nevertheless, recent studies reported that the voltage profile of the first lithiation in an amorphous Si anode was flatter than the subsequent profiles, indicating that a two-phase reaction had occurred during the first cycling [5, 27]. The TEM experiments by Wang *et al.* (2013) [5] and McDowell *et al.* (2013) [27] revealed a two-phase lithiation behaviour in the amorphous Si. A phase boundary between the lithiated amorphous Li_xSi and pure amorphous Si regions was distinguished during the lithiation (Figure 2.10) since the high concentration of Li at the phase boundary was needed to break covalent bonding of the amorphous Si. As the bond breaking process is slower than the diffusion of Li in the Li_xSi phase, the kinetics of the lithiation is controlled by the breaking of Si bonds at the interface. The interfacial boundary finally disappeared in subsequent cycles, and the reaction changed to be a single-phase, which is similar to that observed for the crystalline Si [27]. A molecular modelling study [5] additionally confirms the phase boundary formation in the amorphous Si, where the concentration of the Li was high at the amorphous-amorphous interface in the lithiated Si phase (Figure 2.2C). This phenomenon leads to the dissolution of the Si atoms by breaking the covalent bonding in the amorphous Si, which finally facilitates the two-phase lithiation (Figure 2.2D).

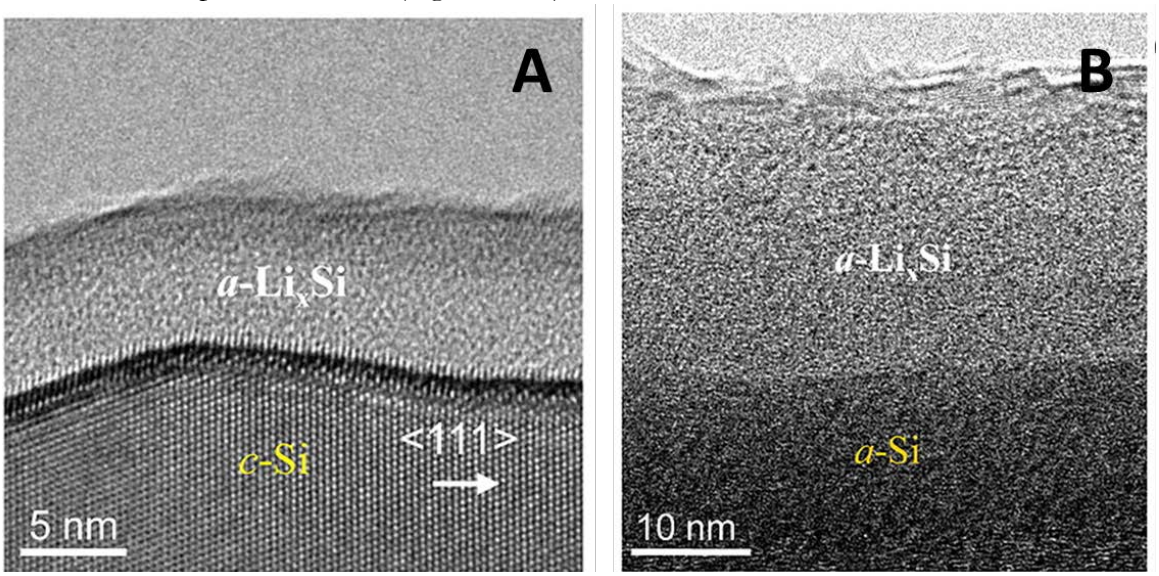


Figure 2.10. A two-phase lithiation mechanism in A) a crystalline Si and B) an amorphous Si; a phase boundary between Si and Li_xSi can be observed in both the crystalline and amorphous Si, but it clearly distinguishes as a sharp interface in the crystalline material [5].

2.2.2) Volume change and fracture induction in amorphous Si

Although the lithiation process of the amorphous Si is similar to that of crystalline Si in the first lithiation, the amorphous Si shows better battery performance than the crystalline Si. This is because the amorphous structure is more stable and will not disintegrate during repeated cycling [28]. Hence, the structural change and fracture behaviour in amorphous Si is significantly different from crystalline Si. In order to thoroughly understand the enhanced battery result, it is necessary to study the stress-induced fracture evolution in amorphous Si

Regarding the two-phase mechanism in the first cycle, a change of Li concentration across the interface in the amorphous Si causes strain discrepancy between the lithiated and unlithiated phases. Compressive hoop stress is then induced in the Si core, while the tensile hoop stress happens at the lithiated Si region (Figure 2.11C). The tensile hoop stress at the surface eventually causes fracture initiation at the material surface, which similarly occurs in crystalline Si. Nonetheless, the concentration of Li required for breaking the Si-Si bonds in the amorphous material is lower than that in the crystalline Si and the interfacial reaction proceeds linearly with time. This leads to less stress building up and dramatic volume change at the phase boundary. Also, the diffusion rate of Li into the Li_xSi phase in amorphous Si material is not as sluggish as in the crystalline Si material. The Li diffusivity in the amorphous Si ($1.25x10^{-9}$-$3.69x10^{-8}$ cm^2/s) is 10 times higher than that in the crystalline Si ($1.67x10^{-10}$-$4.88x10^{-9}$ cm^2/s) [2]. The high diffusion rate of Li in amorphous Si thereby causes reduced tension at the material surface. However, a single-phase mechanism was found on subsequent cycles, which was attributed to possible Li trapping inside the Si matrix and structural change after delithiation. Thus, the lithium easily breaks up the Si structure, which finally leads to the uniform lithiation occurring throughout the Si material [5, 10, 27].

In the case of the single-phase mechanism during the subsequent cycling, diffusion-induced stress is generated from the Li concentration gradient in the amorphous Si. When lithiated, the outer

region of the material expands, but the inner area containing a lower Li concentration increases less in volume. Then, during the early stages of the lithiation, the compressive hoop stress is formed at the outer shell, while the tensile hoop stress occurs in the interior material. This mechanism of stress induction is known as a differential concentration effect. In later lithiation stages, the tensile hoop stress could be induced by a pushing-out effect owing to the volume expansion of the inner material. If the pushing-out effect is sufficiently large, the initial compressive hoop stress at the surface will become tensile stress, promoting crack formation at the material surface (Figure 2.11A). The hoop stress also reverses during the delithiation in amorphous Si (Figure 2.11B) [10].

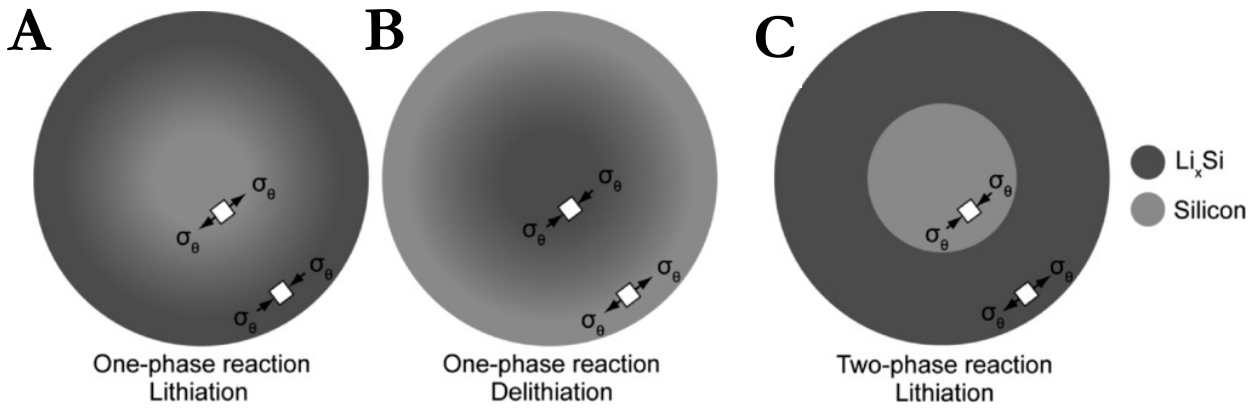


Figure 2.11. Schematics showing that A) single-phase lithiation in amorphous Si leads to compressive hoop stress near the surface and tensile hoop stress inside the particle, B) single-phase delithiaiton in lithiated amorphous Si which was not crystallised into the $Li_{15}Si_4$ results in the tensile hoop stress near the surface and compressive hoop stress inside the particles and C) two-phase lithiation of amorphous Si which has a sharp interface separating two phases with different Li concentrations causes compressive hoop stress in the Si core and tensile hoop stress at the lithiated Si area (shade of grey colour represents the concentration of Li) [10].

Interestingly, the volume expansion in the amorphous Si is found to be isotropic (Figure 2.12), which is completely different from the anisotropic expansion in the crystalline Si. Such isotropic expansion is observed both inside and outside amorphous Si nanotubes. The material radially expands without preferential directions. A simulation study by Wang *et al.* indicates that the isotropic volume expansion of the amorphous Si is attributed to the hoop stress uniformly distributed in the material during the lithiation (Figure 2.7C) [3]. The hoop stress was zero at the Si core and increased radially at the lithiated Si shell without preferential locations. Therefore, the homogeneous hoop stress and

uniform stress relaxation result in better fracture resistance in amorphous Si, which finally leads to its superior battery performance compared to crystalline Si.

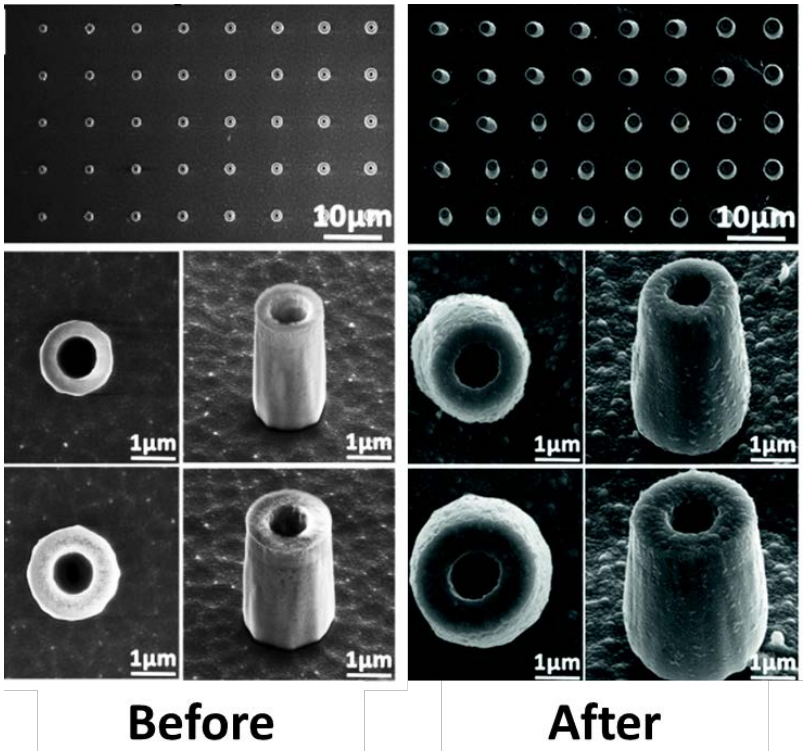


Figure 2.12. SEM images of amorphous Si nanotubes before and after lithiation; the isotropic expansion occurred both inside and outside the amorphous Si NTs [3].

2.2.3) Size-dependent fracture of amorphous Si

Due to the different stress build-up process in amorphous Si materials, the critical size of the amorphous Si for fracture is larger (870 nm in diameter of NPs) than the crystalline material [27, 28]. Even if the two-phase reaction takes place in the first lithiation, there are several reasons to describe the different size-dependent fracture behaviour in amorphous Si. First, the tensile stress build-up in amorphous Si due to isotropic expansion is less than that in the anisotropic crystalline Si. The reaction rate at the interfacial boundary in amorphous Si increases linearly with time. Therefore, the hydrostatic stress in amorphous Si is lower than that in crystalline Si during the lithiation, leading to less volume expansion observed at the interface [27]. Moreover, the size-dependence of fracture for amorphous Si is attributed to the diffusion rate of the lithium into the material matrix. It is because stress

generation in a single-phase material is related to the Li diffusion. Less stress builds up in a nano-sized material because Li diffuses more rapidly into it [18].

To prevent possible fracture formation in the Si NP materials developed in this work, their diameters were controlled to be less than the critical fracture size of both crystalline and amorphous Si. Furthermore, MWCNTs which have a good mechanical property (Young's modulus of 950 GPa) were composited with Si so as to alleviate the strain induced from the volume expansion of Si during lithiation. Si NPs were also coated on the MWCNTs with specified spacing. Therefore, free spaces for volume expansion were provided, leading to the improvement of electrode stability upon cycling.

2.3) Conclusions

The lithiation in the first cycle for both crystalline and amorphous Si takes place via a two-phase reaction. However, there are significant differences in stress evolution and volume expansion in these two different materials. In the lithiation of crystalline Si, the stress development is controlled by the reaction at the boundary, which separates two phases with the Li concentration. The compressive hoop stress is generated at the inner Si region of the material, while the tensile hoop stress, which promotes the fracture is introduced at outer lithiated Si. Additionally, the lithiation and volume expansion in the crystalline Si is anisotropic, resulting in a faceted Si inside the material.

On the other hand, the Li concentration in the lithiated phase of the amorphous Si is lower than that of the crystalline Si during the two-phase reaction in the first lithiation. The reaction rate at the phase boundary of the amorphous Si increases linearly with time, but it is extremely slow during the lithiation of the crystalline Si. The isotropic volume expansion also occurs in the amorphous Si. Therefore, there is less built-up stress and a less dramatic volume change in the amorphous Si than in the crystalline Si. Nevertheless, the single-phase reaction is observed to occur in the following lithiation for both crystalline and amorphous Si. During the single-phase lithiation, the compressive hoop stress is formed near the surface, and the tensile hoop stress is developed in the core. Thus, the

tensile hoop stress facilitates crack formation at the material surface due to the volume expansion of the inner material.

Although the two-phase lithiation occurs in the first cycle for both materials, the critical size of the amorphous Si NP for fracture is larger (870 nm) than that of the crystalline Si (150 nm) because of the different stress evolution processes in these materials. The morphologies of Si also influence the critical size for fractures due to the different volume change behaviour. Si NWs (300 nm in critical diameter) tend to have less hoop stress than Si NPs (150 nm in critical diameter) as they could also expand in the axial direction. The volumetric swelling ratio of Si NPs also sharply increases when their diameters become larger during lithiation, thus causing higher induced stress for fractures in Si NPs compared to Si NWs. Finally, the critical size of crystalline Si depends on crystallographic orientations due to their anisotropic volume expansion. It is concluded that Si with <110> orientation has a larger critical size (*ca.* 360 nm in diameter of Si nanopillars) compared to other <100> and <111> orientations due to its smaller number of preferred fracture sites and a lower concentration of the stress for fractures in Si at the orientation.

In short, the detail of the lithiation, stress evolution and fracture formation of the Si materials (both crystalline and amorphous Si) discussed in this chapter will be beneficial for the development of the Si anode materials in this and further works. The understanding of these processes, including the effect of crystallinity, size and morphology of the Si materials, has been implemented in this work to impede fracture formation and to enhance the battery performance of the Si anodes. The size of both crystalline and amorphous Si nanoparticles synthesised in this work was controlled to be less than the critical diameter, so as to avoid fractures in the electrode materials for the purpose of improving battery stability. To tackle the huge volume expansion problem in Si anodes, a new material designed by integrating Si materials with MWCNTs, to provide the strain relaxation for the Si, is developed in this work. Si NPs coated on MWCNTs have defined spacings between them, allowing

free spacing to accommodate the volume expansion of Si during cycling. These informed material design decisions were aimed at improving the overall battery performance of the Si-CNT electrode and the success of this objective is discussed in further detail in subsequent chapters.

2.4) References

1. Lee, S.W., et al., *Anomalous Shape Changes of Silicon Nanopillars by Electrochemical Lithiation.* Nano Letters, 2011. **11**(7): p. 3034-3039.
2. Johari, P., Y. Qi, and V.B. Shenoy, *The Mixing Mechanism during Lithiation of Si Negative Electrode in Li-Ion Batteries: An Ab Initio Molecular Dynamics Study.* Nano Letters, 2011. **11**(12): p. 5494-5500.
3. Wang, C., et al., *Anisotropic expansion and size-dependent fracture of silicon nanotubes during lithiation.* Journal of Materials Chemistry A, 2019. **7**(25): p. 15113-15122.
4. Kim, H., et al., *Structure and Properties of Li−Si Alloys: A First-Principles Study.* The Journal of Physical Chemistry C, 2011. **115**(5): p. 2514-2521.
5. Wang, J.W., et al., *Two-Phase Electrochemical Lithiation in Amorphous Silicon.* Nano Letters, 2013. **13**(2): p. 709-715.
6. Liu, X.H., et al., *Size-Dependent Fracture of Silicon Nanoparticles During Lithiation.* ACS Nano, 2012. **6**(2): p. 1522-1531.
7. Kim, S.-P., D. Datta, and V.B. Shenoy, *Atomistic Mechanisms of Phase Boundary Evolution during Initial Lithiation of Crystalline Silicon.* The Journal of Physical Chemistry C, 2014. **118**(31): p. 17247-17253.
8. Liu, X.H., et al., *In situ atomic-scale imaging of electrochemical lithiation in silicon.* Nat Nano, 2012. **7**(11): p. 749-756.
9. Ryu, I., et al., *Microscopic model for fracture of crystalline Si nanopillars during lithiation.* Journal of Power Sources, 2014. **255**: p. 274-282.
10. McDowell, M.T., et al., *25th Anniversary Article: Understanding the Lithiation of Silicon and Other Alloying Anodes for Lithium-Ion Batteries.* Advanced Materials, 2013. **25**(36): p. 4966-4985.
11. Jung, S.C., J.W. Choi, and Y.-K. Han, *Anisotropic Volume Expansion of Crystalline Silicon during Electrochemical Lithium Insertion: An Atomic Level Rationale.* Nano Letters, 2012. **12**(10): p. 5342-5347.
12. Ozanam, F. and M. Rosso, *Silicon as anode material for Li-ion batteries.* Materials Science and Engineering: B.
13. Ashuri, M., Q. He, and L.L. Shaw, *Silicon as a potential anode material for Li-ion batteries: where size, geometry and structure matter.* Nanoscale, 2016. **8**(1): p. 74-103.
14. Chan, C.K., et al., *High-performance lithium battery anodes using silicon nanowires.* Nat Nano, 2008. **3**(1): p. 31-35.
15. Liu, X.H., et al., *Anisotropic Swelling and Fracture of Silicon Nanowires during Lithiation.* Nano Letters, 2011. **11**(8): p. 3312-3318.
16. Goldman, J.L., et al., *Strain Anisotropies and Self-Limiting Capacities in Single-Crystalline* **3***D Silicon Microstructures: Models for High Energy Density Lithium-Ion Battery Anodes.* Advanced Functional Materials, 2011. **21**(13): p. 2412-2422.
17. Jia, Z. and T. Li, *Intrinsic stress mitigation via elastic softening during two-step electrochemical lithiation of amorphous silicon.* Journal of the Mechanics and Physics of Solids, 2016. **91**: p. 278-290.
18. Ryu, I., et al., *Size-dependent fracture of Si nanowire battery anodes.* Journal of the Mechanics and Physics of Solids, 2011. **59**(9): p. 1717-1730.
19. Ma, Z., et al., *Critical silicon-anode size for averting lithiation-induced mechanical failure of lithium-ion batteries.* RSC Advances, 2013. **3**(20): p. 7398-7402.

20. An, Y., et al., *Mitigating mechanical failure of crystalline silicon electrodes for lithium batteries by morphological design.* Physical Chemistry Chemical Physics, 2015. **17**(27): p. 17718-17728.
21. McDowell, M.T., et al., *Studying the Kinetics of Crystalline Silicon Nanoparticle Lithiation with In Situ Transmission Electron Microscopy.* Advanced Materials, 2012. **24**(45): p. 6034-6041.
22. Chen, L.B., et al., *An amorphous Si thin film anode with high capacity and long cycling life for lithium ion batteries.* Journal of Applied Electrochemistry, 2009. **39**(8): p. 1157-1162.
23. Kulova, T.L., et al., *Lithium intercalation into amorphous-silicon thin films: An electrochemical-impedance study.* Russian Journal of Electrochemistry, 2006. **42**(7): p. 708-714.
24. Kulova, T.L., et al., *Lithium insertion into amorphous silicon thin-film electrodes.* Journal of Electroanalytical Chemistry, 2007. **600**(1): p. 217-225.
25. Baranchugov, V., et al., *Amorphous silicon thin films as a high capacity anodes for Li-ion batteries in ionic liquid electrolytes.* Electrochemistry Communications, 2007. **9**(4): p. 796-800.
26. Cui, L.-F., et al., *Crystalline-Amorphous Core−Shell Silicon Nanowires for High Capacity and High Current Battery Electrodes.* Nano Letters, 2009. **9**(1): p. 491-495.
27. McDowell, M.T., et al., *In Situ TEM of Two-Phase Lithiation of Amorphous Silicon Nanospheres.* Nano Letters, 2013. **13**(2): p. 758-764.
28. Berla, L.A., et al., *Robustness of amorphous silicon during the initial lithiation/delithiation cycle.* Journal of Power Sources, 2014. **258**: p. 253-259.
29. Gu, M., et al., *Electronic Origin for the Phase Transition from Amorphous LixSi to Crystalline Li15Si4*. ACS Nano, 2013. 7(7): p. 6303-6309.
30. Obrovac, M.N. and L.J. Krause, *Reversible Cycling of Crystalline Silicon Powder.* Journal of The Electrochemical Society, 2007. **154**(2): p. A103-A108.
31. Ogata, K., et al., *Revealing lithium–silicide phase transformations in nano-structured silicon-based lithium ion batteries via in situ NMR spectroscopy.* Nature Communications, 2014. **5**(1): p. 3217.
32. Iaboni, D.S.M. and M.N. Obrovac, *Li15Si4Formation in Silicon Thin Film Negative Electrodes.* Journal of The Electrochemical Society, 2015. **163**(2): p. A255-A261.

Chapter 3

Experimental methodologies

In this chapter, the fundamentals of synthesis and characterisation methods will be mainly studied. The chapter will be organised as follows. First, synthesis set-ups and experimental parameters for the controlled production of the Si-CNT material using a combination of aerosol-assisted and atmospheric-pressure chemical vapour deposition (AACVD and APCVD) will be introduced. The techniques employed to study the physical and chemical properties of Si-CNT based material will then be examined in the second section. The techniques include scanning electron microscopy (SEM), transmission electron microscopy (TEM), energy-dispersive X-ray spectroscopy (EDX), scanning transmission electron microscopy (STEM), X-ray photon spectroscopy (XPS), X-ray diffraction (XRD), Raman spectroscopy, thermogravimetric analysis and four-point-probe measurements. The galvanostatic cycling method used to test the battery performance of the fabricated Si-CNT electrodes will also be discussed. Next, the procedures for material preparation, electrode fabrication used in this work will be described. The cell assembly process and battery performance testing will be explained in the last section.

3.1) Synthesis methodologies

A principle of the CVD method, such as a mechanism of material growth and factors that affect the growth rates, are discussed. The section is focused on reviewing the fundamentals of two different CVD types, including AACVD and APCVD since they were employed to prepare MWCNTs and Si-CNT based materials. Regarding the AACVD method, the two possible mechanisms of the CNT growth and the parameters for the SWCNT and MWCNT formation are also studied. Then, the characteristics of APCVD methods used for depositing Si on buckypapers (BPs) are reviewed. The

gas mixture was used in APCVD to tackle the method issues such as the mass transport limitation. Furthermore, the reaction mechanism of Si growth on a substrate is investigated later in this section.

3.1.1) Principles of a chemical vapour deposition method

CVD is a process where a thin solid material is coated on a heated substrate via a chemical reaction from a gas phase [4, 10]. This method is usually utilised to deposit various kinds of materials because it can produce conformal and high purity films with a fast deposition rate [11]. The general mechanism of the CVD method is displayed in Figure 3.1. The process involves (1) precursor gases transported into a reactor, (2) intermediated reactants formed from the precursor gas, (3) the reactant diffusing through the boundary layer to a heated substrate, (4) gas adsorption on the substrate surface, (5) reactions taking place at the substrate surface, (6) desorption of by-product gases from the substrate surface, and (7) by-product gases exhausting from the chamber. Note, a boundary layer formed due to laminar flow in which the gas velocity is varied from a wall to the point that where the velocity is the highest. The thickness boundary layer also increases with lower the gas velocity and with increasing distance from an inlet [12].

Moreover, the CVD method is usually operated at high temperature (600-1500 ^{o}C). The precursors contain reactive gases such as methane, acetylene, and silane, inert gases such as nitrogen and argon, and reducing gases such as hydrogen [4, 13]. The inert gas acts as a carrier gas and also removes excess precursor and by-product gases, while the reducing gas eliminates unwanted impurities and oxide layers on the material surface [14]. The material growth rate in the CVD method can be determined by many parameters, mainly by changing the temperature and pressure of the reactor. At lower temperature, the deposition rate is controlled by the kinetics of chemical reactions found either in the gas-phase or on the substrate surface. The growth rate of films rises exponentially with the substrate temperature as referred to the Arrhenius equation (growth rate α exp (E_A/RT), where E_A is the activation energy, R is the gas constant, and T is the temperature). By controlling the substrate

surface temperature, a uniform film thickness can be obtained. When the temperature increases, the reaction rate improves significantly, causing mass transport-limited reactant diffusion through the boundary layer to the substrate. The growth rate is independent of the temperature and consequently controlled by the mass-transport diffusion of the reactant. In addition, the operating pressure of the reactor can influence the growth rate. At extremely low pressure, the thickness of the boundary layer is small due to the high gas velocity (Bernoulli's principle) [12]. The mass transport rate is in this case fast since the reactant easily diffuses through the thin boundary layer. Hence, the material growth is controlled by the surface reactions, which is a limiting step in low pressure CVD [13].

In this work, two types of CVD methods were employed for material syntheses. AACVD was initially used to synthesise MWCNTs; as the precursor is continuously delivered into the reactor, this method could produce a large quantity of MWCNTs. Also, APCVD was carried out to prepare Si-CNT based materials. The gas mixture was applied in the APCVD method to avoid a rapid reaction rate which results in a reactant diffusion limitation. Thus, the uniformity and structure of the material can be easily controlled in the system. The detail of these methods will be discussed in the next sections.

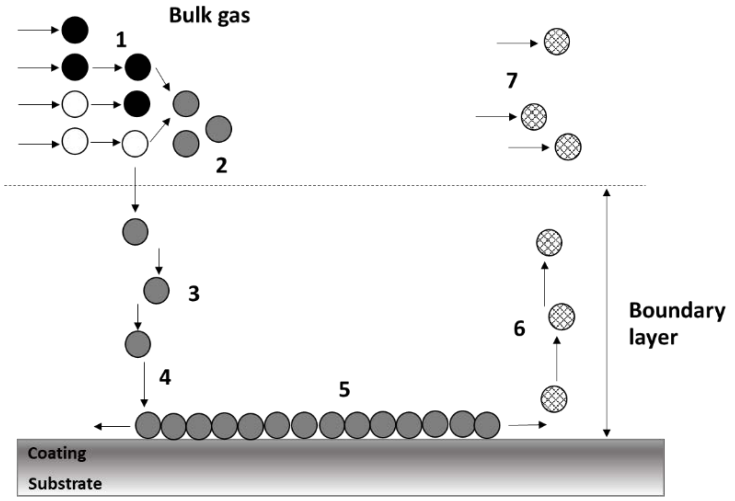


Figure 3.1. A schematic diagram showing mechanistic steps of the CVD process for coating a thin film on a substrate; the process includes 1) gases conveyed into a furnace, 2) intermediate reactant formed, 3) the reactant diffused through the boundary layer to a heated substrate, 4) gas adsorbed on the surface of the substrate, 5) reactions occurred at the substrate surface, 6) by-product gases desorbed from the substrate surface, and 7) exhausted from the furnace [4].

3.1.2) Aerosol assisted chemical vapour deposition (AACVD)

AACVD is the most effective method for synthesis of large amounts of CNTs since the mixture of liquid hydrocarbon and catalyst precursors is continuously fed into the reactor. Since the liquid hydrocarbon has an ability to dissolve organometallic compounds which behaves as a source of catalysts, an extra catalyst preparation is not required [15]. This technique can produce various types of CNTs, such as MWCNTs [48, 49] and SWCNTs [50]. However, the additional step is necessary for the system to atomise the liquid precursors before a thermal decomposition process. Therefore, the AACVD method was conducted in this work to synthesise MWCNTs as it can be easier to grow vast quantities of uniform MWCNTs (*ca.* 2 g in 30 minutes).

The AACVD system based on the ultrasonic atomisation process consists of a piezo generator. By varying the voltage and frequency of the generator, an ultrasonic wave is propagated into a liquid, leading to high-pressure (compression) and low-pressure (rarefaction) cycles (Figure 3.2A). In the low-pressure cycle, small bubbles are created as the applied negative pressure disrupts cohesive forces of liquid molecules. These bubbles then collapse since the pressure of surroundings in the compression cycle exceeds their surface tension [2]. This process known as cavitation releases a large amount of energy, causing an increase of local temperature (up to *ca.* 2450^{o}C) due to a slow thermal transport in the medium [16]. An aerosol starts to form at a gas-liquid interface (red circle, Figure 3.2B) due to the cavitation explosion. That is, the cavity collapses at the boundary leading to a liquid jet and thus the formation of small liquid droplet. In addition, the aerosol formation is depended on physical properties of the liquid, such as surface tension and viscosity [17]. The aerosol formation rate is decreased when the viscosity or surface tension of the liquid is higher. Particularly, the aerosol hardly forms in viscous liquid since its strong intermolecular force resists the cavitation formation. The high surface tension within the liquid also hinder the bubble collapse [18]. As the temperature strongly affects these liquid properties, the aerosol generator then has an extra coil to cool down the heated

liquid; that is, the cavitation and aerosol generation rates are controlled and additionally the concentration of the precursor remains constant. Then, the produced aerosol is continuously carried by an inert gas through a quartz tube into a reactor. The operating temperature for MWCNT synthesis is generally around 600-900 °C. The vapour is transported towards the substrate where it reacts chemically in the heterogeneous gas-solid phase to produce MWCNTs [19]. Additionally, ethylbenzene and ferrocene were used as carbon and iron catalyst sources in this work since a high-yield of MWCNTs with low catalyst residue could be obtained [15].

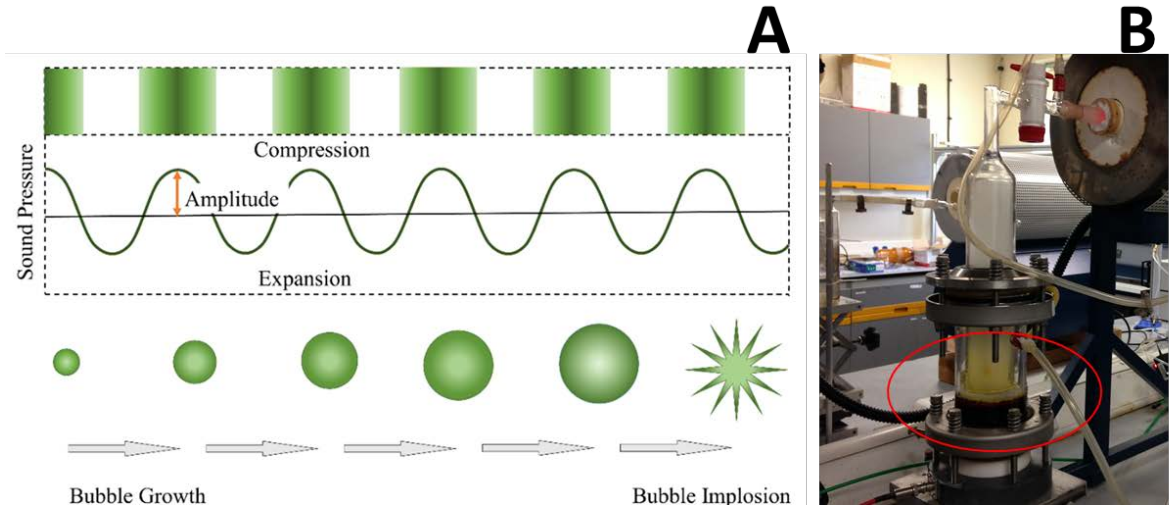


Figure 3.2. A) A sonication mechanism and a cavitation formation within the liquid [2], and B) aerosol initially forming on the surface of a precursor in the aerosol generator.

The formation of the CNTs in CVD is based on a vapour-solid-liquid (VLS) mechanism. In the VLS process, a hydrocarbon decomposition occurs on the metal catalyst particles which are heated above their metal-carbon eutectic temperature. The carbon then absorbs and diffuses into the catalyst particle forming a liquid metal-carbide alloy. When the alloy becomes supersaturated, the carbon precipitates out and finally CNTs begin to grow [6]. Nevertheless, there are various debated growth mechanisms of CNTs. The two general cases are a tip-growth model and a base-growth model. Regarding the tip-growth model, carbon decomposes on the top of the metal surface and diffuses down to the bottom. CNTs then grow out across the metal bottom, pushing the catalyst particles off the substrate due to a weak interaction between a catalyst and a substrate (Figure 3.3A).

On the other hand, the interaction of the substrate and the metal are strong in the base-growth model. Carbon decomposes and diffuses in the same way as in the tip-growth case, but the growth of CNTs fails to push the catalyst particle up. Thus, the CNT growth is forced to emerge out from the tip of the catalyst (Figure 3.3B) [6].

Furthermore, types of CNTs synthesised from the CVD methods are strongly depended on several parameters. High-temperature CVD (900-1200 °C) is required for SWCNT growth due to the high formation energy of SWCNTs compared to MWCNTs. The formation of SWCNTs is favoured when the catalyst size is smaller than 3 nm [20], while MWCNTs typically form when the particle is larger than 10 nm [6]. In addition, most hydrocarbon precursors can be used to synthesise MWCNTs. The common hydrocarbons for MWCNT synthesis, including benzene and acetylene, are unstable at high temperature, causing a huge quantity of carbon decomposition leading to the MWCNT growth. In contrast, SWCNTs can grow from a limited range of hydrocarbons which have high thermal stability (900-1200 °C) such as methane and carbon monoxide [6].

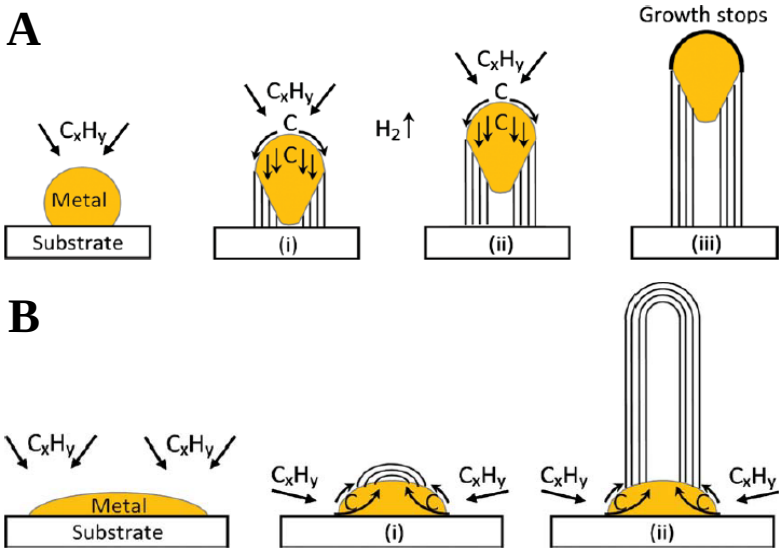


Figure 3.3. The growth mechanism of MWCNTs - A) a tip-growth model, where MWCNTs emerge out from the bottom of the metal catalyst, pushing the catalyst particles off the substrate and B) a base-growth model, where MWCNTs start to grow from the top of the catalyst [6]. The type of growth mechanism depends on the interaction between the catalyst and the substrate.

3.1.3) Atmospheric-pressure CVD with a gas mixture system for Si deposition

Silicon is usually deposited on a substrate using different types of the CVD method, which are listed in Table 3.1. The CVD methods are classified by the pressure, temperature, and energy source. In general, three primary morphologies of the Si films could be achieved by the CVD process: an amorphous film, an epitaxial film, and a polycrystalline film. An amorphous film is generally deposited at an extremely high growth rate and low temperature where the diffusion of the surface reactant is slower than the new growth of the Si species on the surface. Regarding an epitaxial film, a low growth rate is required; thus, the surface diffusion is fast in comparison with the film formation. The high temperature is also preferred because it increases the surface mobility of reactant. In addition, the formation of a polycrystalline film is often achieved at intermediated temperature and growth rate between epitaxy and amorphous films [13].

The Si films, especially crystalline films, are mostly grown using APCVD method. However, this method has various shortcomings, such as diffusion limitation, since it operates at high temperature and the reaction rate is thus faster than the diffusion rate [21]. At atmospheric pressure and high temperature, the formation of aerosol particles (mostly amorphous hydrogenated Si) is additionally found due to homogeneous silane pyrolysis in the gas phase instead of at the substrate surface [22]. The aerosol particles incorporated in a deposited film eventually cause surface roughness, poor adherence and reduced quality of material [12]. These problems can be resolved by using an LPCVD method [23]. The LPCVD shows many advantages for Si deposition, such as uniformity of material thickness and high reproducibility. Nevertheless, its drawbacks are high costs and lower deposition rates [24]. It also uses pure silane gas (SiH_4) which is pyrophoric as a precursor [13].

Table 3.1. Common silicon CVD processes classifying by pressure and temperature [10].

Method	Pressure (Torr)	Temperature (^{o}C)
Ultrahigh-vacuum CVD (UHVCVD)	10^{-3}-10^{-2}	500-727
Low-pressure CVD (LPCVD)	0.1-1	627-727
Atmospheric-pressure CVD (APCVD)	760	827-1127
Plasma-enhanced CVD (PECVD)	10^{-3}-1	27-327
Photochemical CVD (PHOTOCVD)	0.1-10	27-327

Therefore, APCVD with a gas mixture system was conducted in this work for Si deposition on the BP. This gas mixture system set-up prevented drawbacks of the normal APCVD (mainly limiting reactant transfer to a substrate) [23]. The principle of the gas mixture system is illustrated in Figure 3.4 in which SiH_4 molecules are surrounded by Ar molecules. That is, the number of the SiH_4 molecules in the mixture gas system is less than that in the pure gas system (based on Dalton's law of partial pressure). As a result, the rate of Si deposition is slowed down similarly as it happens in LPCVD. The developed system allows to control the homogeneity and consistency of the Si deposition since a reaction rate is decreased to be comparable with the mass transport in the APCVD system. Hence, the APCVD associated with the gas mixture system will be efficient for Si deposition. It is safer and cheaper than LPCVD since diluted silane gas was used, and no additional vacuum pump was required to reduce the pressure in the system.

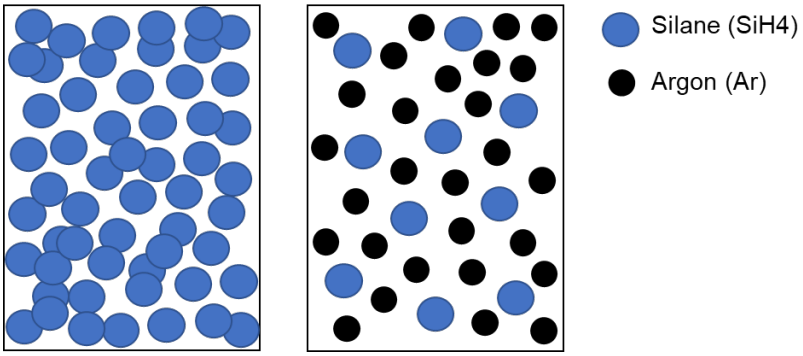


Figure 3.4. APCVD setup showing the molcules of SiH_4 in the pure gas and mixture gas system; the SiH_4 molecules are surrounded by Ar molecules in the mixture gas system resulting in a reduced number of SiH_4 molecules presence in this system.

A simple thermal decomposition reaction of SiH_4 in the CVD method is given by [10].

$$SiH_4\ (g) \rightarrow Si\ (s) + 2H_2\ (g) \quad (3.1)$$

The mechanism of the SiH_4 decomposition includes reactant gas adsorption, surface reaction, and by-product hydrogen desorption steps (Figure 3.5). However, the pyrolysis of SiH_4 consists of numerous intermediates species and steps owing to the weak Si-H and Si-Si bonds in silane. Three-parallel reactions for the Si deposition are expressed as follows [21].

$$SiH_4\ (g) \rightarrow SiH_2\ (g) + H_2\ (g) \quad (3.2)$$

$$SiH_2\ (g) + * \rightarrow SiH_2\ (s) \quad (3.3)$$

$$SiH_2\ (s) \rightarrow Si\ (s) + H_2\ (g) + * \quad (3.4)$$

The initial step of the Si deposition is the production of silylene (SiH_2), formed by the dissociation of SiH_4 at 900-1100 ^oC (Reaction 3.2). SiH_2 gas is then adsorbed on a reactive surface site at the substrate (*) (Reaction 3.3) [21]. In this step, the adsorption can cause defects such as amorphous Si due to the misorientation of SiH_2 [25]. The hydrogen is subsequently desorbed and creates dangling bonds or a reaction site on the Si surface (Reaction 3.4). Thus, the growth rate of the Si film is determined by the final step as the reaction site is created only when the hydrogen desorption taken place. In addition, the chemical reaction mainly occurs on the surface of the substrate rather than in the gas phase (aerosol formation) if there is the large amount of H_2 as a carrier gas [10].

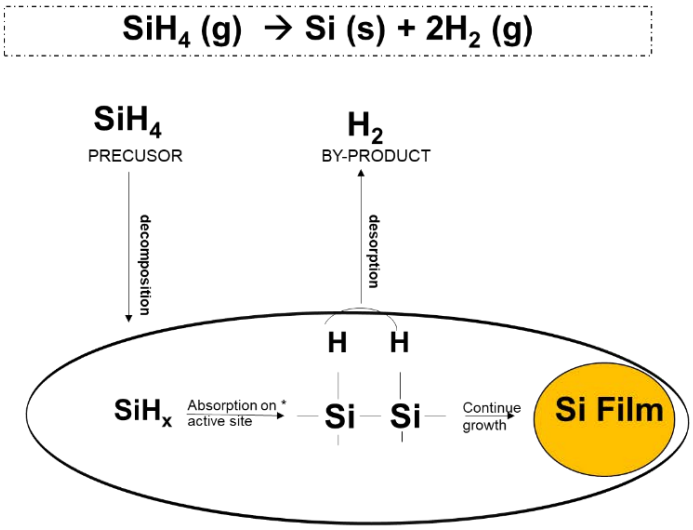


Figure 3.5. A schematic mechanism of Si film deposition on the substrate using SiH_4 as a precursor; the overall reaction of SiH_4 pyrolysis is exhibited.

In this work, the structure and amount of Si coating on BPs in the Si-CNT material were controlled by adjusting the experimental parameters such as temperatures, reaction times and concentration of precursor gases. The BP was perpendicular to the gas flow direction in order to reduce the influence of the concentration gradient and geometric effects on the material. Additionally, the APCVD system was carried out to coat amorphous carbon on the Si-CNT based materials. The thermal decomposition of hydrocarbon gases simply caused amorphous carbon deposited on the material. The precursor gas was changed from silane to methane or acetylene gases (carbon sources), and the operating temperature was reduced to be 700-900 °C.

3.2) Characterisation techniques

This section discusses the fundamentals of the characterisation techniques used to investigate the physical and chemical properties of Si-CNT based materials. Firstly, methods including SEM, TEM, EDX, STEM, XPS, XRD, Raman spectroscopy, TGA and four-point probe resistivity measurement, are reviewed. The galvanostatic cycling method, which was employed to test the battery performance of fabricated electrodes, is subsequently discussed. After this theoretical discussion, the characterisation outcomes of specific data which are useful for this research are studied.

3.2.1) Scanning electron microscopy (SEM)

In this work, scanning electron microscopy (SEM) was employed to study the morphology of a material surface via both secondary electron (SE) and backscattering electron (BSE) emission. SEM (Zeiss-Merlin) with 5 kV of accelerating voltage, and *ca.* 99 pA of the probe current was used. The samples were imaged without performing any pre-imaging coating procedure. Electron microscopy is based on the interaction between electrons and a sample. When an electron beam strikes a specimen surface, the interaction between incident electrons and the surface generates SE, BSE and X-ray radiation (Figure 3.6A). In SEM (Figure 3.6B), the electron beam is thermionically emitted and rapidly accelerated towards an anode to energy between 1 kV to 30 kV (5 kV in this work). The beam is constricted by a set of magnetic lenses (condenser and objective lenses) before hitting a specimen. The SE and BSE emitted from the sample are detected by specific detectors. The electrical signals are amplified and transformed into an image which is displayed on a screen.

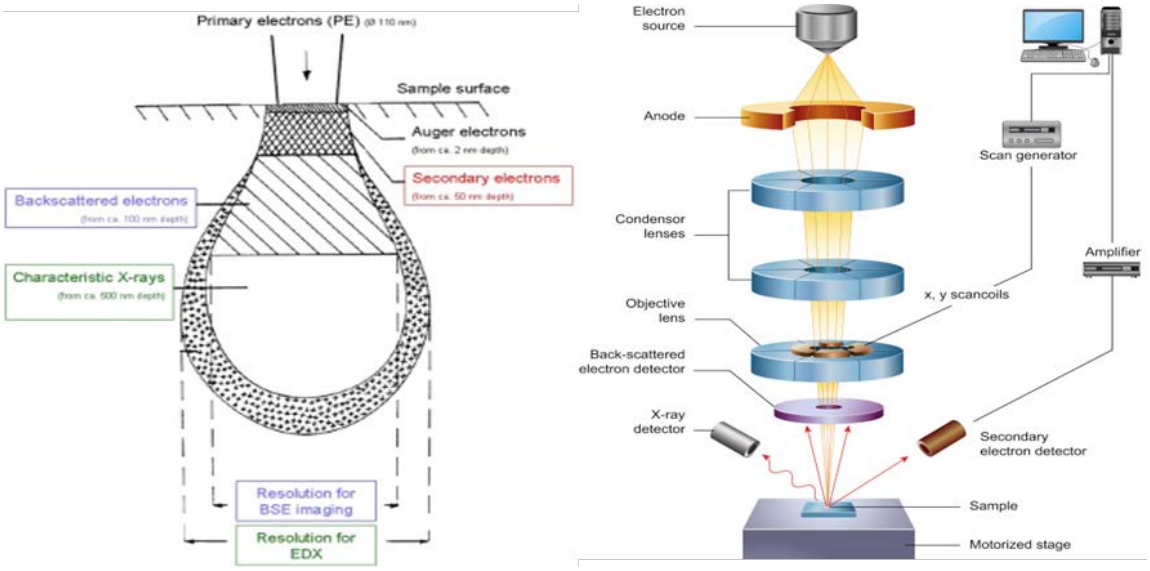


Figure 3.6. The interaction between incident electrons and samples (left); when an electron beam hits on a sample surface, the interaction between electrons and the surface generate SE, BSE and X-ray radiation [8] and a schematic of scanning electron microscopy (right) [3].

The SE provides information about the sample topology. It is surface-sensitive as the SE originates from the surface due to inelastic collisions between the electron beam and the sample [26]. In this work, SEM was carried out to characterise the morphology of the Si-CNT based materials and to study the morphological change of Si-CNT materials before and after battery testing. The BSE generated through elastic interactions between the electron beam and the sample also gives useful information on the elemental composition of the examined material surface. This is because the BSE signal is sensitive to the atomic mass of the elements in the sample. Since large atoms scatter more electrons than small atoms when the beam hits the sample, a stronger signal is observed in materials with higher atomic mass [26]. Because Si elastically scatters more electrons due to its high atomic number compared to carbon, Si can easily be distinguished from carbon in Si-CNT material as it shows brighter spots in a SEM image generated by BSE (Figure 3.7).

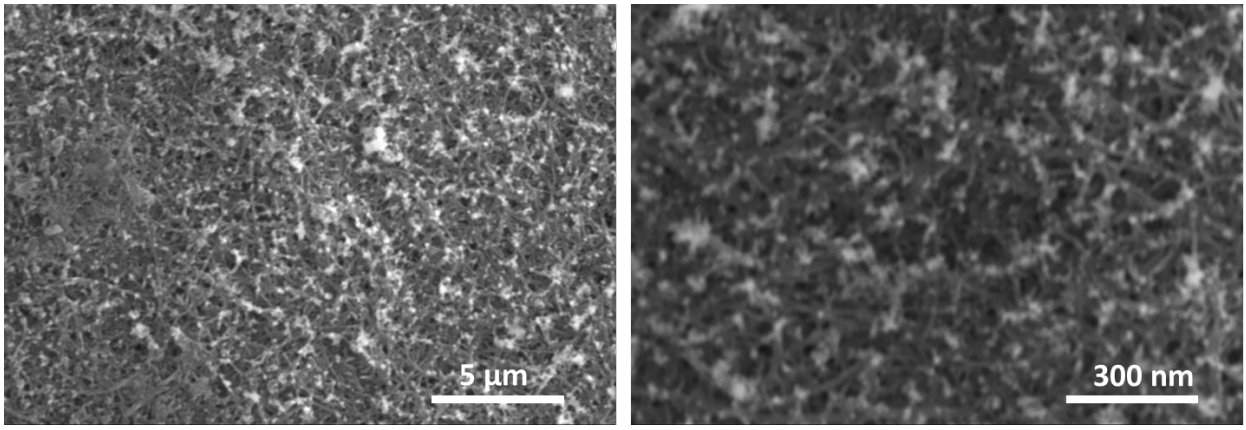


Figure 3.7. SEM images of Si-CNT materials at low and high magnifications. Si (higher atomic number) scatters more electrons than the lighter carbon, thus revealing brighter in the SEM image.

3.2.2) Transmission electron microscopy (TEM)

TEM was applied in this work to investigate the morphology of the manufactured Si-CNT based materials. MWCNTs, silicon nanoparticles (Si NP) structures, as well as amorphous carbon layers coated on Si-CNT based materials, were examined. Importantly, TEM images were used to analyse the SiC formation by distinguishing different lattice spacings in the materials. In this work, TEM (JEOL 3000F) with accelerating voltage in the range of 300 kV was used. The electron beam in

TEM is produced by a thermionic gun and accelerated to an energy of 50-300 keV in a column under a vacuum of 10^{-7} Torr. The electron beam is demagnified, and its diameter is controlled by two condenser lenses. An aperture situated between two condenser lenses is restricts the convergence angle, which is the angle of the incident beam on the sample. The electron beam is then passed through the specimen before getting into a magnetic lens. An image is focused by an objective lens and magnified by intermediate and projector lenses to form a bright-field image on a fluorescent screen (left, Figure 3.8A). Moreover, the contrast between two different areas in the resulting TEM image is due to electron scattering in the sample [27]. The electrons change their amplitude due to their interaction with the sample, resulting in contrast in the image. For example, areas in the sample which are thicker and/or have a higher atomic number appear darker since more electrons are strongly scattered when hit by the primary electron beam. The scattered electrons are also blocked by the objective aperture, eventually resulting in fewer electrons transmitting through this area [28]. For example, the iron catalyst inside MWCNTs shows a strong contrast in Figure 3.8B because it scattered more electrons due to its higher atomic number compared to carbon. Hence, this technique provides useful information on the internal structure and morphology of the sample.

Moreover, the electron diffraction pattern can be projected on the screen by removing the objective aperture. The area of the specimen where the diffraction pattern is obtained can be controlled by an aperture located in the image plane of the objective lenses (right, Figure 3.8A). This mode of the operation is known as selected area electron diffraction (SAED). It is normally used for characterising the crystal structure of the materials and indicating material types which can be polycrystalline, single crystalline or amorphous [26, 29]. That is, a polycrystalline material shows a ring pattern, while single crystalline and amorphous materials exhibit spot and diffuse ring patterns, respectively. In this study, SAED was used to confirm the presence of SiC interface between Si NPs and MWCNTs in order to support the results from TEM images. The lattice spacings of the Si-CNT-

SiC-C material could be calculated by dividing the camera constant (the distance from the sample to the imaging plane) by the measured ring radius in the SAED pattern (Figure 3.8C). The calculated lattice spacings could identify the component by matching them with the known lattice spacing of Si, SiC and C from International Centre for Diffraction Data (ICDD) databases. For instance, the lattice spacing calculated from the radius of the 5th ring was *ca.* 0.24 nm, thus corresponding to the lattice spacing of (111) in β-SiC [30].

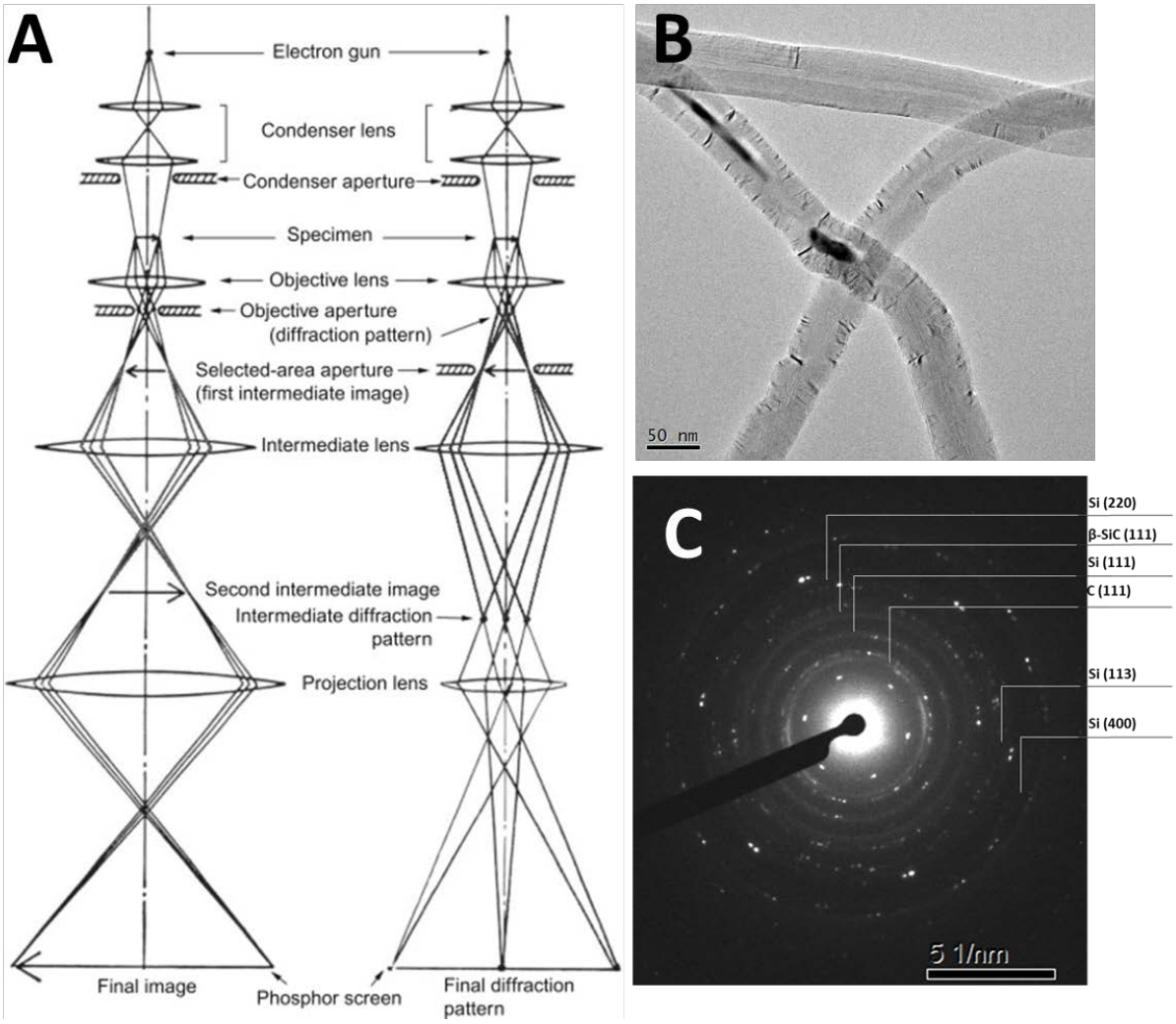


Figure 3.8. A) Diagrams for imaging (left) and diffraction (right) in a transmission electron microscopy [3], B) TEM image of MWCNTs showing a contrast between iron catalysts and MWCNTs, and C) SAED of the Si-CNT-SiC-C material indicating the presence of SiC in the material.

3.2.3) Energy-dispersive X-Ray Spectroscopy (EDX/EDS)

EDX was employed to study the elemental composition presented in the Si-CNT based materials. In this research, SEM equipped with EDX (Oxford Instruments) was used. 30 kV accelerating voltage and 500 pA probe current were applied. The used SEM is equipped with an energy-dispersive spectrometer, which measures the number and energy of the X-ray released from the sample and which can generate a complete spectrum of the X-rays emitted from the material surface. As shown in Figure 3.9A, when the incident electron beam hits the atom in the material, the electron in the inner shell ejects and creates an electron-hole. The electron vacancy is filled by the electron from the outer shell. Consequently, an X-ray is emitted to balance the energy difference between higher-energy and lower-energy electron shells. As the X-ray energy is a characteristic of the element which depends on atomic mass [26], this technique was thus used to characterise the composition of Si in the Si-CNT materials. For example, the EDX maps (Figure 3.9B, D-E) showed that a Si coating layer was present on the MWCNT paper. The EDX spectrum additionally confirmed that the Si-CNT material consists of Si, C, O and Fe (Figure 3.9C). The iron and oxygen can be attributed to the residual catalyst and silicon oxide, respectively. Moreover, EDX was conducted to examine SEI formation on the material surface and a change of Si-CNT electrode composition after a battery cycling test.

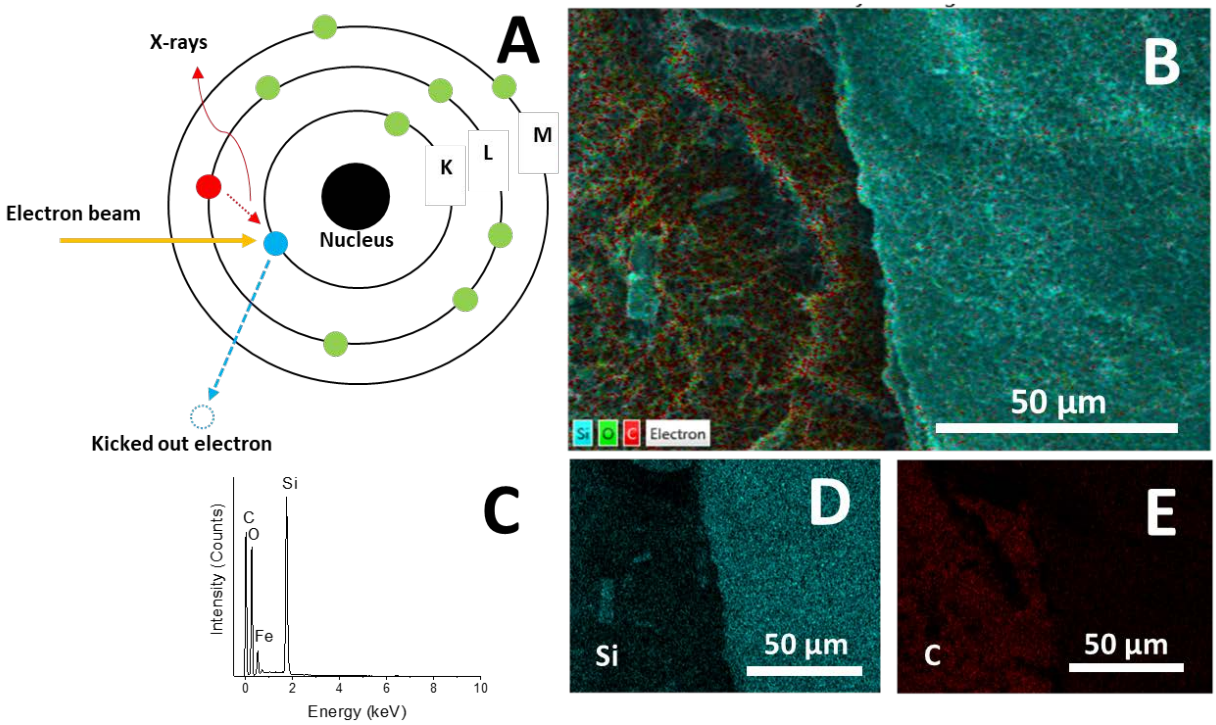


Figure 3.9. A) A schematic of an atom where X-ray is emitted; the inner electron is firstly rejected from the atom due to the electron bombardment and the hole is filled by the outer electron. The change of the state of the electron releases X-rays which can be detected by a detector, B-E) EDX maps showing Si coating on the BP and EDX spectrum confirming the component of the Si-CNT material.

3.2.4) Scanning transmission electron microscopy (STEM)

STEM combines the fundamentals of TEM and SEM. In STEM mode, an electron beam scans over the sample area (in the same way as SEM does) and an image is additionally produced by electrons transmitted through the materials (similar to a TEM technique). This STEM technique is used for imaging and studying nanostructured materials as it provides different types of information such as the structure and elemental composition of the material [31]. Multiple detectors were employed simultaneously in each scan, including SE, BSE, bright-field (BF), annular dark-field (ADF) and high-angle annular dark-field (HAADF) detectors. The BF detector detects transmitted electrons, and ADF and HAADF detectors collect electrons which scatter through at a small angle and scatter out at a high angle, respectively [28]. The spatial resolution is improved in STEM because of high accelerating voltage used in this technique, causing the decrease of electron wavelength (according to de Broglie

and Abbe's equations) [31]. Additional signals such as X-rays and electron energy loss due to the interaction between the electron beam and specimen are obtained by X-ray and EELS detectors.

The electron microscopes are also equipped with the STEM mode. For example, additional scan coils and detectors can be installed in TEM (Figure 3.10A). The scan coil is used to deflect the beam and thus creates a scanning beam for the STEM mode [28]. In contrast, STEM detectors can be moved into a sample chamber in SEM (Figure 3.10B). In this work, STEM imaging in Zeiss-Merlin with 15 kV of accelerating voltage and 500 pA of probe current was achieved to investigate the morphology and structure of the Si-CNT based materials. Furthermore, it was employed to confirm that the material structure is conserved after coating MWCNTs with Si and amorphous carbon. STEM was used with EDX to provide elemental analysis of Si-CNT based materials. For instance, for materials where STEM images showed a uniform Si NP coating on MWCNTs, EDX maps additionally confirmed the elemental composition in the material (Figure 3.10C).

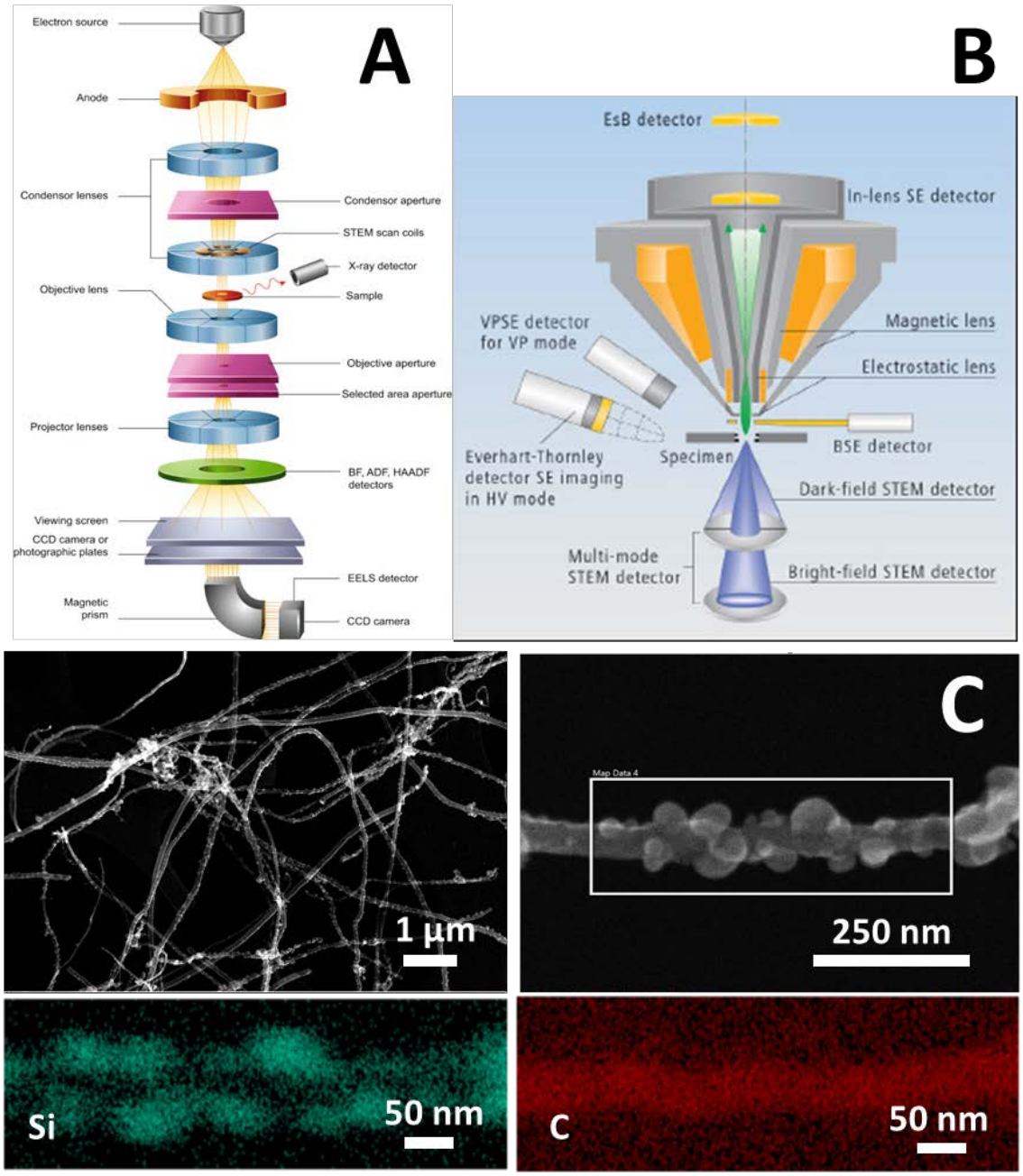


Figure 3.10. STEM scan coil installed in A) TEM [7] and B) STEM detectors placed in a sample chamber of SEM [9], and C) STEM image of Si-CNT-C material and EDX elemental mapping of silicon and carbon showing their uniform distribution of Si NPs on the MWCNT.

3.2.5) X-ray photoelectron spectroscopy (XPS)

XPS is a spectroscopic technique which is applied to analyse the elemental composition, chemical state and electronic state of elements within a material surface. In this work, the chemical

composition of the Si-CNT based materials, including silicon and carbon, was examined using the XPS technique. In particular, this technique was employed to confirm SiC presence in the Si-CNT-C material. Al Kα emission with a photon energy of 1486.6 eV was used as an X-ray source in this study. XPS involves a photoemission process in which an X-ray beam ejects photoelectrons from a specimen surface (Figure 3.11A). The kinetic energy and the number of electrons emitted from the top 1-10 nm of the material are detected. The balance between the X-ray beam having constant energy (hv) and kinetic energy of the photoelectron (E_k) is shown as

$$hv = E_k + E_B + \phi \quad (3.5)$$

Where E_B is the binding energy of the electron attracted to nucleus relative to Femi level, and ϕ is a work function of the spectrometer. As a result, the binding energy of the electron can be determined because X-ray energy and the work function are known, and the kinetic energy of the photoelectron is recorded by a detector. Therefore, the binding energy presented in the XPS spectrum is calculated to identify elements and chemical bonding states on the sample surface [32, 33]. When starting XPS analysis, a wide spectrum scan is firstly studied to confirm total elemental compositions of the materials because each element has a specific binding energy and thus a characteristic XPS peak [34]. For example, the XPS spectrum showed that the Si-CNT-C material consisted of carbon, oxygen and silicon (Figure 3.11B). A high-resolution scan of the peaks is obtained subsequently in order to examine chemical states of elements. Since elements in different states and environments provide different characteristic binding energies, the chemical state can be acquired by fitting these XPS peaks. The high-resolution Si2p spectrum revealed that SiO_2, SiC and Si material was present on the Si-CNT-C surface (Figure 3.11C). The doublet peaks of Si corresponded to spin-orbit splitting as unpaired electrons left after the photoemission. They arranged their spin parallel or antiparallel to orbital angular momentum resulting in two different energy states [34].

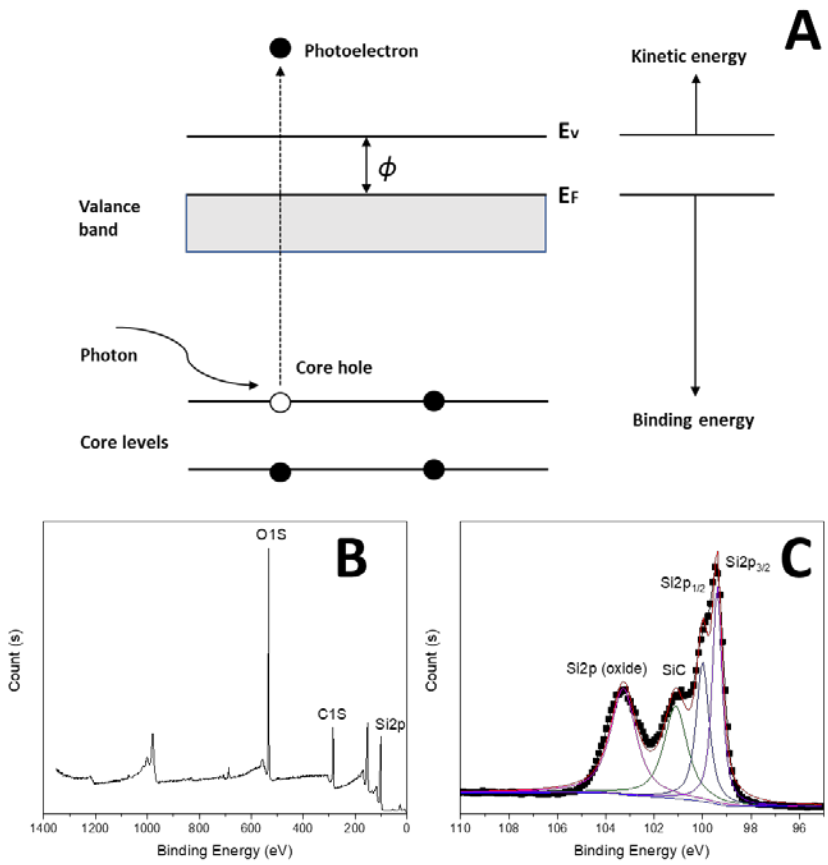


Figure 3.11. A) A diagram of a photoemission process; photoelectrons escape from the specimen surface due to the irradiation of X-ray beam, B) XPS survey spectrum, and C) high-resolution Si2p spectrum of Si-CNT-C (CH_4) material confirming unexpected SiC formation after coating amorphous carbon on the material.

3.2.6) X-ray Diffraction (XRD)

XRD is an analytical technique utilised to examine the structures of crystalline materials. Here, the crystalline structure and phase of Si in the Si-CNT based-materials was identified using this technique. In addition, this method was used to investigate SiC in Si-CNT-SiC-C materials. In this work, the material was placed on a low-background silicon holder, and XRD was carried out in Brucker X-ray diffraction with Cu ($K_{\alpha 1}$) radiation (λ= 1.5406 Å). In this method, X-ray diffraction takes place when a monochromatic beam of X-rays strikes a material and is scattered in a different direction with no energy adsorption. The X-ray diffraction by a crystal lattice is explained by Bragg's Law. For a crystalline material (Figure 3.12A), X-ray beams are scattered from different lattice planes which are separated by the interplanar distance (d). The scattered rays are in phase (constructive

interference) for specific angles of the incident X-rays on the crystal (θ). The path difference between the reflected rays (2dsin θ) is equal to a number of the X-ray wavelengths (nλ) as expressed in the Bragg's equation (Equation 3.6).

$$n\lambda = 2d \sin\theta \quad (3.6)$$

During XRD analysis, the X-ray beam irradiates the sample containing small crystals in random orientations at an angle of θ. The beam angle is increased by rotating a specimen or a beam source; while the detector records X-ray intensity at an angle of 2θ from the beam path. The measurement result (the so-called diffraction pattern) is a plot of X-ray intensity versus the angle between the incident and the diffracted X-ray beam (2θ). The directions and intensities of diffracted X-Rays are attributed to the material structures. Thus, the XRD pattern can identify structures, phases, crystal orientations of the materials by comparing with reference patterns from a database [35-37]. The XRD pattern of the Si-CNT based material, for instance, is shown in Figure 3.12B. The limitation of XRD is presented in the graph as only a crystalline carbon structure shows a distinctive diffraction pattern. However, X-rays are diffracted in all directions from amorphous carbon due to its random arrangement, causing a flat diffraction pattern. The position of the peak could also be used to calculate the d-spacing of the material (Equation 3.6), *e.g.* d-spacing of C (002) was 0.34 nm calculated from a peak position at 26.1 degrees.

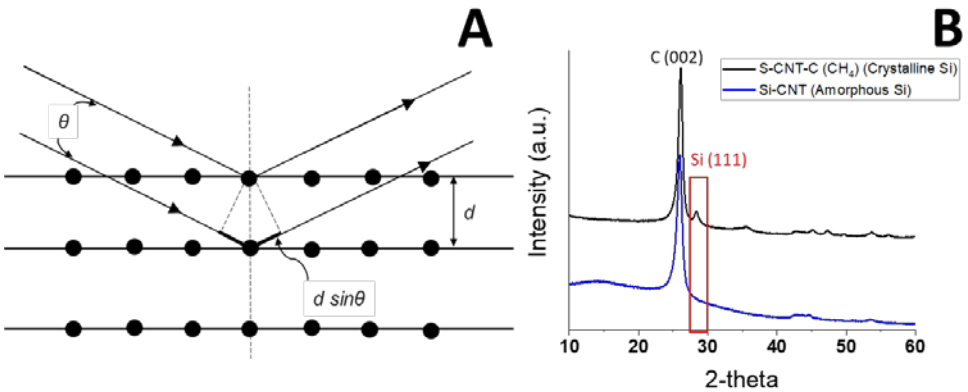


Figure 3.12. A) A scheme of X-rays reflection based on Bragg's Law; X-ray beams are scattered from different lattice planes which are divided by the interplanar distance (d) and B) XRD patterns of Si-CNT based material, Si peak can be observed only in the material which consisted of crystalline Si.

3.2.7) Raman spectroscopy

Raman spectroscopy is a spectroscopic technique based on inelastic scattering of monochromatic light from a laser source which is known as Raman scattering. The experiments in this study were carried out using a Horiba LabRAM ARAMIS Raman spectroscope with a laser wavelength of 532 nm. When a laser irradiates the sample, light can be scattered by atoms or molecules in two different ways, namely elastic and inelastic scattering. In the case of elastic scattering, the scattered light has the same frequency with the incident light, whereas in the case of inelastic scattering it has a different frequency from the incident light. The frequency shifts of photons which are either losing energy (Stokes scattering) or gaining energy (anti-Stokes scattering) are attributed to the vibrations of the atoms or molecules. Nevertheless, a vibrational mode will be Raman active if a variation in the polarizability of molecules occurs during the vibrational motion. These vibrational transitions are usually found in symmetric stretching of the molecular bonds. Hence, Raman spectroscopy is applied to gain insight into molecular structures of the materials since the vibrational frequencies in the Raman spectrum are specific to molecules, chemical bonding and intermolecular bonds [36, 38].

In this research, Raman spectroscopy was conducted to analyse the material structure, especially Si in the Si-CNT based materials by identifying the unique fingerprint of the substance. This technique was useful for confirming the existence of amorphous Si in the material since XRD could not detect it. Also, the Raman spectroscopy was used to study MWCNTs in BPs since two prominent peaks (named the G and D bands) are typically observed in carbon materials. For example, D and G bands are presented in the Raman spectrum of the MWCNT 45 (Figure 3.13A). The G peak at 1580 cm^{-1} is assigned to the in-plane stretching vibration of sp^2 carbon atoms (E_{2g} symmetry). It is the first-order Raman process in which a photon with a specific energy and momentum hits the sample and is scattered with different energy and momentum. The energy change of the scattered photon is due to

the atomic vibration known as a phonon. However, this phonon has a very small momentum compared to the size of the lattice cell; thus, the momentum change is almost zero [39]. In contrast, the D band at 1350 cm^{-1} relates to in-plane breathing vibration of the benzene rings (A_{1g} symmetry, Figure 3.13B). The D band is observed when defects are presented [5]. These defects cause a double-resonance process, which involves one phonon process and intervalley elastically scattering of the electron between the corner of the hexagon ring [40]. Thus, the D band represents disordered graphitic structures in the material [38]. The ratio between the intensities of the D and G bands (I_D/ I_G) is usually used to define the quality of the carbon material; that is, a large value of I_D/I_G means a high defect density in the material. The FWHM of the G band is also considered to evaluate the graphitisation of materials, *i.e.* a decrease of the G-FWHM indicates a structural change of carbon from turbostratic to graphitic [38].

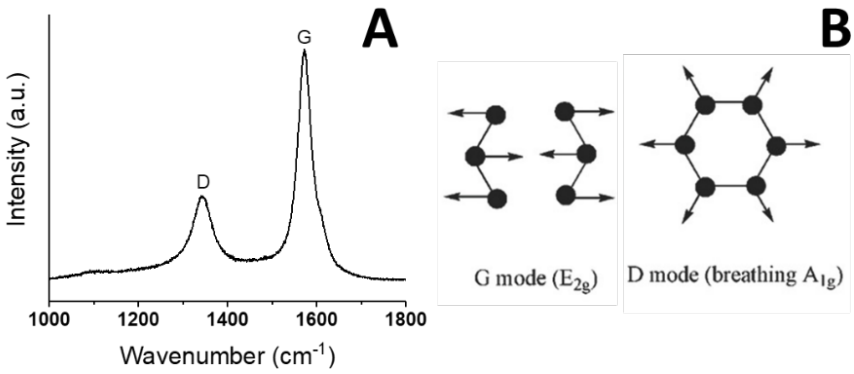


Figure 3.13. A) Raman spectrum of MWCNT 45 showing the characteristic D and G peaks of carbon material and B) the carbon atom movement in the D and G vibration modes [5].

3.2.8) Thermogravimetric analysis (TGA)

TGA is a thermal analysis method in which the change in sample weight is measured as a function of temperature or time. In this study, TGA (Perkin Elmer Pyris) was used to investigate the percentage of catalysts in MWCNTs and the percentage of Si in the Si-CNT based material. The temperature range for the analysis was 25-700 °C with a heating rate of 10 °C/min, and an air flow rate of 20 ml/min. In the TGA measurement, a sample pan is placed on a precision balance which is located inside a furnace. The furnace is heated, and the weight change of the sample is recorded over

a range of temperatures. The sample environment is controlled by flowing inert or reactive gases in the furnace. Lastly, the thermogravimetric result is presented as a graph of the mass percentage of the initial sample versus temperature or time of the measurement. The mass change in the TGA curve is related to the properties of the sample and can be used for determining the composition and impurities in the sample. The decomposition temperature can be used to evaluate the thermal stability of the materials. It is noted that the decomposition temperature of the materials is also affected by the measurement conditions (heating rate, gas flow rate, sample mass, *etc.*) [41, 42]. For instance, the TGA curve of MWCNT 45 is shown in Figure 3.14. The MWCNT 45 had an average oxidation temperature of 588 °C, and the percentage of MWCNTs in the sample was 96.6 wt.% (the other 3.4 wt.% was identified as catalyst residue which remains even at 700 °C).

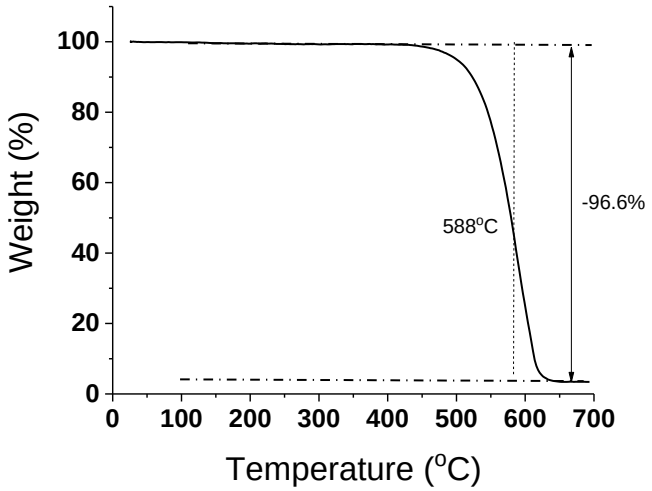


Figure 3.14. TGA curve of MWCNT 45; the average oxidation temperature of the material was 588 °C and the MWCNT content was 96.6 wt.%

3.2.9) Four-point-probe resistivity measurement

The four-point-probe technique is a method for measuring the electrical resistivity of materials. In this research, the four-point-probe method was conducted to examine the electrical resistivity of BPs and the Si-CNT based material in order to confirm the practical use of the material as a free-standing electrode (without current collectors). The electrical resistivity of the electrode (including active materials and current collectors) is a vital factor for operating LIBs since it relates to

an initial electronic resistance of the battery (Equation 3.7). The electronic resistance causes ohmic polarisation in the cell (mentioned in Chapter 1). That is, the high resistivity of electrodes prevents lithiation from occurring at a voltage with low polarisation [43]. The high resistance also limits the rate capability of the electrode since the current flow is impeded, leading to a heat generation in the battery [44]. According to previous studies, the minimum electronic conductivity of the electrode for achieving high-rate cycling should be 0.01 S/cm [45, 46].

During the measurement, four individual probes are collinear and equally separated (Figure 3.15). This set-up prevents the contact resistance, which generally takes place between the material and the probes. Therefore, a resistance result from this technique is more accurate and can be easier to clarify than results from a two-point-probe technique. In the four-point-probe set-up, a current flows into a sample via two outer probes, while potential distribution is measured by the two inner probes. The probes are set at equal interval X, and the equations for the resistance (R) calculation are shown as follows [47].

$$R = \frac{\rho l}{wt} = \frac{\rho l}{A} \tag{3.7}$$

$$\Delta R = \rho \left(\frac{dx}{A}\right) \tag{3.8}$$

Where ϱ is the resistivity, w and l are the widths and the length of the sample, dx is the differential length, t is the thickness of the sample, and A is the surface area where the current passes through. Note, the distance between probes are equal ($X=X_1=X_2=X_3$). In the case of a thin film sample for which the thickness is significantly less than X, A is equal to $2\pi Xt$, and the resistance can be determined as follows [47, 48]

$$R = \int_{X_1}^{X_2+X_3} \rho \frac{dx}{2\pi Xt} = \int_{X}^{2X} \rho \frac{dx}{2\pi Xt} = \frac{\rho}{2\pi t} \ln 2 \tag{3.9}$$

The superposition of the current at the two outer probe results in

$$R = \frac{V}{2I} \tag{3.10}$$

When combining Equation 3.9 with Equation 3.10, the film resistivity is given by

$$\rho = \frac{\pi t}{ln2}\left(\frac{V}{I}\right) = 4.53t\left(\frac{V}{I}\right) \tag{3.11}$$

To prevent round-off errors, a square sample (w=l) is used in this work. By considering both Equation 3.7 and 3.11, the sheet resistance (R_s) of the square thin film is then defined as

$$R_s = \frac{\rho}{t} = 4.53\frac{V}{I} \tag{3.12}$$

The resulting four-point-probe resistivity value is in terms of the sheet resistance (Ohm/sq). The bulk resistivity is therefore calculated by multiplying the sample thickness with the sheet resistance. The conductivity value of the bulk sample can then be determined as it is the reciprocal of the resistivity [47]. For example, the sheet resistance of BP 45 was 3.6 Ohm/sq, and its thickness was 125 micron. Hence, the resistivity and conductivity of BP 45 were 0.045 Ohm-cm and 22.2 S/cm, respectively.

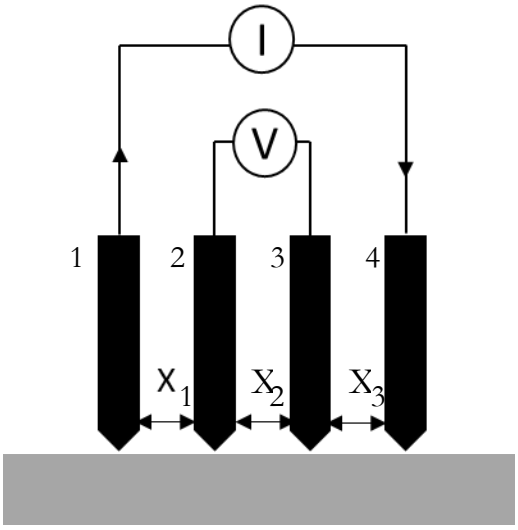


Figure 3.15. A schematic of the four-point probe measurement; the probes are set colinearly at equal spacing X, while the voltage and the current are measured separately.

3.2.10) Galvanostatic cycling

Galvanostatic cycling is the main technique which was used to test cell performance in this work as it provides useful information, such as cycling stability, specific/areal capacity and voltage profiles of the electrode. In this research, cycling tests were carried out on Maccor Battery Test System at 30 °C. Regarding the galvanostatic cycling technique, a steady current is applied to the cell where

the electric potential is recorded as a function of time (Figure 3.16A) [1, 49]. The potential vs time curve is known as a charge-discharge graph. Charge and discharge currents applied to the cell are usually defined as the C-rate. The C-rate is a rate of the battery which is charged or discharged to its maximum capacity, *i.e.* the C/2 rate means that the current discharges the battery in two hour [44].

The graphs which are a result of BP 45 electrode tested at C/5 rate are, for example, shown in Figure 3.16B. The capacity of the electrode could be calculated from the area under the current-time graph (left, Figure 3.16B). The charge-discharge graph (right, Figure 3.16B) additionally provides important details of the BP 45 electrode such as open-circuit voltage (2.75 V) and voltage profiles of the electrode upon cycling. The voltage change observed in the graph indicates an increase of polarisations due to reactions occurring in the electrode. For instance, two plateaus in the first discharge curve can be attributed to the SEI formation (0.8 V) [50], and the Li-ion insertion into the carbon material (0.25 V) [51]. Furthermore, the cell was set to discharge to the low cut-off potential and to charge to the high cut-off potential during the measurements. In this work, the discharge and charge potentials were limited to be 0.05 V and 2 V, respectively, to avoid Li plating and parasitic reactions in the battery. Therefore, the stability of the battery test cells would be improved using these limitations [52].

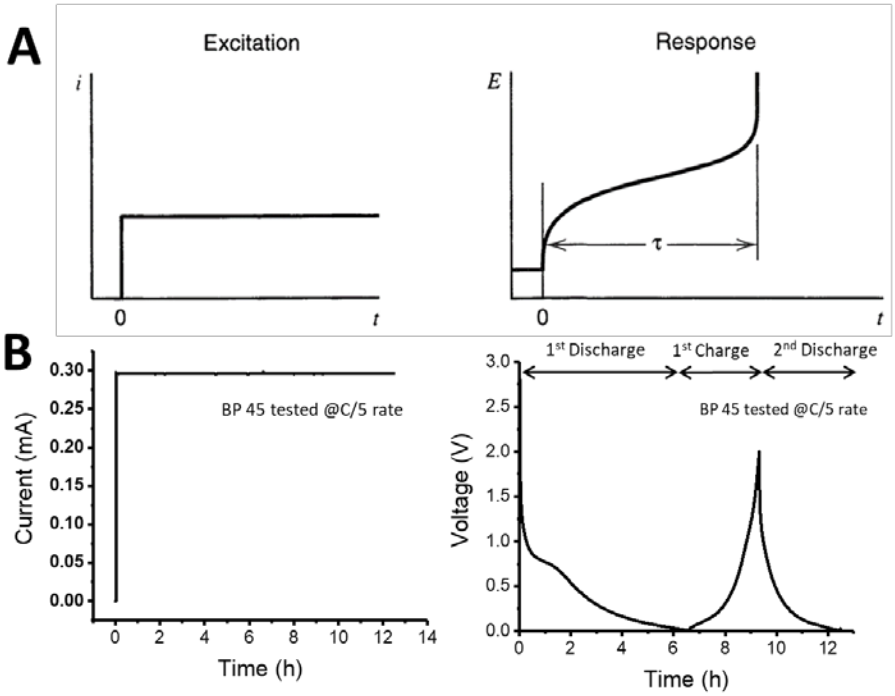


Figure 3.16. A) A galvanostatic cycling technique showing a constant current applied to the tested cell (excitation) and the potential determined as a function of time (response) [1], B) the current-time and charge-discharge graphs of BP 45 tested at C/5 rate; its capacity could be determined by calculating the area of the current-time graph, while plateaus in the discharge curve indicated the SEI formation (0.8 V) and Li insertion into the carbon (0.25 V).

3.3) Material synthesis and fabrication of electrodes in this work

In this section, the experimental set-up and the conditions of CVD methods for synthesising MWCNTs and Si-CNT based materials (Si-CNT, Si-CNT-C, Si-CNT-SiC, and Si-CNT-SiC-C) are shown. In addition, the fabrication of buckypapers, pure MWCNTs and Si electrodes are presented.

3.3.1) Synthesis of MWCNTs

Aerosol-assisted CVD was used to synthesise MWCNTs in this work. The AACVD experiments done here follow optimised AACVD procedures outlined in previous reports where ferrocene was selected as a catalyst and ethylbenzene as a carbon source [15, 53]. Briefly, a mixture of 5 wt.% ferrocene (Sigma-Aldrich, 95%, $C_{10}H_{10}Fe$) and 95 wt.% ethylbenzene (Sigma-Aldrich, 95%, C_8H_{10}) was fed by an aerosol generator into a quartz tube which was placed in the furnace (Figure

3.17). This experiment was carried out at a temperature of 800 °C under 1000 sccm of argon flow (BOC, 99.998%, Ar, 200 bar).

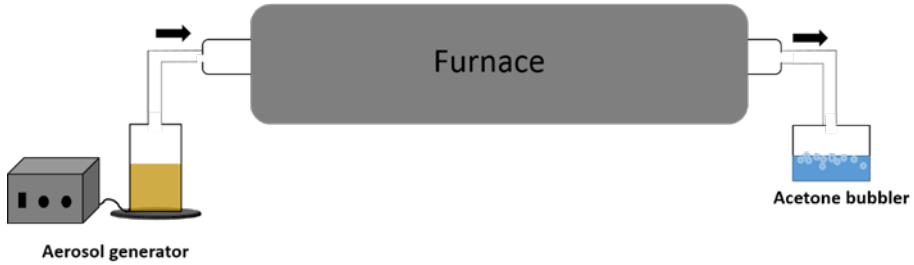


Figure 3.17. A schematic diagram showing the experiment set up of the used AACVD apparatus for MWCNTs synthesis.

3.3.2) Fabrication of buckypapers

BPs were fabricated using a standard vacuum filtration method. In-house MWCNTs and MWCNTs purchased from Nanocyl (Nanocyl7000) were debundled and dispersed in ethanol (Merck, 99%, C_2H_5OH) using an ultrasonic bath (45 kHz, 25 °C for 5 hours). Directly after sonication, the suspension was stirred by a magnetic stirrer overnight. The dispersion was then centrifuged at 3250 rpm for 20 minutes in order to separate supernatant (well-dispersed MWCNT suspension) from sediment (aggregated MWCNTs). The dispersed MWCNT solution was then filtered through a polymer membrane (Whatman, 16mm, 0.4 microns). The MWCNT paper was thus formed on the top of the membrane and then dried at 80 °C in a vacuum oven overnight. Finally, the BP was peeled off from the filter membrane.

3.3.3) Fabrication of pure MWCNT electrodes

A pure MWCNT electrode was prepared by mixing MWCNT powder with carboxymethyl cellulose binder (Sigma Aldrich, Mw 700000, CMC) in water. The mixture was ball-milled at 300 rpm for 2 hours. The MWCNT slurry was cast on a copper foil (Alfa Aesar, 99.8%, 0.025 mm thick) after being cut into electrodes with 11 mm of diameter.

3.3.4) Synthesis of Si-CNT materials

The Si-CNT paper was prepared using APCVD. The BPs were placed on an alumina boat (Figure 3.18). This alumina boat was then placed inside the reactor (550 °C), which was purged with argon gas (BOC, 99.998% Ar, 200 bar) in order to remove oxygen and air in the system for 30 minutes. The furnace was subsequently shifted over the sample before flowing 200 sccm of silane mixture gas (BOC, 500 ppm SiH_4 with Ar, 150 bar) for 5 minutes. The furnace was moved back while the sample was cooled down under Ar atmosphere before unloading. The BP was weighed before and after APCVD to calculate the amount of Si deposition. This measurement can accurately evaluate the amount of Si deposited on the BP as opposed to using a thickness measurement which suffers from the fact that the Si structure can have different densities ($\varrho_{c\text{-}Si}$ = 2.33 g cm^{-3}, $\varrho_{a\text{-}Si}$ = 1.75-2.2 g cm^{-3} [54]).

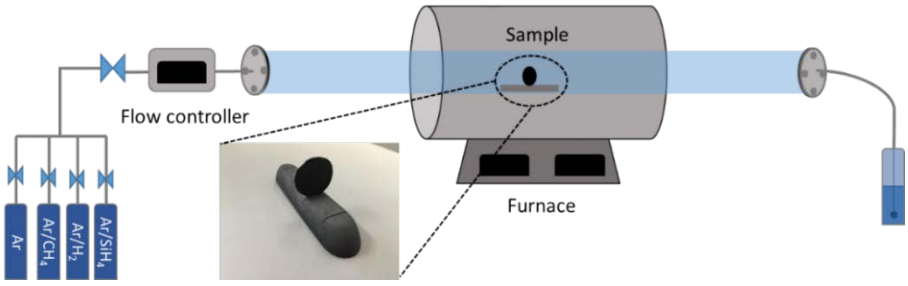


Figure 3.18. A schematic revealing the APCVD method for Si deposition on a BP by using a gas mixture set-up.

3.3.5) Preparation of the Si-CNT-SiC-C nanocomposites

3.3.5.1) Free-standing Si-CNT-SiC material

After synthesising the Si-CNT material as described in section 3.3.4, the furnace temperature was increased to 990, 1000, 1100, and 1200 °C (instead of cooling). After reaching this temperature, the material was annealed for 30 minutes, resulting in the formation of a SiC interface between Si NPs and the MWCNT walls within the BP.

3.3.5.2) Amorphous C coating on Si-CNT-SiC materials (Si-CNT-SiC-C)

Amorphous carbon was deposited on the Si-CNT-SiC material by running 20 sccm methane gas (BOC, 250 ppm CH_4 with Ar, 200 bar) with 180 sccm Ar for 2 minutes at 1000 °C, followed by cooling in Ar.

3.3.5.3) Amorphous C coating on Si-CNT materials using methane gas (Si-CNT-C, CH_4, Case I)

Amorphous C was deposited on the pure Si-CNT material by running 400 sccm methane gas (BOC, 250 ppm CH_4 with Ar, 200 bar) for 10 minutes at 900 °C, followed by cooling in Ar.

3.3.5.4) Amorphous C coating on Si-CNT materials using acetylene gas (Si-CNT-C, C_2H_2, Case II)

The amorphous C was deposited on the pure Si-CNT material by running 1 sccm acetylene gas (BOC, 98.5% C_2H_2, 15.5 bar) with 200 sccm Ar for 5 minutes at 700 °C, followed by cooling in Ar.

3.3.6) Fabrication of pure Si electrodes

The Si NP powder (GETNANOMATERIALS, 99%, 30-50 nm) was mixed with carboxymethyl cellulose (Sigma Aldrich, Mw 700000, CMC) and carbon black (Alfa Aesar, 99.9 %) in a ratio of 6:2:2 NMP (Merck, 95%, NMP). The mixture was mixed using ball-milling at 300 rpm for 1 hour. After that, the slurry was cast on a Cu foil (Alfa Aesar, 99.8%, 0.025 mm thick) (Figure 3.19). The electrode was dried at 100 °C for 2 hours before being cut into discs of 20 mm in diameter.

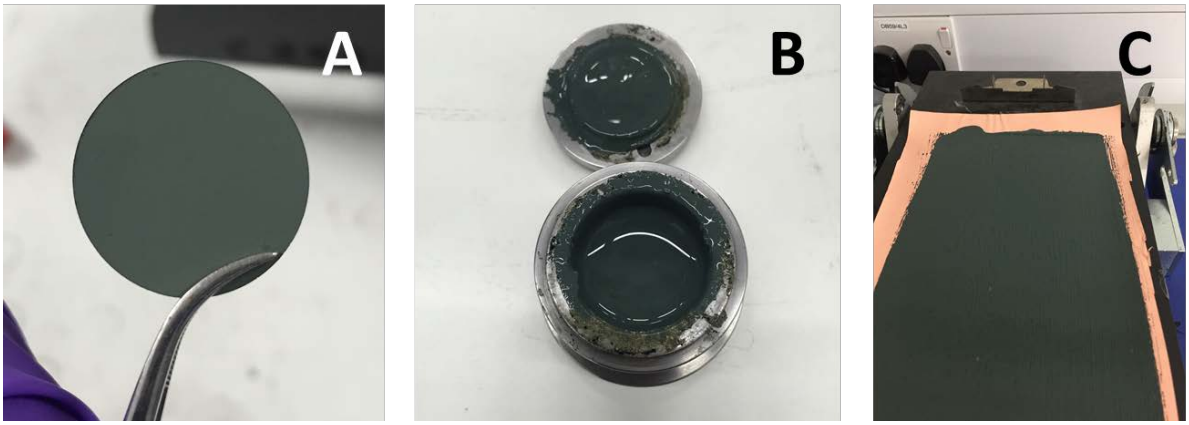


Figure 3.19. Photographs showing A) a conventional Si electrode made by uniformly casting B) Si mixture paste on C) a copper foil current collector.

3.4) Cell assembly and battery testing in this work

Battery fabrication of both coin-cells and pouch-cells, using the previously prepared electrodes, is shown in this section. The procedures for battery testing these cells in order to study the battery performance of the as-prepared electrode are further explained. Finally, the preparation of the post-cycling electrode is presented.

3.4.1) Fabrication of coin cell and pouch cell batteries

The fabricated electrodes were used as a working electrode, and a Li foil (Sigma Aldrich, 99.9%) was applied as a counter electrode. A glass fibre separator (Whatman, GF/F glass fibre filter paper) was immersed with electrolyte (Merck, LP30, 1 M $LiPF_6$ in 1:1 EC/DMC). The coin cell (CR2325) and pouch cell (5 cm x 5cm) were fabricated (Figure 3.20) in the Ar-filled glovebox (0.1 ppm H_2O and O_2). Pouch cells were made similarly to the coin cell configuration, but thin strips of Cu foil were used instead of stainless-steel cases to provide the electron pathway.

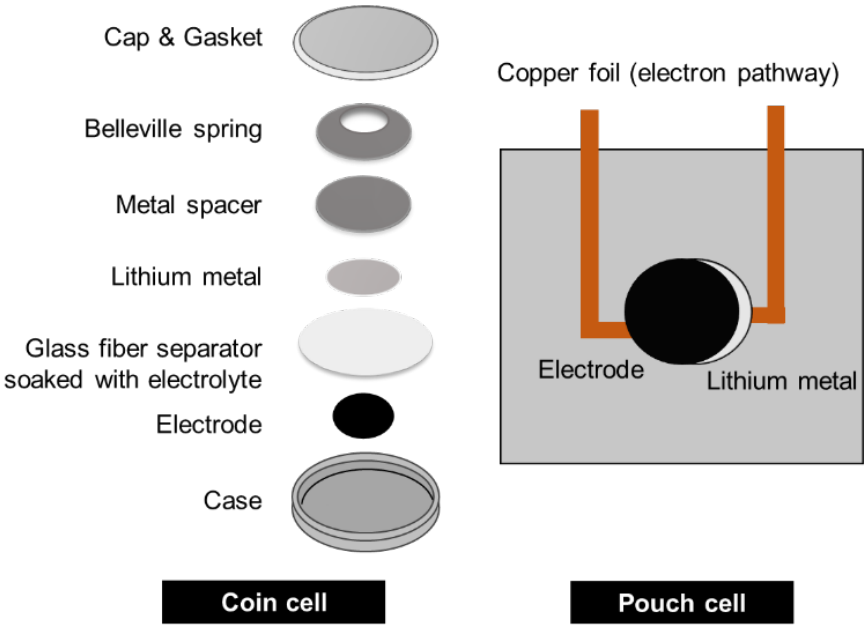


Figure 3.20. A scheme exhibiting the coin cell battery (left) and pouch cell battery (right) configurations.

3.4.2) Battery performance testing

The coin-cells were tested for battery performance by Maccor battery tester at 30 °C. The voltage range was 0.05-2 V vs Li/Li^+. The current charge was kept constant during the stability study, and the C-rate was varied from slow to fast for the rate testing. Note that C-rate was calculated from the capacity of the active material. Finally, the pouch cells were tested at 0.1 mA using Biologic battery tester.

3.5) Preparation the electrode for post-cycling analysis in this work

The coin-cell battery was stopped after delithiation at 2 V vs Li/Li^+. The coin-cell batteries were then disassembled before the electrode was washed by dimethyl carbonate (DMC) several times.

3.6) Conclusions

In this chapter, the working principles of two CVD methods, *i.e.* AACVD and APCVD, were discussed. Specifically, their potential use in MWCNTs and Si-CNT materials fabrication. AACVD was used to synthesise large quantities (2 g) of MWCNTs of uniform MWCNTs reasonably fast (30

minutes). Then, the APCVD was used to deposit Si on BPs because it could tackle the diffusion limitation in the normal APCVD; the reaction rate in the system is slowed down by reducing the partial pressure of silane gas. This modified system proposed in this study is cheaper, safer and easier to operate than LPCVD. The principal studies of these synthesis processes are useful to develop effective procedures in this research. That is, the types of CNTs are easily controlled by varying the experimental parameters of the AACVD method such as catalyst particle sizes, temperature and types of a carbon source. Moreover, the structure of the Si deposition can be determined by reaction temperature and a gas diffusion rate in APCVD. After the synthesis, physical and chemical properties of the Si-CNT material were subsequently investigated using numerous characterisation methods, *i.e.* SEM, TEM, EDX, STEM, XPS, XRD, Raman spectroscopy, TGA and four-point probe measurement. The fundamentals of these characterisation techniques were discussed in this chapter. Understanding the background of these methods is crucial since it guides how to perform them in order to obtain the desired information. In addition, the battery performance of the Si-CNT electrode was tested using the galvanostatic cycling technique. It is a simple technique; thus, no special skill is needed to operate the method. Various data could also be gained from this technique, such as capacity and cycling behaviour of the electrode. Finally, the material preparation, electrode fabrication and battery testing procedures applied in this research were explained in the chapter.

3.7) References

1. Bard, A.J. and L.R. Faulkner, *Electrochemical Methods: Fundamentals and Applications, 2nd Edition*. 2000: Wiley Textbooks.
2. Shojaeiarani, J., D. Bajwa, and G. Holt, *Sonication amplitude and processing time influence the cellulose nanocrystals morphology and dispersion*. Nanocomposites, 2020. **6**(1): p. 41-46.
3. Kogure, T., *Chapter 2.9 - Electron Microscopy*, in *Developments in Clay Science*, F. Bergaya and G. Lagaly, Editors. 2013, Elsevier. p. 275-317.
4. V.K.Sarin, A.K.P.a., *Basic Principles of CVD Thermodynamics and Kinetics*, in *Chemical Vapor Deposition*, T.S.S. Jong-Hee Park, Editor. 2001, ASM International: USA. p. 23-43.
5. Trusovas, R., et al., *Recent Advances in Laser Utilization in the Chemical Modification of Graphene Oxide and Its Applications*. Advanced Optical Materials, 2016. **4**(1): p. 37-65.
6. Kumar, M. and Y. Ando, *Chemical Vapor Deposition of Carbon Nanotubes: A Review on Growth Mechanism and Mass Production*. Journal of Nanoscience and Nanotechnology, 2010. **10**(6): p. 3739-3758.

7. Inkson, B.J., *2 - Scanning electron microscopy (SEM) and transmission electron microscopy (TEM) for materials characterization*, in *Materials Characterization Using Nondestructive Evaluation (NDE) Methods*, G. Hübschen, et al., Editors. 2016, Woodhead Publishing. p. 17-43.
8. Henning, S. and R. Adhikari, *Chapter 1 - Scanning Electron Microscopy, ESEM, and X-ray Microanalysis*, in *Microscopy Methods in Nanomaterials Characterization*, S. Thomas, et al., Editors. 2017, Elsevier. p. 1-30.
9. GmbH, C.Z.M., *High Resolution Imaging of Biological Samples Using Scanning Electron Microscopes and The ATLAS*. AZoM.
10. Jasinski, J.M. and S.M. Gates, *Silicon chemical vapor deposition one step at a time: fundamental studies of silicon hydride chemistry*. Accounts of Chemical Research, 1991. **24**(1): p. 9-15.
11. P.Ho, J.R.C.a., *Introduction to Chemical Vapor Deposition (CVD)*, in *Chemical Vapor Deposition*, T.S.S. Jong-Hee Park, Editor. 2001, ASM international: USA. p. 1-22.
12. Pierson, H.O., *3 - The Chemistry of CVD*, in *Handbook of Chemical Vapor Deposition (CVD) (Second Edition)*, H.O. Pierson, Editor. 1999, William Andrew Publishing: Norwich, NY. p. 68-83.
13. Hitchman, A.C.J.a.M.L., *Chapter 1 Overview of Chemical Vapour Deposition*, in *Chemical Vapour Deposition: Precursors, Processes and Applications*, A.C. Jones and M.L. Hitchman, Editors. 2009, The Royal Society of Chemistry. p. 1-36.
14. Park, J.H. and T.S. Sudarshan, *Chemical Vapor Deposition*. Surface engineering series. 2001: ASM International.
15. Meysami, S.S., et al., *Aerosol-assisted chemical vapour deposition synthesis of multi-wall carbon nanotubes: II. An analytical study*. Carbon, 2013. **58**: p. 159-169.
16. Suslick, K.S., D.A. Hammerton, and R.E. Cline, *Sonochemical hot spot*. Journal of the American Chemical Society, 1986. **108**(18): p. 5641-5642.
17. Lozano, A., et al. *Influence of liquid properties on ultrasonic atomization*. 2017.
18. Vernès, L., M. Vian, and F. Chemat, *Chapter 12 - Ultrasound and Microwave as Green Tools for Solid-Liquid Extraction*, in *Liquid-Phase Extraction*, C.F. Poole, Editor. 2020, Elsevier. p. 355-374.
19. Joubert, M.L.a.J.C., *The Pyrosol Process or the Pyrolysis of an Ultrasonically Generated Aerosol*, in *Chemistry of Advanced Materials*, C.N.R. Rao, Editor. 1993, Blackwell Scientific Publications: Oxford, UK.
20. Prasek, J., et al., *Methods for carbon nanotubes synthesis—review*. Journal of Materials Chemistry, 2011. **21**(40): p. 15872-15884.
21. Jasinski, J.M., B.S. Meyerson, and B.A. Scott, *Mechanistic Studies of Chemical Vapor Deposition.* Annual Review of Physical Chemistry, 1987. **38**(1): p. 109-140.
22. A. Onischuk, A. and V. N. Panfilov, *Mechanism of thermal decomposition of silanes.* Russian Chemical Reviews, 2001. **70**(4): p. 321-332.
23. Lee, J.H., S.H. Moon, and S.-W. Rhee, *Simulation of silicon film growth by silane decomposition at low pressures and temperatures*. Korean Journal of Chemical Engineering, 1992. **9**(1): p. 8-15.
24. Shishkovsky, I.V. and P.N. Lebedev, *3 - Chemical and physical vapor deposition methods for nanocoatings*, in *Nanocoatings and Ultra-Thin Films*, A.S.H. Makhlouf and I. Tiginyanu, Editors. 2011, Woodhead Publishing. p. 57-77.
25. Tao, M., *Crystal Growth in Silicon Chemical Vapor Deposition from Silane*. Journal of The Electrochemical Society, 1997. **144**(6): p. 2221.
26. Goodhew, P.J., J. Humphreys, and R. Beanland, *Electron Microscopy and Analysis, Third Edition*. 2000: Taylor & Francis.
27. Gilmore, C.M., *Materials Science and Engineering Properties, SI edition* 2015: Cengage Learning.
28. Williams, D.B. and C.B. Carter, *Transmission Electron Microscopy: A Textbook for Materials Science*. Cambridge library collection. 2009: Springer US.
29. McLaren, A.C., *Transmission Electron Microscopy of Minerals and Rocks*. 2 ed. Cambridge Topics in Mineral Physics and Chemistry. 1991, Cambridge: Cambridge University Press.
30. McCaffrey, J., *Easy Guide to Calibrating TEM's and STEM's.* Microscopy Today, 2005. **13**(4): p. 28-35.
31. Pennycook, S.J., et al., *Scanning Transmission Electron Microscopy for Nanostructure Characterization*, in *Scanning Microscopy for Nanotechnology: Techniques and Applications*, W. Zhou and Z.L. Wang, Editors. 2007, Springer New York: New York, NY. p. 152-191.

32. Konno, H., *Chapter 8 - X-ray Photoelectron Spectroscopy*, in *Materials Science and Engineering of Carbon*, M. Inagaki and F. Kang, Editors. 2016, Butterworth-Heinemann. p. 153-171.
33. Wagner, J.M., *X-ray Photoelectron Spectroscopy*. 2011: Nova Science Publishers.
34. Moulder, J.F. and J. Chastain, *Handbook of X-ray Photoelectron Spectroscopy: A Reference Book of Standard Spectra for Identification and Interpretation of XPS Data*. 1992: Physical Electronics Division, Perkin-Elmer Corporation.
35. Iwashita, N., *Chapter 2 - X-ray Powder Diffraction*, in *Materials Science and Engineering of Carbon*, M. Inagaki and F. Kang, Editors. 2016, Butterworth-Heinemann. p. 7-25.
36. Duckett, S., B. Gilbert, and M. Cockett, *Foundations of Molecular Structure Determination*. 2015: Oxford University Press.
37. Sergeev, G.B., *3 - Experimental Techniques*, in *Nanochemistry*, G.B. Sergeev, Editor. 2006, Elsevier Science: Amsterdam. p. 37-45.
38. Kaburagi, Y., A. Yoshida, and Y. Hishiyama, *Chapter 7 - Raman Spectroscopy*, in *Materials Science and Engineering of Carbon*, M. Inagaki and F. Kang, Editors. 2016, Butterworth-Heinemann. p. 125-152.
39. Dresselhaus, M.S., A. Jorio, and R. Saito, *Characterizing Graphene, Graphite, and Carbon Nanotubes by Raman Spectroscopy*. Annual Review of Condensed Matter Physics, 2010. **1**(1): p. 89-108.
40. Sattler, K.D., *Handbook of Nanophysics: Nanotubes and Nanowires*. Handbook of Nanophysics. 2010: CRC Press.
41. West, A.R., *Solid State Chemistry and Its Applications*. 1991: Wiley.
42. Chen, M.-m., *Chapter 12 - Thermal Analysis*, in *Materials Science and Engineering of Carbon*, M. Inagaki and F. Kang, Editors. 2016, Butterworth-Heinemann. p. 249-272.
43. Ozanam, F. and M. Rosso, *Silicon as anode material for Li-ion batteries*. Materials Science and Engineering: B.
44. Buchmann, I. and I. Cadex Electronics, *Batteries in a Portable World: A Handbook on Rechargeable Batteries for Non-engineers*. 4 ed. 2016: Cadex Electronics.
45. Tian, R., et al., *Quantifying the Effect of Electronic Conductivity on the Rate Performance of Nanocomposite Battery Electrodes*. ACS Applied Energy Materials, 2020. **3**(3): p. 2966-2974.
46. Mistry, A., et al., *Analysis of Long-Range Interaction in Lithium-Ion Battery Electrodes*. Journal of Electrochemical Energy Conversion and Storage, 2016. **13**(3).
47. Li, M.-Y., et al., *Analysis of variance on thickness and electrical conductivity measurements of carbon nanotube thin films*. Measurement Science and Technology, 2016. **27**(9): p. 095004.
48. Chan, J. *Four-Point Probe Manual*. 1994; Available from: http://www.fourpointprobes.com/four-point-probe-manual/.
49. Linden, D. and T.B. Reddy, *Handbook of batteries*. 2002, New York: McGraw-Hill.
50. Fong, R., U. von Sacken, and J.R. Dahn, *Studies of Lithium Intercalation into Carbons Using Nonaqueous Electrochemical Cells*. Journal of The Electrochemical Society, 1990. **137**(7): p. 2009-2013.
51. Yuqin, C., et al., *Irreversible capacity loss of graphite electrode in lithium-ion batteries*. Journal of Power Sources, 1997. **68**(2): p. 187-190.
52. Beattie, S.D., et al., *Understanding capacity fade in silicon based electrodes for lithium-ion batteries using three electrode cells and upper cut-off voltage studies*. Journal of Power Sources, 2016. **302**: p. 426-430.
53. Meysami, S.S., et al., *Aerosol-assisted chemical vapour deposition synthesis of multi-wall carbon nanotubes: I. Mapping the reactor*. Carbon, 2013. **58**: p. 151-158.
54. Renner, O. and J. Zemek, *Density of amorphous silicon films*. Czechoslovak Journal of Physics B, 1973. **23**(11): p. 1273-1276.

Chapter 4

Free-standing Si-CNT anode for Li-ion batteries

In this chapter, buckypapers (BPs) fabricated from in-house-produced and commercial MWCNTs were used as a free-standing electrode in LIBs. These flexible BPs showed a good electrical conductivity (*ca.* 22-16 S/cm), which is higher than the minimum electrode conductivity (0.01 S/cm) for achieving high-rate cycling [2]. However, when testing as an anode material for LIBs, the BP electrode showed a relatively low specific capacity (*ca.* 290-100 mAh/g) compared to a commercial graphite anode (372 mAh/g). Amorphous silicon nanoparticles (Si NPs) were then deposited on the MWCNTs in a BP in order to improve the capacity of the electrode. Unfortunately, the Si-CNT electrode exhibited poor capacity retention (0.09 mAh/cm^2 after 300 cycles). After cycling, cracking and a structural change of Si NPs was observed. The Si NPs were also detached from the MWCNT wall, causing a dramatic loss in capacity of the Si-CNT electrode. Hence, the results confirmed that MWCNTs in the form of BPs were not adequate to provide the stress relaxation due to the excessive volume change of Si NPs. In addition, the weak interface between Si NPs and MWCNTs was not capable of attaching the Si NPs when changing in volume during the cycling.

4.1) Introduction

Free-standing electrodes made with MWCNT papers or BPs without binders and current collectors (Figure 4.1A-C) have been studied as LIB electrodes to tackle conventional electrode issues. Since the BP is bendable and rollable (Figure 4.1D-E) [1, 4, 5], it will be beneficial for current development technologies in flexible electronic devices such as smartphones, smartwatches and ultrathin tablets. However, these BPs showed a low specific capacity when testing them as a free-

standing electrode in the battery. For example, Chew *et al.* (2009) prepared binder-free films using a vacuum filtration by mixing different types of CNTs and surfactants to improve dispersion. The flexible MWCNT film showed a capacity of 300 mAh/g after 40 cycles. However, these films consisted of carbon black additives and needed an additional step to remove the surfactant during the filtration method [7]. The MWCNT paper was also studied as an anode material for LIBs by Landi *et al.* (2009). This MWCNT paper exhibited a specific capacity of 225 mAh/g after 20 cycles [8] which was still lower than the commercial graphite anode.

Although the BPs exhibit a poor specific capacity, they have outstanding properties such as mechanical strength and electrical and thermal conductivities, which make them suitable for use as a free-standing electrode to support other active materials. In particular, BPs fabricated from MWCNTs have high tensile strength (5-200 GPa) and Young's modulus (1.2 TPa) [9]. Note that the mechanical properties, including stiffness and Young's modulus, depend on their diameter and the number of MWCNT walls. The Young's modulus and bending stiffness of MWCNTs increase with the diameter of the nanotube and the number of the walls [10, 11]. Thus, BPs with high stiffness can be fabricated from MWCNTs of larger diameter. Furthermore, BPs have high electrical conductivity (54-23 S/cm) [12] and thermal conductivity (472-766 W/mK) [13]. The electrical and thermal conductivities of the BPs are dependent on many parameters, *i.e.* the density and alignment of the BP, the type of MWCNTs used, treatment and fabrication methods [5]. In addition, the mechanical property and electrical conductivity of BPs are different from individual MWCNTs due to low tube-tube interactions limiting the stress transferred and electrical transport between the nanotubes [14, 15]. Nonetheless, the study of the mechanical property and thermal conductivity of BPs is out of the scope of this work. Only the electrical conductivity of the material was tested to confirm its use as a free-standing electrode; that is, its electrical conductivity should be high enough to accomplish the battery cycling (also discussed in Chapter 3).

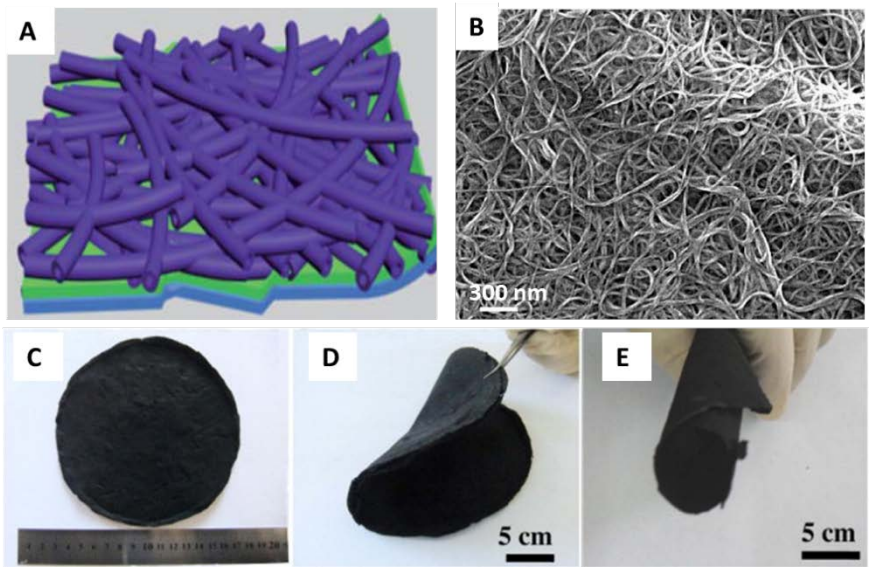


Figure 4.1. A) A schematic diagram showing the configuration of the buckypaper [1], B) SEM images of the buckypaper showing bundles of entangled carbon nanotubes [3], C) a photograph of buckypaper electrode showing its smooth surface, and D-E) photographs of a buckypaper showing its bendability; it can be bended and rolled [6].

Significant effort has been dedicated towards replacing the graphitic anode with silicon because the Si anode has a high theoretical gravimetric capacity (4200 mAh/g) [16] and low operating voltage (0.4 V vs Li/Li^+) [17]. Nevertheless, undesirable large volume changes (300-400%) of Si electrodes during cycling are a major problem which results in Si pulverisation and instability of the SEI layer [18, 19]. Thus, Si-based electrodes suffer from dramatic capacity fading and poor cycling stability; severely limiting the viability of Si electrodes in commercial applications [19-22]. One method of tackling the problems associated with pure Si electrodes involves merging silicon and carbon materials in nanocomposites [17, 19, 23]. In particular, MWCNTs possess superior mechanical stability and excellent electronic conductivity compared to other carbon materials [24]. As discussed in Chapter 1, the MWCNTs could minimise the strain induced due to the volume expansion during the lithiation of Si. Therefore, it is useful to composite MWCNTs in the configuration of BPs with Si in order to address the volume change problems in the Si materials.

In this work, MWCNTs were synthesised using AACVD. Free-standing BPs were made from MWCNTs synthesised in-house as well as from commercial sources. The electrical conductivity of

BPs was tested, and its high flexibility was reported. BPs were utilised as an anode in LIB coin-cells to study the cycling performance. Finally, pouch cells were also fabricated to examine cycling performance. In the pouch-cell configuration, a free-standing electrode was assembled, and it was possible to eliminate the effect of the stainless-steel components present in the coin-cell batteries. Following testing, BPs were coated with amorphous Si in order to enhance the capacity of the electrode. The free-standing Si-CNT material was fabricated into coin-cells, and the cycling performance was tested in order to compare the results against a pure Si electrode. Finally, the structural morphology before and after cycling was examined using various characterisation methods such as SEM, EDX, TEM, *etc.*

4.2) Experimental

Different MWCNTs were first synthesised and uniformly dispersed in ethanol in order to fabricate BPs. Details of MWCNT synthesis and BP fabrication are shown in section 3.3.1-3.3.2 in Chapter 3. The BPs were fabricated into both coin-cells and pouch-cells and tested their cycling performance as a free-standing electrode. Next, Si was deposited on the BPs using APCVD with silane gas used as the precursor. Coin-cell batteries with Si-CNT electrodes were assembled to examine the battery performance of Si-CNT electrode to compare the results to BP and pure Si electrodes. The experimental details of the Si-CNT synthesis are presented in section 3.3.4. Note, the procedures of conventional MWCNTs and pure Si electrodes are also shown in section 3.3.3 and 3.3.6, respectively. In addition, the battery testing and post-cycling analysis of the BP and Si-CNT electrodes are outlined in section 3.4 and 3.5 in Chapter 3.

4.3) Characterisation

The morphology and structure of MWCNTs, BPs and Si-CNT materials were studied using SEM, TEM, and XRD techniques. These materials were examined in terms of their physical and chemical properties via EDX, Raman spectroscopy, TGA and XPS. The electrical conductivity of BPs

and Si-CNT materials was also measured by a four-point probe setup. The details of these characterisation methods, including measurement setups, were discussed in section 3.2 in Chapter 3.

4.4) Results and discussions

4.4.1) Morphological, structural and chemical characterisation of the MWCNTs

MWCNTs varying in length and diameter were successfully synthesised via AACVD by changing the synthesis time. The morphologies of carpet-like MWCNTs are shown in Figure 4.2 and Supporting Figures 4.1-4.2. MWCNTs synthesised at 15, 30, 45, and 60-min reaction times are denoted by MWCNT 15, MWCNT 30, MWCNT 45, and MWCNT 60, respectively. Increasing synthesis time is correlated with the production of longer MWCNTs. The diameter of the in-house MWCNTs (29-50 nm) was significantly larger than commercial MWCNTs (9-12 nm). The structure of MWCNTs was further characterised using TGA and Raman spectroscopy. As shown in Figure 4.2E, MWCNT 45 had the lowest amount of iron catalyst residue (3.4 wt.%) and high thermal stability (588 ^{o}C) compared to other types of MWCNTs. Residual iron catalysts in MWCNT samples could show adverse effects when utilised as a anode material, such as an additional capacity [25]; therefore it is desirable to have the residual iron content as low as possible. The Raman spectra of all MWCNT samples revealed the characteristic D (1350 cm^{-1}) and G (1580 cm^{-1}) peaks (Figure 4.1F). All in-house synthesised MWCNTs demonstrated similar ratios between the intensities of the D and G bands (I_D/I_G) as well as similar full width at half maximum (FWHM) of the G bands. As mentioned in Chapter 3, these two quantities are usually calculated to evaluate the graphitic quality of the carbon material produced [26]. Thus, the quality of the in-house MWCNTs was not significantly different. Nevertheless, the quality of in-house MWCNTs was much better compared to the commercial MWCNTs, which had an I_D/I_G ratio of 1.02 and 11 wt.% of Fe catalyst residue (Supporting Figure

4.3). Due to these results, the MWCNT 45 sample was selected for further study due to the low Fe catalyst content, which is more desirable for utilisation as a LIB electrode material.

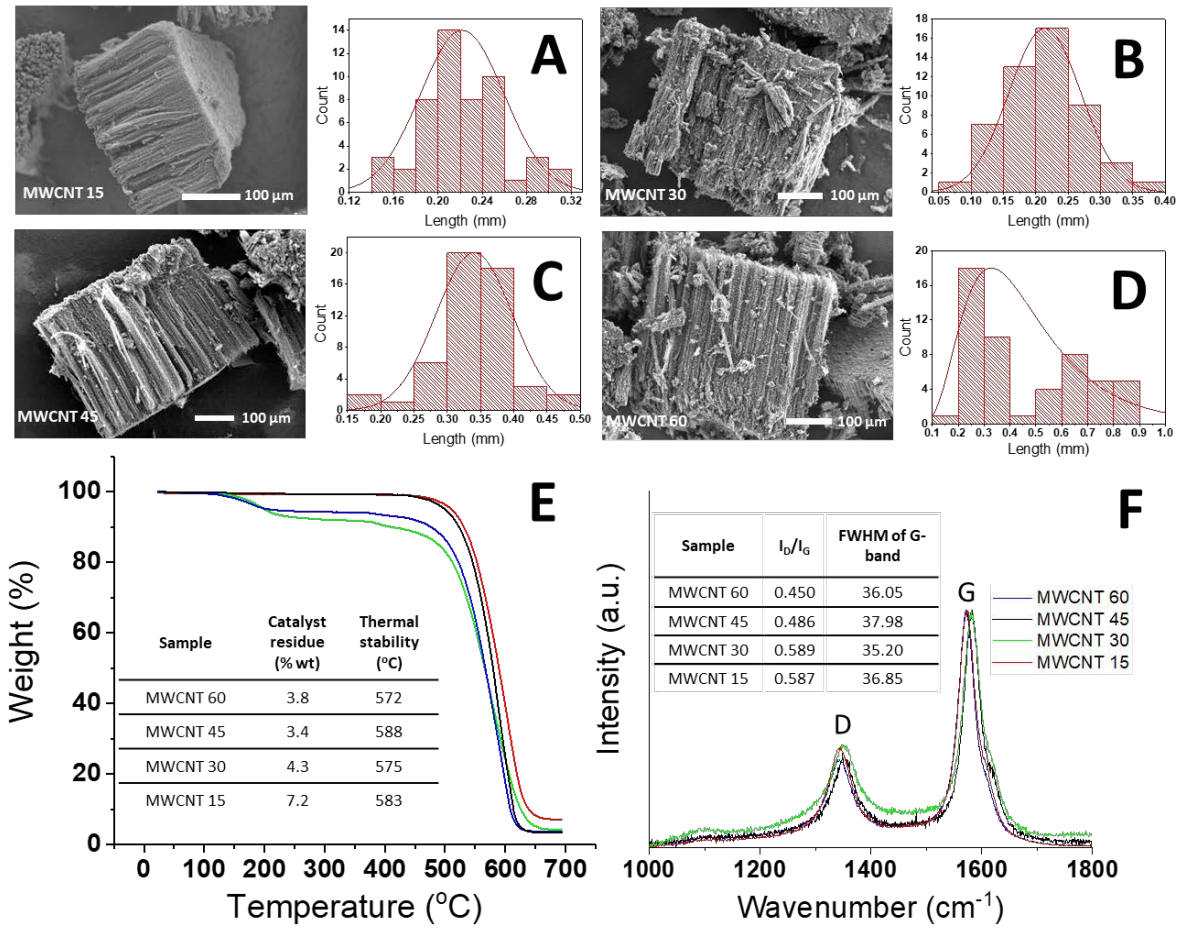


Figure 4.2. SEM images and length histogram of A) MWCNT 15, B) MWCNT 30, C) MWCNT 45, D) MWCNT 60 confirming a tendency to produce longer MWCNTs with longer synthesis time, E) thermal gravimetric graphs of the MWCNTs showing the decomposition of the MWCNTs after 590 °C under air atmosphere, and F) Raman spectra of the MWCNTs revealing the characteristic peaks (D and G bands) of the carbon material in the samples.

MWCNT 45 was firstly used as an electrode material in a coin-cell battery. MWCNT 45 were mixed with additives and casted on a copper foil before being cut into a disc. As a result, it is difficult to mix MWCNTs with binders and to disperse them in a solvent even when ultrasonication and ball-milling were used. This was attributed to the tube-tube interactions creating dense bundles of MWCNTs. This can cause inhomogeneous material coatings on the copper foils (Supporting Figure

4.4), leading to poor electrical conductivity throughout the electrodes. Therefore, this kind of electrode was not suitable to test the battery performance further.

4.4.2) Morphological, structural and chemical characterisation of the buckypapers

The issue of inhomogeneous MWCNT coatings mentioned above could be overcome using a BP as a free-standing electrode. BP 45, fabricated from MWCNT 45, had an oval shape with some rough edges (inset in Figure 4.3A). The BP 45 was 16 mm in diameter and around 125 microns thick. SEM images (Figure 4.3) reveal the homogeneous surface of the BP with small pores (average Feret diameter of *ca.* 69.5 nm, Supporting Figure 4.5) between entangled MWCNTs. Since the radii of Li^+ and solvated Li^+ are 0.078 [27] and 0.26 nm [28] respectively, the BP thereby facilitated electrolyte and Li ion penetration. Also, the bulk density of the BP 45 was *ca.* 0.2 g/cm^3, which was less than the true density of the MWCNTs (2.1 g/cm^3). The porosity of the BP was then calculated to be 90.5%. The high porosity of the electrode could enhance the capacity retention as pores or channels provide a space for volume expansion of the material upon charging [29, 30]. Therefore, the high porosity of the BP could alleviate stress of the electrode during lithiation, leading to an improvement of the battery stability.

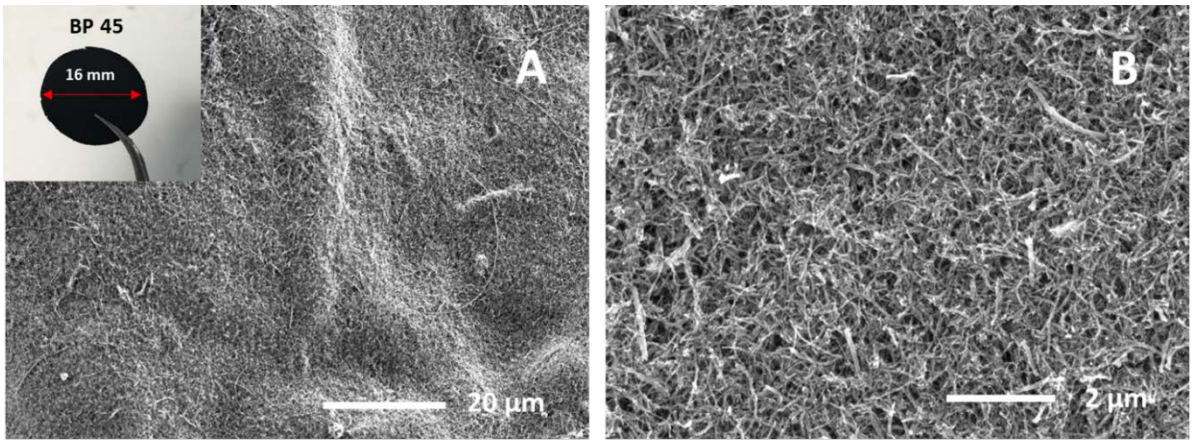


Figure 4.3. A) SEM image and inset photograph showing a flat surface and a free-standing feature of BP 45, and B) SEM image at high magnification revealing the smooth surface of BP 45 with small pores of the entangled MWCNTs.

In addition, TEM showed that the preparation of BP 45 did not damage the MWCNT structure and did not create defects on MWCNT walls (Supporting Figure 4.6A). As presented in the EDX maps and spectra (Supporting Figure 4.6B-C), the BP 45 consisted of mostly carbon with a small trace of iron catalysts. However, these catalysts were believed to be trapped in the MWCNTs, which would not strongly affect the performance of MWCNT papers when used as an anode in LIBs.

The electrical conductivity of the BP 45 was determined via a four-point-probe instrument. The general bulk electrical conductivity of the BP 45 was 22.22 S/cm. Furthermore, commercial MWCNTs were used to fabricate buckypapers (C-BP). The conductivity of the BP 45 made from in-house MWCNTs was 27% higher than that of the BP made from commercial MWCNTs indicating good quality of the in-house MWCNTs. Compared to other free-standing materials such as carbon film, graphite and graphene papers (Table 4.1), the BPs in this work reveal superior electrical conductivity. The BPs also had a higher electrical conductivity than the minimum electrode conductivity (0.01 S/cm [2]) for attaining fast-rate cycling, thus confirming suitability as an electrode material.

Table 4.1. The electrical conductivity of the materials confirming outstanding electrical conductivity of BPs compared to other materials.

Materials	Electrical conductivity (S/cm)	References
Carbon film	1	[31]
Graphite paper	12	[32]
Graphene oxide paper	8.5×10^{-4}	[33]
Highly reduced graphene oxide paper	1.7	[33]
Carbon black paper	0.9	[32]
Graphene paper	14	[32]
BP from in-house MWCNT 45) (BP 45)	**22.22**	**This work**
BP from the commercial MWCNTs (C-BP)	**16.02**	**This work**
Buckypapers	54-23	[12]
Commercial MWCNTs	10^4-10^6	commercial specification
Copper foil	6.25×10^2	commercial specification

Figure 4.4 shows the degree of flexibility of the BP 45 and C-BP samples. The BPs were flexible enough to withstand mechanical manipulation. The C-BP could be bent over 180 degrees due to small diameter and thin walls of the commercial MWCNT (9-12 nm of diameter, Supporting Figure 4.3) resulting in low stiffness and Young's modulus of the material (as discussed in the introduction). However, BP 45 could be bent around 160 degrees without cracking due to the high stiffness of larger and thick MWCNTs. Therefore, these BPs were suitable to be used as free-standing electrodes in LIBs without the presence of the metal foils as current collectors.

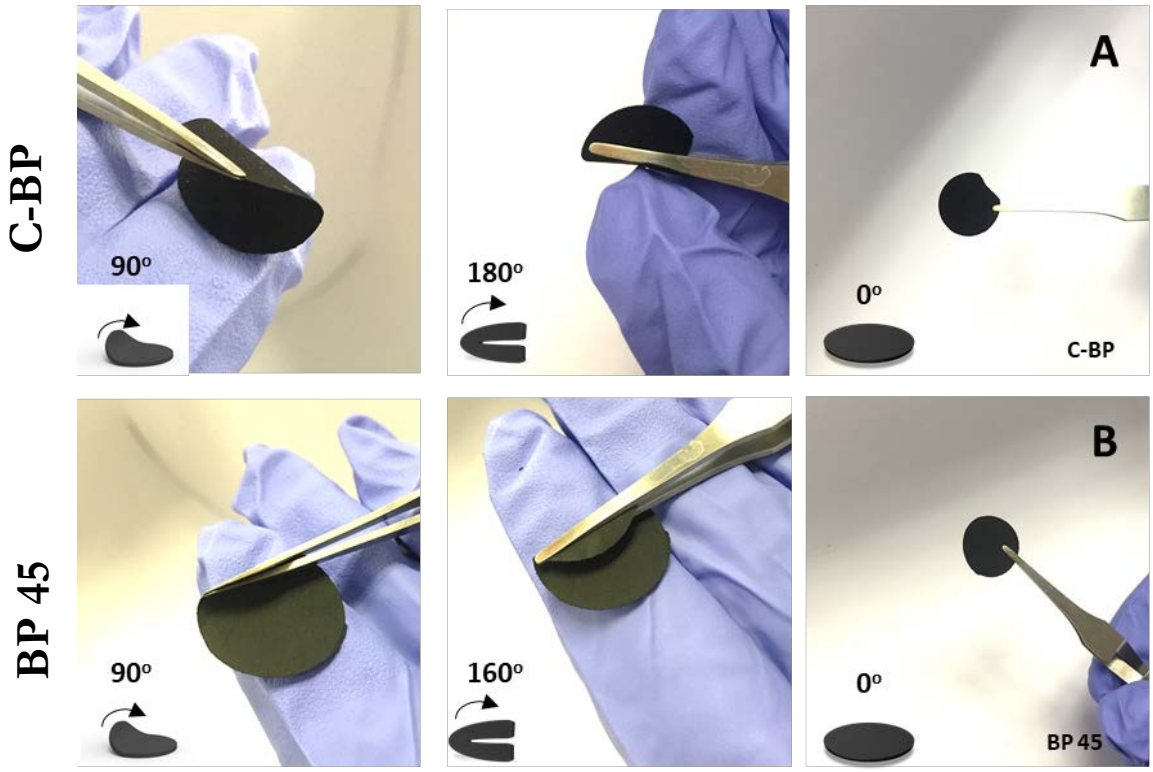


Figure 4.4. Photographs of A) C-BP and B) BP 45 showing the flexibility of both types of BPs; the C-BP could be bent to 180 degree while the BP 45 could be bend to 160 degrees.

4.4.3) Cell fabrication and electrochemical tests of the buckypaper electrodes

The BP 45 was tested as a working electrode in coin-cell batteries. The battery cycling performance of the BP 45 anode at C/5 rate is shown in Figure 4.5A. BP 45 exhibited an initial discharge capacity of 0.84 mAh/cm^2 (specific capacity of 297 mAh/g, volumetric capacity of 70 mAh/cm^3) and an initial charge capacity of 0.31 mAh/cm^2 (110 mAh/g, 25.83 mAh/cm^3, specific and volumetric capacities respectively). The coulombic efficiency in the first cycle was around 36.97% due to a large irreversible capacity from SEI layer formation. It was expected that the SEI layer was formed both on the surface and inside the pores of the material because of the high porosity of BP 45. The areal capacity was stable at around 0.30 mAh/cm^2 (106 mAh/g, 25 mAh/cm^3) with 99% of coulombic efficiency after 300 cycles.

Also, the discharge-charge characteristics of the BP 45 electrode are presented in Figure 4.5B. Two voltage plateaus were observed in the 1st cycle. The higher plateau at about 0.7 V was attributed

to the SEI formation [34], while the lower plateau from 0.25-0 V was assigned to the Li-ion insertion into the carbon material [35]. The dQ/dV profiles of the electrode are shown in Figure 4.5C. Both peaks at *ca.* 0.62 and 0.54 V resulted from the SEI layer formation on the surface and inside MWCNTs because of Li insertion into MWCNTs [36, 37]. Moreover, the sharp oxidation peak at 0.25 V and the reduction peak at 0.01 V corresponded with the Li-ion insertion and de-insertion from the graphitic materials, respectively [7]. The rate capability of BP 45 as a function of C-rate from C/10 to C was also tested (Figure 4.5D). The areal discharge capacities of the BP 45 were *ca.* 0.53, 0.41, 0.28 and 0.20 mAh/cm^2 at C/10, C/5, C/2 and C, respectively. As a result, the BP 45 still exhibited a good capacity even at a high C-rate. Besides, when the C-rate decreased back to C/10, the capacity increased to 0.47 $mAh/cm^{2,}$ which suggests a high degree of reversibility of the BP electrode.

As explained before, the length, diameter, and defects affect the performance of the MWCNT paper anode materials. To test this, BPs made from different types of MWCNTs, including C-BP and BP 45 were applied directly as electrodes in coin-cell battery performance tests. These BP samples were described as BP 15, BP 30 and BP 60 due to the corresponding MWCNTs the BPs were fabricated from. The results of the cycling performance are shown in Supporting Figure 4.7 and summarised in Supporting Table 4.1. Interestingly, the C-BP exhibited the highest irreversible capacity in the 1^{st} cycle (*ca.* 1400 mAh/g) due to the tendency of the C-BP to shed graphene layers during the lithium insertion because of the thin walls of the commercial MWCNTs [38]. According to these results, the BP 60 stored more Li-ions than other BP types since MWCNT 60 has larger and longer channels for Li to insert and for electrolyte molecules to access through open-ends [39]. However, the capacity of BP 60 decreased slightly during cycling. Therefore, Li ions are hardly extracted from the BP 60 electrode due to limited Li-ion diffusion from the nanotubes and high charge transfer resistance. That means the Li ions could penetrate into MWCNTs but had difficulty exiting upon increasing the MWCNTs length [40, 41].

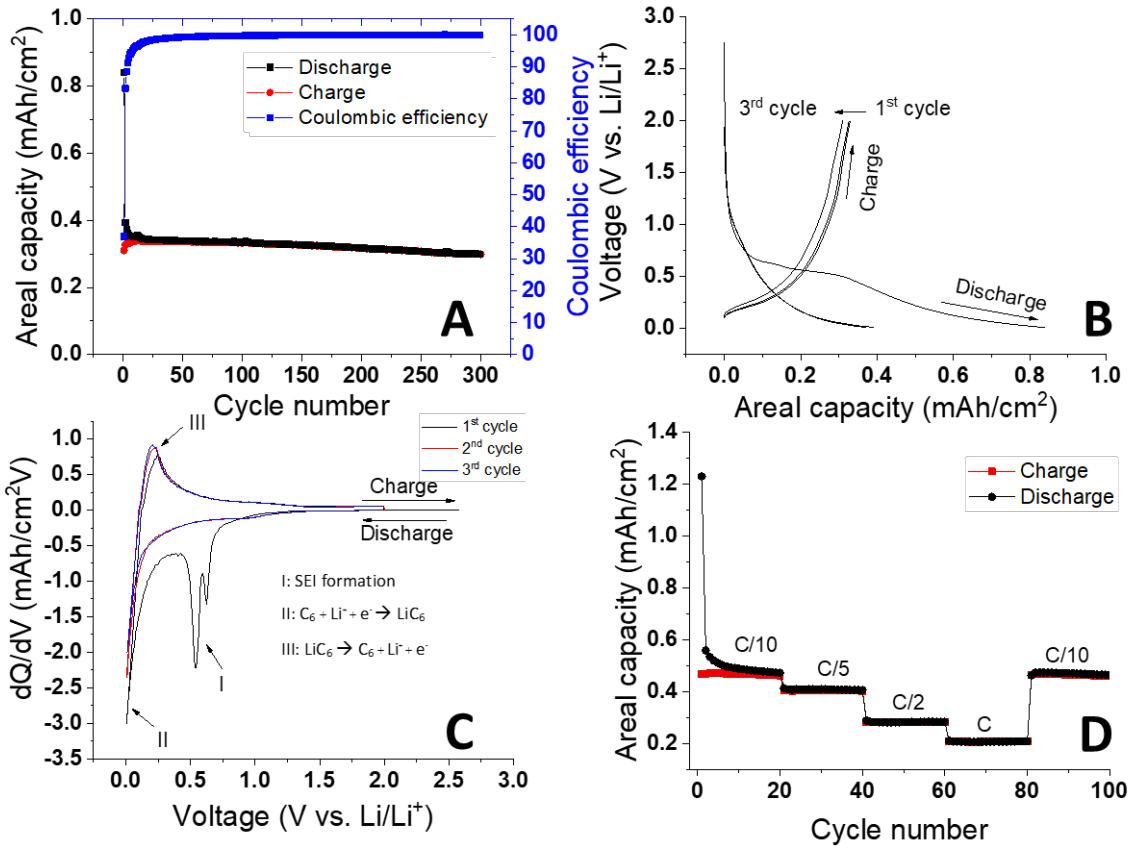


Figure 4.5. A) The charge-discharge graph of the BP revealing the areal capacity of 0.3 mAh/cm² after 300 cycles at C/5 rate, B) the voltage profiles of the BP showing high irreversible capacity of the electrode in the 1st cycle, C) the dQ/dV charts showing the Li-ion storage mechanism of the BP electrode, and D) the rate capability plot of the BP electrode showing the good battery performance of the BP electrode at different C-rate testing.

4.4.4) The battery design and the effect of the cell component study

Pouch cells were fabricated using BP 45 as an electrode to study the effect of cell fabrication. This type of cell design removes the effect of stainless-steel components to confirm the performance of the BP 45. The result showed that the BP 45 had a good performance with an areal capacity of 0.27 mAh/cm^2 at the 1st discharge, which slightly increased and stabilised at around 0.28 mAh/cm^2 after 300 cycles (Figure 4.6). The capacity of the BP 45 in the coin-cell battery was 0.31 and 0.30 mAh/cm^2 at the 1st and 300th cycle, respectively. This confirmed that the stainless-steel part of coin-cell batteries inevitably influenced the overall capacity of the electrode. As the area of the steel case expected to be in contact with the electrolyte is about 2.00 cm^2, this could lead to a reaction between an iron oxide layer on the stainless-steel component and the electrolyte and finally contribute an additional capacity

to the electrodes. Hence, it strongly suggested that the cell capability was attributed to the conductive BP 45 instead of other components in the coin cells since the areal capacity of the electrodes in coin-cell and pouch-cell batteries was similar.

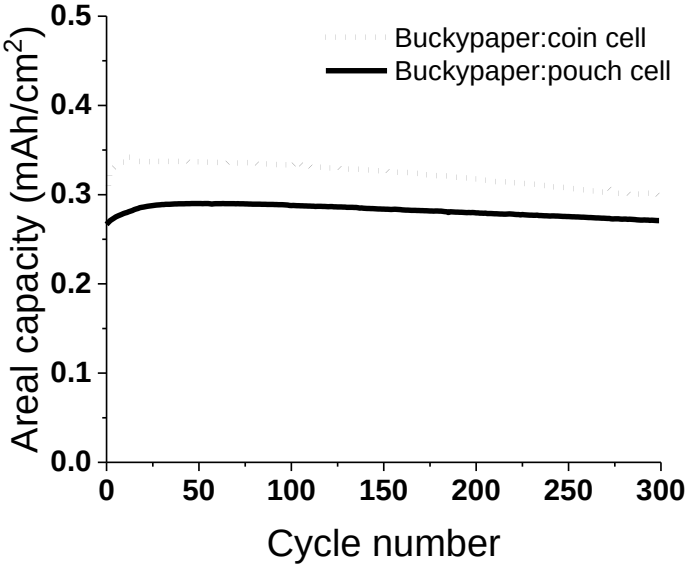


Figure 4.6. The battery performance of the BPs electrode in the coin cell and pouch cell battery configurations confirming that the capacity is mostly attributed from the BP electrode instead of the cell components.

4.4.5) Post-cycling analysis of the BP electrode

The tested coin-cell battery was disassembled post-cycling to study the morphology of the BP 45 electrode. The SEM images of the BP 45 before and after cycling are shown in Figure 4.7. The BP 45 still maintained its structure and morphology after testing. In addition, the SEI layer can be observed on the surface of the electrode even after it was washed with DMC to remove some salts as confirmed by EDX shown in Supporting Figure 4.8. Finally, it implied that BP 45 had high mechanical stability, making it suitable for a free-standing electrode in the LIBs.

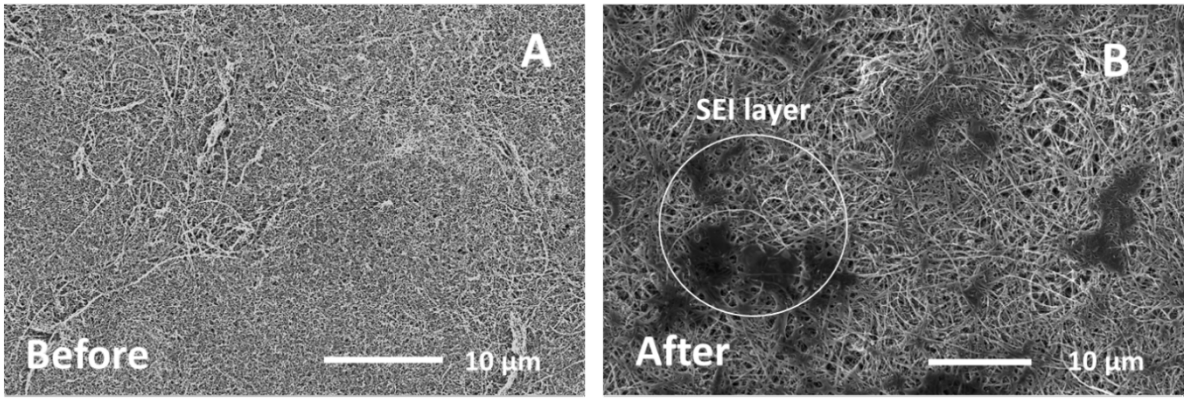


Figure 4.7. SEM images of the BP A) before and B) after battery testing showing its surface without structural change.

To conclude, the electrical and mechanical stability of the fabricated BP 45 were outstanding with regards to their use as a free-standing electrode. However, the capacity of BPs fabricated in this work is relatively low (*ca.* 290-100 mAh/g) compared to commercially available graphite (372 mAh/g). Thus, BPs should be applied as a free-standing electrode to support other active materials which have high theoretical capacity alternatively. To this end, it was decided to introduce Si to the MWCNTs in order to enhance the battery performance.

4.4.6) Morphological, structural, and chemical characterisation of free-standing Si-CNT electrodes

Silicon was successfully coated on BP 45 using APCVD in order to improve the battery capability of the pure BP; a schematic diagram of the targeted Si-CNT structure is illustrated in Figure 4.8A. According to a previous study, the spacing between Si NPs allows for volumetric expansion upon lithiation to form a Li-Si alloy. The space required for the unavoidable 400% volume change of the original Si NPs is approximately 1.6 times the NPs radius and can prevent nanoparticle pulverisation [24]. In addition, Damale *et al.* (2016) [42] reported a computational study of the effect of Si configurations in a silicon-carbon nanotube anode and investigated changes in mechanical integrity during electrochemical cycling. Compared to other structures such as Si film or Si coaxial coating on MWCNTs, Si NPs exhibited the lowest stress induced during cycling because they can

expand radially in all directions. As discussed in Chapter 2, accumulated stress in Si during repeated cycling could induce fractures in the electrode, thereby resulting in a significant capacity loss. Hence, the Si-CNT material which consisted of Si NPs coated on the MWCNT walls was believed to achieve the good battery performance when tested as a free-standing electrode in LIBs.

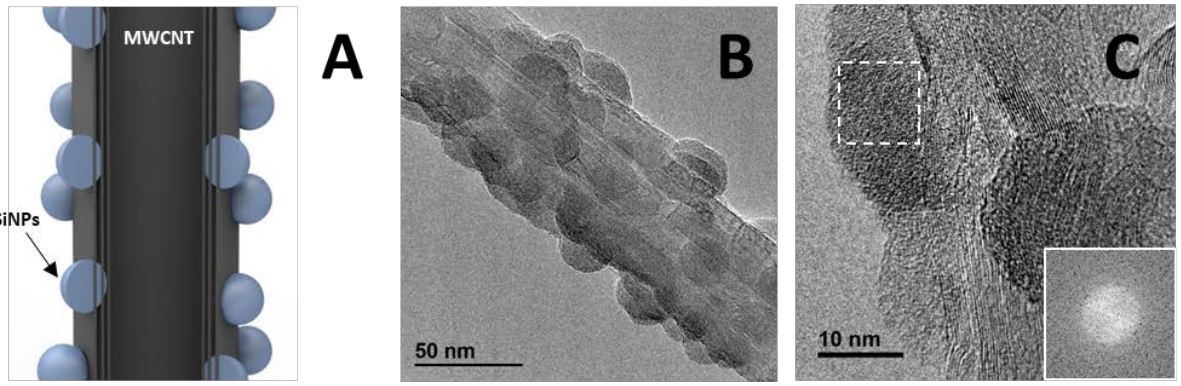


Figure 4.8. A) A schematic and B) TEM image of the Si-CNT material structure showing silicon nanoparticles coated on the surface of the carbon nanotubes, and C) TEM image and fast Fourier transformation of the selected image area revealing the diffuse rings of amorphous Si.

Figure 4.8B-C shows HRTEM images of the Si-CNT material. The Si NPs were uniformly distributed on MWCNTs since the MWCNTs provided a nucleation site for Si NPs growth [24]. The Si NPs, with an average size of 10-15 nm, had an amorphous structure which was confirmed by the absence of the lattice planes and the presence of diffuse rings in fast Fourier transform (FFT) of the selected image area (Figure 4.8C). The BP 45 functioned as an electrically conductive network for facilitating Li ion and electrolyte diffusion. Moreover, the diameter of the Si NPs was less than the critical size of amorphous Si (870 nm); thus, the NPs would not break or fracture during lithiation [24, 43]. SEM and EDX images also indicated the uniformity of the Si NPs on the BP 45 (Supporting Figure 4.9-4.10).

The chemical characterisation of the Si-CNT material was conducted by analysing different crystalline structures. Only the diffraction peak (002) of the carbon material at around 25.9-26° was observed by XRD (Figure 4.9). This plane diffraction of the hexagonal graphitic structure indicated

the existence of MWCNTs in the Si-CNT material [24, 44]. As a result, the deposited Si on the BP 45 was amorphous due to the absence of the Si peak, in agreement with TEM and FFT results.

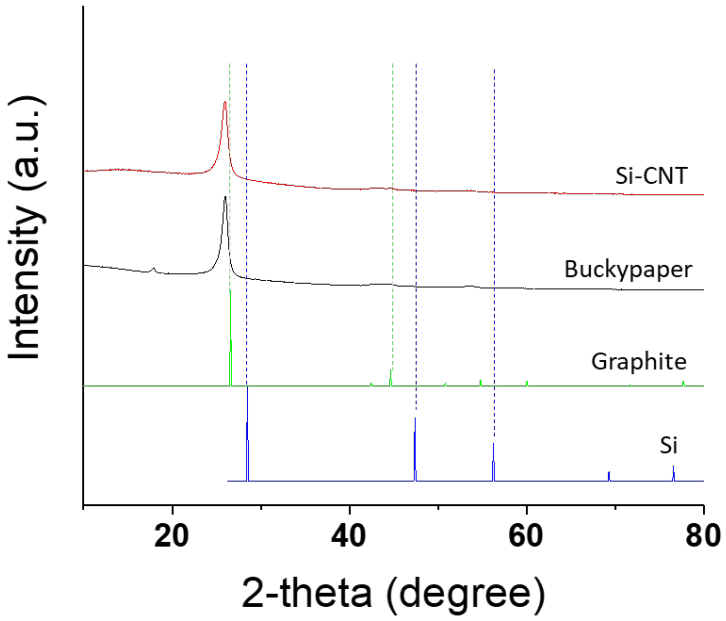


Figure 4.9. A) XRD patterns of Si-CNT and reference materials; an absence of Si peaks confirms an amorphous Si structure in the Si-CNT material.

Although the Si peak could not be found in the XRD pattern of Si-CNT material, a broad scan analysis of XPS showed major peaks that corresponded to carbon (C1s), oxygen (O1s), and silicon (Si2p) in the Si-CNT material (Figure 4.10A). The Si-CNT material presented Si doublet related peaks at 99.4 and 100.1 eV. However, the peak at 103.4 eV confirmed small traces of SiO_2 in the material which formed through sample preparation (Figure 4.10B) [45]. Two main peaks of the C1s band are also shown in the Si-CNT material at 284.6 and 285.8 eV, which could be assigned to C-C and C-O bonds in MWCNTs (Figure 4.10C) [46]. Additionally, the Raman spectra of Si-CNT clearly showed the presence of amorphous Si and MWCNTs in the material (Supporting Figure 4.11). According to the literature (Chapter 2), it was expected that the battery performance of the Si-CNT electrode will be improved compared to pure crystalline Si since the amorphous Si has less dramatic volume change than crystalline Si and MWCNTs would be able to act as a mechanical support to alleviate the stress induced from the volume expansion during cycling.

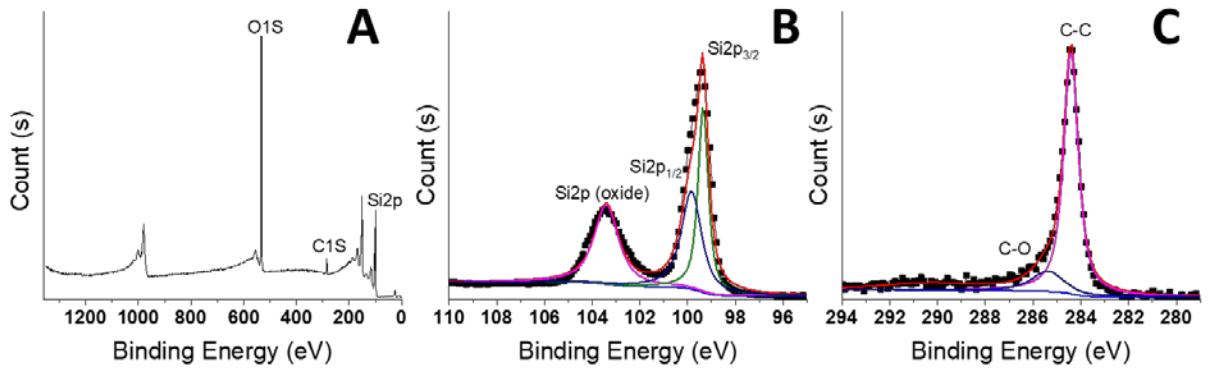


Figure 4.10. A) XPS survey spectrum, and high-resolution spectra of the Si-CNT material corresponding to B) Si2p and C) O1s confirming the Si structure in the Si-CNT material.

The electrical conductivity of the Si-CNT material was tested using the four-point probe instrument. In general, the conductivity of Si is $4x10^{-6}$ S/cm at room temperature, while conducting non-metallic materials such as carbon materials (graphite, MWCNTs or graphene) show high electrical conductivity, similar to metals [30, 47]. The electrical conductivity of the Si-CNT material was 15.5 S/cm (Table 4.2). As a result, MWCNTs within BP 45 significantly improved the electrical conductivity of Si. Conversely, conventional Si electrodes (consisting of Si NPs mixed with binder and carbon additives) show an electrical conductivity of 10^{-1}-10^{-5} S/cm. Therefore, MWCNTs provide a conductive network modifying the overall conductivity of Si electrodes. The conductivity enhancement allowed rapid charge transportation and thus confirmed practical suitability of a free-standing Si-CNT anode in LIBs.

Table 4. 2. The electrical conductivity of BP 45 and Si-CNT material revealing good conductivity of the free-standing Si-CNT materials compared to conventional Si electrodes.

Sample	Electrical conductivity (S/cm)	Reference
BP 45	**22.22**	**This work**
Si-CNT	**15.50**	**This work**
Conventional Si nanopowder electrode	$1.4x10^{-3}$	[48]
Si and C coated VACNTs	0.33	[48]
Pure Si	$4x10^{-6}$	[49]

4.4.7) Cell fabrication and electrochemical tests of the free-standing Si-CNT electrodes

The Si-CNT electrode was assembled into coin-cell batteries using Li foil as a counter electrode. The cycle performance of the Si-CNT based on the C/5 rate is shown in Figure 4.11A. The Si-CNT anode demonstrated the charge and discharge capacities of the first cycle around 7.10 mAh/cm^2 (specific capacity of 3758 mAh/g, volumetric capacity of 355 mAh/cm^3) and 5.93 mAh/cm^2 (3139 mAh/g, 297 mAh/cm^3) respectively with 83.5% coulombic efficiency. The irreversible capacity of the first cycle was attributed to the SEI formation. Irreversible lithium oxide and lithium silicates were also formed in the first cycle due to the presence of SiO_2 on the unprotected material surface during preparation [50]. However, the areal capacity significantly decreased in the subsequent cycles, reducing to only 0.09 mAh/cm^2 (49 mAh/g, 5 mAh/cm^3) at the 300^{th} cycle. This significant capacity drop was due to the formation of unstable SEI layers caused by repeated volume changes during cycling. The SEI layer formation increased the internal impedance and decreased the electrochemical reactivity because of the accumulation of insulating SEI substances [51]. Additionally, the weak interaction between MWCNTs and Si NPs lead to the disconnection of the Si from MWCNTs, resulting in a loss of available active mass and a dramatic decrease in capacity [24]. Due to the poor battery performance of the Si-CNT, cracks and structural change were expected to occur in the electrode. Therefore, a post-cycling test was necessary to confirm structural changes had occurred. Nevertheless, when compared to the pure Si electrode made from the conventional method, the Si-CNT electrode revealed better capacity retention indicating a small improvement by combining the Si NPs with MWCNTs (Supporting Figure 4.12). The enhancement was attributed to the function of MWCNTs in terms of mitigating the strain caused by the volume expansion of Si during the battery testing.

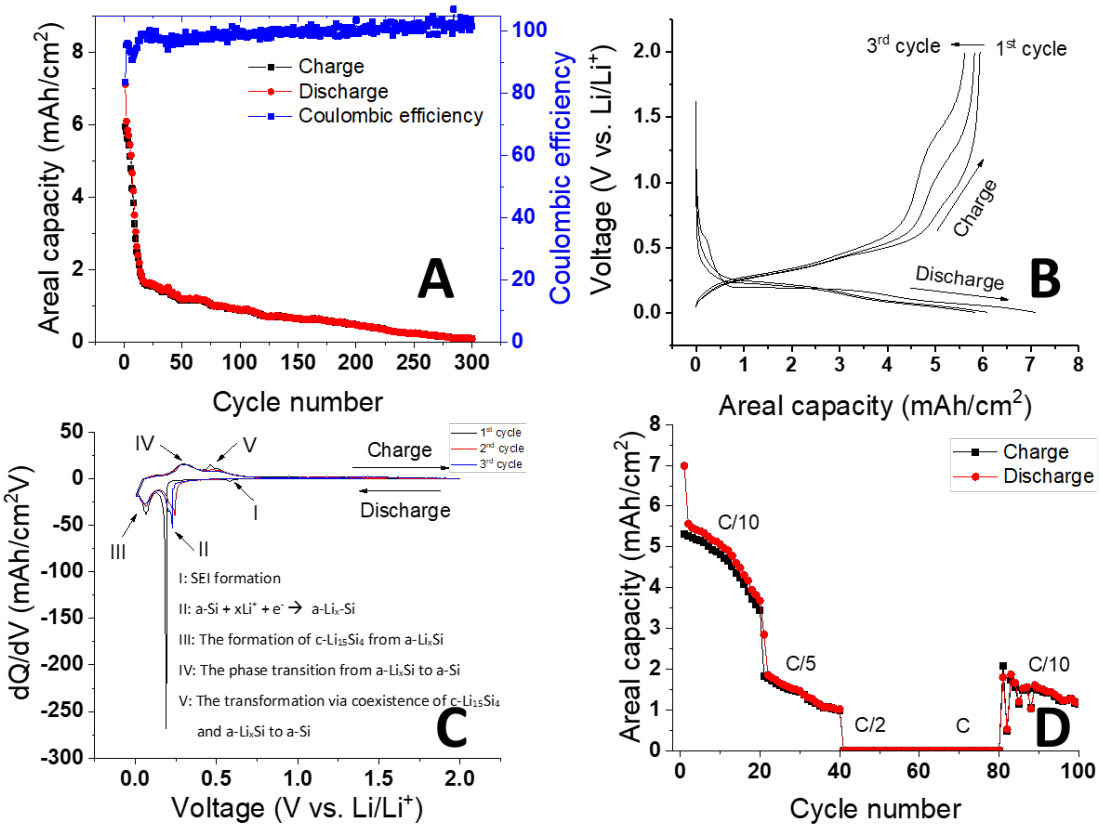


Figure 4.11. A) The charge-discharge graph of Si-CNT electrode showing the areal capacity of 0.09 mAh/cm² after 300 cycles at C/5 rate, B) the voltage profiles of the Si-CNT electrode confirmed the two-phase lithiation of crystalline Si, C) the differential areal capacity plot of the Si-CNT electrode presenting the Li-ion storage mechanism of the electrode, D) the rate capability graph of the Si-CNT electrode revealing poor battery performance of the Si-CNT electrode at faster-charging rates.

The voltage profile of the Si-CNT is shown in Figure 4.11B. The first discharge graph revealed a significant drop in the potential with two observed plateaus. The first plateau at *ca.* 0.6 V vs Li/Li^+ was attributed to the SEI formation while the plateau at *ca.* 0.2 V corresponded to the two-phase lithiation of the amorphous Si [52, 53]. Also, the charge curve showed an incremental change at *ca.* 0.3 and 0.5 V vs Li/Li^+, which was associated with the delithiation of amorphous Li_xSi to amorphous Si [52, 54]. In subsequent cycles, the plateau characteristics from the first cycles were not observed, indicating a single-phase reaction in the amorphous Si [54, 55]. In addition, a differential capacity plot of the Si-CNT electrode, shown in Figure 4.11C, was undertaken to study the lithiation and delithiation reactions within the electrode. In the first cycle, a small cathodic peak at about 0.6 V indicated SEI formation on the electrode surface [56]. The peak at 0.2 V was assigned to the long plateau in Figure

4.11B, which was considered as a two-phase region. These two phases corresponded to the metastable Li-Si formation of unlithiated amorphous silicon (a-Si) and partially lithiated silicon (Li_xSi) (discussed in Chapter 2). The two-phase reaction continued until the voltage reached 0.1 V, where the complete lithiation of amorphous Si yielded amorphous Li_xSi [24, 57]. The small peak at 0.07 V represented the formation of crystalline $Li_{15}Si_4$ from amorphous Li_xSi [58, 59]. Moreover, two oxidation peaks were shown at 0.3 V and 0.5 V corresponding to the phase transition between amorphous Li_xSi and amorphous Si by dealloying of Li [57, 59, 60]. During the 2nd cycle, the reduction peak shifted to the higher voltage of *ca.* 0.22 V, which was attributed to reactivity improvement of the electrode after the 1st cycle [57, 60]. This peak shift indicated a lower energy barrier for a single-phase reaction [61]. Finally, the curves of the delithiation reaction completely overlapped, confirming the absence of any additional reactions [57].

The rate capability of the Si-CNT electrode is presented in Figure 4.11D. The cells were tested at a C-rate of C/10 for 20 cycles. The cycling rate was raised continuously to C/5, C/2, C and finally returned to C/10. The first charge and discharge capacities of the Si-CNT electrode at the C/10 rate were 5.31 and 6.99 mAh/cm^2, respectively. At the C/5 rate of cycling, the average areal capacity was about 1.5 mAh/cm^2. However, at higher C-rates, the cells could not store Li ions exhibiting an areal capacity of 0.01 mAh/cm^2. When decreasing the C-rate back to C/10, the areal capacity of the Si-CNT electrode increased back to 1.8 mAh/cm^2. The unsatisfactory rate performance of the Si-CNT can be explained by induction of charging-rate-dependent stress in the electrode; the faster charging rate leads to higher stress and more crack nucleation to occur [62]. Thus, fracture may take place at the fast charging rate causing loss of active material. Also, the rate capability of the electrode is poor due to a thick SEI layer formation on the electrode. As the volume change of the Si could not be tackled in the Si-CNT electrode, the SEI layer continuously formed, increasing a Li diffusion pathway which finally reduced the rate capability of the electrode [63].

4.4.8) Post-cycling analysis of the free-standing Si-CNT electrode

To clearly explain the poor battery performance of the Si-CNT electrode, the morphological change of the electrode after battery cycling was studied using SEM, EDX, and TEM. The post-cycling SEM images after 300 cycles are shown in Figure 4.12. The alteration of the Si-CNT electrode was observed. The sample surface became a rough solid film which was caused by the repeated deposition of SEI layers during the cycling test [64]. Cracks and fractures also developed on the surface of the electrode (Figure 4.12B), thus clarifying the capacity fade and failure of cells after 300 cycles. However, the nanostructure of the material was not visible. The elemental composition of the SEI layer on the electrode surface was confirmed by EDX images (Supporting Figure 4.13). Therefore, an additional washing step, washing in dimethyl carbonate (DMC), was needed before characterisation to remove the SEI layer. DMC can dissolve an outer organic layer of SEI and leave a thin inorganic layer on the material surface [65].

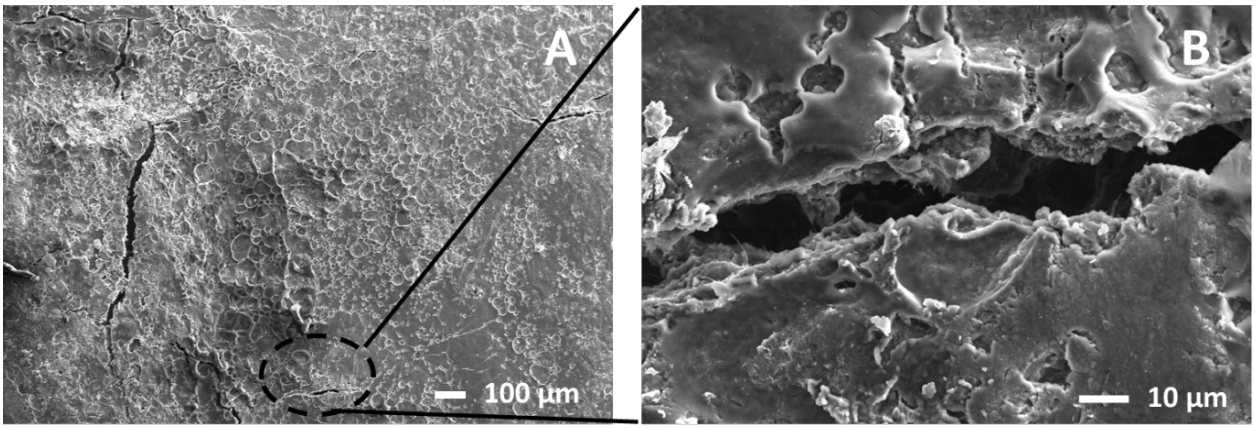


Figure 4.12. Post-cycling SEM images of the Si-CNT electrode at A) low and B) high magnification showing cracking observed on the Si-CNT electrode surface after battery testing.

In addition, structural changes in the Si-CNT material were confirmed by TEM. It can be clearly seen that the Si-CNT material altered its previous configuration after the cycling test, and only the structure of the MWCNTs could be preserved (Figure 4.13). Rough and irregular features of Si, instead of nanoparticles, were coated on the MWCNTs. Some Si NPs also detached from the MWCNTs; inferred by spherical voids found on the MWCNT surface. The post-cycling morphology was thereby consistent with the poor battery performance of Si-CNT electrode.

Moreover, the uneven MWCNT surface was assigned to the SEI layer if the electrode was not completely washed with DMC before the characterisation.

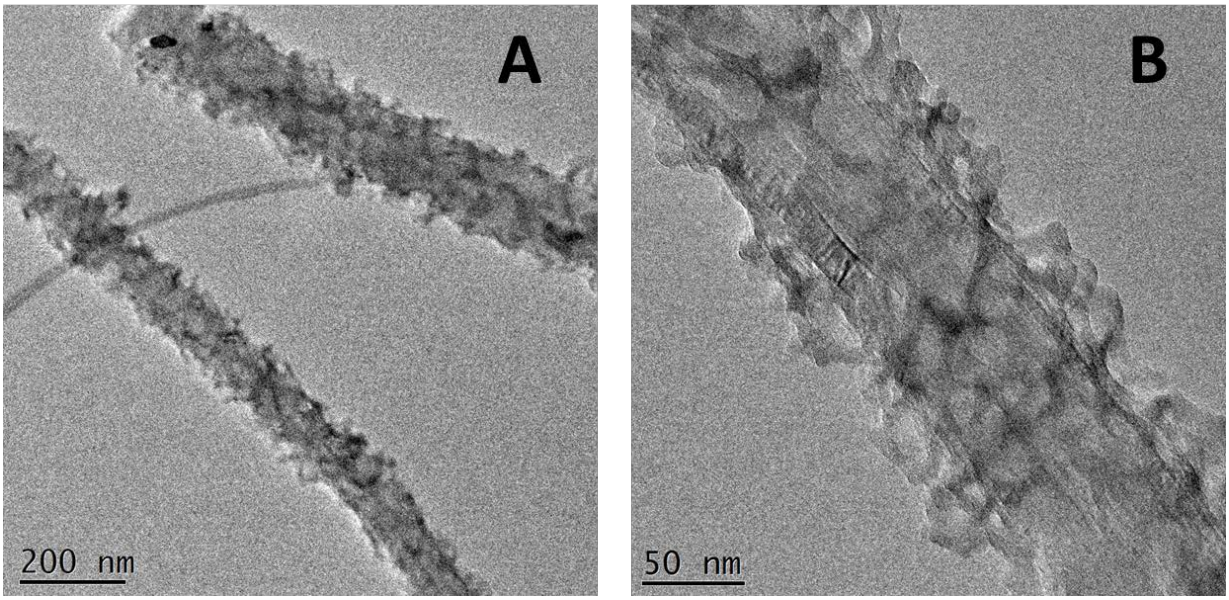


Figure 4.13. Post-cycling TEM images of the Si-CNT electrode at A) low and B) high magnification; a significant change of the Si structure can be observed after cycling.

When comparing the Si-CNT electrode with BP 45 and the pure Si electrode, the stability of the Si-CNT electrode was inferior although the areal capacity of the Si-CNT electrode was higher than others (Figure 4.14A-B). According to the electrochemical and post-cycling results, the Si NP growth on the MWCNT walls was not enough to both enhance the battery performance and address the Si stability problem. MWCNTs could not sufficiently accommodate the stress building up in the Si NPs due to the associated volume expansion. The crack formation and the detachment of Si NPs occurred in the material, thus resulted in the dramatic capacity loss of the Si-CNT electrode.

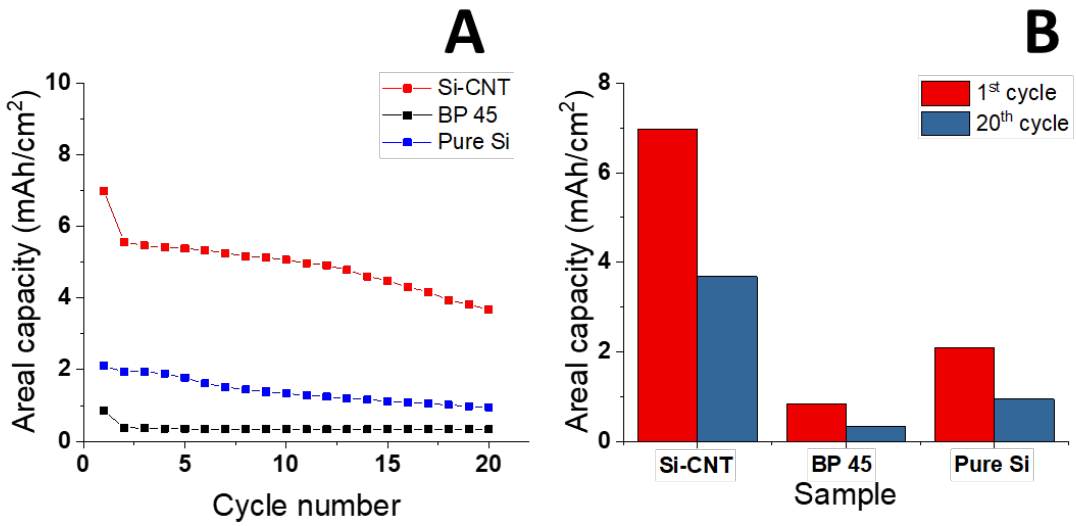


Figure 4.14. A) The areal capacity of Si-CNT, BP 45 and pure Si electrodes tested at C/10 rate confirming the higher areal capacity of Si-CNT electrode compared to others and B) a bar chart showing the areal capacity of all materials at 1st cycle and 20th cycle; the areal capacity of Si-CNT electrode was the highest indicating that this electrode is promising to study further for improving the stability of the electrode.

4.5) Conclusions

BPs were fabricated using MWCNTs which were synthesised by varying the AACVD synthesis time. After characterisation, BP 45 fabricated from MWCNT 45 was selected for further study due to MWCNT 45 having the least amount of catalyst residue present (3.4 wt.%) and being of good quality relative to other synthesised MWCNT samples. C-BP was also fabricated from commercial MWCNTs in order to compare the performance of the BP made from in-house MWCNTs. The electrical conductivity of BP 45 was 27% higher than that of C-BP. Therefore, it indicated that in-house MWCNTs have better quality than the commercially available MWCNTs. The battery performance tests showed that BP 45 had a higher capacity (0.3 mAh/cm^2) than C-BP (0.18 mAh/cm^2) after 300 cycles. However, the capacity of pure BP (around 290-100 mAh/g) described in this chapter was relatively low compared to commercially available anode materials, *i.e.* graphite (372 mAh/g).

Due to the low capacity of BP 45, amorphous Si NPs were deposited on the outer walls of the MWCNTs within BP 45 in order to improve the battery performance. The Si-CNT electrode revealed

an areal capacity of 7.10 mAh/cm^2 for the 1st cycle. In comparison to BP 45, the Si-CNT material showed poorer stability (0.09 mAh/cm^2 after 300 cycles) as well as low rate capability. After cycling, cracking was found on the Si-CNT electrode, while no fracture could be observed on BP 45. Moreover, the Si structure in the Si-CNT material was severely damaged, and the Si NP was detached from the MWCNT surface according to TEM examination.

To conclude, MWCNTs in the Si-CNT material were not sufficient to accommodate the volume change of the Si NPs during the repeated cycling, causing crack formation in the electrode and poor battery performance. The Si NPs disconnected from the MWCNT walls due to the weak interface between the two materials, which led to a significant diminishing in capacity of the Si-CNT electrode. Although the Si-CNT electrode had a higher capacity than the BP 45 electrode, the capacity retention of this electrode needs improvement through developing the material structure design before utilisation as a commercial anode material. Hence, modification of the free-standing Si-CNT material, such as coating with carbon and developing a strong interfacial connection between Si and MWCNTs, was required to enhance the final battery performance in the next chapter.

4.6) References

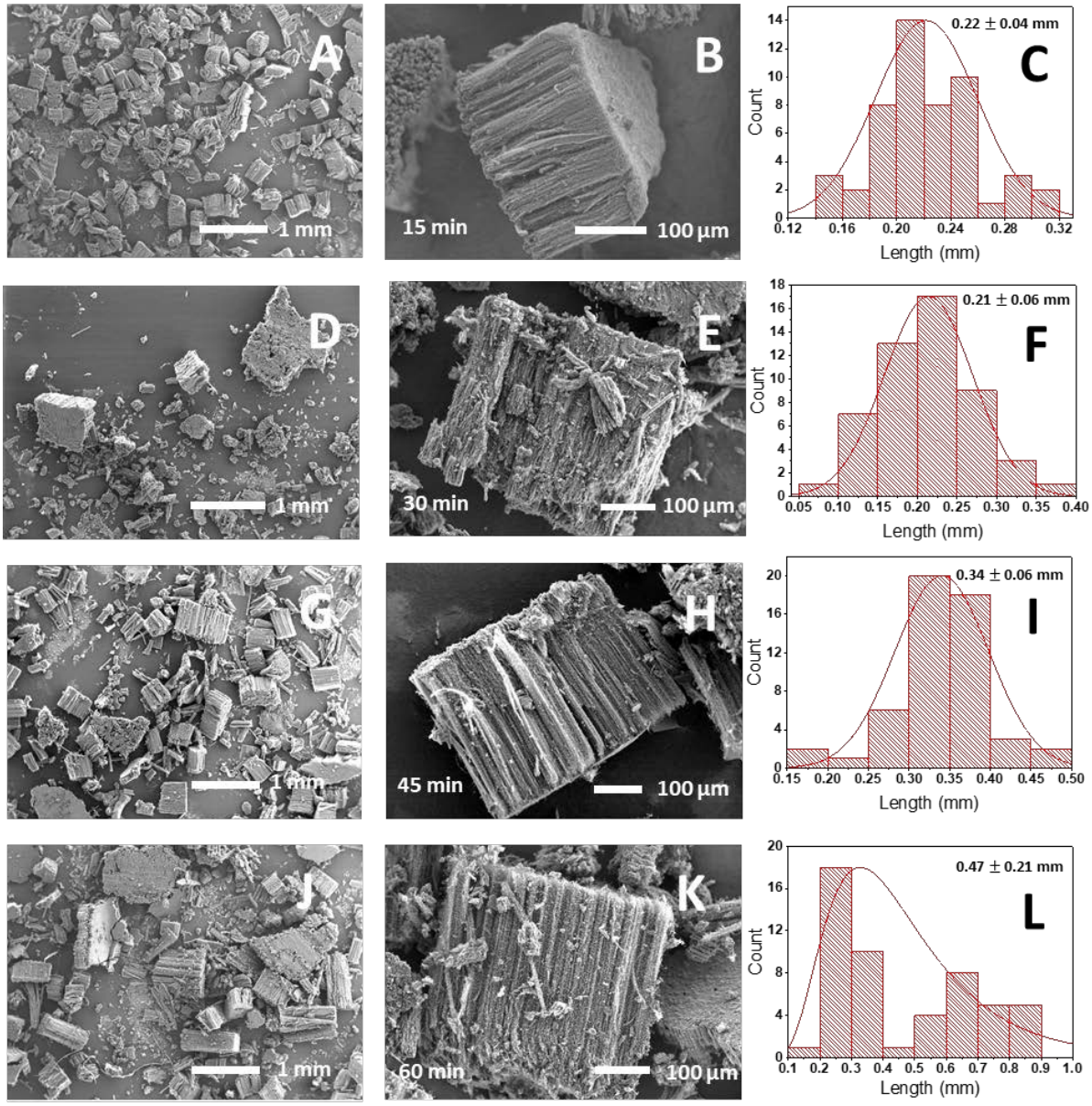
1. Li, X., et al., *Novel approach toward a binder-free and current collector-free anode configuration: highly flexible nanoporous carbon nanotube electrodes with strong mechanical strength harvesting improved lithium storage.* Journal of Materials Chemistry, 2012. **22**(36): p. 18847-18853.
2. Tian, R., et al., *Quantifying the Effect of Electronic Conductivity on the Rate Performance of Nanocomposite Battery Electrodes.* ACS Applied Energy Materials, 2020. **3**(3): p. 2966-2974.
3. Endo, M., et al., *'Buckypaper' from coaxial nanotubes.* Nature, 2005. **433**: p. 476.
4. Che, J., P. Chen, and M.B. Chan-Park, *High-strength carbon nanotube buckypaper composites as applied to free-standing electrodes for supercapacitors.* Journal of Materials Chemistry A, 2013. **1**(12): p. 4057-4066.
5. Arif, M.F., S. Kumar, and T. Shah, *Tunable morphology and its influence on electrical, thermal and mechanical properties of carbon nanostructure-buckypaper.* Materials & Design, 2016. **101**: p. 236-244.
6. Wen, G., H. Yu, and X. Huang, *Synthesis of carbon microtube buckypaper by a gas pressure enhanced chemical vapor deposition method.* Carbon, 2011. **49**(12): p. 4067-4069.
7. Chew, S.Y., et al., *Flexible free-standing carbon nanotube films for model lithium-ion batteries.* Carbon, 2009. **47**(13): p. 2976-2983.
8. Landi, B.J., et al., *Multi-Walled Carbon Nanotube Paper Anodes for Lithium Ion Batteries.* Journal of Nanoscience and Nanotechnology, 2009. **9**(6): p. 3406-3410.
9. Ma, P.-C., et al., *Dispersion and functionalization of carbon nanotubes for polymer-based nanocomposites: A review.* Composites Part A: Applied Science and Manufacturing, 2010. **41**(10): p. 1345-1367.

10. Loiseau, A., et al., *Understanding Carbon Nanotubes: From Basics to Applications*. 2006: Springer Berlin Heidelberg.
11. Kalamkarov, A.L., et al., *Analytical and numerical techniques to predict carbon nanotubes properties.* International Journal of Solids and Structures, 2006. **43**(22): p. 6832-6854.
12. Hu, Y., et al., *Comparative study of structure, mechanical and electromagnetic interference shielding properties of carbon nanotube buckypapers prepared by different dispersion media.* Materials & Design, 2019. **184**: p. 108175.
13. Zhang, L., et al., *High-Density Carbon Nanotube Buckypapers with Superior Transport and Mechanical Properties.* Nano Letters, 2012. **12**(9): p. 4848-4852.
14. Salvetat, J.-P., et al., *Elastic and Shear Moduli of Single-Walled Carbon Nanotube Ropes.* Physical Review Letters, 1999. **82**(5): p. 944-947.
15. Liu, X.H. and J.Y. Huang, *In situ TEM electrochemistry of anode materials in lithium ion batteries.* Energy & Environmental Science, 2011. **4**(10): p. 3844-3860.
16. Wen, C.J. and R.A. Huggins, *Chemical diffusion in intermediate phases in the lithium-silicon system.* Journal of Solid State Chemistry, 1981. **37**(3): p. 271-278.
17. Zhang, W.-J., *A review of the electrochemical performance of alloy anodes for lithium-ion batteries.* Journal of Power Sources, 2011. **196**(1): p. 13-24.
18. Chan, C.K., et al., *High-performance lithium battery anodes using silicon nanowires.* Nat Nano, 2008. **3**(1): p. 31-35.
19. Kasavajjula, U., C. Wang, and A.J. Appleby, *Nano- and bulk-silicon-based insertion anodes for lithium-ion secondary cells.* Journal of Power Sources, 2007. **163**(2): p. 1003-1039.
20. Beaulieu, L.Y., et al., *Colossal Reversible Volume Changes in Lithium Alloys.* Electrochemical and Solid-State Letters, 2001. **4**(9): p. A137-A140.
21. Chan, C.K., et al., *Surface chemistry and morphology of the solid electrolyte interphase on silicon nanowire lithium-ion battery anodes.* Journal of Power Sources, 2009. **189**(2): p. 1132-1140.
22. Oumellal, Y., et al., *The failure mechanism of nano-sized Si-based negative electrodes for lithium ion batteries.* Journal of Materials Chemistry, 2011. **21**(17): p. 6201-6208.
23. Park, J.-K., *Anode materials*, in *Principles and Applications of Lithium Secondary Batteries*. 2012, Wiley-VCH p. 380 pages.
24. Wang, W. and P.N. Kumta, *Nanostructured Hybrid Silicon/Carbon Nanotube Heterostructures: Reversible High-Capacity Lithium-Ion Anodes.* ACS Nano, 2010. **4**(4): p. 2233-2241.
25. Bhattacharya, P., et al., *Iron Oxide Nanoparticle-Encapsulated CNT Branches Grown on 3D Ozonated CNT Internetworks for Lithium-Ion Battery Anodes.* Advanced Functional Materials, 2018. **28**(29): p. 1801746.
26. Kaburagi, Y., A. Yoshida, and Y. Hishiyama, *Chapter 7 - Raman Spectroscopy*, in *Materials Science and Engineering of Carbon*, M. Inagaki and F. Kang, Editors. 2016, Butterworth-Heinemann. p. 125-152.
27. Kotz, J., P. Treichel, and J. Townsend, *Chemistry and Chemical Reactivity*. Available Titles OWL Series. 2008: Cengage Learning.
28. Skarmoutsos, I., et al., *Li+ Solvation in Pure, Binary, and Ternary Mixtures of Organic Carbonate Electrolytes.* The Journal of Physical Chemistry C, 2015. **119**(9): p. 4502-4515.
29. Deng, T. and X. Zhou, *The preparation of porous graphite and its application in lithium ion batteries as anode material.* Journal of Solid State Electrochemistry, 2016. **20**(10): p. 2613-2618.
30. Chae, S., et al., *Confronting Issues of the Practical Implementation of Si Anode in High-Energy Lithium-Ion Batteries.* Joule, 2017. **1**(1): p. 47-60.
31. Kupperman, D.S., C.K. Chau, and H. Weinstock, *Electrical resistivity of carbon films.* Carbon, 1973. **11**(3): p. 171-175.
32. Marinho, B., et al., *Electrical conductivity of compacts of graphene, multi-wall carbon nanotubes, carbon black, and graphite powder.* Powder Technology, 2012. **221**: p. 351-358.
33. Vallés, C., et al., *Flexible conductive graphene paper obtained by direct and gentle annealing of graphene oxide paper.* Carbon, 2012. **50**(3): p. 835-844.
34. Fong, R., U. von Sacken, and J.R. Dahn, *Studies of Lithium Intercalation into Carbons Using Nonaqueous Electrochemical Cells.* Journal of The Electrochemical Society, 1990. **137**(7): p. 2009-2013.
35. Yuqin, C., et al., *Irreversible capacity loss of graphite electrode in lithium-ion batteries.* Journal of Power Sources, 1997. **68**(2): p. 187-190.

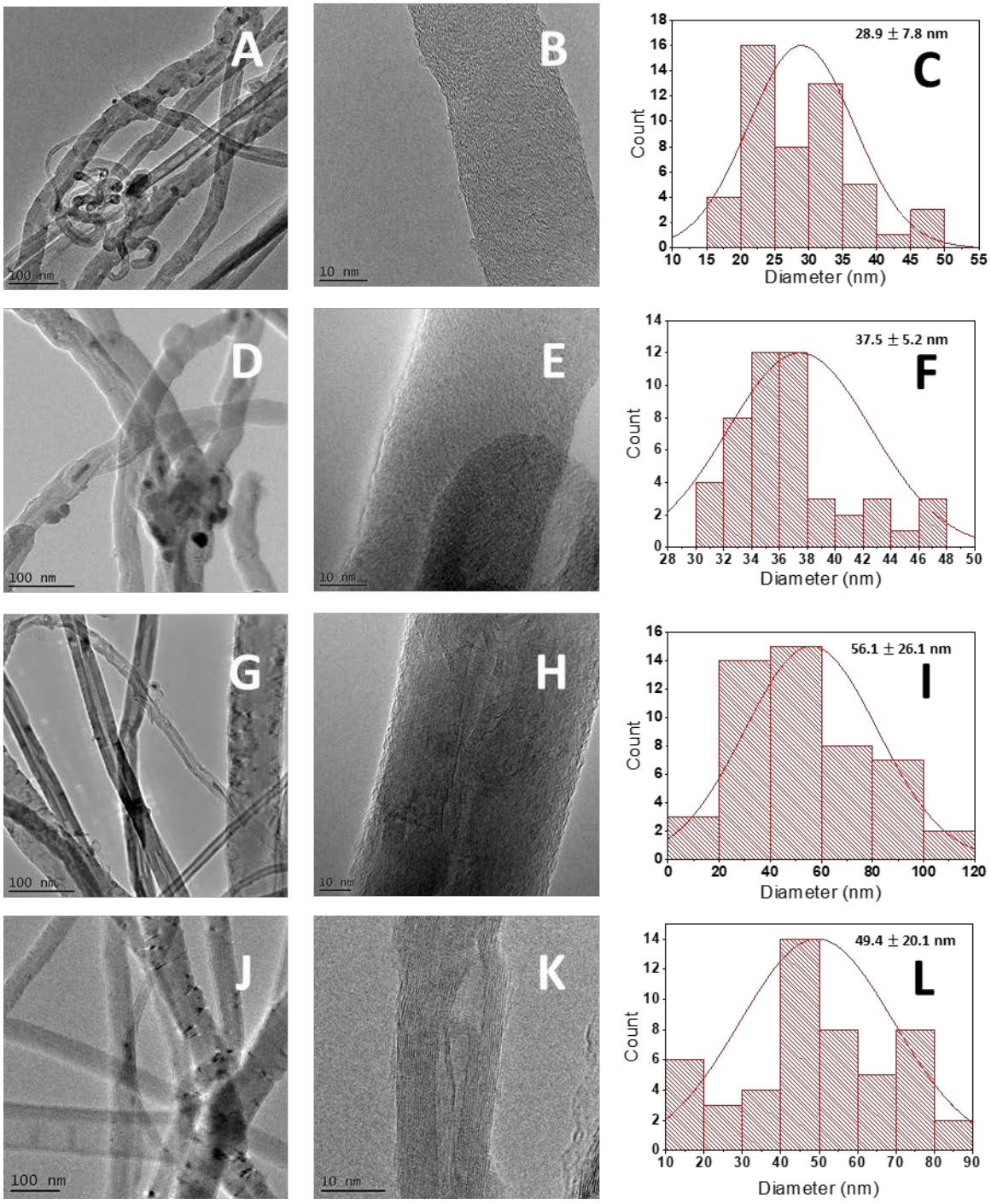
36. Cevher, O., U. Tocoglu, and H. Akbulut, *Amorphous ATO and amorphous ATO based composite anodes for Li-ion batteries.* International Journal of Hydrogen Energy, 2014. **39**(36): p. 21429-21434.
37. Tocoglu, U., et al., *Coaxial silicon/multi-walled carbon nanotube nanocomposite anodes for long cycle life lithium-ion batteries.* Applied Surface Science, 2014. **305**: p. 402-411.
38. Zhang, D., et al., *Exfoliation from carbon nanotubes versus tube size on lithium insertion.* Electrochemistry Communications, 2011. **13**(2): p. 125-128.
39. Zhao, M., et al., *Curvature-induced condensation of lithium confined inside single-walled carbon nanotubes: First-principles calculations.* Physics Letters A, 2005. **340**(5): p. 434-439.
40. Yang, S., et al., *A comparative study of electrochemical properties of two kinds of carbon nanotubes as anode materials for lithium ion batteries.* Electrochimica Acta, 2008. **53**(5): p. 2238-2244.
41. Wang, X.X., et al., *Preparation of Short Carbon Nanotubes and Application as an Electrode Material in Li-Ion Batteries.* Advanced Functional Materials, 2007. **17**(17): p. 3613-3618.
42. Damle, S.S., et al., *Effect of silicon configurations on the mechanical integrity of silicon–carbon nanotube heterostructured anode for lithium ion battery: A computational study.* Journal of Power Sources, 2016. **304**: p. 373-383.
43. Li, H., et al., *A High Capacity Nano - Si Composite Anode Material for Lithium Rechargeable Batteries.* Electrochemical and Solid-State Letters, 1999. **2**(11): p. 547-549.
44. Epur, R., M.K. Datta, and P.N. Kumta, *Nanoscale engineered electrochemically active silicon–CNT heterostructures-novel anodes for Li-ion application.* Electrochimica Acta, 2012. **85**: p. 680-684.
45. Katar, S., et al., *Silicon Encapsulated Carbon Nanotubes.* Nanoscale Research Letters, 2010. **5**(1): p. 74-80.
46. Wepasnick, K.A., et al., *Chemical and structural characterization of carbon nanotube surfaces.* Analytical and Bioanalytical Chemistry, 2010. **396**(3): p. 1003-1014.
47. Callister, W.D. and W.D. Callister, *Fundamentals of materials science and engineering : an interactive etext.* 2001, New York: Wiley.
48. Evanoff, K., et al., *Towards Ultrathick Battery Electrodes: Aligned Carbon Nanotube – Enabled Architecture.* Advanced Materials, 2012. **24**(4): p. 533-537.
49. Halliday, D., R. Resnick, and J. Walker, *Fundamentals of Physics.* 2013: Wiley.
50. Liu, Z., et al., *Silicon oxides: a promising family of anode materials for lithium-ion batteries.* Chemical Society Reviews, 2019. **48**(1): p. 285-309.
51. Ko, M., S. Chae, and J. Cho, *Challenges in Accommodating Volume Change of Si Anodes for Li-Ion Batteries.* ChemElectroChem, 2015. **2**(11): p. 1645-1651.
52. Gohier, A., et al., *High-Rate Capability Silicon Decorated Vertically Aligned Carbon Nanotubes for Li-Ion Batteries.* Advanced Materials, 2012. **24**(19): p. 2592-2597.
53. Cui, L.-F., et al., *Crystalline-Amorphous Core−Shell Silicon Nanowires for High Capacity and High Current Battery Electrodes.* Nano Letters, 2009. **9**(1): p. 491-495.
54. Erika, B., et al., *High-performance flexible nanoporous Si-carbon nanotube paper anodes for micro-battery applications.* Nanotechnology, 2016. **27**(24): p. 245401.
55. Fu, K., et al., *Aligned Carbon Nanotube-Silicon Sheets: A Novel Nano-architecture for Flexible Lithium Ion Battery Electrodes.* Advanced Materials, 2013. **25**(36): p. 5109-5114.
56. Chen, W., et al., *Mesoporous Silicon Anodes Prepared by Magnesiothermic Reduction for Lithium Ion Batteries.* Journal of The Electrochemical Society, 2011. **158**(9): p. A1055-A1059.
57. Epur, R., et al., *Scribable multi-walled carbon nanotube-silicon nanocomposites: a viable lithium-ion battery system.* Nanoscale, 2015. **7**(8): p. 3504-3510.
58. Chou, S.-L., et al., *Silicon/Single-Walled Carbon Nanotube Composite Paper as a Flexible Anode Material for Lithium Ion Batteries.* The Journal of Physical Chemistry C, 2010. **114**(37): p. 15862-15867.
59. Wang, W., R. Epur, and P.N. Kumta, *Vertically aligned silicon/carbon nanotube (VASCNT) arrays: Hierarchical anodes for lithium-ion battery.* Electrochemistry Communications, 2011. **13**(5): p. 429-432.
60. Yu, W.-J., et al., *Lithiation of Silicon Nanoparticles Confined in Carbon Nanotubes.* ACS Nano, 2015. **9**(5): p. 5063-5071.
61. Wang, X.-L. and W.-Q. Han, *Graphene Enhances Li Storage Capacity of Porous Single-Crystalline Silicon Nanowires.* ACS Applied Materials & Interfaces, 2010. **2**(12): p. 3709-3713.

62. Bhandakkar, T.K. and H. Gao, *Cohesive modeling of crack nucleation in a cylindrical electrode under axisymmetric diffusion induced stresses.* International Journal of Solids and Structures, 2011. **48**(16): p. 2304-2309.
63. Eftekhari, A., *Lithium-Ion Batteries with High Rate Capabilities.* ACS Sustainable Chemistry & Engineering, 2017. **5**(4): p. 2799-2816.
64. Lee, J.G., et al., *Mechanical Damage of Surface Films and Failure of Nano-Sized Silicon Electrodes in Lithium Ion Batteries.* Journal of The Electrochemical Society, 2017. **164**(1): p. A6103-A6109.
65. Fears, T.M., et al., *Evaluating the solid electrolyte interphase formed on silicon electrodes: a comparison of ex situ X-ray photoelectron spectroscopy and in situ neutron reflectometry.* Physical Chemistry Chemical Physics, 2016. **18**(20): p. 13927-13940.
66. Evanoff, K., et al., *Ultra Strong Silicon-Coated Carbon Nanotube Nonwoven Fabric as a Multifunctional Lithium-Ion Battery Anode.* ACS Nano, 2012. **6**(11): p. 9837-9845.
67. Gaisler, S.V., et al., *Analysis of Raman spectra of amorphous-nanocrystalline silicon films.* Physics of the Solid State, 2004. **46**(8): p. 1528-1532.
68. Graczykowski, B., et al., *Thermal conductivity and air-mediated losses in periodic porous silicon membranes at high temperatures.* Nature Communications, 2017. **8**(1): p. 415.

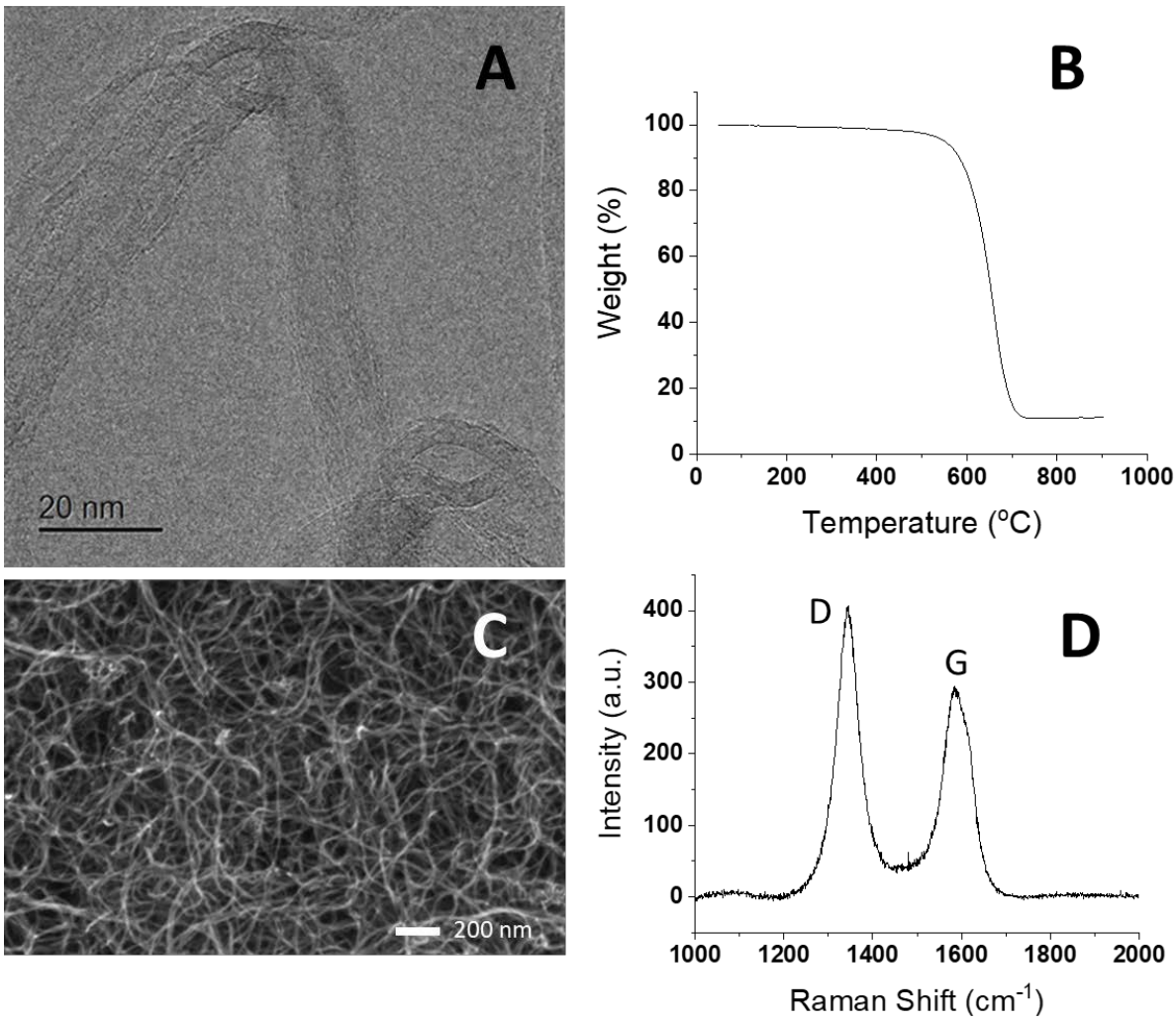
4.7) Supporting information



Supporting Figure 4.1. SEM images and length histogram of A-C) MWCNT 15, D-F) MWCNT 30, G-I) MWCNT 45 and J-L) MWCNT 60 revealing the effects of the synthesis time to the length of CNTs; when increasing synthesis time, the length of the nanotubes was longer.

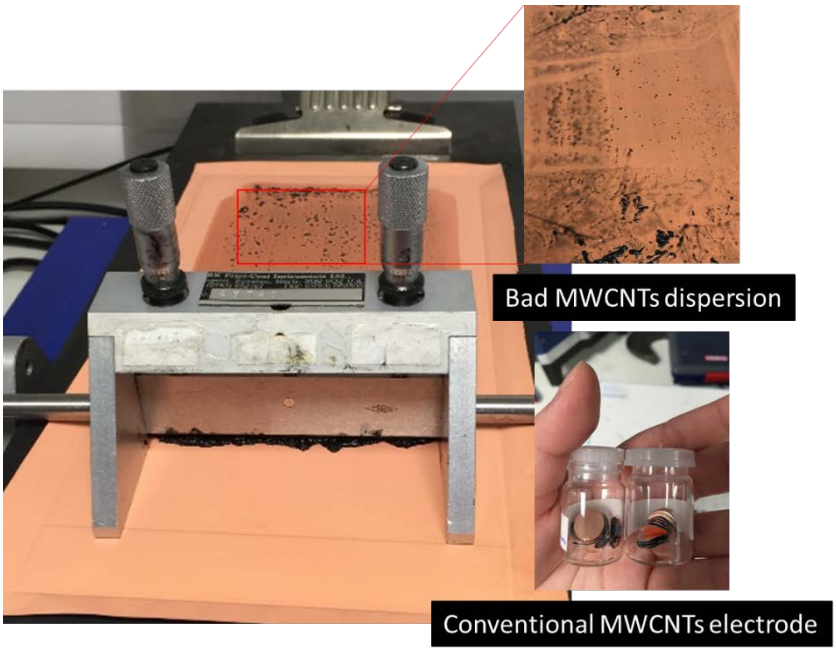


Supporting Figure 4.2. TEM images and a diameter histogram of A-C) MWCNT 15, D-F) MWCNT 30, G-I) MWCNT 45 and J-L) MWCNT 60; there is no tendency to increase the diameter of MWCNTs when the synthesis time was varied.

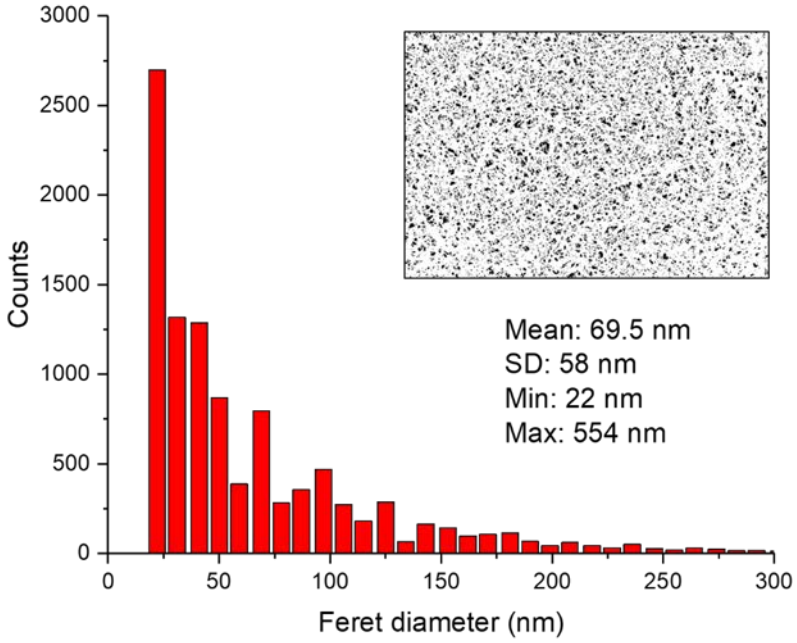


Supporting Figure 4.3. A) TEM images of the commercial MWCNTs showing small diameter (9-12 nm) of C-MWCNT, B) TGA graph of C-MWCNT presenting 11 wt.% catalyst in the material, C) a SEM image of the C-BP surface showing bundles of MWCNTs, and D) Raman spectrum of the C-BP revealing the D and G bands of the carbon material.

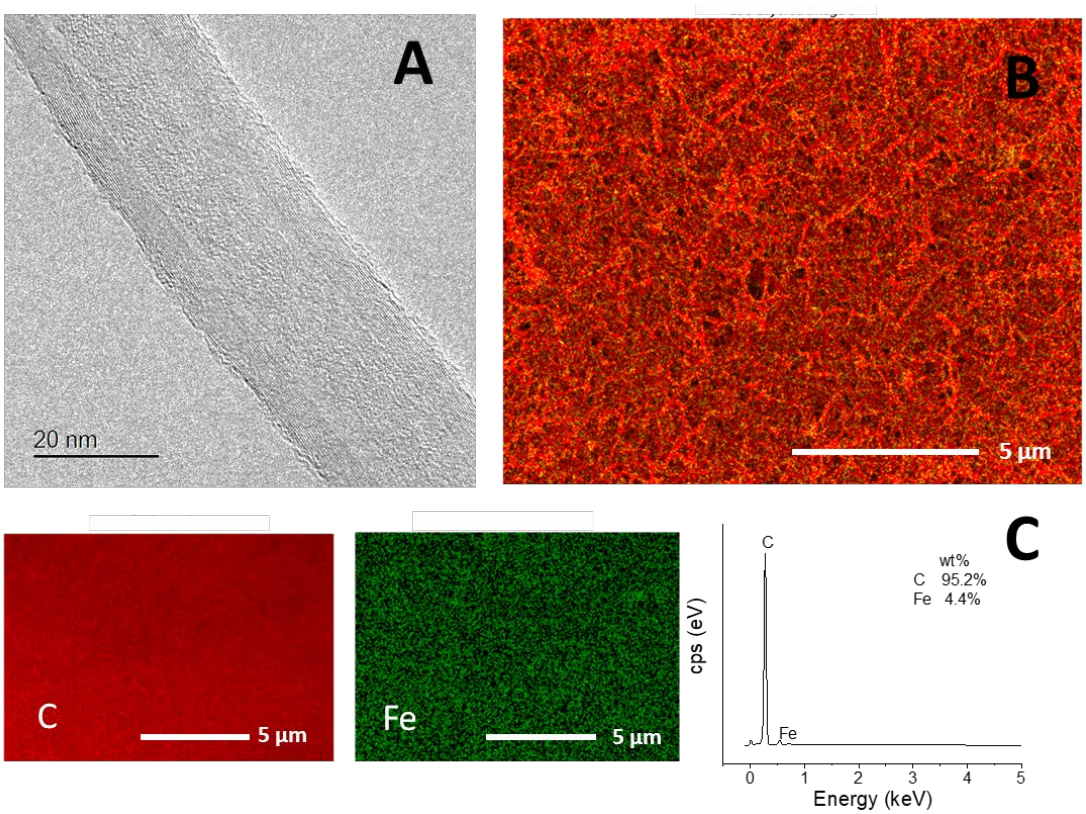
The diameter of C-MWCNT was around 9-12 nm with a wall thickness of about 3-5 nm. TGA revealed that the C-MWCNT had higher thermal stability (662 °C) with 11 wt.% of catalyst residue. SEM showed a smooth surface of C-BP without bundles of MWCNTs. The Raman spectrum exhibited the characteristic peaks of carbon materials (G and D bands). The I_D/I_G ratio of the C-BP is around 1.019 while the FWHM is 73.62 cm^{-1}.



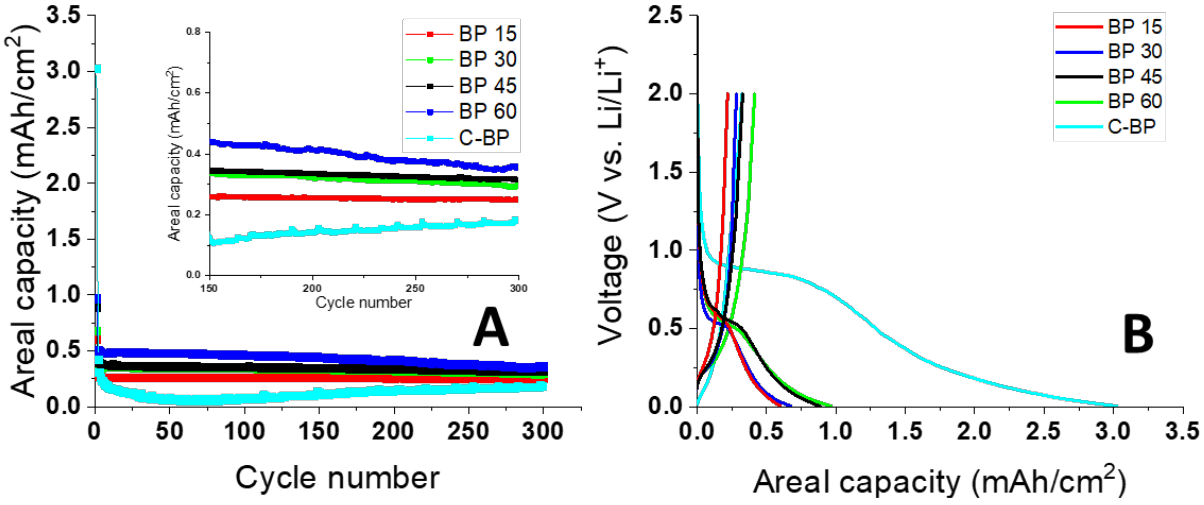
Supporting Figure 4.4. Photographs of MWCNT dispersion casted on the copper foil demonstrating bad dispersion of MWCNTs coated on the current collector (Cu).



Supporting Figure 4.5. The Feret diameter distribution of the BP 45 calculated from the SEM image; it confirms that the buckypaper contains both mesopores and macropores.



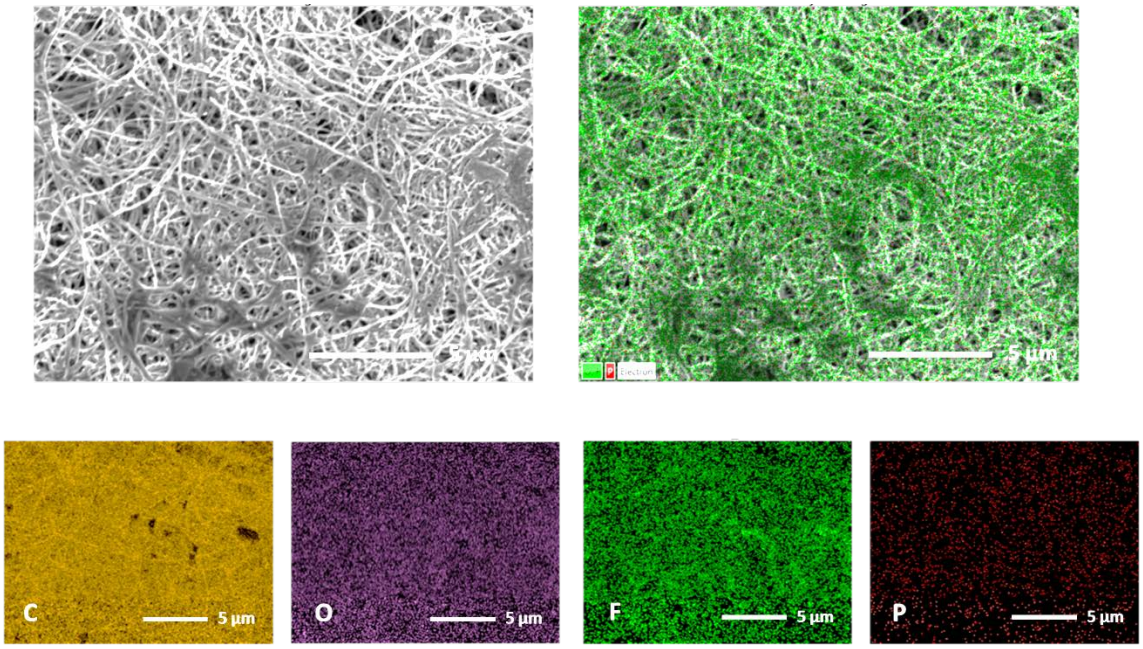
Supporting Figure 4.6. TEM image confirming A) the stable structure of the MWCNTs after buckypaper fabrication, and B-C) EDX elemental maps showing the elemental components of the BP 45.



Supporting Figure 4.7. A) The areal capacity and B) the charge-discharge plots (1st cycle) of the different types of buckypapers showing the effect of MWCNT structures to the battery performance.

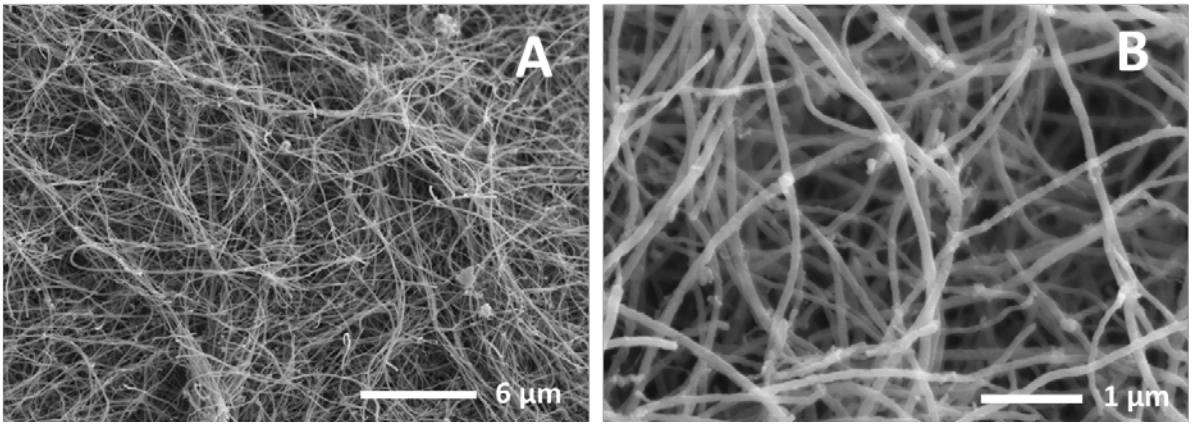
Supporting Table 4.1. The capacity and coulombic efficiency of the buckypaper electrodes.

Sample	C-BP	BP 15	BP 30	BP 45	BP 60
1st discharge capacity (mAh/g)	1500	293.3	238.8	297.2	286.4
(mAh/cm^2)	**3.02**	**0.6**	**0.67**	**0.86**	**0.97**
(mAh/cm^3)	251.7	50	55.8	71.7	80.8
1st charge capacity(mAh/g)	160.2	107.1	100	109.9	122.7
(mAh/cm^2)	**0.33**	**0.22**	**0.28**	**0.33**	**0.41**
(mAh/cm^3)	27.5	18.3	23.3	27.5	34.2
2nd discharge capacity (mAh/g)	207.9	135.4	126.6	139.1	150.1
(mAh/cm^2)	**0.42**	**0.28**	**0.36**	**0.42**	**0.51**
(mAh/cm^3)	35	23.3	30	35	42.5
300th discharge capacity (mAh/g)	89.5	122.3	104.3	105.9	104.8
(mAh/cm^2)	**0.18**	**0.25**	**0.3**	**0.32**	**0.36**
(mAh/cm^3)	15	20.8	25	26.7	30
300th Coulombic efficiency	**97%**	**99.9%**	**99.9%**	**99.9%**	**99.9%**

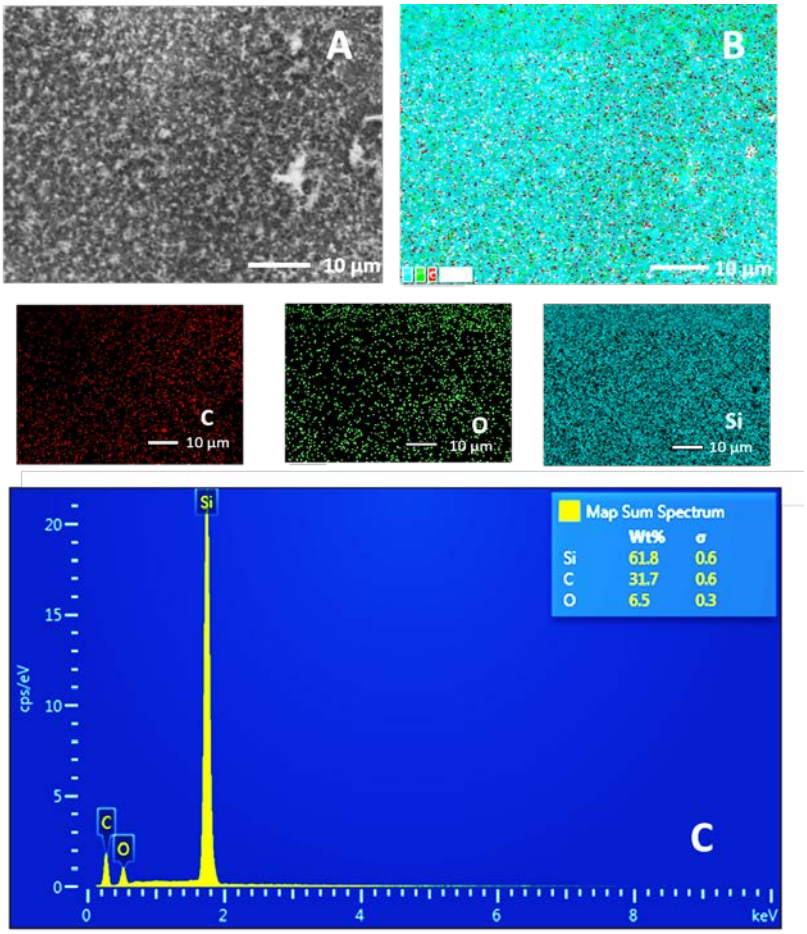


Supporting Figure 4.8. SEM and EDX elemental maps of the BP 45 electrode after battery cycling showing the component of SEI layer coated on the electrode surface.

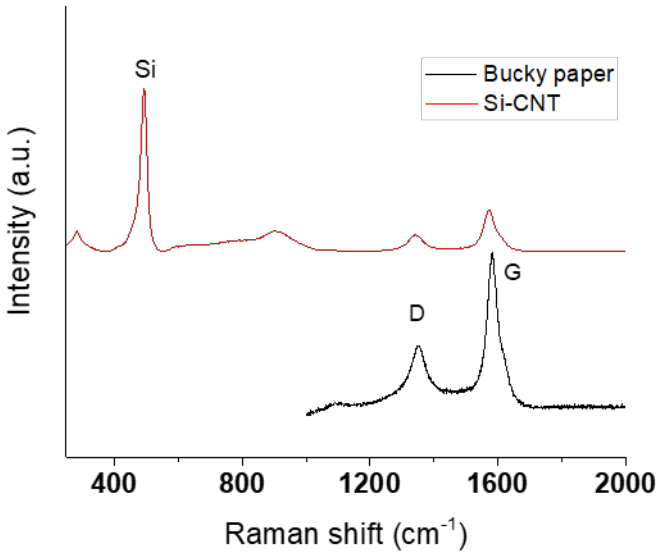
The EDX maps showed a component of the Si-CNT material. The carbon signal was associated to MWCNTs while the silicon map refers to Si NPs coating on the BP. Some oxygen signals were present arising from SiO_2 due to the material being in contact with air during transportation and characterisations.



Supporting Figure 4.9. A-B) SEM images of the Si-CNT electrode; a rough surface of MWCNTs presents Si NPs coated on the BP.

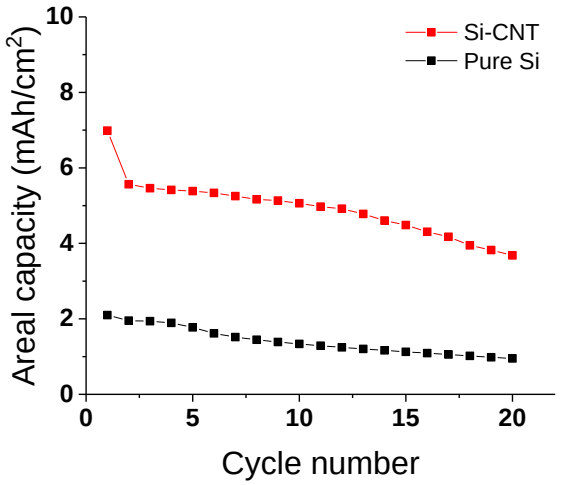


Supporting Figure 4.10. A) SEM image and B-C) EDX maps and spectrum showing the component of the Si-CNT material.

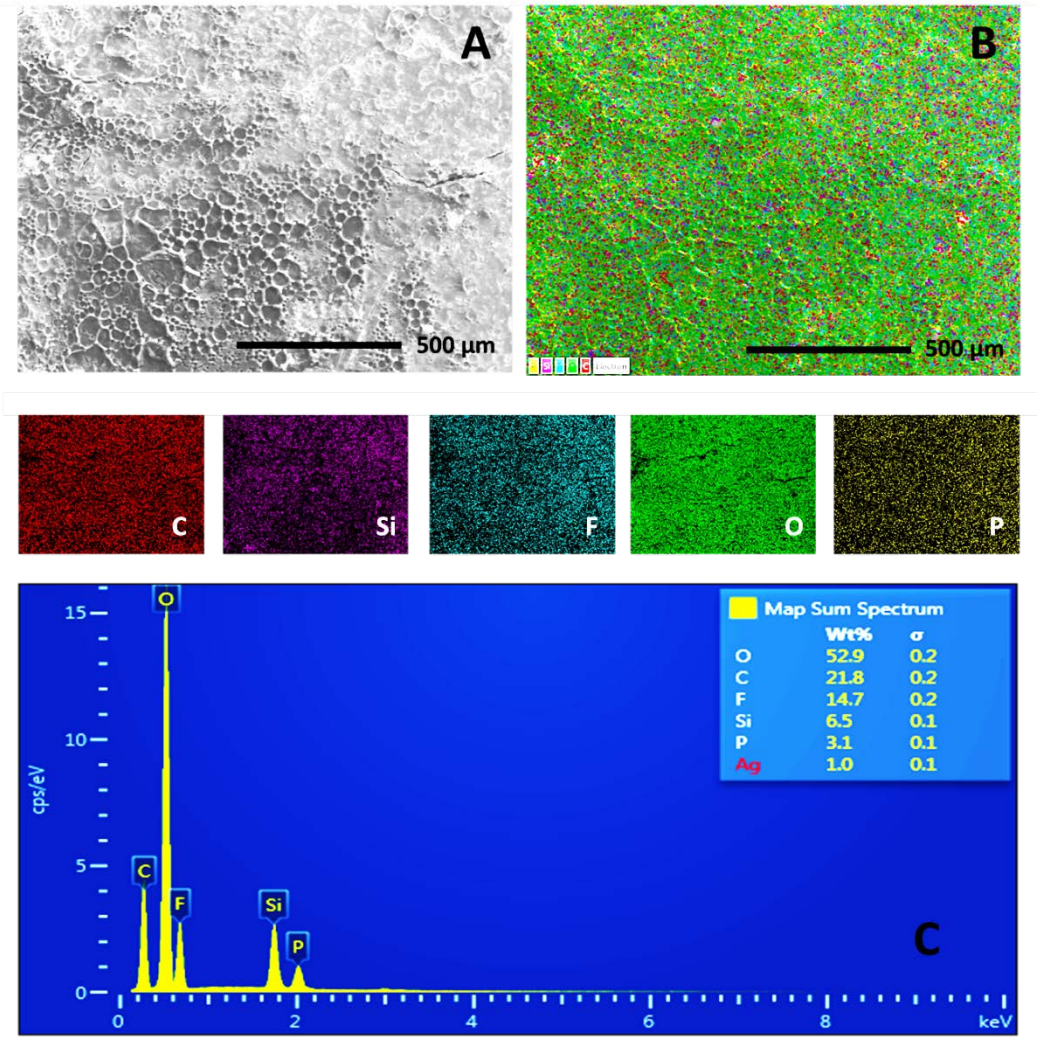


Supporting Figure 4.11. Raman spectra confirming the structure of the Si-CNT material.

Amorphous Si peaks were seen after Si coating at around 290, 480 and 910 cm^{-1} [37, 54, 66-68]. The Si-CNT material also exhibited D-band (disorder carbon) and G-band (graphitic carbon) peaks associated to the MWCNTs at 1350 cm^{-1} and 1580 cm^{-1}. Interestingly, the intensity of D and G bands reduced while the G peak shifted to a lower wavenumber. The decrement of the intensity was because of the Si coating on the MWCNTs while the G peak downshifts were attributed to disorder and defects of carbon structures which occur during the Si deposition [55].



Supporting Figure 4.12. The areal capacities of Si-CNT and pure Si electrodes at C/10 rate; the Si-CNT electrode showed better performance than the pure Si electrode after 20 cycles which confirmed the effect of MWCNTs on Si materials.



Supporting Figure 4.13. A) SEM image and B) EDX maps of the Si-CNT after cycling over 300 cycles C) EDX spectrum showing the surface of the electrode was covered by SEI layers.

The Si-CNT electrode after battery cycling composed of silicon, carbon and, additional elements such as fluorine (F), oxygen (O), and phosphorus (P) which corresponded to SEI layer formation on the Si-CNT electrode. The SEI layers generally consist of organic and inorganic compounds such as Li_2CO_3, Li_2O, and LiF. These species are present in the LP 30 electrolyte used in the LIB.

Chapter 5

Si-CNT-SiC-C hybrid materials for anodes in Li-ion batteries

In the previous chapter, the Si-CNT electrode showed poor battery performance (0.09 mAh/cm^2 after 300 cycles) and cracking was found on the Si-CNT electrode after the battery cycling. The Si NPs were also detached from the MWCNT walls due to the weak interface between these two materials resulting in significant capacity loss of the Si-CNT electrode. In this chapter, amorphous carbon was coated on the Si-CNT material to improve the stability of the electrode by preventing direct contact between Si and the electrolyte. However, silicon carbide was observed in the material after the high-temperature coating process. The stability enhancement of the Si-CNT-C electrode was mainly due to a trace of SiC present in the material. Therefore, SiC interface was further developed in the Si-CNT material before coating the material with an amorphous carbon layer in order to form a strong connection between MWCNTs and Si NPs. This chapter investigates the SiC interface between Si NPs and MWCNTs and shows the effects on the performance of the electrode. The result exhibited the capacity retention improvement of the Si-CNT-SiC-C (0.55 mAh/cm^2) compared to the Si-CNT electrode (0.09 mAh/cm^2) after 300 cycles. The battery performance enhancement is attributed to the robust SiC interface in the Si-CNT-SiC-C material, which could prevent the detachment of Si NPs from MWCNTs. The post-cycling analysis confirmed the morphology of the Si-CNT-SiC-C material structure without cracks after the battery testing. Thus, the SiC could mitigate the stress due to the volume expansion of Si and then prevent the fractures induced upon repeated cycling.

5.1) Introduction

According to the previous part of the research, the specific capacity of the Si-CNT material in the first few cycles (*ca.* 3100 mAh/g) was found to be higher than that of the graphite anode (372 mAh/g). Nevertheless, the battery cells showed poor capacity retention after 300 cycles (0.09 mAh/cm^2 and 49 mAh/g), which was caused by the fractures in the material induced during cell cycling. Therefore, it can be implied that MWCNTs in the form of BPs are insufficient to handle the stress evolution caused by the volume changes in these Si anode materials.

Other approaches such as coating protective carbon on the Si anode then need to be developed in order to tackle the Si problem further. As also explained in Chapter 1, the coated carbon inhibits direct contact between Si and the electrolyte and consequently reduces the electrolyte/electrode interfacial side reactions, resulting in improved battery performance. More importantly, it preserves the structural stability of the anode materials as the carbon is mechanically flexible [2-5]. However, the carbon coating layer still fails to reduce the volume expansion occurring at the Si anode [6]. Therefore, the challenge of this approach is to form a stable carbon coating which would not break during Si lithiation/delithiation.

Another issue with Si-CNT anodes is the interfacial instability due to the weak bonding at the interface of the materials; that is the Si NPs are anchored with the MWCNTs by an amorphous carbon layer. As presented in the previous chapter, Si NPs lose their contact with MWCNTs in the Si-CNT material during repeated cycling because of the significant volume changes. This problem then causes the dramatic loss of a capacity in the Si-CNT electrode. Therefore, the development of a strong interface between Si and MWCNTs needs to be achieved to address this issue. This interface is also an important enhancement of the performance in both stability and rate capability [7, 8].

Recently, Jiang *et al.* (2016) investigated the interfacial bonding effects between Si NPs and MWCNTs on the Si/CNT nanocomposites by increasing the synthesis temperatures for annealing the Si/CNT material (500-1100 °C) [1]. The beta silicon carbide (β-SiC) interface was found when the annealing temperature reached 1000 °C because of the reaction between carbon atoms on the surface of MWCNTs and Si NPs (Figure 5.1A). When the annealing temperature was increased to 1300 °C, the sidewalls of MWCNTs were completely damaged and transformed to the SiC phase (Figure 5.1B). The Si/CNT materials annealed at 1000 °C delivered a discharge capacity of 938 mAh/g after 100 cycles (Figure 5.1C). The result indicated that Si/CNT materials with limited SiC interfaces could distribute a high capacity and cycling stability. Whilst, the complete Si conversion to SiC resulted in a significant decrease in capacity (~400 mAh/g), the study showed how the strong SiC interface between Si NPs and MWCNTs could buffer the large volume change during alloying and dealloying of the Si materials [1].

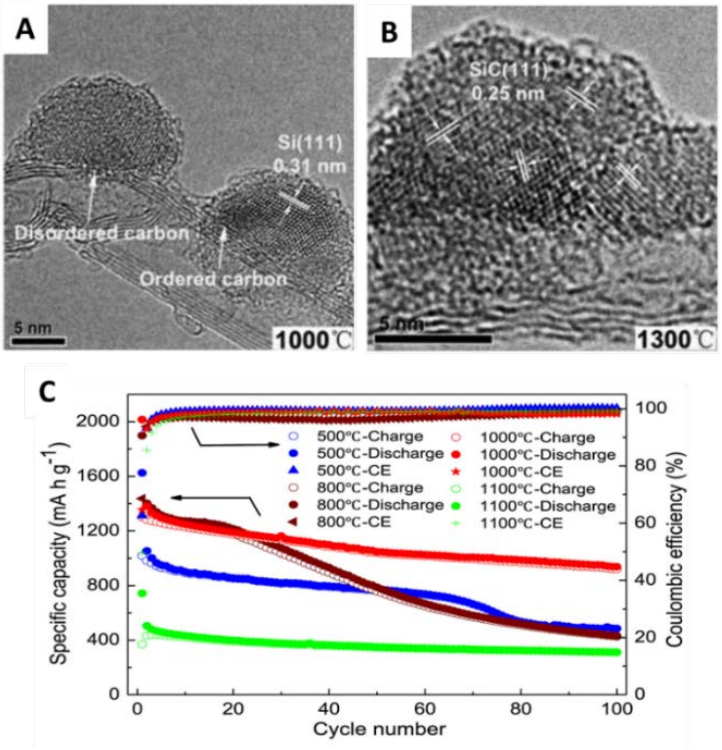


Figure 5.1. A-B) TEM images of the Si/MWCNT after annealing at 1000 °C and 1300 °C showing the silicon carbide formation on the surface of MWCNTs, and C) the battery performance of the annealing Si/MWCNT electrodes showing the stability improvement after annealing the material at high temperature (1000 °C) to form silicon carbide interface [1].

Previously, SiC has been considered electrochemically inactive in LIBs; thus, many studies attempted to prevent the formation of SiC in silicon-carbon materials during material synthesis [9-11]. Nonetheless, some studies reported that SiC has the ability to store Li ions and could act as an anode with a good capacity as well as moderate capacity retention [12-14]. Zheng and Xu (2014) [12] demonstrated the reaction mechanism of a SiC anode. The reaction mechanism of SiC with Li is the conversion reaction where SiC reversibly converts to Si followed by Si alloy reaction with Li as shown below.

$$SiC + 4Li^+ + 4e^- \leftrightarrow Si + Li_4C \quad (5.1)$$

$$Si + 4.4Li^+ + 4.4e^- \leftrightarrow Li_{4.4}Si \quad (5.2)$$

Based on this mechanism, the theoretical capacity of SiC is calculated to be 2638 mAh/g. However, the experimental results revealed that the SiC film could only deliver a reversible capacity of 309 mAh/g over 60 cycles [12]. Additionally, Huang *et al.* (2018) found that the SiC film had lower coulombic efficiency in the first cycle than Si anodes; consequently, there should be an additional irreversible reaction occurring in the SiC anode. They then suggested another possible reaction mechanism to describe amorphous SiC films as follows [13].

$$SiC + xLi^+ + xe^- \leftrightarrow Li_xSi_yC + (1-y)\ Si \quad (5.3)$$

Noticeably, SiC could also perform as a buffer matrix for the Si material due to its high hardness (*ca.* 18 GPa). That is, it could minimise the stress-induced during lithiation, leading to an enhancement of the mechanical stability and capacity retention of the electrode [13]. Thus, the SiC interface between Si and MWCNTs is another important factor that should be considered for the possible improvement of the Si-CNT anode in terms of cycling performance.

In this chapter, SiC interfaces were developed between Si NPs and MWCNTs. Amorphous carbon was simultaneously coated on the Si-CNT material. The experimental conditions, including temperature and carbon sources, were studied systemically to obtain the desired structures of the Si-

CNT-SiC-C materials. Consequently, these Si-CNT-SiC-C materials were tested as free-standing anodes in LIBs in order to investigate the structural and interfacial effects on the battery performance. Post-cycling analysis of the electrode was carried out after battery testing. Finally, the pouch cells were assembled using free-standing Si-CNT-SiC-C electrodes in order to confirm their battery performance by removing the stainless-steel effect in the coin cell configuration.

5.2) Experimental

The synthesis of the Si-CNT based material is explained in section 3.3.5 in Chapter 3. Briefly, the structure of the Si-CNT material was first modified by implementing an amorphous carbon coating. The strong SiC interface was then developed between the Si NPs and MWCNTs. Both coin-cells and pouch-cells were fabricated using these materials to test the battery performance. The details of the electrode fabrication and battery testing are shown in section 3.4 in Chapter 3. Also, the electrodes were disassembled, and the post-cycling analysis was conducted in which procedures are shown in section 3.5 in Chapter 3.

5.3) Characterisation

The morphologies of the Si-CNT-C and Si-CNT-SiC-C materials were investigated using SEM and TEM. The electron diffraction and the nano-beam electron diffraction were obtained by using TEM. The chemical structures were investigated using Raman spectroscopy, XPS and XRD. The composition of the materials was studied using EDX. The electrical conductivity of the materials was also tested using four-point probe measurements. Note that the material characterisation details were explained in section 3.1 in Chapter 3.

5.4) Results and discussions

As a result of the poor cycling stability exhibited by the Si-CNT composite in battery testing (Chapter 4), an amorphous carbon layer was used to coat the materials in order to address the problem since it expectedly prevents direct contact between Si and the electrolyte and provides the integrity of the material. In this chapter, methane gas was initially chosen for coating the Si-CNT material (Case I, Figure 5.2). However, traces of SiC were found in the material most probably due to the high temperature (900 °C) involved in the experiment. Therefore, acetylene gas was chosen instead due to its lower decomposition temperature (700 °C) (Case II, Figure 5.2) in order to impede the SiC formation.

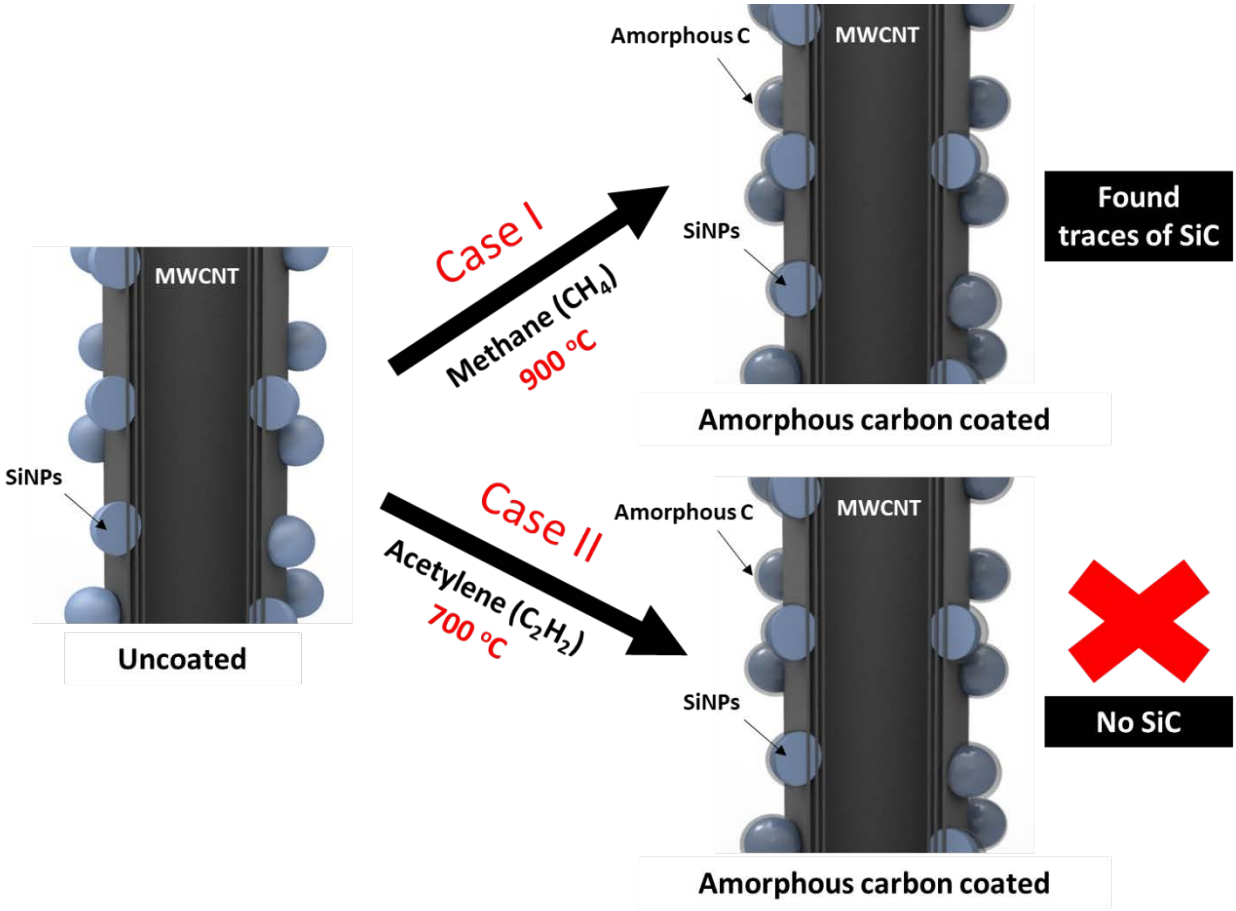


Figure 5.2. Schematic diagrams showing the amorphous carbon coating process in which two carbon sources were used (Case I: methane gas and Case II: acetylene gas); traces of SiC were found in the material after coating in Case I due to the high temperature (900 °C) used in the experiment.

5.4.1) Morphological, structural, and chemical characterisation of the Si-CNT-C (CH_4) material, Case I

The Si-CNT materials were first coated with amorphous carbon using methane gas as a carbon source (Case I). The scheme of the desired Si-CNT-C (CH_4) is shown in Figure 5.3A. A thin amorphous carbon layer of 8-10 nm in thickness was successfully coated on the MWCNTs by a methane decomposition method (Figure 5.3B). The previous study found that the amorphous carbon had small open channels (0.16-0.18 nm of a radius) which allowed only Li to penetrate through and impeded direct contact between Si NPs and the electrolyte [15]. Thus, the SEI layer was stabilised on the flexible carbon surface instead of on the Si NPs during cycling leading to the reduction in irreversible capacity. In addition, the Si NPs deposited on the outer wall of MWCNTs within BP 45 changed its phase to a crystalline structure due to the higher temperature involved in this experimental step (900 °C). The crystalline Si was confirmed by the presence of a spot pattern in the FFT of the selected image area in Figure 5.3C. The Si NPs had an average diameter of 40-50 nm, which was still less than the critical diameter of the crystalline Si (150 nm) (Figure 5.3C). The increase of the Si NP diameter in the Si-CNT-C comparing to the Si-CNT is owing to a sintering effect where the diffusion and the dentification of the material cause the excess energy reduction when increasing the temperature [16].

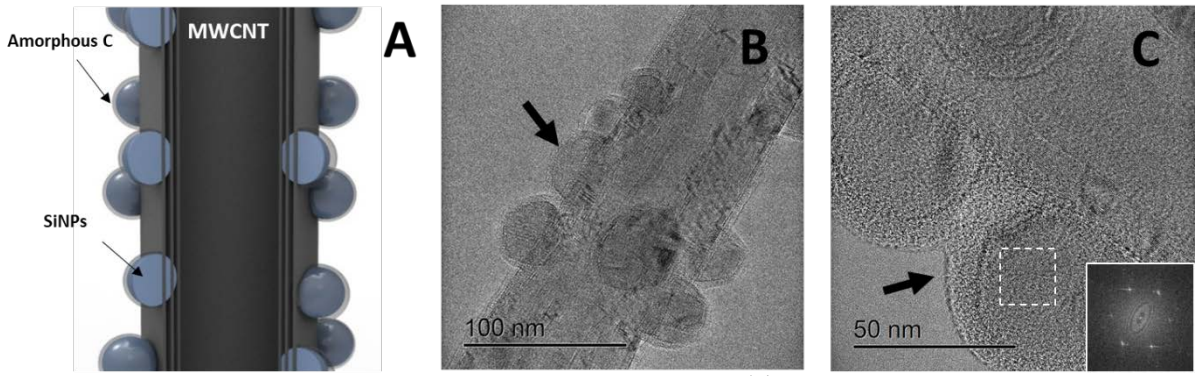


Figure 5.3. A) A schematic of the desired structure of Si-CNT-C after coating amorphous carbon and B) TEM image of Si-CNT-C (CH_4) material (Case I) showing thick amorphous carbon (8-10 nm) coated on the material surface, and C) TEM image and fast Fourier transformation of the selected image area showing the spot pattern of crystalline Si.

In addition, no thick layer of the coated carbon was observed on the surface of the Si-CNT-C (CH_4) material, indicating that the carbon was not only coated on the top surface but also deposited throughout the BP (Supporting Figure 5.1). The structure of the Si-CNT-C (CH_4) material was studied further using XRD and Raman spectroscopy. The crystalline structure of Si was observed after the amorphous carbon deposition, which agreed with TEM images (Figure 5.4). The Si peaks were shown at 28.5°, 47.4°, and 56.2° which were indexed to (111), (220), and (311) planes of pure Si, respectively [1, 17]. Unforeseen, small peaks were observed at 35.7° and 60.1° which could be assigned to (111) and (220) planes of β-SiC in the Si-CNT material after coating with amorphous carbon [1]. Note that thermal decomposition of methane usually happens at a very high temperature (800-1300 °C). Therefore, the temperature for amorphous carbon coating was high enough for the SiC formation. Also, the Si peak in Raman spectrum of the Si-CNT-C (CH_4) material shifted to 500-510 cm^{-1} which most probably attributed to nanocrystalline Si formed after increasing the temperature during the amorphous carbon coating process (Supporting Figure 5.2) [18, 19].

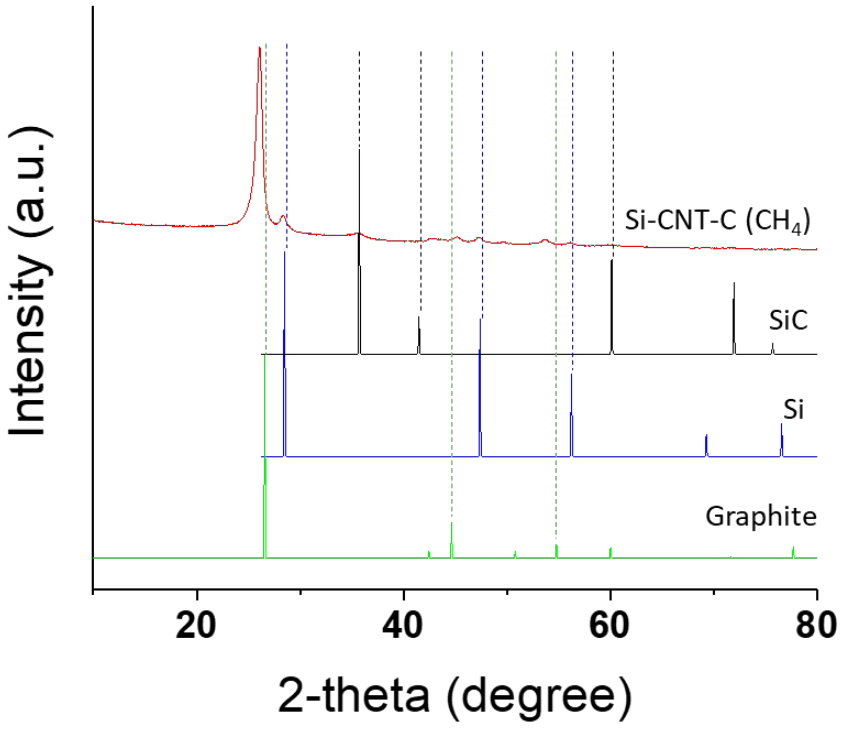


Figure 5.4. XRD patterns of Si-CNT-C (CH_4) material (Case I); a small SiC peak can be seen confirming SiC in the Si-CNT-C (CH_4) material.

XPS analysis indicated that the Si-CNT-C (CH_4) material consisted of silicon, carbon, and oxygen (Figure 5.5A). The Si-CNT-C (CH_4) revealed Si doublet and SiO_2 related peaks at 99.4, 100.1, and 103.4 eV, respectively, which was consistent with the Si-CNT material [20]. Unexpectedly, an additional silicon carbide peak was observed at 101.1 eV on the surface of the Si-CNT-C (CH_4) material (Figure 5.5B) [21]. In terms of C1s, two main peaks were shown in the material at 284.6 and 285.8 eV which were assigned to C-C and C-O bonds in BP 45 [22] and an additional peak at 282.9 eV relating to SiC (Figure 5.5C) [20]. Thus, it confirmed the existence of SiC in the Si-CNT-C (CH_4) material.

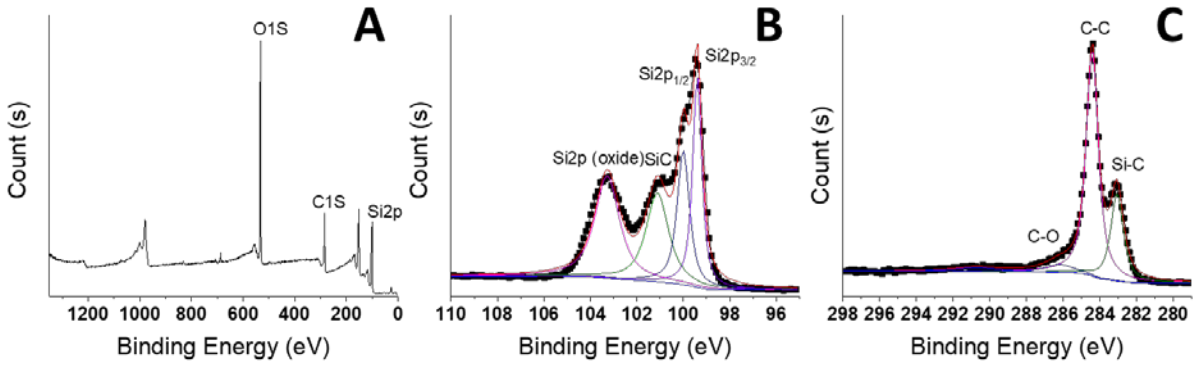


Figure 5.5. A) XPS survey spectrum and high-resolution spectra of Si-CNT-C (CH_4) material (Case I) corresponding to B) Si2p and C) O1s presenting unpredicted SiC formation after coating amorphous carbon by using methane as a carbon source at 900 °C.

5.4.2) Cell fabrication and electrochemical tests of the Si-CNT-C (CH_4) electrode, Case I

The Si-CNT-C (CH_4) material was tested as an anode in the coin-cell batteries (Figure 5.6). The areal capacities of the Si-CNT-C (CH_4) electrode of the first charge and discharge were 3.23 mAh/cm^2 (2816 mAh/g of a specific capacity, 162 mAh/cm^3 of a volumetric capacity) and 2.30 mAh/cm^2 (1993 mAh/g, 115 mAh/cm^3) respectively with coulombic efficiency of 70.8%. The discharge areal capacity was 0.37 mAh/cm^2 (323 mAh/g, 19 mAh/cm^3) after 300 cycles with 99.9% coulombic efficiency. This confirmed the expected stability improvement of the Si-CNT-C (CH_4) electrode compared to the Si-CNT electrode in which the capacity dropped to 0.09 mAh/cm^2 after

300 cycles. Note, this Si-CNT-C (CH_4) material contains a trace of SiC. Hence, the explanation of the battery performance enhancement was unclear and required further study.

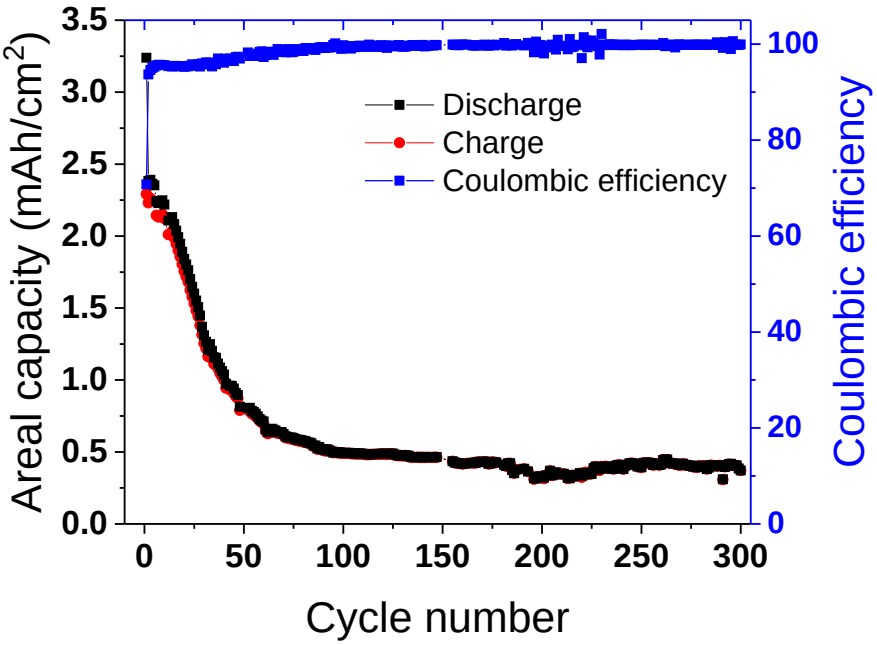


Figure 5.6. The charge-discharge graph of the Si-CNT-C (CH_4) electrode showing the areal capacity of 0.37 mAh/cm² after 300 cycles at C/5 rate.

A plateau in voltage vs capacity and a peak in dQ/dV vs voltage at around 0.15 V (Figure 5.7A-B) in the first cycle confirmed the presence of a crystalline Si phase in the material. In the subsequent cycle, the two peaks at 0.22 V and 0.08 V were identified, which indicated the lithiation of amorphous Si [7]. Interestingly, the small oxidation peak at 0.1 V in the Si-CNT-C (CH_4) electrode was distinguished from the Si-CNT electrode which was ascribed to the reaction of Li with Si in the SiC network confirming the existence of SiC in the electrode [12].

Nevertheless, it was still not clear whether the good battery performance of the Si-CNT-C (CH_4) electrode resulted from amorphous carbon coating or traces of SiC. The experiment on coating carbon on the Si-CNT was therefore adapted in which acetylene gas was used as a carbon source instead due to its lower thermal decomposition temperature in order to study an actual effect of amorphous carbon coating on the Si-CNT materials.

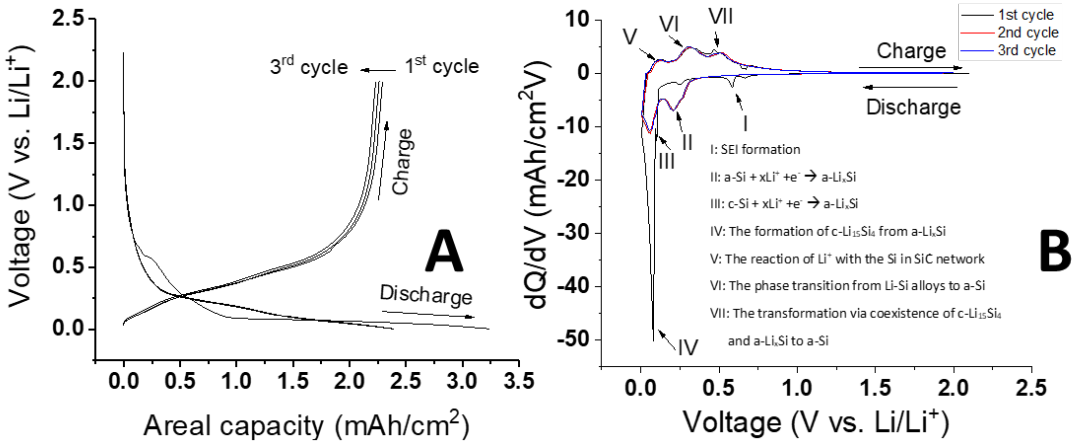


Figure 5.7. A) The voltage profiles of Si-CNT-C (CH_4) revealing the lithiation of crystalline Si due to a presence of the plateau at 0.15 V in the 1st cycle, and B) the differential areal capacity plot presenting the Li ion storage mechanism of the Si-CNT-C (CH_4) electrode.

5.4.3) Morphological, structural, and chemical characterisation of the Si-CNT-C (C_2H_2) material, Case II

Based on the results obtained from a previous section, the new acetylene gas set-up was used to coat amorphous carbon on the Si-CNT material. Since the acetylene gas decomposition occurred at a lower temperature (700 °C) than methane gas, the formation of SiC could be prevented. The morphology of the Si-CNT-C (C_2H_2) material was shown in Figure 5.8. The Si NPs were attached on the wall of MWCNTs with amorphous carbon of 3-8 nm thick (Figure 5.8B). Similar to the previous Si-CNT-C (CH_4) condition, the Si NPs deposited on the MWCNT wall partially agglomerated with an average diameter of 20-30 nm. The Si NPs also changed their phase to a polycrystalline structure, which was confirmed by the ring pattern in the FFT of the selected image area (Figure 5.8C).

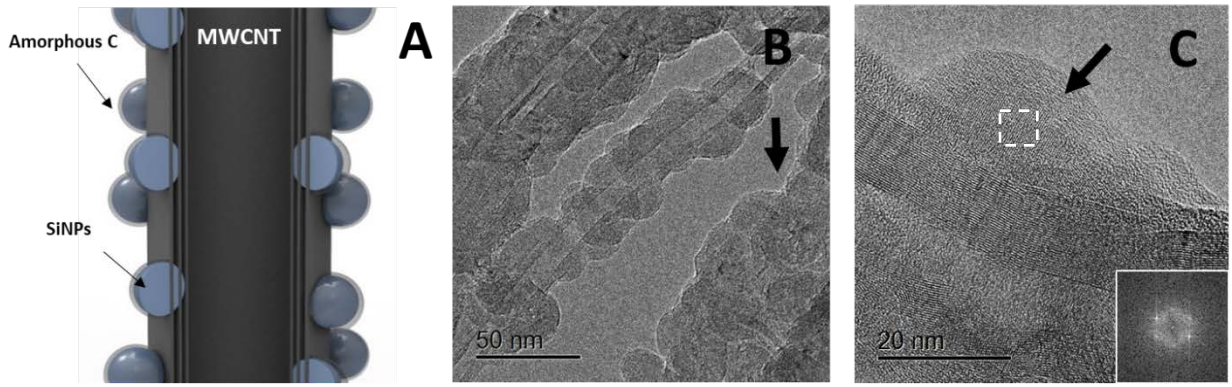


Figure 5.8. A) A schematic of the desired structure of Si-CNT-C and B-C) TEM images presenting the thin amorphous carbon (3-8 nm) coated on the Si-CNT-C (C_2H_2) material (Case II); C) fast Fourier transformation of the selected image area also present the ring pattern of polycrystalline Si.

The structure of the new Si-CNT-C (C_2H_2) material was characterised using XRD and Raman spectroscopy. All peaks corresponding to Si and carbon were shown in Figure 5.9. However, the peak of the Si and SiC could not be distinguished. That is, no formation of crystalline Si and SiC occurred within the Si-CNT-C (C_2H_2) material. In contrast, the broad Si peak was observed in the Raman spectrum of the Si-CNT-C (C_2H_2) material indicating the presence of both amorphous and nanocrystalline Si structures in the material (Supporting Figure 5.3).

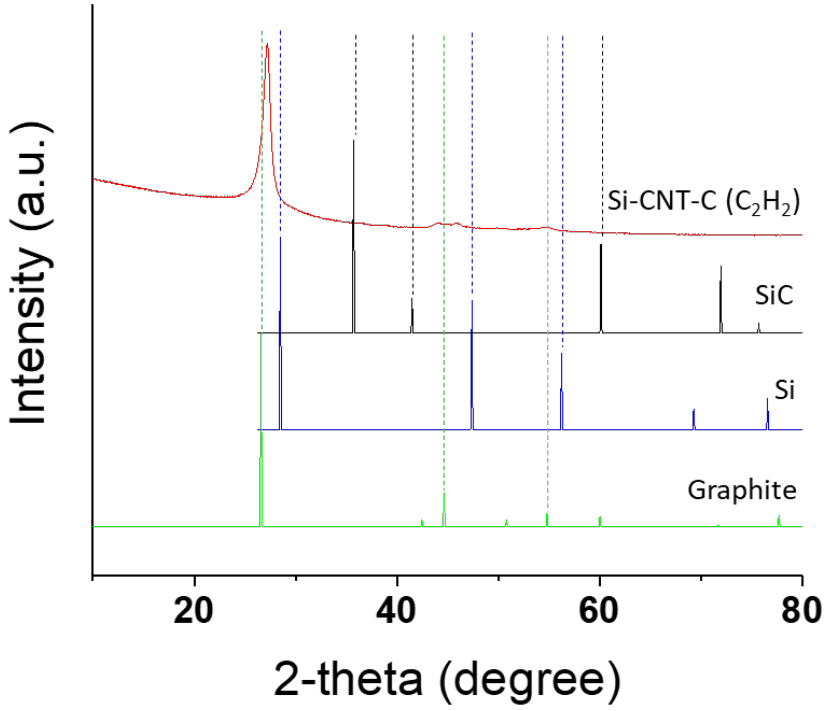


Figure 5.9. XRD patterns of Si-CNT-C (C_2H_2) material (Case II) confirming that SiC did not form in the material after amorphous coating.

Additionally, XPS measurements were carried out to analyse the structure of the Si-CNT-C (C_2H_2) material (Figure 5.10A). Nevertheless, the peak attributed to the SiC material was not be found in the Si-CNT-C (C_2H_2) material (Figure 5.10B-C).

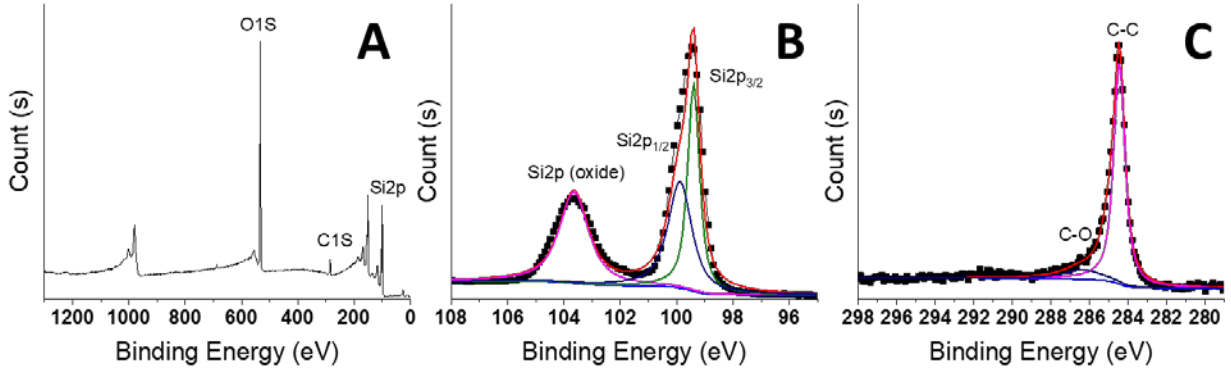


Figure 5.10. A) XPS survey spectrum and high-resolution spectra of Si-CNT-C (C_2H_2) material (Case II) corresponding to B) Si2p and C) O1s; no silicon carbide formation occurred after coating amorphous carbon using acetylene gas.

5.4.4) Cell fabrication and electrochemical tests of the Si-CNT-C (C_2H_2) electrode, Case II

Coin-cell batteries were assembled using the Si-CNT-C (C_2H_2) electrode; the electrochemical performance of the electrode is shown in Figure 5.11. The first charge and discharge areal capacities of the Si-CNT-C (C_2H_2) electrode were 4.93 mAh/cm^2 (3171 mAh/g of a specific capacity and 247 mAh/cm^3 of a volumetric capacity) and 3.84 mAh/cm^2 (2468 mAh/g, 192 mAh/cm^3) respectively with 77.8% of coulombic efficiency. However, the capacity gradually dropped in the subsequent cycles to 0.17 mAh/cm^2 (108 mAh/g, 9 mAh/cm^3) with 99.8% of coulombic efficiency after 300 cycles.

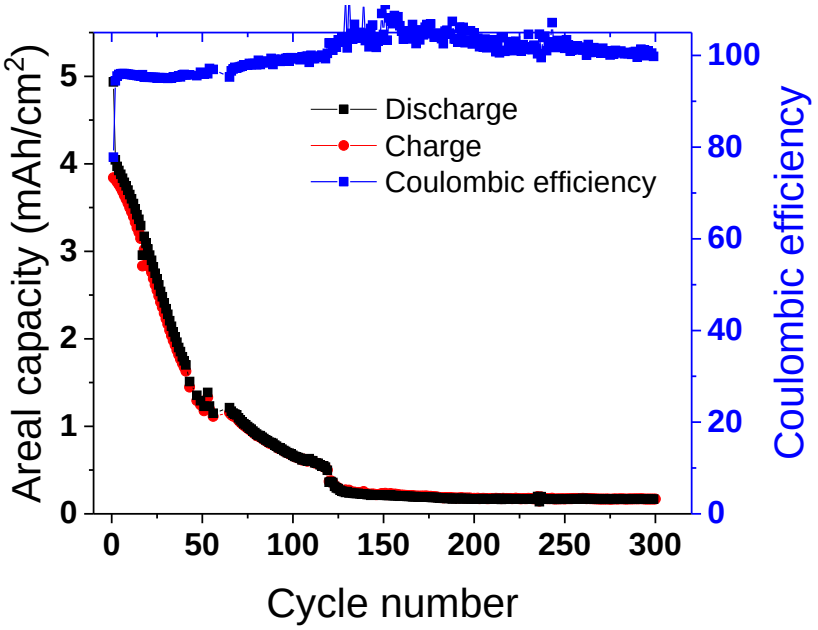


Figure 5.11. The charge-discharge graph of the Si-CNT-C (C_2H_2) electrode (Case II) showing the areal capacity of 0.17 mAh/cm² after 300 cycles at C/5 rate.

A plateau in the voltage profile of the Si-CNT-C (C_2H_2) (Figure 5.12A) and a peak at 0.14 V in the dQ/dV graph of the material (Figure 5.12B), found only in the first cycle, corresponded to the lithiation of crystalline Si in the two-phase region [23]. Both the cathodic peaks and the anodic peaks revealed only the features of the Si lithiation/delithiation. That is, no peak of SiC was observed compared to the previous Si-CNT-C (CH_4) electrode.

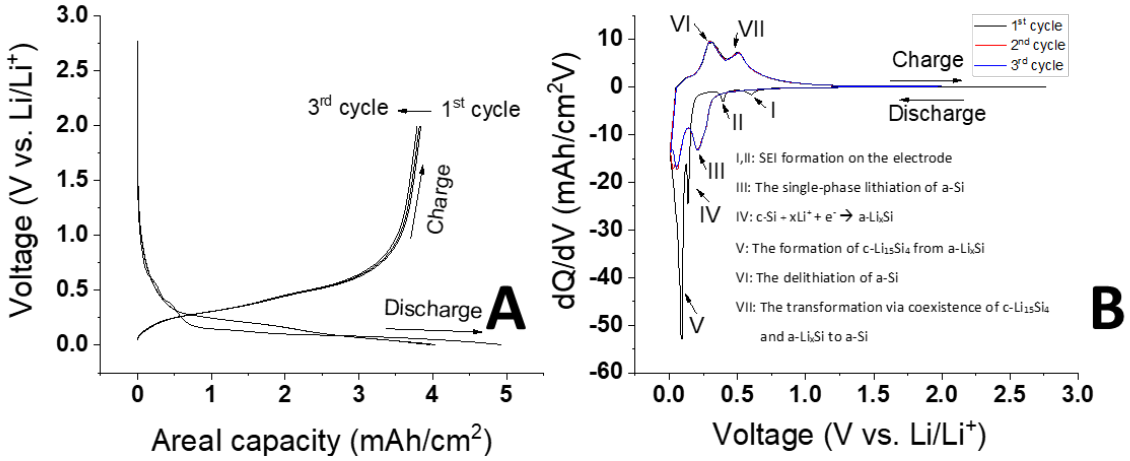


Figure 5.12. A) The voltage profiles of Si-CNT-C (C_2H_2) revealing a plateau at 0.14 V in the 1st cycle which confirms the lithiation of crystalline Si in the two-phase region, and B) the differential areal capacity plot revealing the lithiation/delithiation process of the Si-CNT-C (C_2H_2) electrode.

When comparing Case I and Case II (Figure 5.13), it was confirmed that the Si-CNT with amorphous carbon coating was not sufficient to boost the capacity retention of the Si-CNT electrode. Although the amorphous carbon maintained coverage of the Si NPs during volume expansion and prevented the Si NPs from direct exposure to the electrolyte, resulting in SEI formation only on its surface, Si NPs were still able to detach from MWCNTs. Also, Case I showed that the presence of SiC improves the battery performance of the electrode, relative to the presence of SiC. Thus, the development of the SiC at the interface between Si and MWCNTs in the Si-CNT material needs to be examined further as it expects to address the detachment of Si NPs leading to the advancement of the battery performance.

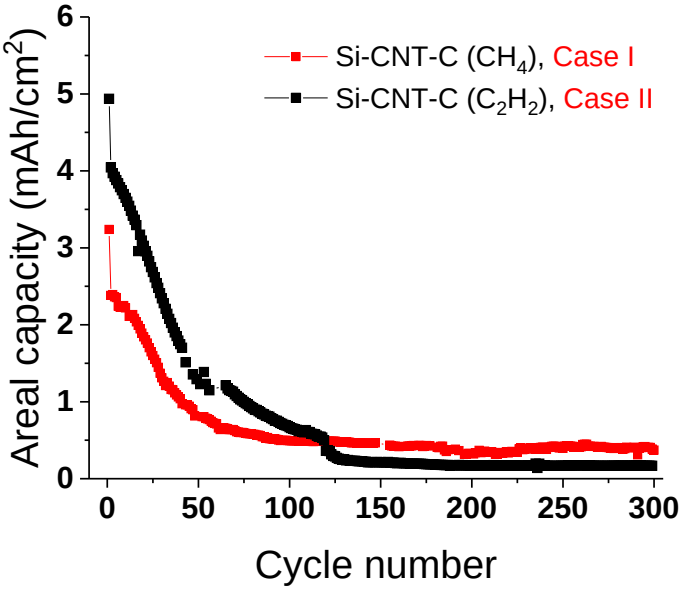


Figure 5.13. The battery performance of Si-CNT-C (CH_4) (Case I) and Si-CNT-C (C_2H_2) (Case II) confirming the superior stability of the Si-CNT-C (CH_4) (Case I) due to a presence of SiC in the material.

5.4.5) Morphological, structural, and chemical characterisation of the Si-CNT-SiC-C material

According to the previous Si-CNT-C result, it was decided to further develop the SiC interface between the two materials through a thermal annealing method. The phase diagram of the Si-C system indicates that the formation of SiC from silicon and carbon materials can occur at 1000 ºC (Supporting Figure 5.4) [24]. According to thermodynamic data, at room temperature, the Si-C reaction to form SiC has a negative free energy of formation; thus, SiC theoretically forms at a lower temperature via the Si-C reaction [25]. This study aimed at forming a SiC interface in the material instead of changing Si to SiC completely due to the poor electrochemical properties of SiC. Hence, the annealing temperature of the Si-CNT was varied in order to achieve this objective.

When annealing the Si-CNT-SiC-C material at 990 ºC and 1000 ºC, the Si NPs were partially immersed into the wall of the MWCNTs (Figure 5.14A-B). Since Si was not molten at this temperature and diffusion of Si atoms was slow [26, 27], SiC initially formed at the interface between Si NPs and MWCNTs due to the reaction between carbon atoms of MWCNTs and Si. Additionally, previous work suggested that the formation of Si-C chemical bonding often occurs at the MWCNT surface, which contained defects and disordered carbon [1]. However, most of the Si NPs were found located inside the walls of the MWCNTs upon increasing the annealing temperature to 1100 ºC (Figure 5.14C) and finally fully interacted with the MWCNTs at 1200 ºC causing complete conversion to SiC (Figure 5.14D). It was found that the Si NP was molten in this temperature and transformed its structure before SiC formation. The details will be discussed further.

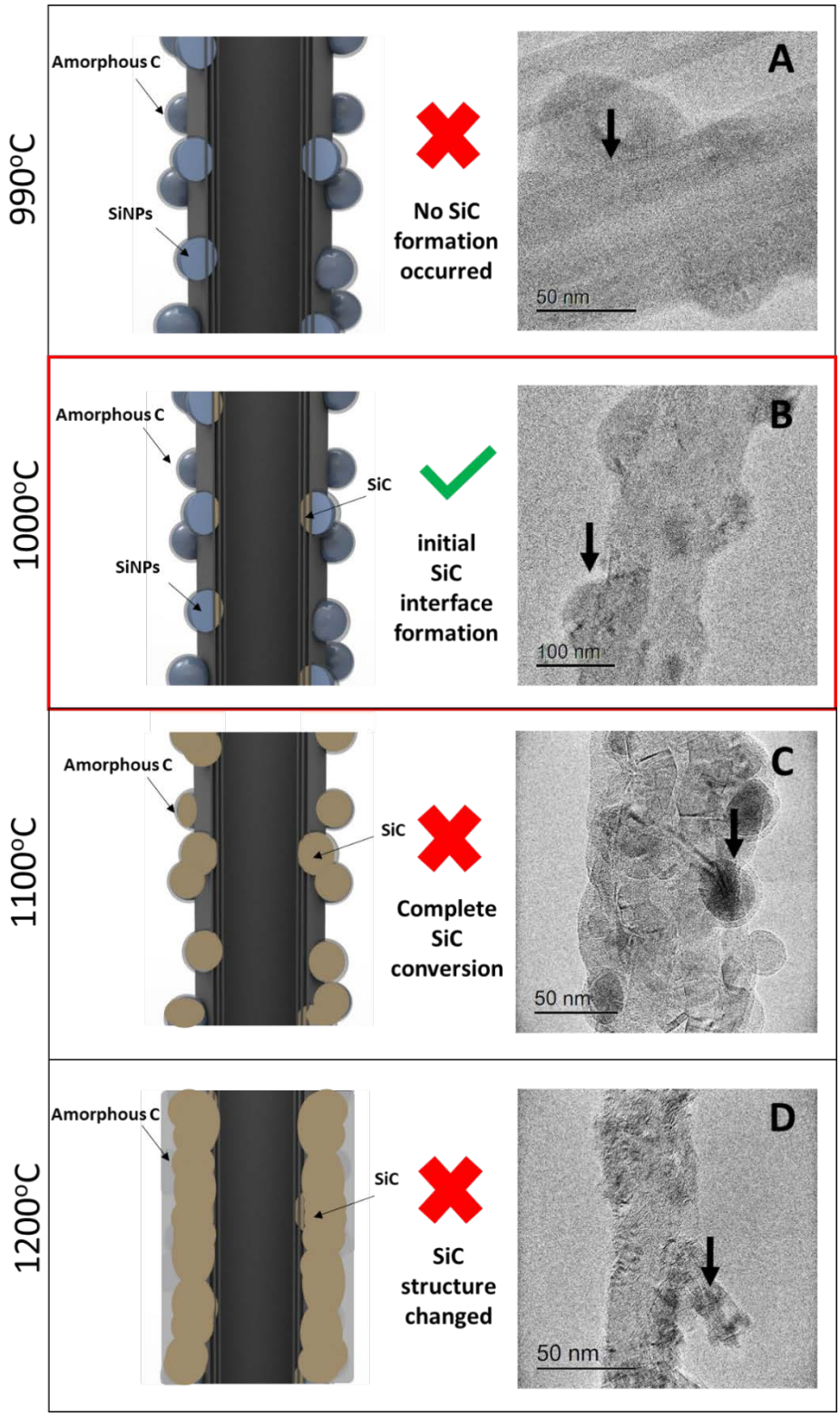


Figure 5.14. Schematic and TEM images of Si-CNT-SiC-C materials showing the SiC formation in the material at the different annealing temperature conditions A) 990 °C, B) 1000 °C, C) 1100 °C and D) 1200 °C; the SiC initially formed when the temperature reaching 1000 °C and the Si NP immersed inside MWCNTs to completely form SiC at 1100-1200 °C.

High-resolution TEM analysis was carried out to confirm the formation of the SiC interface in the Si-CNT-SiC-C (990-1000 °C) (Figure 5.15). In the 990 °C condition, only the lattice spacing of the Si was observed in the material (Figure 5.15B). However, when increasing the temperature to 1000 °C, the Si NPs clearly showed resolvable lattice spacings of 0.31, 0.25, and 0.34 nm corresponding to the (111) planes of Si, SiC, and MWCNT, respectively (Figure 5.15D). Thus, the β-SiC interface was formed between Si NPs and MWCNTs after annealing the material at the temperature higher than 1000 °C; that is, the carbon atom of MWCNT was partly consumed to the reaction with Si to form SiC interface at this temperature, which is in agreement with the previous study [1]. Note, the reaction of Si and C below the eutectic temperature (1404 °C) frequently forms β-SiC (cubic SiC, zincblende structure) which is the most stable phase of SiC at a temperature below 2545 °C [28].

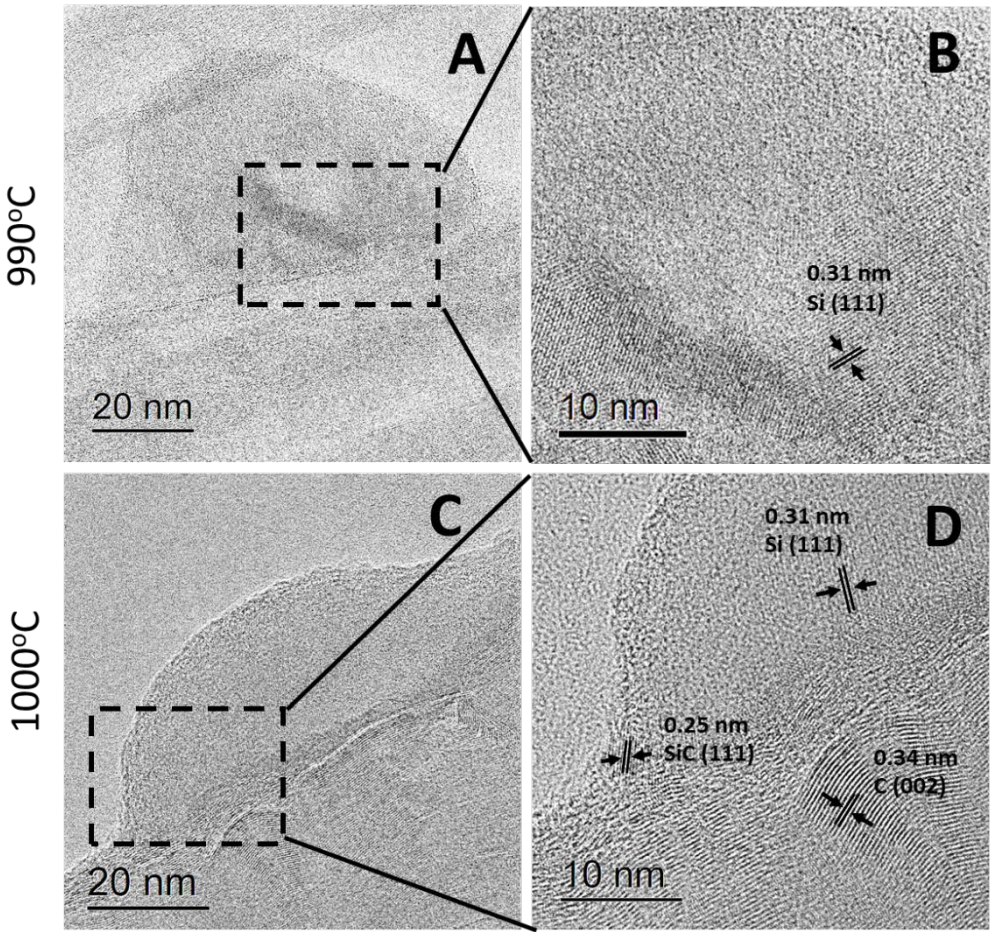


Figure 5.15. HRTEM images of Si-CNT-SiC-C materials annealed at A-B) 990 °C and C-D) 1000 °C ; the observed lattice spacing confirms the silicon carbide formation after increasing the annealing temperature to 1000 °C.

The Si-CNT materials were annealed to 1100 °C and 1200 °C, and the corresponding TEM images of these Si-CNT-SiC-C materials are shown in Figure 5.16. The Si NPs almost entirely transformed to SiC at 1100 °C (Figure 5.16B). The Si lattice spacing was hardly seen in this Si-CNT-SiC-C condition, and most Si NPs were submerged inside the wall of the nanotubes. When the annealing temperature is higher, the MWCNT walls were more damaged due to the formation of β-SiC. Lastly, the Si NPs at 1200 °C entirely changed to the SiC layer on the surface of the MWCNTs as seen in Figure 5.16D. It was expected that the Si NP melted and changed its structure before the formation of SiC took place in the liquid phase instead of the solid phase. This is due to the high temperature during the experiment, since the melting point of Si NPs is less than that of the bulk Si (1414 °C) [29, 30].

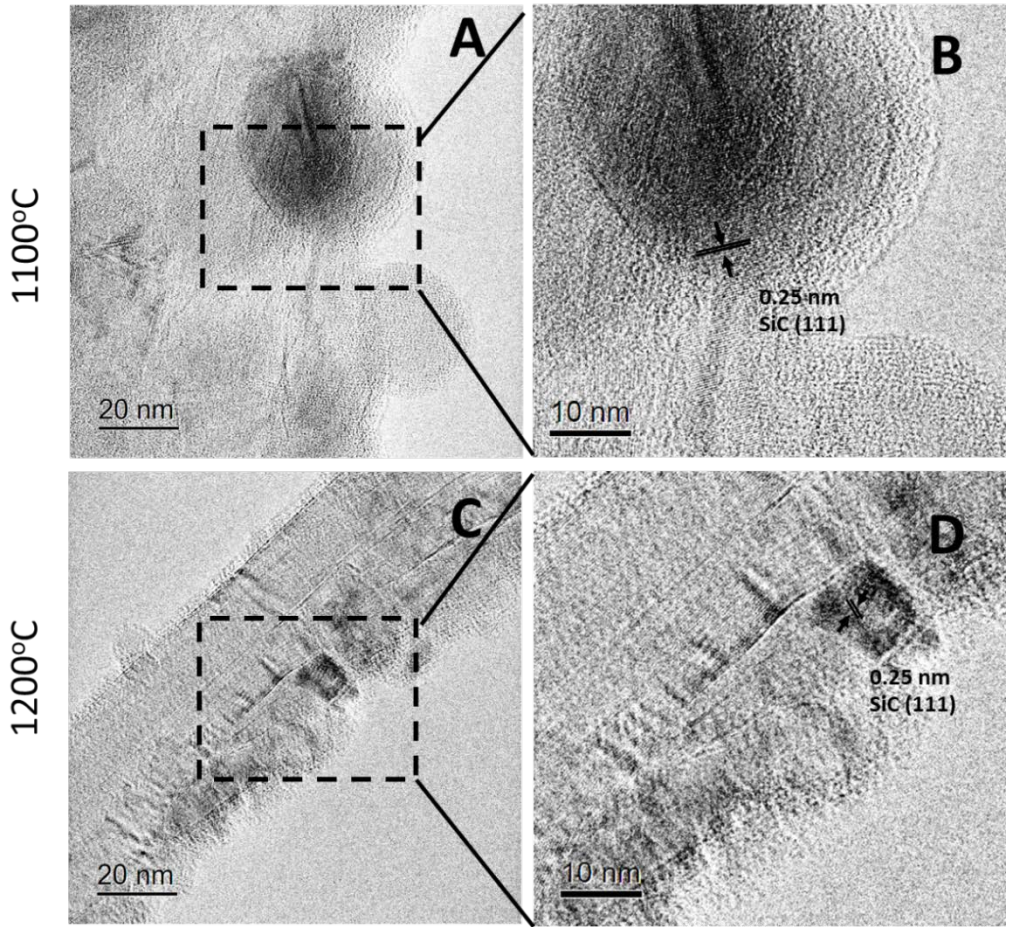


Figure 5.16. HRTEM images of Si-CNT-SiC-C materials annealed at A-B) 1100 °C and C-D) 1200 °C; the Si was almost completely converted to SiC after 1100 °C, SiC also changed to a layered structure after increasing the temperature to 1200 °C.

All Si-CNT-SiC-C conditions revealed SiC characteristic peaks at 35.7° and 60.1°, which corresponded to (111) and (220) planes of β-SiC (Figure 5.17). As a result, SiC was partly converted from Si in the Si-CNT-SiC-C material at 990 °C. Also, the Si-CNT-SiC-C annealed at 1000 °C presented the pure Si peaks at 28.5° and 47.4° which were assigned to (111) and (220) planes indicating the crystalline Si in the material. However, when increasing the annealing temperature to 1100 °C and 1200 °C, the Si-CNT-C materials exhibited only SiC peaks; no Si peaks could be observed. Thus, pure Si completely changed to SiC at these high temperatures in agreement with the previous TEM images.

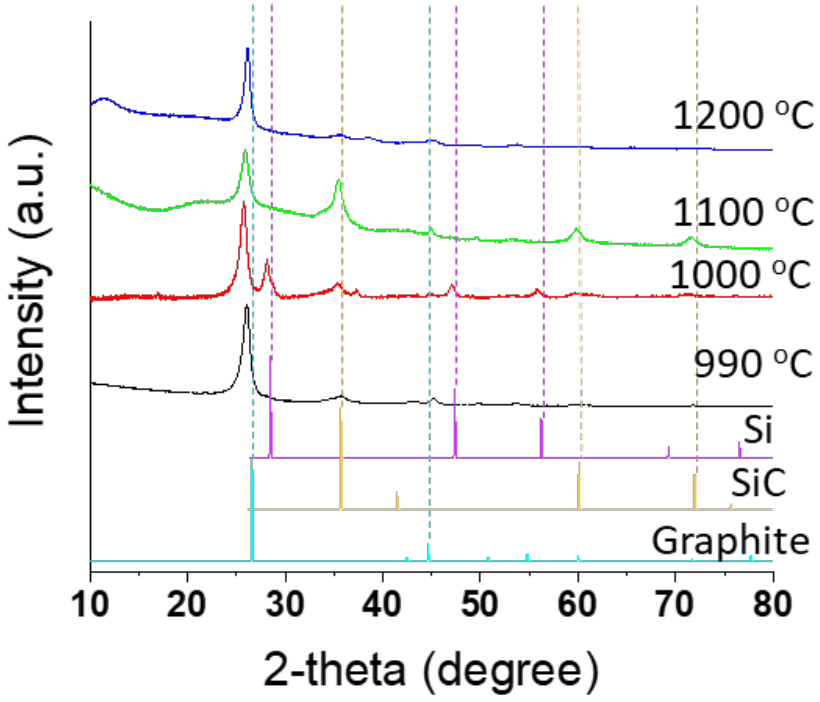


Figure 5.17. XRD patterns of Si-CNT-SiC-C materials showing the change of the Si structure at different annealing temperature conditions; SiC was partly formed at 1000 °C as Si peak can be still detected in this material condition but Si completely converted to SiC at 1100 °C.

Following the results of the previous analysis, The Si-CNT-SiC-C (1000 °C) was selected for further study as it consisted of both Si and a SiC interface. The Si-CNT-SiC-C was characterised by the selected area of the material for electron diffraction (ED) to examine the SiC interface formation. This selected area electron diffraction (SAED) pattern as shown in Figure 5.18B could be indexed to (111), (220), (113), (400) planes of Si, (111) plane of C, and (111) plane of β-SiC respectively. The nano-beam electron diffraction was performed to further analyse the interfacial SiC between Si NPs and

MWCNTs (Figure 5.18C-D). The nano-beam diffraction pattern (NBDP) recorded at the specific Si particle was assigned to (111) plane of Si, (111) plane of C, and (200), (113) planes of β-SiC, confirming SiC interface in the Si-CNT-SiC-C material.

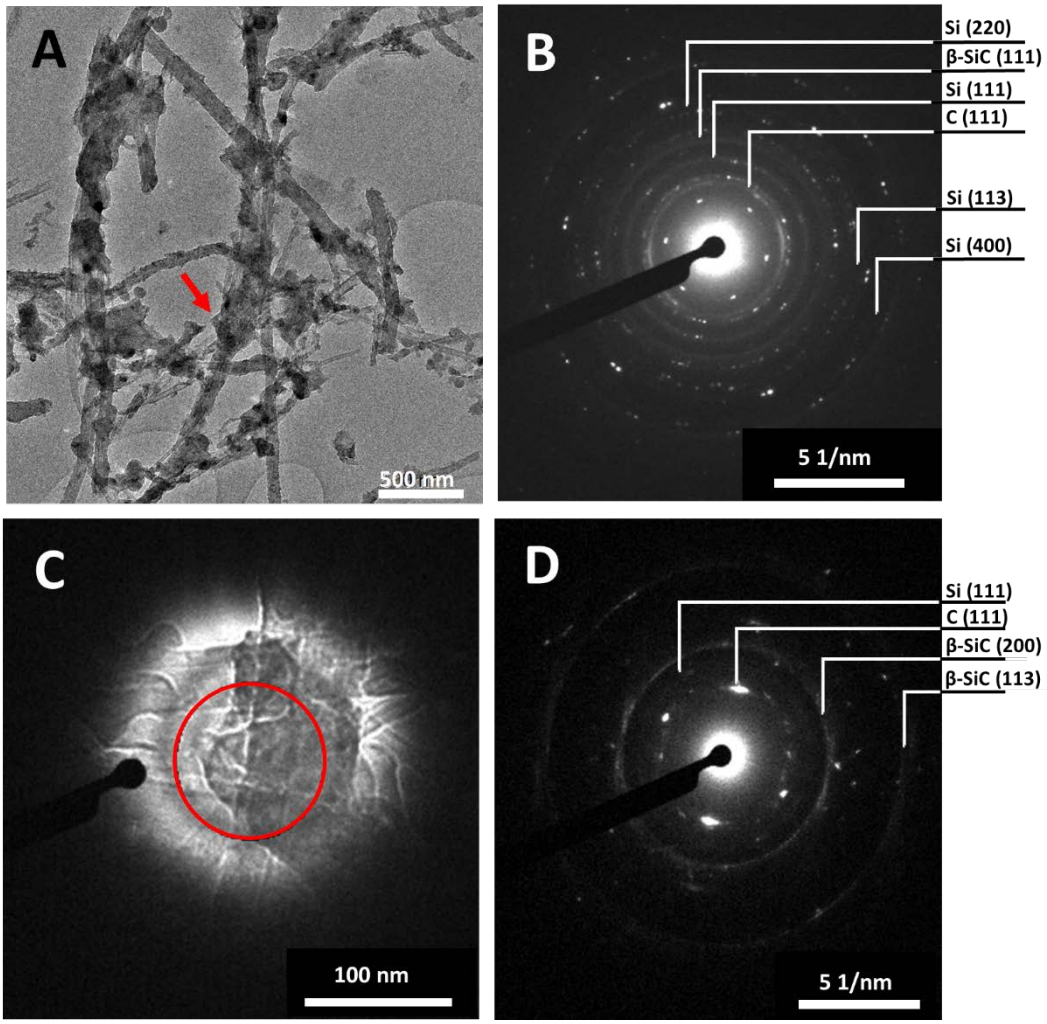


Figure 5.18. A) SEM image showing the selected area of the material for studying the electron diffraction, B) electron diffraction pattern from the area revealing the diffraction pattern of SiC, C) SEM image showing selected particle for electron diffraction, and D) NBDP from the area confirming the silicon carbide interface of the Si-CNT-SiC-C material (1000 °C annealing temperature condition).

The cross-sectional SEM images and EDX data of the Si-CNT-SiC-C (1000 °C) material are presented in Supporting Figure 5.5 to show the morphology of the material before testing the battery performance. The Si-CNT-SiC-C (1000 °C) electrode was around 200 μm thick and loose bundles of MWCNTs within BP 45 created open channels for electrolyte transport through the electrode.

The electrical conductivity of these Si-CNT based materials is presented in Table 5.1. As reported in the previous chapter, the Si-CNT material exhibited lower electrical conductivity (15.5 S/cm) than the pure BP 45 due to the low conductivity of Si. Nonetheless, the electrical conductivity of the Si-CNT-SiC-C (1000 °C) material increased to 25 S/cm, which was better than that of the Si-CNT based materials and other conventional Si electrodes. Its electrical conductivity was also higher than the minimum electrode conductivity for achieving fast-rate cycling (0.01 S/cm) [31, 32]. Therefore, the excellent conductivity of both BP 45 and the amorphous carbon, as well as better contact at the SiC interface in the material could potentially lead to the Si-CNT-SiC-C electrode being utilised as a binder-free and current-collector-free anode.

Table 5.1. The conductivity of the as-prepared materials showing the good conductivity of the free-standing Si-CNT-SiC-C materials compared to other materials.

Sample	Conductivity (S/cm)	Reference
Buckypaper (BP 45)	**22.22**	**This work**
Si-CNT	**15.50**	**This work**
Si-CNT-C	**17.66**	**This work**
Si-CNT-SiC-C	**25.02**	**This work**
Buckypaper made from commercial MWCNTs (C-BP)	**16.02**	**This work**
Conventional Si nanopowder electrode	$1.4x10^{-3}$	[5]
Si and C coated VACNTs	0.33	[5]
Pure Si	$4x10^{-6}$	[33]
Pure SiC	*ca.* $1.7x10^{-1}$	[34]
Carbon film	1	[35]

5.4.6) Cell fabrication and electrochemical tests of the Si-CNT-SiC-C electrode

The coin-cells were fabricated using the Si-CNT-SiC-C (1000 °C) material to test the battery performance. The Si-CNT-SiC-C electrode showed good stability over 300 cycles, although the areal capacity was not high. This Si-CNT-SiC-C electrode presented the first charge and discharge capacities of 2.01 mAh/cm^2 (2853 mAh/g of a specific capacity, 101 mAh/cm^3 of a volumetric capacity) and 1.18 mAh/cm^2 (1675 mAh/g, 59 mAh/cm^3) respectively, accounting for 58.7% of coulombic efficiency (Figure 5.19). The low coulombic efficiency of Si-CNT-SiC-C comparing to Si-CNT was

attributed to the irreversible reaction of SiC interface in the materials; the Li ions were consumed to form the Li_xSi_yC resulting in a high irreversible capacity (as shown in Equation 5.3). The irreversible capacity in the first cycle was also due to SEI layer formation, which could be improved further by electrolyte additives. This electrode showed promising performance which was stable at *ca.* 0.65 mAh/cm^2 with 99% coulombic efficiency after the 100^{th} cycle. After cycling over 300 cycles at the C/5 rate, this electrode had good capacity retention. The 300^{th} discharge capacity of the Si-CNT-SiC-C electrode was 0.55 mAh/cm^2 (775 mAh/g, 28 mAh/cm^3) with over 99.7% of coulombic efficiency. The good stability of the Si-CNT-SiC-C electrode was due to the strong SiC interface between Si NPs and MWCNTs. Nevertheless, the low areal capacity of the Si-CNT-SiC-C electrode resulted from low capacity of SiC material and a small amount of Si in the material; Si was used to form the SiC interface whose electroactivity is lower. The incomplete conversion reaction of SiC (Equation 5.1) also reduced the capacity of the electrode. Additionally, the volumetric capacity of the Si-CNT-SiC-C was relatively poor for implementation as a commercial anode material. This was caused by a low material density of the Si-CNT-SiC-C electrode due to the high porosity of BPs (calculation shown in the previous chapter) and small amounts of initial Si loading. Note, other Si-CNT-SiC-C materials made at different annealing temperature conditions were studied for electrochemical performance (Supporting Figure 5.6). It confirmed that the Si-CNT-SiC-C (1000 °C) electrode had a better battery performance than other Si-CNT-SiC-C electrodes.

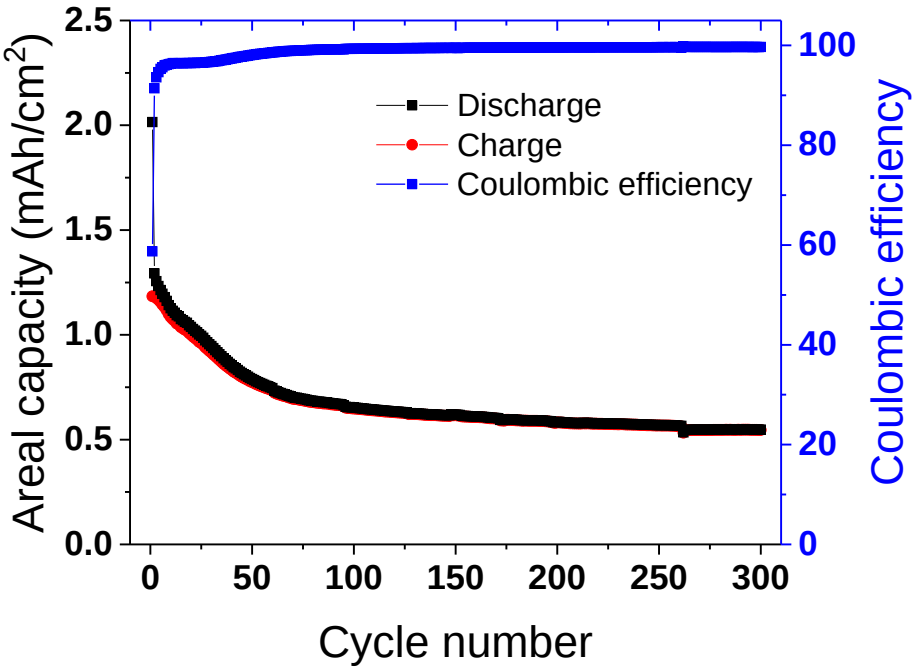


Figure 5.19. The charge-discharge graph of the Si-CNT-SiC-C (1000 °C) electrode showing the areal capacity of 0.55 mAh/cm² after 300 cycles at C/5 rate.

The charge-discharge characteristic curves, as well as the dQ/dV graphs, are presented in Figure 5.20. The plateau of the first discharge at 0.7 V (Figure 5.20A) was attributed to the SEI formation, which matched with a peak of the first cycle in Figure 5.20B. In the 1st cycle of the dQ/dV graph, the sharp cathodic peak at 0.15 V was assigned to the two-phase lithiation of crystalline Si [23, 36] which is in agreement with the flat plateau at 0.15 V of the initial discharge curve. The slope voltage profile and the bell-shaped cathodic peaks at 0.22 and 0.1 V seen in the 2nd and 3rd cycle referred to the lithiation of single-phase amorphous Li_xSi with different site energy in the structure [37]. In terms of anodic peaks, the peaks at 0.32 V and 0.47 V indicated the phase transition from Li-Si alloys to amorphous Si [23, 38] and a reaction of two phases of crystalline $Li_{15}Si_4$ and amorphous Li_xSi respectively [37].

The additional oxidation peak at 0.12 V which was found as a small peak in the Si-CNT-C (CH_4) electrode, was observed in the Si-CNT-SiC-C material. The peak was assigned to the reaction of Li with SiC in the material [12]. The possible reaction mechanism of Li with SiC was shown in

Equation 5.1. The reversible reaction of SiC with Li indicating the active role of the SiC interface. Note that the Si-CNT-SiC without amorphous carbon coating was also synthesised and its structure is presented in Supporting Figure 5.7. The result confirmed that the existence of the amorphous carbon layer also improved the performance of the Si-CNT-SiC material by preserving the structural stability and preventing direct contact between Si NPs and the electrolyte (Supporting Figure 5.8). Thus, the SEI formation was limited to the outer surface of the flexible amorphous carbon; the unstable SEI formation caused by the volume change of the Si material was reduced. Nevertheless, the poor battery performance of pure SiC electrodes (commercial and in-house SiC) confirmed the low electroactivity of pure SiC in LIBs (Supporting Figure 5.9-5.10).

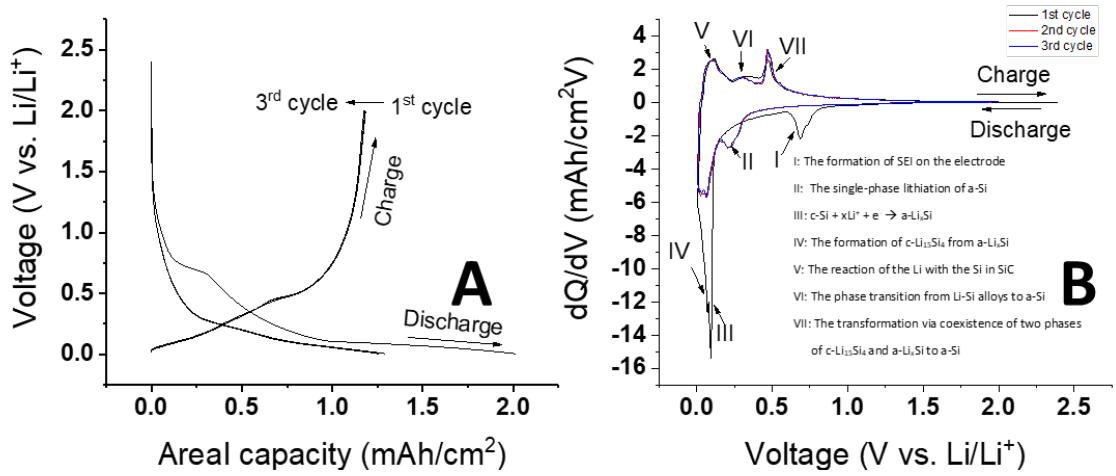


Figure 5.20. A) The voltage profiles of the Si-CNT-SiC-C (1000 °C) electrode showing a plateau at 0.15 V in the first cycle which attributes to the two-phase lithiation of crystalline Si in the material, and B) the differential areal capacity plot of the Si-CNT-SiC-C electrode showing Li ion storage mechanism of the electrode.

Compared to the BP 45, both the SiC interface and an amorphous carbon coating of the Si-CNT-SiC-C could enhance the stability of the electrode (Figure 5.21A). This electrode showed good capacity retention with the areal capacity of 0.95 mAh/cm^2 after 100 cycles which was double that of the BP 45 (0.46 mAh/cm^2). Also, the rate capability of BP 45 and Si-CNT-SiC-C electrodes was investigated, shown in Figure 5.21B. The Si-CNT-SiC-C electrode indicated a reasonable rate capability compared to BP 45. The first charge and discharge capacities of the Si-CNT-SiC-C electrode at C/10 were 4.59 and 3.65 mAh/cm^2, respectively, with a coulombic efficiency of 79%. The

coulombic efficiency was around 96% after the 2nd cycle. When the cycle rate was increased to C/5, C/2, and C, the Si-CNT-SiC-C electrode exhibited areal capacities of 2.3, 0.87 and 0.27 mAh/cm^{2,} respectively. Upon decreasing the C-rate back to C/10, the areal capacity rapidly increased to 2.10 mAh/cm^2. Therefore, the good capacity retention and rate capability confirmed the battery performance enhancement of Si-CNT-SiC-C anode.

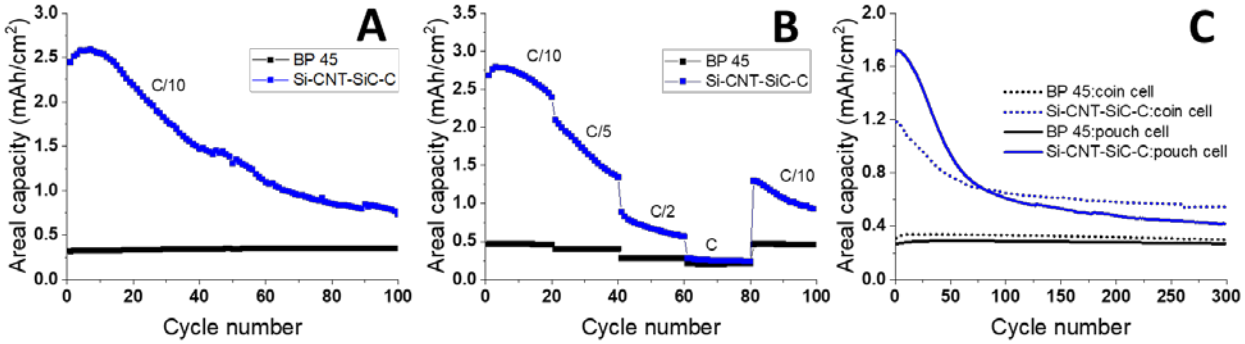


Figure 5.21. A) The areal capacity graph of BP 45 and Si-CNT-SiC-C electrodes tested at C/10 showing that the capacity of Si-CNT-SiC-C electrode (0.95 mAh/cm²) is double to that of the pure BP electrode (0.46 mAh/cm²) after 100 cycles, B) the rate capability graph of these electrodes showing superior battery performance of Si-CNT-SiC-C than the buckypaper at the fast C-rates, and C) the areal capacity plot of buckypaper and Si-CNT-SiC-C coin cells and pouch cells carried out at 1 mA showing the influence of the coin-cell components on the battery performance of the free-standing electrodes.

5.4.7) The battery performance of the Si-CNT-SiC-C pouch cell

Considering negative/positive (N/P) ratio of full cell batteries, the battery performance of the Si-CNT-SiC-C electrode was relatively acceptable for a commercial $LiCoO_2$ cathode. Moreover, to confirm the performance of the free-standing Si-CNT-SiC-C electrode by eliminating the stainless-steel effect in the coin cell configuration, pouch cells were fabricated. The Si-CNT-SiC-C electrode in the pouch cell still showed better performance than BP 45 (Figure 5.21C). The Si-CNT-SiC-C electrode demonstrated an areal capacity of 1.69 mAh/cm^2 during the first cycle, which steadily decreased to approximately 0.45 mAh/cm^2 at 300 cycles. The results indicated that the areal capacity between these two electrodes was not significantly different. That is, the battery capability mostly resulted from the Si-CNT-SiC-C electrode rather than other components of the battery. Therefore, these Si-CNT-SiC-C materials are promising for use as free-standing electrodes in LIBs.

5.4.8) Post-cycling analysis of the Si-CNT-SiC-C electrode

To study change of the electrode morphology after the 300 cycling tests, the Si-CNT-SiC-C cell was disassembled for a post-cycling analysis. Cross-sectional SEM images of the Si-CNT-SiC-C electrode post-cycling are shown in Figure 5.22. The thickness of the Si-CNT-SiC-C material changed to 310 microns after battery cycling, indicating the effect of Si volume expansion (Figure 5.22C). The material became dense with small voids which is considerably different from the material tested before (Figure 5.22D). It was suspected that the electrolyte diffused through the BP 45 pores to form a thick SEI layer inside the pores [39]. Thus, the interior SEI formation result could explain the high irreversible capacity of the Si-CNT-SiC-C electrode during the first few cycling. Thus, this issue could be addressed by using electrolyte additives which will be discussed in the next chapter.

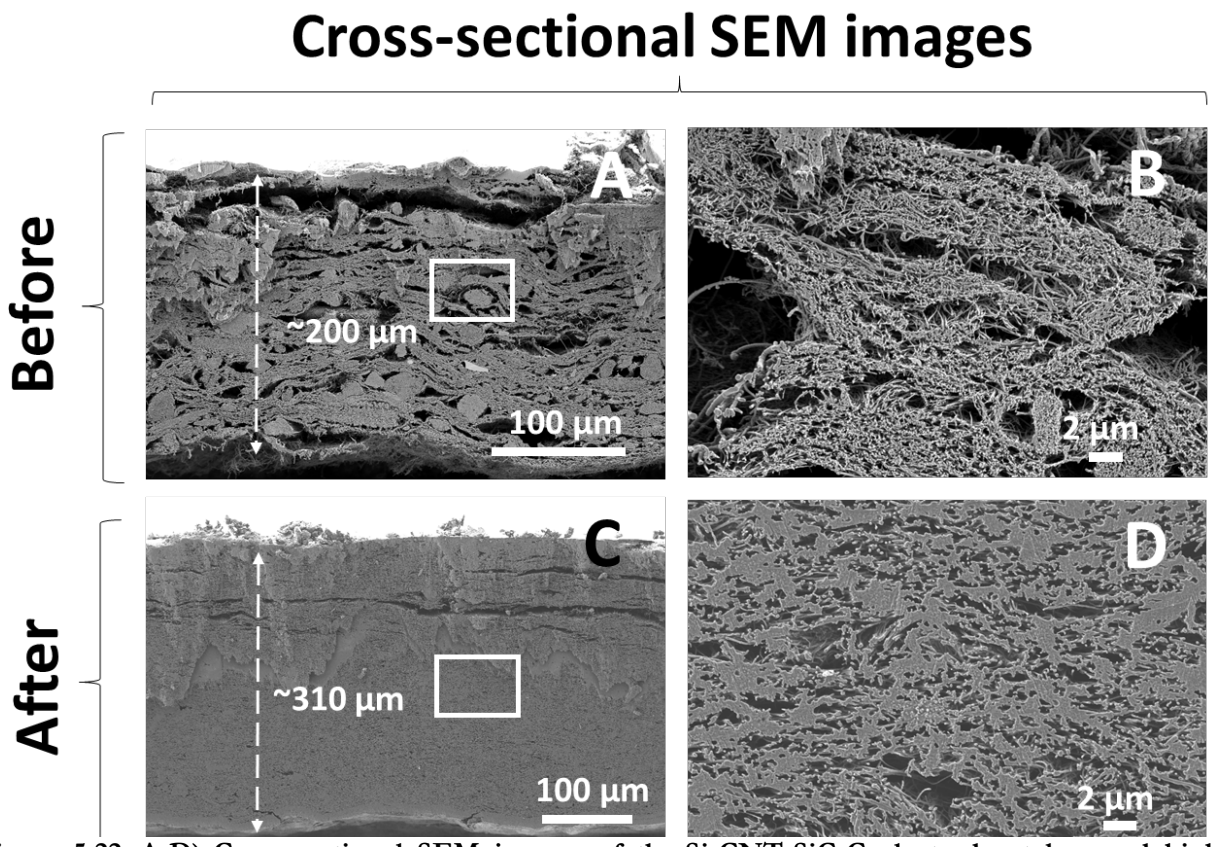


Figure 5.22. A-D) Cross-sectional SEM images of the Si-CNT-SiC-C electrode at low and high magnification before and after 300 cycles showing the increase in the electrode thickness from 200 microns to 310 microns after battery testing; voids in the BP also became smaller after cycling which is due to the SEI formation inside the pores.

Additionally, the surface of the Si-CNT-SiC-C electrode was smooth without cracking after 300-testing cycles (Figure 5.23C-D). That is, the Si-CNT-SiC-C material was not pulverised during cycling and still had a well-defined structure. Therefore, the strong SiC interface between Si NPs and MWCNTs (within the BP 45) could avoid the Si NP dislocation and the pulverisation of the electrode during repeated cycling. The SiC also acted as an interfacial buffer to alleviate the stress induced from the volume change of Si due to its high hardness. The structure of the material was thereby maintained without fractures. However, the coating formed on the material after cycling was believed to be the SEI layer (Figure 5.23D) which was confirmed by EDX measurements (Supporting Figure 5.11).

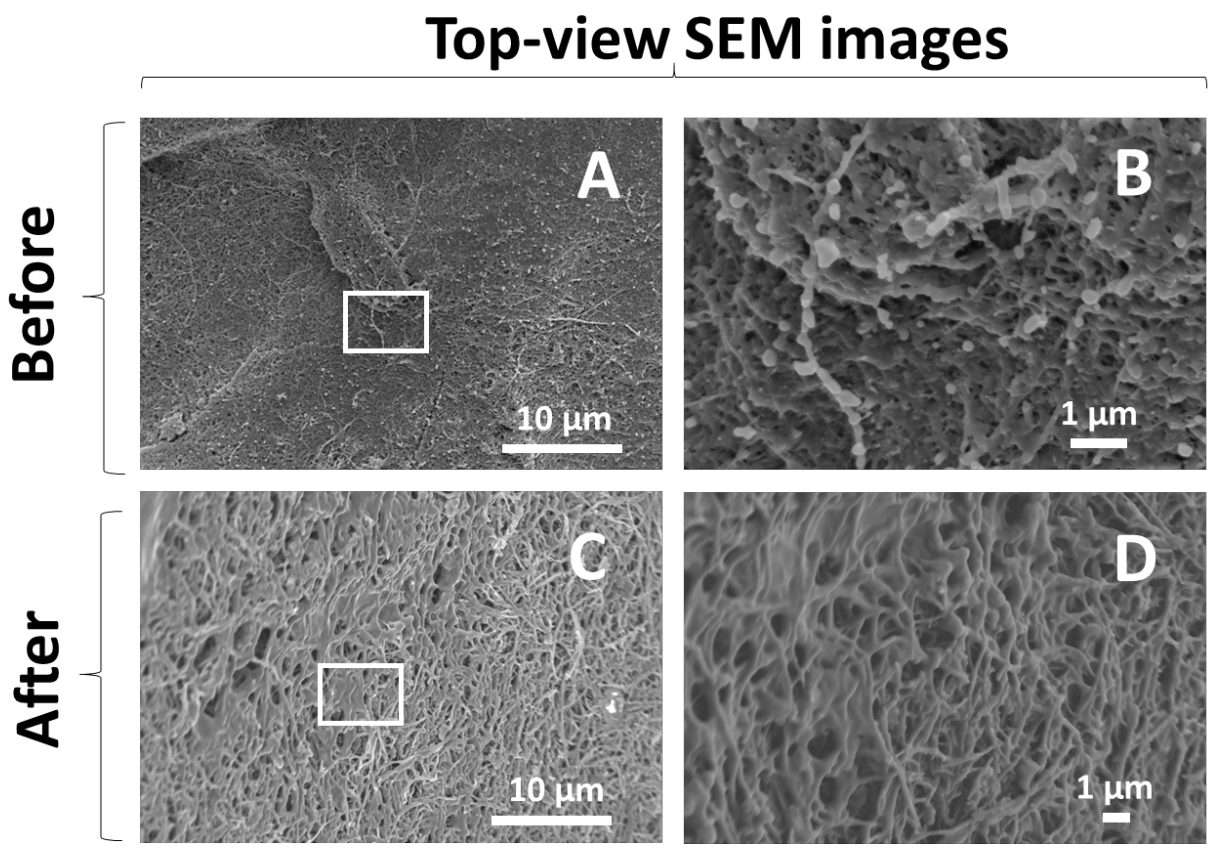


Figure 5.23. A-D) SEM images at a low and high magnification of Si-CNT-SiC-C surface before and after the 300-cycling test showing the thick SEI layer formation on the surface of the electrode after cycling; cracking cannot be observed on the electrode surface after 300th cycle of the battery testing.

It could be concluded that the Si-CNT-SiC-C electrode exhibited considerable improvement of cycling stability on account of the SiC interface in this material. However, the areal capacity of the Si-CNT-SiC-C electrode was lower than the Si-CNT and Si-CNT-C (C_2H_2) electrodes due to the presence of SiC whose electroactivity is low in the material (Figure 5.24A and summary in Table 5.2). Figure 5.24B shows the capacity difference between the 1st and 300th cycle which confirmed the good capacity retention of the Si-CNT-SiC-C electrode. Note, the areal capacity of the electrode was strongly dependent on the Si loading in the materials [40, 41]. Compared to previous studies (summary in Supporting Table 5.1), the Si-CNT-SiC-C electrode had better performance than the conventional Si/C coated on Cu electrode, although this material had Si loading below 1.1 mg/cm^2. The capacity of the anode electrodes also related to the current density since the capacity was higher at very low

current density than the capacity measuring at high current density. Therefore, it was difficult to distinguish the better anode materials among different experiments, especially considering that some of the initial Si loadings were consumed to create the SiC interface. Finally, the battery performance enhancement of the Si-CNT-SiC-C electrode was mostly attributed to the strong SiC interface between Si NPs and MWCNTs. The interfacial SiC securely bonds the Si NPs on the MWCNT walls, preventing the dislocation of the Si NPs and thus the pulverisation of the electrode during repeated cycling. The SiC could also minimise the induced stress due to the volume change of Si, confirmed by the conservation of the structural electrode after the post-cycling. In addition, the amorphous carbon coating provided the cohesion of the material and allowed only Li to penetrate through it into Si NPs; that is, the SEI layer was strictly formed on the surface of the amorphous carbon. The unstable SEI formation due to the volume change of the Si was then tackled, eventually improving the battery stability of the electrode.

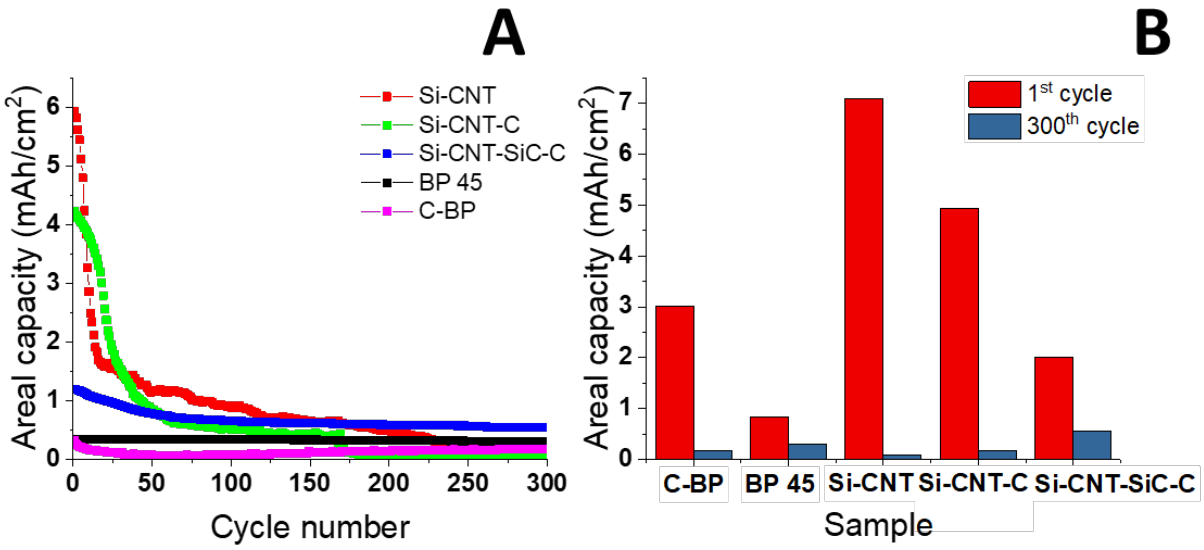


Figure 5.24. A) The areal capacity of all Si-CNT based electrodes tested at C/5 showing the best stability of the Si-CNT-SiC-C electrode when compared with the materials prepared in this work, and B) the bar chart showing the areal capacity of all materials at 1st cycle and 300th cycle; the areal capacity difference between 1st and 300th of Si-CNT-SiC-C electrode is the lowest indicating the best capacity retention after 300 cycles than other electrodes.

Table 5.2. The battery performance of all as-prepared electrodes showing the best battery performance of the Si-CNT-SiC-C electrode compared to other electrodes in this work.

Sample	Areal capacity (mAh/cm^2)		Specific capacity (mAh/g)		Volumetric capacity (mAh/cm^3)	
	1st cycle	300th cycle	1st cycle	300th cycle	1st cycle	300th cycle
Buckypaper (C-BP)	3.02	0.18	1500	90	302	18
Buckypaper (BP45)	0.84	0.30	297	106	70	25
Si-CNT	7.10	0.09	3758	49	355	5
Si-CNT-C (C_2H_2)	4.93	0.17	3171	108	247	9
Si-CNT-SiC-C	**2.01**	**0.55**	**2853**	**775**	**101**	**28**

5.5) Conclusions

In this chapter, the Si-CNT material was coated by amorphous carbon using two carbon sources, (Case I) methane gas and (Case II) acetylene gas. In Case I, the trace of SiC was observed in the fabricated material, while only amorphous carbon was deposited on the outer surface of Si NPs in Case II. After electrode fabrication in the coin-cell batteries, the battery performance of electrodes was examined in both Case I and Case II. The result indicated that SiC improved the battery performance and amorphous carbon layer coating in Case II was insufficient for electrode stability enhancement. Hence, SiC interface was further developed between Si NPs and MWCNTs by annealing the Si-CNT material at high-temperature range (990-1200 °C). After annealing at 1000 °C a partial SiC interface was introduced in the Si-CNT material. When increasing the annealing temperature to 1100 °C, Si was completely converted to SiC. Battery testing confirmed that the SiC interface enhanced the stability of the Si-CNT-SiC-C (1000 °C) electrode by firmly bonding Si NPs on the MWCNT surface and thus avoiding the disconnection of Si upon the cycling. The Si-CNT-SiC-C electrode showed the areal capacity of 0.55 mAh/cm^2 with 99.7% of coulombic efficiency after 300 cycles. However, higher concentrations of SiC in the material reduced battery performance

because of its poor electroactivity for Li storage. According to post-cycling analysis, the Si-CNT-SiC-C material maintained its original structure without cracks after battery cycling.

To conclude, the Si-CNT-SiC-C electrode showed better capacity retention compared to the conventional pure Si electrode and other Si-CNT based materials because of the development of the robust SiC interface and amorphous carbon coating on the material. The interfacial SiC prevented the detachment of Si NPs from MWCNT walls and thus the pulverisation of the electrode during repeated cycling. The SiC also suppressed the stress evolution from the volume expansion of Si upon lithiation due to its high hardness. Moreover, the amorphous carbon coating could reduce the unstable SEI formation during the cycling by hindering the direct contact between Si NPs and the electrolyte; the SEI formation was restricted on the flexible amorphous carbon layer during cycling. Nevertheless, the capacity enhancement of the Si-CNT-SiC-C material needs to be developed further due to the low performance resulting from the presence of SiC leading to poor electroactivity in the material. Notably, the volumetric capacity of the Si-CNT-SiC-C electrode is still inadequate for implementation as a commercial anode in LIBs because of low material density and high porosity of the electrode. Therefore, suggestions and future works will be presented in the next chapter.

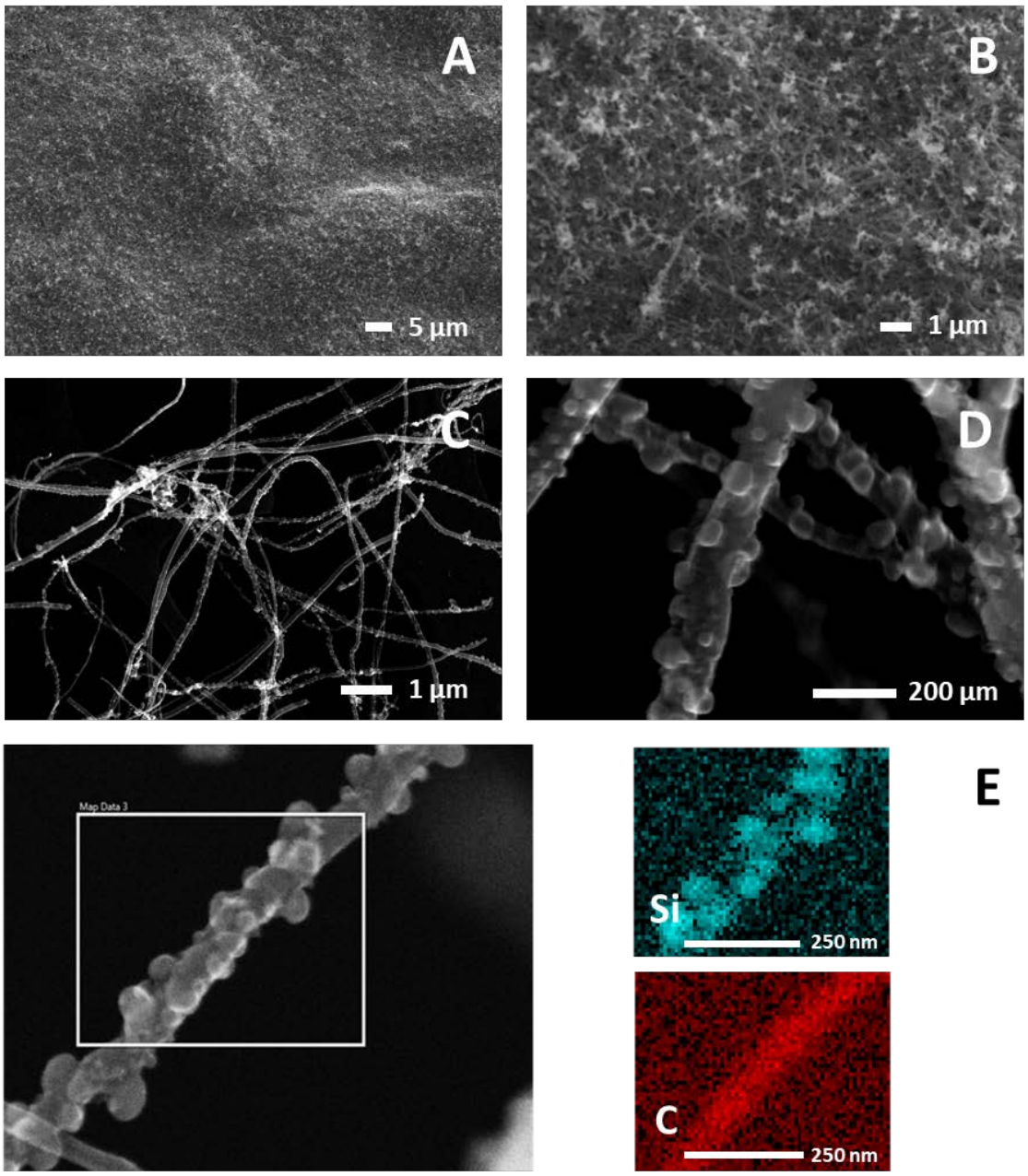
5.6) References

1. Jiang, Y., et al., *Interfacial engineering of Si/multi-walled carbon nanotube nanocomposites towards enhanced lithium storage performance.* Carbon, 2016. **107**: p. 600-606.
2. Su, L., Y. Jing, and Z. Zhou, *Li ion battery materials with core–shell nanostructures.* Nanoscale, 2011. **3**(10): p. 3967-3983.
3. Joe, M., et al., *An ideal polymeric C60 coating on a Si electrode for durable Li-ion batteries.* Carbon, 2014. **77**: p. 1140-1147.
4. Ng, S.H., et al., *Amorphous Carbon-Coated Silicon Nanocomposites: A Low-Temperature Synthesis via Spray Pyrolysis and Their Application as High-Capacity Anodes for Lithium-Ion Batteries.* The Journal of Physical Chemistry C, 2007. **111**(29): p. 11131-11138.
5. Evanoff, K., et al., *Towards Ultrathick Battery Electrodes: Aligned Carbon Nanotube – Enabled Architecture.* Advanced Materials, 2012. **24**(4): p. 533-537.
6. Liu, X.H., et al., *Ultrafast Electrochemical Lithiation of Individual Si Nanowire Anodes.* Nano Letters, 2011. **11**(6): p. 2251-2258.
7. Wang, W. and P.N. Kumta, *Nanostructured Hybrid Silicon/Carbon Nanotube Heterostructures: Reversible High-Capacity Lithium-Ion Anodes.* ACS Nano, 2010. **4**(4): p. 2233-2241.

8. Saint, J., et al., *Towards a Fundamental Understanding of the Improved Electrochemical Performance of Silicon–Carbon Composites.* Advanced Functional Materials, 2007. **17**(11): p. 1765-1774.
9. Chang, X., et al., *Direct plasma deposition of amorphous Si/C nanocomposites as high performance anodes for lithium ion batteries.* Journal of Materials Chemistry A, 2015. **3**(7): p. 3522-3528.
10. Wang, W. and P.N. Kumta, *Reversible high capacity nanocomposite anodes of Si/C/SWNTs for rechargeable Li-ion batteries.* Journal of Power Sources, 2007. **172**(2): p. 650-658.
11. Timmons, A., et al., *Studies of Si1 − x C x Electrode Materials Prepared by High-Energy Mechanical Milling and Combinatorial Sputter Deposition.* Journal of The Electrochemical Society, 2007. **154**(9): p. A865-A874.
12. Zhang, H. and H. Xu, *Nanocrystalline silicon carbide thin film electrodes for lithium-ion batteries.* Solid State Ionics, 2014. **263**(Supplement C): p. 23-26.
13. Huang, X.D., et al., *Electrochemical characteristics of amorphous silicon carbide film as a lithium-ion battery anode.* RSC Advances, 2018. **8**(10): p. 5189-5196.
14. Sri Devi Kumari, T., D. Jeyakumar, and T. Prem Kumar, *Nano silicon carbide: a new lithium-insertion anode material on the horizon.* RSC Advances, 2013. **3**(35): p. 15028-15034.
15. Hwang, J., et al., *Computational Evaluation of Amorphous Carbon Coating for Durable Silicon Anodes for Lithium-Ion Batteries.* Nanomaterials, 2015. **5**(4): p. 1654-1666.
16. German, R.M., *Sintering Trajectories: Description on How Density, Surface Area, and Grain Size Change.* JOM, 2016. **68**(3): p. 878-884.
17. Chou, S.-L., et al., *Silicon/Single-Walled Carbon Nanotube Composite Paper as a Flexible Anode Material for Lithium Ion Batteries.* The Journal of Physical Chemistry C, 2010. **114**(37): p. 15862-15867.
18. *Raman scattering of alternating nanocrystalline silicon/amorphous silicon multilayers.* Applied Physics Letters, 1996. **69**(4): p. 523-525.
19. Milovzorov, D.E., *Nonlinear Optoelectronic Devices Based on Nanocrystalline Silicon Films: Acoustoelectrical Switches for Optical Modes, Nonliear Optical Switches and Lasers*, in *Nanocrystal*. 2011, InTech: Rijeka. p. Ch. 0.
20. Katar, S., et al., *Silicon Encapsulated Carbon Nanotubes.* Nanoscale Research Letters, 2010. **5**(1): p. 74-80.
21. Liu, J.W., et al., *Synthesis of SiC nanofibers by annealing carbon nanotubes covered with Si.* Chemical Physics Letters, 2001. **348**(5): p. 357-360.
22. Wepasnick, K.A., et al., *Chemical and structural characterization of carbon nanotube surfaces.* Analytical and Bioanalytical Chemistry, 2010. **396**(3): p. 1003-1014.
23. Obrovac, M.N. and L.J. Krause, *Reversible Cycling of Crystalline Silicon Powder.* Journal of The Electrochemical Society, 2007. **154**(2): p. A103-A108.
24. Haase, V., et al., *The Si-C Phase Diagram*, in *Si Silicon: System Si-C. SiC: Natural Occurrence. Preparation and Manufacturing Chemistry. Special Forms. Manufacture. Electrochemical Properties. Chemical Reactions. Applications. Ternary and Higher Systems with Si and C*, V. Haase, et al., Editors. 1985, Springer Berlin Heidelberg: Berlin, Heidelberg. p. 1-5.
25. Ren, R., Z. Yang, and L.L. Shaw, *Synthesis of Nanostructured Silicon Carbide through an Integrated Mechanical and Thermal Activation Process.* Journal of the American Ceramic Society, 2002. **85**(4): p. 819-827.
26. Limandri, S., et al., *Pressure dependence of the silicon carbide synthesis temperature.* Journal of Applied Physics, 2019. **125**(16): p. 165902.
27. Wieligor, M., Y. Wang, and T.W. Zerda, *Raman spectra of silicon carbide small particles and nanowires.* Journal of Physics: Condensed Matter, 2005. **17**(15): p. 2387-2395.
28. Olesinski, R.W. and G.J. Abbaschian, *The C−Si (Carbon-Silicon) system.* Bulletin of Alloy Phase Diagrams, 1984. **5**(5): p. 486-489.
29. Durand, F. and J.C. Duby, *Carbon solubility in solid and liquid silicon—A review with reference to eutectic equilibrium.* Journal of Phase Equilibria, 1999. **20**(1): p. 61.
30. Rumble, J.R., *CRC handbook of chemistry and physics : a ready-reference book of chemical and physical data.* 2018.
31. Tian, R., et al., *Quantifying the Effect of Electronic Conductivity on the Rate Performance of Nanocomposite Battery Electrodes.* ACS Applied Energy Materials, 2020. **3**(3): p. 2966-2974.
32. Mistry, A., et al., *Analysis of Long-Range Interaction in Lithium-Ion Battery Electrodes.* Journal of Electrochemical Energy Conversion and Storage, 2016. **13**(3).

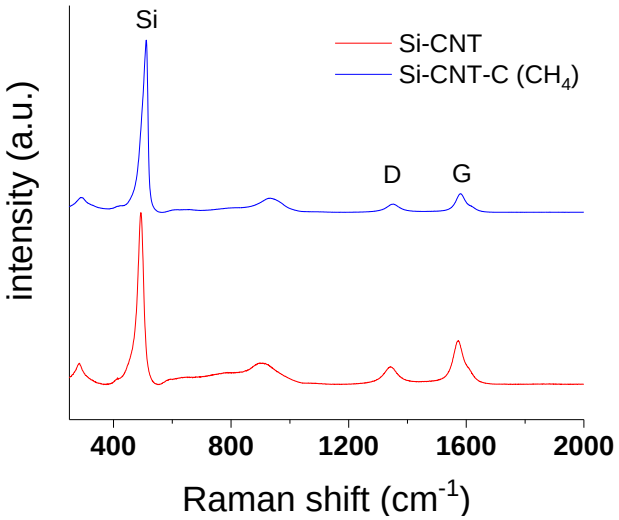
33. Halliday, D., R. Resnick, and J. Walker, *Fundamentals of Physics*. 2013: Wiley.
34. Wang, X.H., et al., *Thermoelectric properties of SiC thick films deposited by thermal plasma physical vapor deposition.* Science and Technology of Advanced Materials, 2003. **4**(2): p. 167-172.
35. Kupperman, D.S., C.K. Chau, and H. Weinstock, *Electrical resistivity of carbon films.* Carbon, 1973. **11**(3): p. 171-175.
36. Fu, K., et al., *Aligned Carbon Nanotube-Silicon Sheets: A Novel Nano-architecture for Flexible Lithium Ion Battery Electrodes.* Advanced Materials, 2013. **25**(36): p. 5109-5114.
37. Cui, L.-F., et al., *Crystalline-Amorphous Core−Shell Silicon Nanowires for High Capacity and High Current Battery Electrodes.* Nano Letters, 2009. **9**(1): p. 491-495.
38. Xu, B., et al., *Stabilization of silicon nanoparticles in graphene aerogel framework for lithium ion storage.* RSC Advances, 2015. **5**(39): p. 30624-30630.
39. Leveau, L., et al., *Silicon nano-trees as high areal capacity anodes for lithium-ion batteries.* Journal of Power Sources, 2016. **316**: p. 1-7.
40. Zhou, M., et al., *High-Performance Silicon Battery Anodes Enabled by Engineering Graphene Assemblies.* Nano Letters, 2015. **15**(9): p. 6222-6228.
41. Chen, Z., et al., *High-Areal-Capacity Silicon Electrodes with Low-Cost Silicon Particles Based on Spatial Control of Self-Healing Binder.* Advanced Energy Materials, 2015. **5**(8): p. 1401826-n/a.
42. Hong, J., et al., *Vertically-aligned silicon carbide nanowires as visible-light-driven photocatalysts.* Applied Catalysis B: Environmental, 2017. **218**(Supplement C): p. 267-276.
43. Wang, C., et al., *Synthesis of SiC decorated carbonaceous nanorods and its hierarchical composites Si@SiC@C for high-performance lithium ion batteries.* Journal of Alloys and Compounds, 2015. **646**(Supplement C): p. 966-972.
44. Biserni, E., et al., *Silicon algae with carbon topping as thin-film anodes for lithium-ion microbatteries by a two-step facile method.* Journal of Power Sources, 2015. **274**: p. 252-259.
45. Erika, B., et al., *High-performance flexible nanoporous Si-carbon nanotube paper anodes for micro-battery applications.* Nanotechnology, 2016. **27**(24): p. 245401.
46. Si, W., et al., *High areal capacity, micrometer-scale amorphous Si film anode based on nanostructured Cu foil for Li-ion batteries.* Journal of Power Sources, 2014. **267**: p. 629-634.
47. Wang, X., et al., *A hierarchical 3D carbon nanostructure for high areal capacity and flexible lithium ion batteries.* Carbon, 2016. **98**: p. 504-509.
48. Marinaro, M., M. Weinberger, and M. Wohlfahrt-Mehrens, *Toward pre-lithiatied high areal capacity silicon anodes for Lithium-ion batteries.* Electrochimica Acta, 2016. **206**: p. 99-107.

5.7) Supporting information

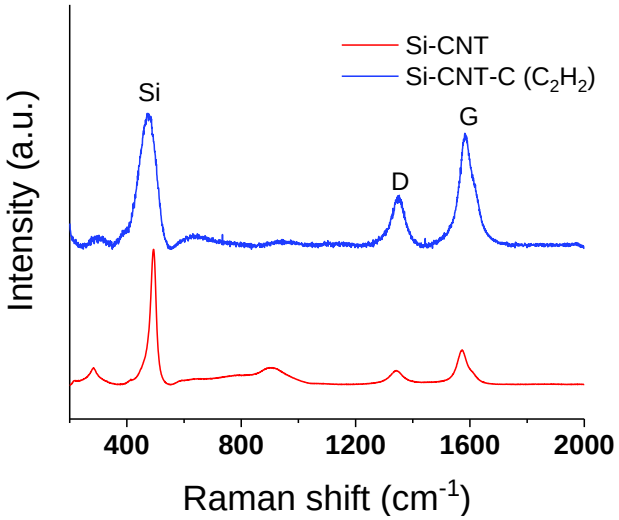


Supporting Figure 5.1. A-B) SEM images at low and high magnification showing the surface of the Si-CNT-C (CH_4) paper, C-D) STEM image of Si-CNT-C (CH_4) and E) EDX elemental mapping of silicon and carbon showing their uniform distribution within the composite material after the amorphous carbon coating was applied.

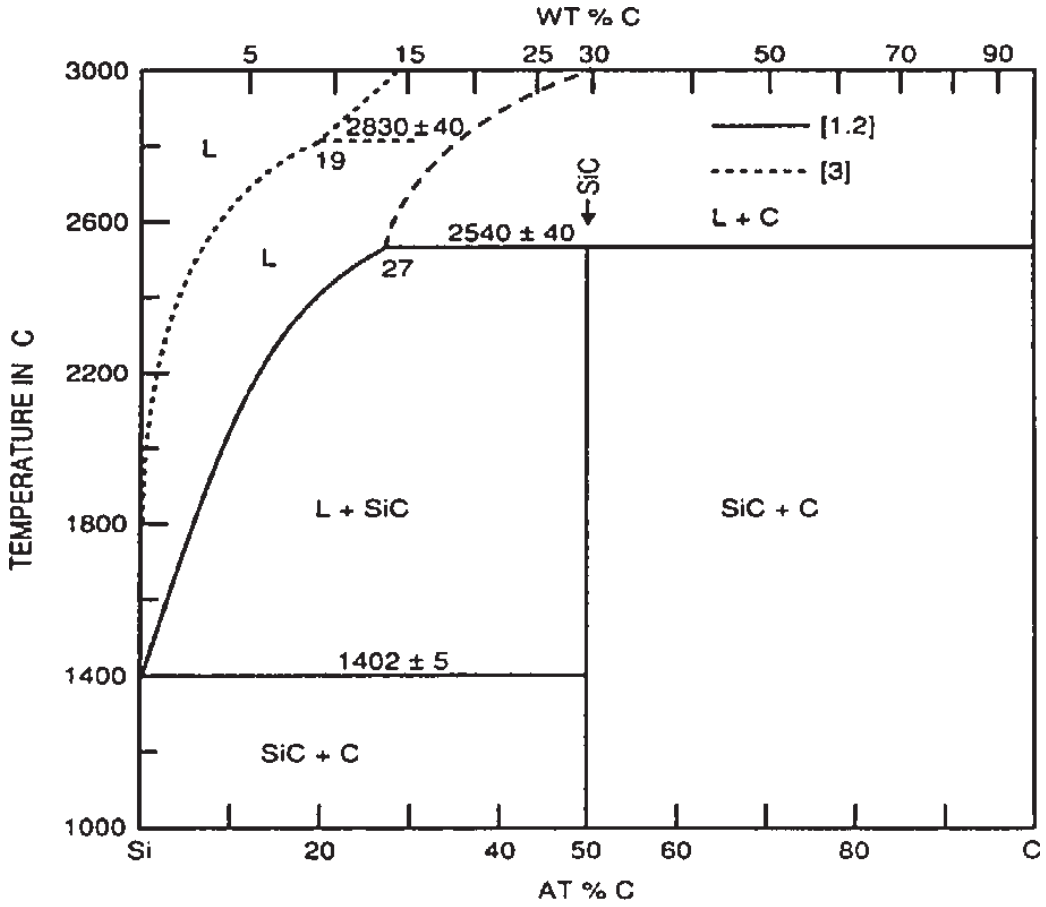
As confirmed by SEM images, the structure change could be not observed after amorphous carbon coating. In addition, STEM images reveal that Si NPs were still well decorated on the individual MWCNTs with defined spacing. EDX technique also shows that the Si-CNT-C (CH_4) consisted of carbon and silicon elements relating to MWCNTs, amorphous carbon, and Si NPs.



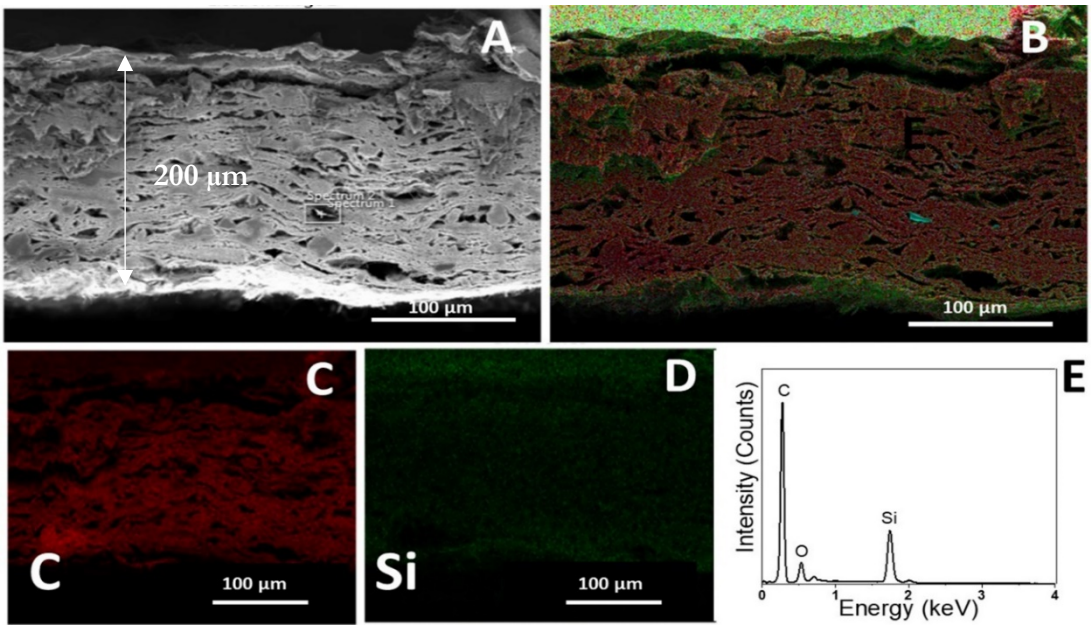
Supporting Figure 5.2. Raman spectra of the Si-CNT-C (CH_4) and Si-CNT materials showing the shift of Si peak in the Si-CNT-C (CH_4) to 500-510 cm^{-1} which assigned to nanocrystalline Si.



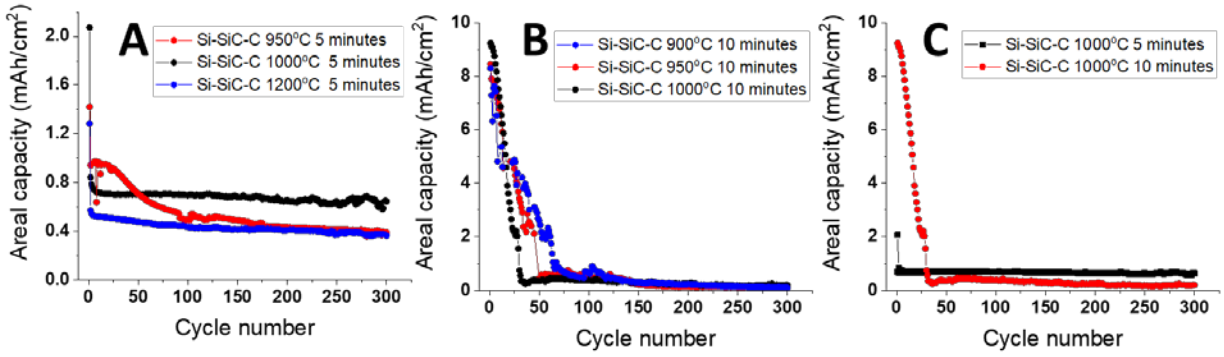
Supporting Figure 5.3. Raman spectra of the Si-CNT-C (C_2H_2) and Si-CNT materials showing the broader Si peak in the Si-CNT-C (C_2H_2) which attributed to a mixture of amorphous and crystalline Si.



Supporting Figure 5.4. A phase diagram of Si-C system [24] showing that SiC can form at 1000°C.

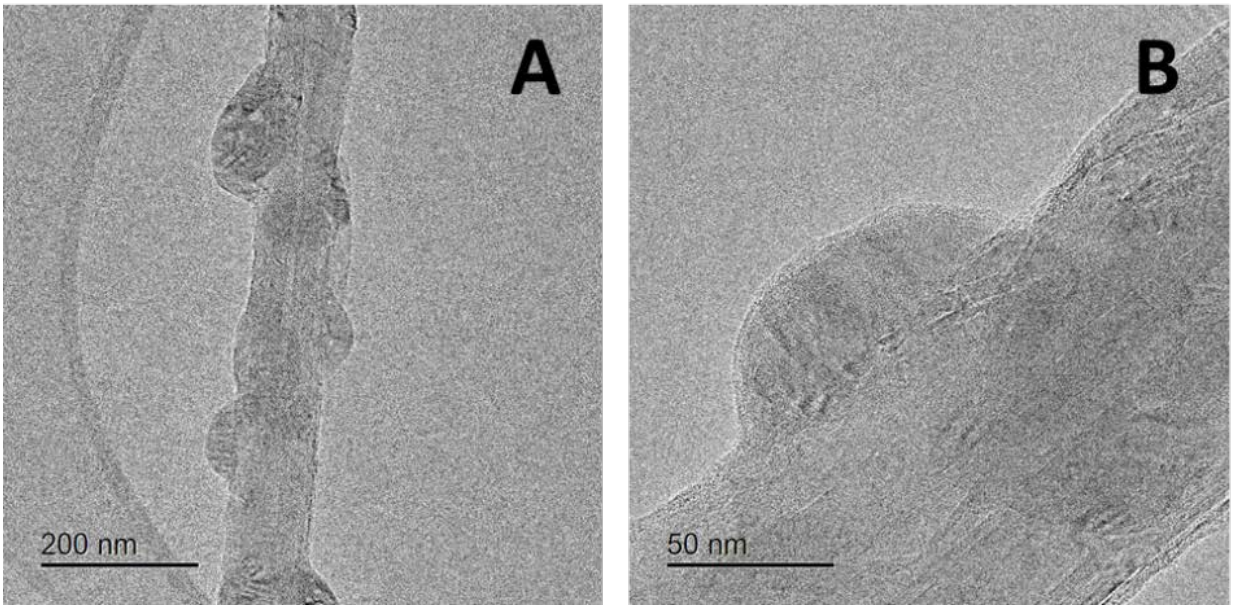


Supporting Figure 5.5. A) A cross-sectional SEM image, B) an EDX mapping image of, and C-D) EDX analysis results showing the structure and component of Si-CNT-SiC-C electrode.



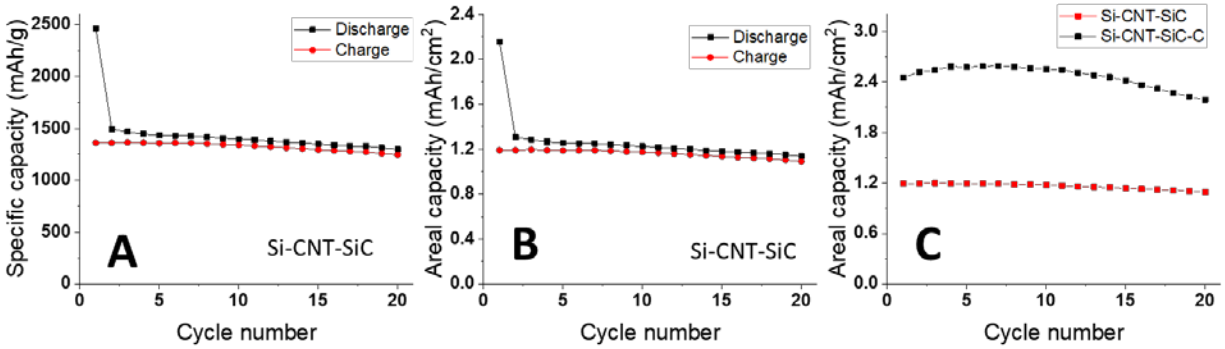
Supporting Figure 5.6. A-C) A differential areal capacity plot of the Si-CNT-SiC-C at different coating time and temperature conditions carried out at C/5 between 0.05 and 2 V; the Si-CNT-SiC-C electrode annealed at 1000 °C for 5 minutes shows good battery stability compared to others.

The different Si-CNT-SiC-C materials were prepared by varying both time and temperature to maximise the battery performance. Supporting Figure 5.6 presents the electrochemical performance of the different Si-CNT-SiC-C electrodes. The Si-CNT-SiC-C at 950 °C condition electrode showed a significant drop of the areal capacity over 300 cycles due to the non-existence/small amount of the SiC interface. Likewise, the Si-CNT-SiC-C at 1200 °C condition electrode exhibited the lowest areal capacity because of the excess of the non-electroactive SiC in the material. Therefore, the suitable SiC interface and amorphous carbon coating are essential factors for the battery performance enhancement in the Si-CNT based electrodes. In order to improve the capacity further, the Si deposition time was increased to 10 minutes. The areal capacity of the Si-CNT-SiC-C at all 10-minute deposition time was boosted up to about 9.2 mAh/cm^2 in the first cycle because of the high amount of Si NPs deposited on the MWCNTs. Interestingly, the areal capacity of these electrodes notably decreased over 50 cycles before remaining stable until 300 cycles. This could be because the annealing time was not long enough to create the SiC after inducing a large amount of the Si on the MWCNTs. Finally, the higher Si content could boost the areal capacity in the first few cycles. However, the key point to enhancing stability was to create a suitable amount of SiC in the Si-CNT based electrode. Therefore, the 5-minute deposition time for Si with 1000 °C annealing temperature was still the best condition to produce the Si-CNT-SiC-C materials in this work.



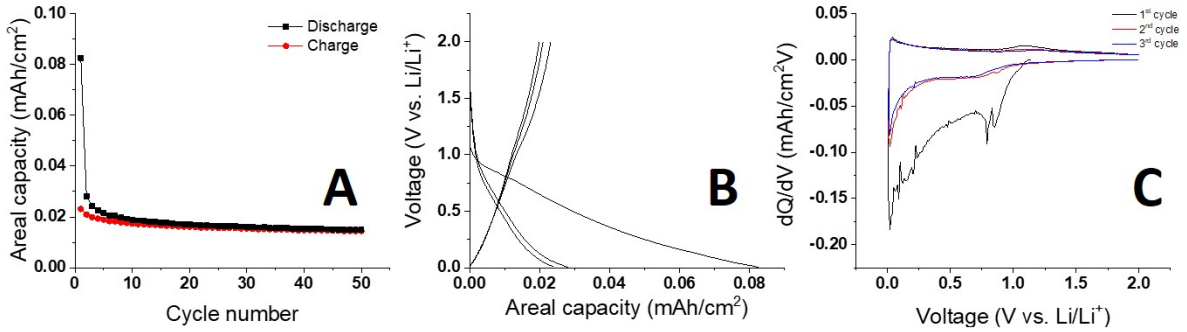
Supporting Figure 5.7. TEM images of the Si-CNT-SiC material (without amorphous coating) at A) low magnification and B) high magnification showing that Si NPs partly immersed inside the wall of MWCNTs indicating the SiC formation after annealing at 1000 °C.

The Si-CNT-SiC shows a similar morphology to the Si-CNT-SiC-C material except for the absence of the amorphous carbon layer outside the Si NPs. The Si NPs were also immersed inside the MWCNTs indicating the SiC interface formation.



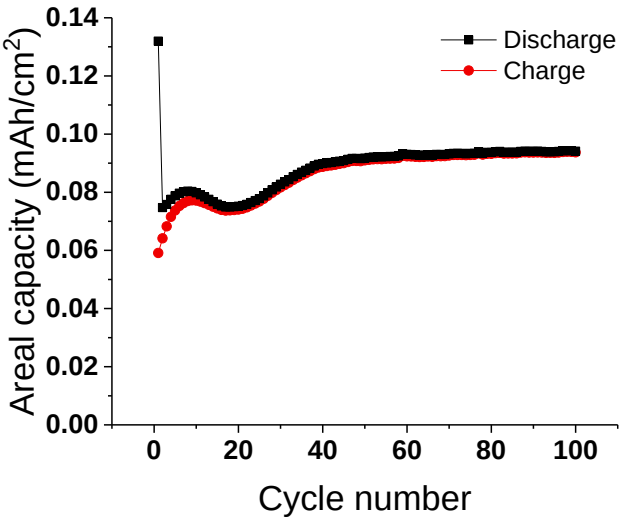
Supporting Figure 5.8. A-C) The areal capacity plots of the Si-CNT-SiC and Si-CNT-SiC-C electrodes carried out at C/10 between 0.05 and 2 V; the presence of amorphous carbon coating (Si-CNT-SiC-C) could improve the battery performance of the Si-CNT-SiC electrode.

The Si-CNT-SiC electrode showed the specific capacities of 2464 mAh/g and 1361 mAh/g at the first discharge and charge respectively, while the areal capacities of the Si-CNT-SiC electrode at the initial cycle were 1.31 and 1.19 mAh/cm^2. The capacity slightly decreased and finally became stable at around 1298 mAh/g and 1.09 mAh/cm^2 after 20 cycles. In addition, the areal capacity of the Si-CNT-SiC electrode was two times less than that of Si-CNT-SiC-C electrode. Therefore, it confirmed the importance of the amorphous carbon coated outside the Si-CNT-SiC material.



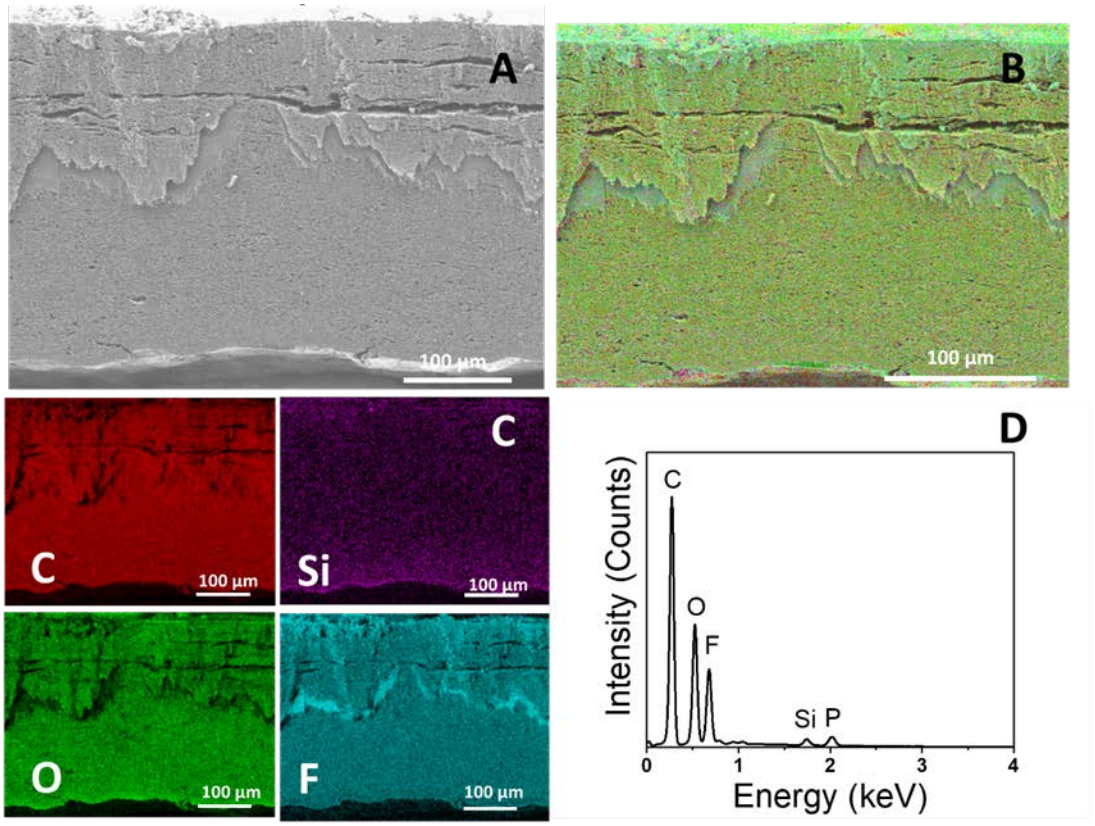
Supporting Figure 5.9. A) The charge-discharge plot showing the battery capability of the pure SiC electrode, B) the voltage profile and C) the differential areal capacity plot carried out at C/5 rate and cycled between 0.05 and 2 V vs Li/Li$^+$ presenting the lithiation/delithiation process of the pure SiC electrode.

The pure SiC was prepared by the calcination method as described elsewhere [42]. The first charge and discharge capacities of the pure SiC electrode were 0.02 and 0.08 mAh/cm^2 with coulombic efficiency of 28%. As a result, the pure SiC was not suitable for anode materials due to its poor electrochemical activity. Although a previous study showed ability of SiC anode material in LIBs, the capacity of this pure SiC was still impractically low compared to Si materials [14]. The sloping voltage profiles and cyclic voltammograms suggested that there was no constitution reaction in the host materials. Although a bump was seen in the first cycle before disappearing in the following cycles, it was a result of the SEI layer formation [43].



Supporting Figure 5.10. The charge-discharge plot showing poor battery performance of the commercial SiC coated on a Cu foil (0.09 mAh/cm^2 after 100 cycles) tested at C/10 rate from 0.05 V to 2 V vs Li/Li$^+$.

The silicon carbide powder purchased from Sigma-Aldrich was mixed with CMC and carbon black in NMP (Sigma Aldrich, 99.5%, C_5H_9NO) before being casted on the copper foil. The electrode was tested for battery performance like the previous SiC electrode. The areal capacity of the SiC electrode was about 0.13 mAh/cm^2 and stable around 0.09 mAh/cm^2 over 100 cycles. Based on the results from the commercial SiC and in-house SiC, it could be strongly confirmed that SiC tended to be poor electroactivity for Li storage.



Supporting Figure 5.11. A) A cross-sectional SEM image of, B) an EDX mapping image of, and C-D) EDX analysis results presenting the SEI component in the Si-CNT-SiC-C material after 300 cycling tests.

Supporting Table 5.1. Comparison of silicon anode performance in LIBs showing the capacity of the materials prepared in this work when compared with other studies.
Note: Free-standing: FS*

Anode	Areal capacity (mAh/cm²)	Cycling stability (mAh/cm²)	Material loading (mg/cm²)	Reference
Carbon-coated porous silicon on Cu	0.195	~ 0.075 after 1000 cycles at 540 μA/cm²	0.092	[44]
Si-CNT paper	1	~ 0.16 after 1000 cycles at 1080 μA/cm²	0.33	[45]
Silicon nano-trees	2.9	~2 after 100 cycles at C/5	1.01	[39]
Si-self-healing polymers (SHP)/CB	1.97	~ 1.7 after 100 cycles at 0.3 mA/cm²	0.72	[41]
Templated carbon bridged oriented grapheme (TCG)-Si	1	~ 0.999 after 200 cycles at 4 A/g	0.8	[40]
Si-CuO/Cu_2O	1.193	~ 0.6 after 200 cycles at 0.225 mA/cm²	1.222	[46]
VACNT-Si on carbon cloth	3.33	~ 2.51 after 200 cycles at 1 mA/cm²	0.79	[47]
Si/C	3.15	~2.3 after 100 cycles at 200 mA/g	3.5	[48]
FS* Si-CNT-SiC-C	**2.01**	**0.55 after 300 cycles at C/5**	**1.1**	**This work**
FS* Si-CNT-C	**4.93**	**0.16 after 300 cycles at C/5**	**N/A**	**This work**
FS* Si-CNT	**7.10**	**0.09 after 300 cycles at C/5**	**N/A**	**This work**
Pure SiC	**0.08**	**0.018 after 50 cycles at C/5**	**0.16 (active materials w/o binders**	**This work**

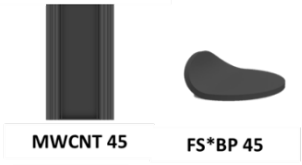
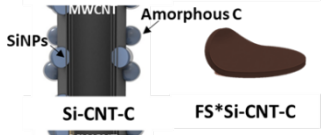
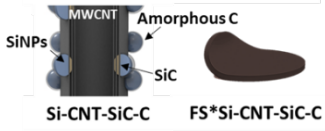
			and additives)	
FS* MWCNT paper	**0.9**	**0.3 after 300 cycles at C/5**	**N/A**	**This work**

Chapter 6

Summary and future work

6.1) Summary of the research

The main aim of this research was to identify a material suitable for replacement of commercially available graphite anodes in LIBs. To do that, BPs made of MWCNTs arranged randomly within flat thin carbon papers, so-called buckypapers, were proposed. First, in-house MWCNTs were synthesised via AACVD to be used for BPs fabrication and further structural modification. The selected AACVD synthesis conditions were studied in order to analyse the quality of the MWCNTs, which allowed for the best quality MWCNT 45 (45 mins of synthesis time) to be selected and used for further BP fabrication (BP 45) due to the lowest amount of catalyst residue (3.4 wt.%). Additionally, commercially available Nanocyl MWCNTs were employed for the BP production (C-BP) as a control material. The result indicated that BP 45 had much higher electrical conductivity and better capacity retention after 300 cycles (0.3 mAh/cm^2) than C-BP (0.18 mAh/cm^2) as shown in Figure 6.1. However, while looking at the capacity of fabricated BPs (*ca.* 290-100 mAh/g, 0.3-0.18 mAh/cm^2, Figure 6.1), it was still not high enough to replace the commercially used graphite anodes (372 mAh/g).

	Electrical conductivity (S/cm)	Areal capacity (mAh/cm²)	Cycling stability after 300 cycles (mAh/cm²)	% Capacity difference from the BP *	Structural conservation after the cycling test
	16.0	3.02	0.18	-40	N/A
	22.2	0.9	0.3	N/A	✓
	15.5	7.10	0.09	-70	✗
	17.7	4.93	0.16	-46.7	N/A
	25.0	2.01	0.55	+83.3	✓

*** The areal capacity of the electrode and BP 45 at 300th cycle were used for the calculation, plus and minus signs define increase and decrease in percentages**

Figure 6.1. The summary of this work; five different types of the free-standing electrodes were prepared. The BP made from in-house MWCNTs showed better battery performance than that of the BP made from the commercial Nanocycl MWCNTs. The Si-CNT-SiC-C electrode showed the best capacity retention after 300 cycles (0.55 mAh/cm²) compared with other electrodes. Its capacity was improved by 83.3% compared with the pure MWCNT paper (BP 45) electrode and the structure of the electrode was maintained after the battery testing.

In order to find a method that enhances the overall battery performance of the electrode, the BP 45 was processed by coating the MWCNTs with Si NPs (named Si-CNT). The Si-CNT exhibited a high areal capacity in the first cycle (7.10 mAh/cm^2), but poor rate capability and capacity stability after 300 cycles (0.09 mAh/cm^2, Figure 6.1). Furthermore, the post-cycling studies, *i.e.* examination of the Si-CNT morphology after the cycling test, demonstrated several cracks within the electrode. The structure of Si NPs in the material exhibited irregular features due to the 300% volume change. According to these findings, it was concluded that the decoration of outermost MWCNT walls with Si NPs was insufficient for enhancing the overall battery performance. Particularly, the MWCNTs

could not accommodate the induced-stress due to a tremendous volume expansion of Si NPs. The detachment of Si NPs from the MWCNT wall upon cycling was observed because of the weak interface between these two materials. Hence, further post-modifications of the Si-CNT material were necessary in order to improve the final performance of the battery.

A thin layer of amorphous carbon was further deposited on the Si-CNT material to improve the stability of the Si-CNT electrode. It was expected that flexible amorphous carbon layer could impede the direct contact between Si NPs and electrolyte by allowing only Li ions to penetrate through, leading to stable SEI formation on its surface during cycling. Two different gas sources were employed in this work: methane (Case I) and acetylene (Case II) to coat amorphous carbon on the Si-CNT material. The trace of SiC material was found in Case I, while only amorphous carbon species were identified on the surface of MWCNTs in Case II. It was observed that the final battery performance at the 300th cycle was significantly enhanced (0.37 mAh/cm^2) by introducing SiC within the Si-CNT-C structure (Case I) in comparison to Case II (0.16 mAh/cm^2). Thus, the amorphous carbon layer coating in Case II was most likely inadequate for electrode stability improvement.

Consequently, it had been decided to post-process the Si-CNT material by annealing it at high-temperature range (990-1200 ^{o}C). This allowed a formation of SiC interface between both Si NPs and MWCNT walls. After annealing at 1000 ^{o}C, the partial SiC interface was formed, but Si was fully transformed to SiC when the annealing temperature reached 1100 ^{o}C. The electrical conductivity of the Si-CNT-SiC-C material was 25 S/cm (Figure 6.1) which is higher than the minimum electrode conductivity value for maintaining high-rate cycling (0.01 S/cm) [3, 4]. Both coin-cells and pouch-cells were then fabricated using the Si-CNT-SiC-C (1000 ^{o}C) electrode. It was found that additional SiC interface in the Si-CNT-SiC-C structure enhanced the capacity retention of the electrode. That is, the strong SiC interface prevented Si NPs from detaching from MWCNTs during the cycling. Additionally, the amorphous carbon coating improved the battery performance of the Si-CNT-SiC

material by maintaining the structural stability and restricting SEI formation on the amorphous carbon layer upon cycling. After 300 cycles, the areal capacity of the Si-CNT-SiC-C electrode reached 0.55 mAh/cm^2 with 99.7% of coulombic efficiency, which was increased by 83.3% compared with the BP 45 electrode (Figure 6.1). Moreover, the post-cycling analysis confirmed that the Si-CNT-SiC-C material preserved its initial structure without cracks after the battery testing, which was not observed in the case of the Si-CNT material.

To conclude, the capacity retention improvement of Si-CNT-SiC-C electrodes when compared with the Si-CNT material was due to the presence of additional SiC interface as well as the amorphous carbon layer. However, the Si-CNT-SiC-C electrodes still had relatively high irreversible capacity in the first few cycles. According to the post-cycling characterisation results, the most probable explanation of this would be the SEI layer formation inside the pores within the electrode. Also, the Si-CNT-SiC-C battery performance with the areal capacity of 0.55 mAh/cm^2 and volumetric capacity of 28 mAh/cm^3 after 300 cycles is significantly inferior when considering the theoretical capacity of Si and other Si studies [5, 6]. This is ascribed to a low material density of the Si-CNT-SiC-C electrodes due to the high material porosity and a small amount of Si within the final structure.

The findings discussed in this work, therefore, show the potential use of the Si-CNT-SiC-C electrode in LIBs. Nevertheless, some further modifications such as increasing Si loading and optimising the electrode porosity are required in order to improve the overall Si-CNT-SiC-C electrode-based battery performance, especially areal and volumetric capacity. The electrolyte additives are required to be used when assembling the battery cell. Since these additives form a flexible SEI on the electrode, this approach will address the unstable SEI formation during the repeated cycling, leading to battery stability enhancement. In addition, further characterisation of the Si-CNT-SiC-C electrode, particularly *in situ* TEM, is necessary to study the structural change of the material in real-time as it will allow a researcher to confirm the structural stability of the Si-CNT-SiC-C electrode upon cycling

due to the presence of the SiC interface. The detail of further work will be discussed in the next paragraph.

6.2) Future work

In order to improve the overall battery performance based on herein investigated Si-CNT-SiC-C electrodes, further research is necessary. The flow chart summarising the future work is shown in Figure 6.2. The further study includes modification of Si-CNT-SiC-C material, adjustment of the cell component, and additional characterisations of the Si-CNT-SiC-C electrode.

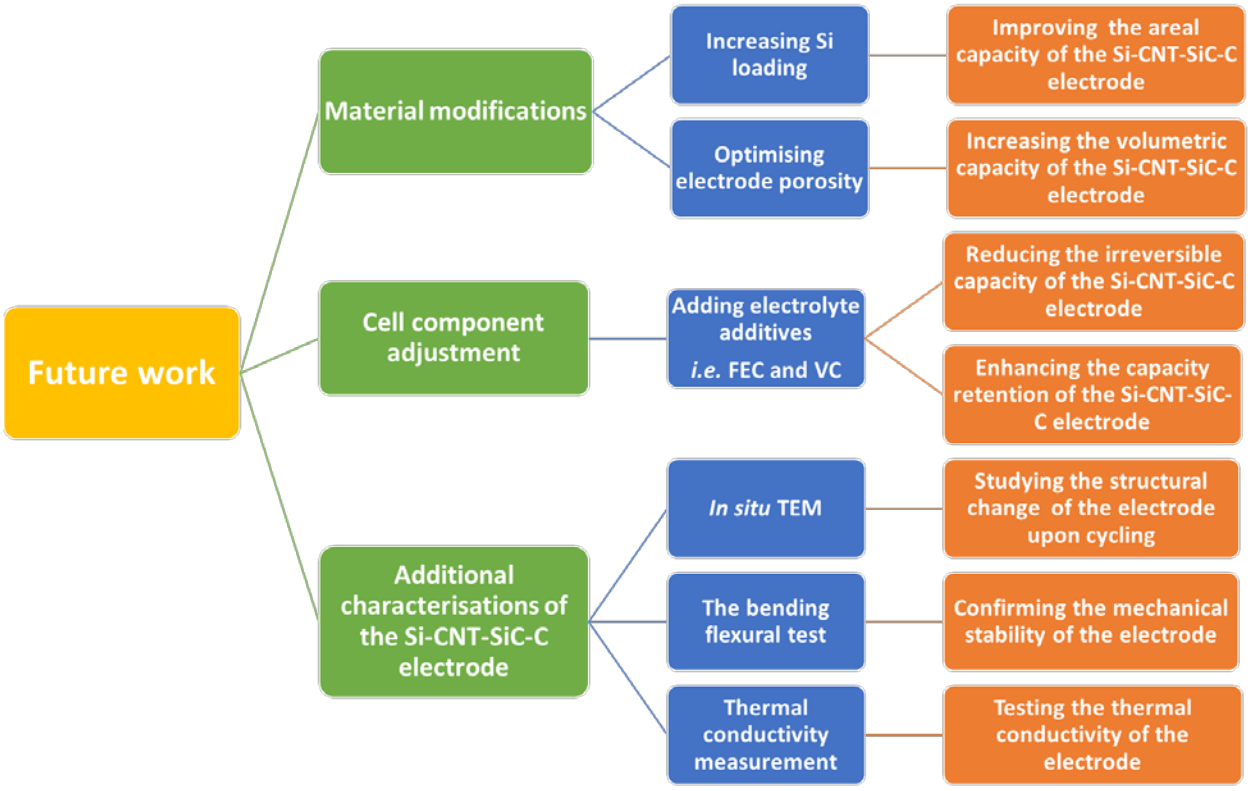


Figure 6.2. The flow chart presenting the summary of the future work; it includes material modifications, cell component adjustment, and additional characterisations of the Si-CNT-SiC-C electrode. The approaches and expected outcomes are shown in blue and orange boxes, respectively.

As shown in Figure 6.2, the material modification will be an important stage for the battery performance development. First, in order to enhance the areal capacity of the Si-CNT-SiC-C electrode, the content of Si in the material should be increased by extending the Si deposition time. It was found that the areal capacity of the Si-CNT-SiC-C electrode was improved when increasing the

percentage of Si coating (Supplementary Figure 5.6). However, its stability was poor, which was most probably due to a small extent of SiC interface formed on the Si-CNT-SiC-C material. Thus, the content of SiC in such electrode needs to be increased to elevate the electrode stability, and that can be achieved by changing the annealing time (more than 30 minutes). Second, the porosity of the Si-CNT-SiC-C electrode needs to be adjusted to increase the volumetric capacity. The void spaces in the Si-CNT-SiC-C material are required for accommodating the volume expansion and reducing mechanical stress generated by the Si lithiation, but the excessive porosity of the material causes a low volumetric capacity and a high irreversible capacity of the electrode. Since the BP is used as a free-standing substrate, the increase of the BP packing density leads to the reduction of the material porosity. The packing density of BP can be easily increased by applying compressive pressure after the fabrication.

The cell component adjustment will be another step for improving battery capability (Figure 6.2). Electrolyte additives such as fluoroethylene (FEC) and vinylene carbonate (VC) would reduce the irreversible capacity and then improve capacity retention of the Si-CNT-SiC-C electrode. This approach will tackle the unstable SEI formation issue because a flexible and stable SEI layer on the Si surface formed by both additives can withstand the stress induction from Si volume change [7]. It is also a simple way to enhance battery performance as only the component of the electrolyte is adjusted with the additives; no material modification is required in this method. The battery performance of Si-CNT-SiC-C electrodes was preliminarily tested with and without additives in the electrolyte, but the details of that additional experiment were not discussed in this work (Figure 6.3). The cell with VC additive showed better cyclability than the cell with the FEC additive. It was due to the fact that the SEI layer is more flexible when using VC additive and thus better resists the volume change of the electrode compared to FEC additive [7]. However, the dramatic capacity drop in the first few cycles was observed, which has not been reported elsewhere [7]. Since the Si-CNT-SiC-C material is highly

porous, it is most probably related to the formation of the additive decomposition products inside the material pores, which is similar to the interior SEI formation in the post-cycling result. Therefore, an *in situ* analysis should be conducted to investigate the effect of additives inside the electrode and to explain the massive capacity drop.

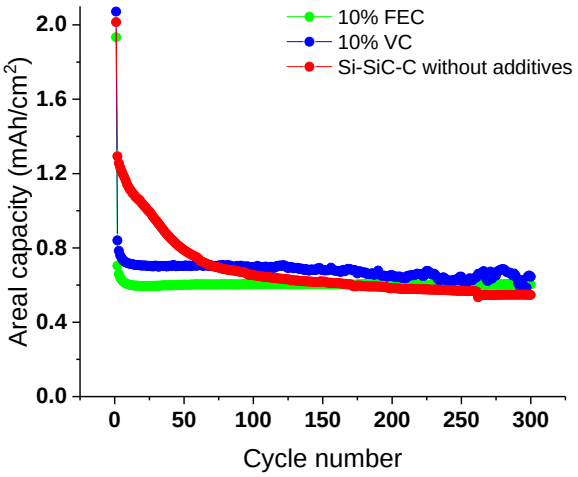


Figure 6.3. The areal capacity of the Si-CNT-SiC-C electrodes made with and without additives (FEC and VC); there is a huge capacity drop in few cycles even though the stability of the electrode was enhanced when additives were added in the electrolyte.

The use of additional characterisation of Si-CNT-SiC-C electrode (Figure 6.2) is necessary to improve the quality of discussion as well as a more in-depth understanding of the phenomena described in this work. The *in situ* TEM should be employed to examine the structural changes of Si NPs attached to MWCNTs during the repeated cycling process. As the *in situ* TEM analysis allows the real-time change of the Si-CNT-SiC-C structure upon battery cycling to be studied, it can be used to explain the SiC stabilisation effect. Understanding of the SiC stabilisation process would enable further material development in order to improve its mechanical stability during cycling. An example of the possible setup of a battery cell within a TEM holder is shown in Figure 6.4 [1]. The sample (Si) and Li metal electrodes are attached to the platinum electrode. A silicon nitride membrane is used to seal the electrolyte while still allowing the electron beam to pass through, enabling imaging (Figure 6.4A). The battery testing equipment such as a potentiostat is connected to the battery cell via wires in the shaft of the TEM holder (Figure 6.4B). Therefore, the preparation of the Si-CNT-SiC-C sample is a main

challenge for the *in situ* TEM study. As the Si-CNT-SiC-C is in the form of the free-standing material, it must be cut and dispersed in the solution before attaching to the Pt electrode. Additionally, one of the difficulties is to mount the material on the electrode without damaging its structure. The main limitation of the *in situ* TEM technique is also similar to a standard TEM, *i.e.*, the size of the sample should be less than 100 nm in order to allow a beam of electrons to transmit through and thus to obtain the high-resolution images of the structure.

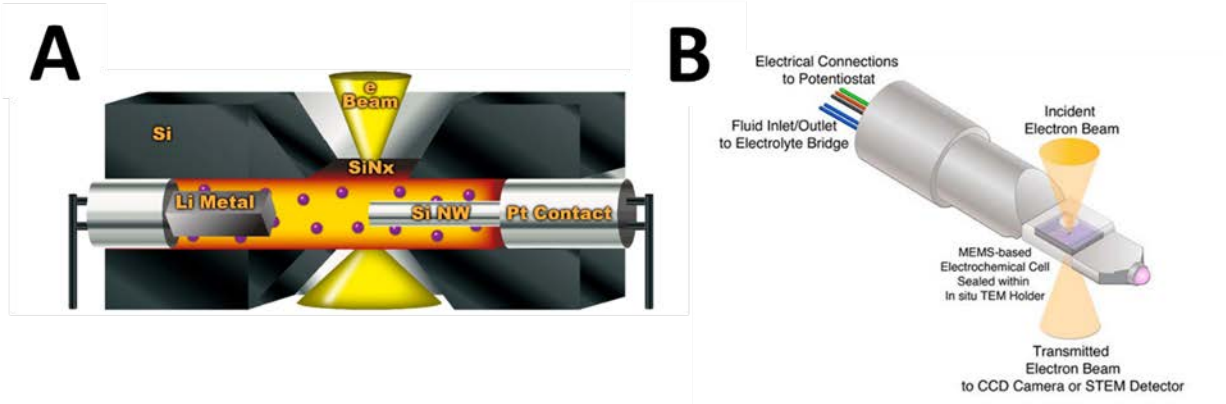


Figure 6.4. A) A configuration of the battery cell in a TEM holder; Si and Li metal are mounted on the Pt electrode and the silicon nitride is used to seal the electrolyte [1]. B) A holder for the in situ TEM study; the battery tester (a potentiostat) is connected to the battery cell via wires in the holder shaft [2].

Furthermore, the mechanical and thermal properties of the Si-CNT-SiC-C electrode should be further investigated. A three-point bending flexural test should be conducted to study the bending modulus of the electrode. Such analysis will allow to explain the mechanical stability of the free-standing Si-CNT-SiC-C electrode. Finally, the thermal measurements will help to evaluate the thermal properties of the Si-CNT-SiC-C materials such as thermal conductivity and heat dissipation manner within a material. That can be easily evaluated by a hot disk transient plane source method and a thermographic camera. Since the high thermal conductivity is beneficial to the heat dissipation inside the battery during the fast-rate cycling, the thermal profile of electrodes during battery testing should be further explored. To sum up, there are a large number of different routes and possibilities to explain

and understand the findings discussed in this work by either modifying the material structure or using additional characterisation tools.

6.3) References

1. Gu, M., et al., *Demonstration of an Electrochemical Liquid Cell for Operando Transmission Electron Microscopy Observation of the Lithiation/Delithiation Behavior of Si Nanowire Battery Anodes.* Nano Letters, 2013. **13**(12): p. 6106-6112.
2. Unocic, R.R., et al., *Direct Visualization of Solid Electrolyte Interphase Formation in Lithium-Ion Batteries with In Situ Electrochemical Transmission Electron Microscopy.* Microscopy and Microanalysis, 2014. **20**(4): p. 1029-1037.
3. Tian, R., et al., *Quantifying the Effect of Electronic Conductivity on the Rate Performance of Nanocomposite Battery Electrodes.* ACS Applied Energy Materials, 2020. **3**(3): p. 2966-2974.
4. Mistry, A., et al., *Analysis of Long-Range Interaction in Lithium-Ion Battery Electrodes.* Journal of Electrochemical Energy Conversion and Storage, 2016. **13**(3).
5. Wang, X., et al., *A hierarchical 3D carbon nanostructure for high areal capacity and flexible lithium ion batteries.* Carbon, 2016. **98**: p. 504-509.
6. Marinaro, M., M. Weinberger, and M. Wohlfahrt-Mehrens, *Toward pre-lithiatied high areal capacity silicon anodes for Lithium-ion batteries.* Electrochimica Acta, 2016. **206**: p. 99-107.
7. Jaumann, T., et al., *Lifetime vs. rate capability: Understanding the role of FEC and VC in high-energy Li-ion batteries with nano-silicon anodes.* Energy Storage Materials, 2017. **6**: p. 26-35.